Shallow-water skimming, skipping and rebound problems

Jia Liu

Department of Mathematics

University College London

A thesis submitted in partial fulfilment

of the requirements for the degree of

Doctor of Philosophy

March 2017

I, Jia Liu confirm that the work presented in this thesis is my own. Where information has been derived from other sources, I confirm that this has been indicated in the thesis.

Abstract

The subject of water-entry related problems has a wide range of applications in industries and natural sciences. In this thesis we study the dynamics of a solid body slamming, skimming, rebounding or sinking in shallow water. We reconcile and extend some existing mathematical models, primarily by exploiting the existence of one or more small parameters via the method of asymptotic expansions, as well as deriving new models of interest.

This thesis begins by providing an overview of the existing solid-liquid impact and skimming modelling; reviews of relevant literatures as well as some key modelling assumptions used throughout the thesis are introduced. The problem of a thin object skimming on a layer of shallow water is analysed in Chapter 2 and 3. A model that describes such an object's motion from its moment of water impact to eventual exit (or sinking) is introduced. Asymptotic behaviours of the object based on its mass, moment of inertia as well various water entry profiles are studied, yielding results in qualitative agreement with physical experiments. We subsequently shift our modelling effort from that of a thin body to one with non-negligible thickness in Chapter 4 and 5. In such case the unknown position of the object's trailing separation edge, as well as its surface curvature pose additional modelling complexities. Chapter 4 focuses on analysing flows in a small region enclosing the object's trailing separation edge; analytical as well as numerical solutions of the flow in this region are presented. Chapter 5 models the complete transition cycle of water entry to water exit for a blunt body. A three-phase planing model is presented based on the presence of a weak adverse pressure gradient at the trailing edge. In Chapter 6 we investigate the phenomenon of a thin object that first undergoes a skimming motion and is subsequently subject to flooding over its upper surface. Numerous conditions are investigated to establish whether such an object is able to re-emerge from

water or sink to the flow bed. We conclude this thesis with summaries of our main results and possible directions of further research.

Contents

Chapter 1

Introduction

1.1 Background overview

Skipping stones, or a game of ducks and drakes as it is also known, is a popular waterside activity. When thrown by a skilled hand, a rock weighting around 200 grams can continuously skip on water well over 100 meters. The current world record stands at eighty-eight skips and was set by Kurt Steiner of USA in 2013. The phenomenon of high velocity solid-fluid impact is of course not limited to recreational activities, and occurs in many disciplines of engineering sciences as well as in our natural world.

A basilisk lizard for example, native to central and south America, can grow up to 70 centimetres in length and weights around 200 grams. The long toes on its rear feet can unfurl wide and scaly skin fringes, which drastically increase the surface area of its feet. When frightened, such a lizard has the ability to sprint, upright, across the surface of water at a speed of 1.5 meters per second by rapidly churning its rear legs, see Fig. 1.1a (National Geographic, 2014). A ship sails through waves as water slams against its hull. Under rough conditions the ship can elevate to a significant height with the wave and experience heavy slamming to its bow and bottom when hitting the trough. Such high velocity impact between the vessel and nearly incompressible seawater creates an enormous

pressure-impulse on its hull, and may result in structural damage, internal frame buckling as well as a vibratory response of the hull, known as "whipping", which in turn poses significant structural stress and fatigue to the hull (American Bureau of Shipping, 2011). Aeroplane-landing on water, or ditching as it is also known, is an emergency landing procedure on water. It has a significant impact on the plane's structural integrity and if performed incorrectly may yield catastrophic consequences. According to the Crew Training Manual for Boeing 737 passenger aircraft (The Boeing Company, 1999), ditching should be carried out at a very low speed of descent of 1 to 1.5m/s and a forward speed of about 50m/s. Such operation is significantly more challenging if severe swells or breaking waves are present in the water. Understanding the dynamics of high velocity solid-liquid impacts therefore has a wide range of industrial, environmental and scientific applications.

Since the pioneering work of [34] on studying the landing of seaplanes there have been continuous researches into this area. Early theoretical developments such as [70, 34, 35] focused on the early stages of vertical impacts by wedge-like objects, where the "dead-rise" angles[1] are small, the impact velocities are assumed to be constant and the penetration depths compared with the spans of the wetted surfaces are small. The fluid under consideration was typically idealized to be incompressible, irrotational and not subject to effects of gravity, surface tension or viscosity. Under these assumptions [35] proposed that at an early impact stage the wedge shaped object can be approximated by an "expanding" flat body; the depth of penetration and resulting free surface elevation at this stage are small, and the splash jets generated by the impact are thin and have insignificant contribution to the free surface flow. Wagner formulated a potential flow problem and linearised the free surface boundary conditions onto one that is at rest, and the roots of spray jets due to impact are linearised onto the surface of the impact body. Impact problems under these impositions are collectively referred to as Wagner flow problems. Considerable amounts of

[1] "Dead-rise" angle: the angle between the tangent to the impact body's surface and the resting fluid's free surface.

(a) A basilisk lizard runs on water.

(b) A stone skips on water.

(c) Surfboard in motion.

(d) Ship slamming in rough sea.

(e) Ice crystals hitting aircraft.

(f) Plane landing in water (ditching).

Figure 1.1: Various modelling applications of solid-fluid impact problems. From top left clock-wise: a) a basilisk lizard running on water; b) a stone skips from water into air; c) a surfboard in planing motion while carrying an adult; d) a ship experiences slamming to its bow and bottom in the open ocean; e) ice-crystals hitting the damp fuselage of an aeroplane; f) an airplane landing on water.

research and experimental studies have been dedicated to the Wagner flow problems since the initial publication of [35]. A comprehensive review of the subject is given by [4], while [46] offers a review of various related numerical solutions and experiments. More recent works by [77, 5] reformulated the Wagner flow problem to one of displacement potentials and found explicit solutions to the Wagner problem for several 3D (three-dimensional) impact body profiles.

Another class of solid-fluid impact problems concerns rigid bodies skimming or skipping on liquid surfaces; the impact velocity is usually oblique to the free surface and the time scale of interest is not limited to the initial stage of impact. The solid-fluid interaction can be separated into three consecutive stages: an initial impact stage, a subsequent planing stage and an eventual water separation or sinking stage. Early works by [7, 8] analysed the steady gliding of a plate on a water stream of finite depth; it is demonstrated, under the assumption of 2D mass continuity condition, the difference in the stream's depths before and after the gliding plate directly influences its lift. [62, 21] subsequently analysed the steady skimming motion of a surf skimmer on shallow water; in order to account for the observed free surface elevation immediately ahead of the skimmer due to water "pile-up" effect, the upstream flow before the skimmer is divided into two regions, and a relation of water depths in these two regions with that of downstream behind the skimmer is obtained via matched asymptotic analysis. [57] deployed similar pressure and momentum jump conditions in [21], a shallow water skipping-stone model was introduced which accounts for the stone's skimming motion and water-exit under hydrodynamical forces. There are also numerous experimental studies on skimming or skipping motions; experiments by [15, 44, 37] offer high quality observational data of thin stones or flat plates skipping on water. These studies demonstrate the free surface elevation and total solid-fluid surface contact area play important roles in the skimming dynamics, the determination of which form integral parts of a water skimming problem.

1.2 Research aim and thesis structure

We begin our thesis by providing a review and generalisations of some existing methods of modelling the free skimming of objects of negligible thickness; we will also obtain, understand and analyse certain new solutions of interest. In particular we shall deploy the method of asymptotic expansions to analyse the effects of various skimming configurations such as contact angle, impact speed and body mass on such object's skimming motion. We shall limit our discussions to water layers of small depths when compared to the skimming bodies' lengths, i.e. suppose the water depth is h and the skimming body's length is L, then $h/L \sim O(\epsilon)$ where ϵ is small ($\epsilon \ll 1$). The model for a thin body is then subsequently extended to incorporate a smoothly curved (blunt) object impacting and skimming on water. The body's planing behaviour and flow solutions are analysed via method of matched asymptotic expansions. We also present a "flooding" model which aims to analyse the motion of an initially skimming thin body that is subsequently subject to over-head flooding. We shall ascertain some conditions under which the body is able to re-emerge from water. Throughout our thesis the fluid's surface tension, gravity and viscosity will be neglected, the justifications of which will be given in each model's development stage. Further we shall also neglect the effects of air cushioning at impact, for relavant analysis on air cushioning effects see [2, 27, 56].

Chapter 2 analyses the skimming of a thin flat plate on shallow water with small contact angle. We shall extend the asymptotic analysis originally introduced by [57]. The early impact time asymptotic analysis work, which reduces the complexity of the skimming model, demonstrates such simplified models are able to capture the essential behaviours of the skimming body and ambient fluid flow. The chapter concludes with discussions on extending the model to incorporate multiple rebounds.

The chapter 3 presents a Liu & Smith paper [40] published in *Proc. R. Soc.* 2014 as part of this doctorate research. The paper is a further extension of the

Hicks & Smith asymptotic model presented in Chapter 2, with new pressure and body response analysis based on increased as well as reduced vertical water entry velocity.

In Chapter 4 we focus on analysing the departure region of a skimming object with a smooth body shape and unknown trailing edge location. Relations between fluid velocity, pressure from underneath the skimming body and the departure surface profile, as well as the downstream fluid velocity are derived. The analytical results and numerical investigations for this model are presented and compared for accuracy.

Chapter 5 extends the Hicks & Smith skimming model to incorporate a body whose contact line with water in two dimensions is parabolic. The skimming process of such a bluff body can be divided into two consecutive stages: an initial impact stage and if condition permits, a subsequent planing stage. Our analysis shows the pressure gradient at the trailing edge plays a critical role in the planing motion of the body. We further present a three-phase planing model for the presence of a weak adverse pressure gradient at the trailing edge.

In Chapter 6 we analyse the motion of a thin body that is initially subject to either partial or complete flooding over its upper surface. We focus our modelling on a surfboard in motion. This "flooding" model assists us in drawing conditions under which a surfboard is either able to maintain its surfing motion or sink further into water and hit the bottom of the water layer.

In Chapter 7 conclusions are drawn and future research is proposed.

Chapter 2

Thin plate skipping on shallow water

2.1 Introduction

The study of solid objects freely skimming and skipping on shallow water is motivated by various industrial, environmental and recreational applications, such as modelling ice crystals hitting wet aircraft fuselages in air; formation of tsunamis by calving glaciers; aircraft landing on water; a game of skipping stones and other similar water entry phenomena [75, 70, 34, 1, 57].

Early models by [62, 21] studied the dynamics of a board skimming on shallow water. [62] provided a steady flow approximation of the pressure underneath a skimming board, and demonstrated that for such a board whose length is much greater than the water depth, the steady flow theory yields remarkable agreement with empirical observations. [21] derived a shallow water steady flow model together with a set of pressure and momentum jump conditions at the leading wetted edge. Neglecting any splash jet and lateral flow components, this model is able to determine the position of the leading wetted edge and hence the area of the contact surface; the hydrodynamic pressure force on the board

was obtained in terms of a lift coefficient based on the ratio of water depths before and after the board. [1] studied the early stage of vertical impact by flat structures onto shallow waters; matched asymptotic analysis was performed in the ambient flow regions surrounding the impact body, from which the effects of the impact body's shape have on the flow and pressure distribution were obtained. [59] modelled a rigid cylinder falling vertically onto a resting water layer as a basis of studying the stabilities of semi-submersed pontoons; a Wagner flow problem was formulated and solved via method of matched asymptotic expansions; the outer flow domain away from the liquid/body contact line was shown to have a self-similar solution, and the inner flow was formulated and solved as a classic jet problem. A study by [67] considered oblique slamming and planing on water by incorporating a tangential velocity component to the Wagner and Korobkin theories of normal impacts; this offers a way of connecting the theories of normal impacts with that of planing and skimming; the vertical velocity of the impact body was assumed to be constant and therefore the rebounding phase was not considered.

In addition to the aforementioned theoretical work, there exist various experimental studies particularly on modelling of skipping stones. [15] monitored the impacts by a stone skipping on water. The observations suggest that a contact angle of $\sim 20°$between the disk and water surface in general gives the minimal time required for a rebound; it was proposed that the spinning motion of the stone during skipping has a gyroscopic stabilising effect, which helps the stone maintain its optimal entry angle during skipping. This experiment was further extended by [44] to incorporate multiple skips. A separate study by [37] examined a flat rectangular paddle with one end attached to a pivot arm and its body planing and skipping on the surface of a shallow stream. The experiment demonstrated that the paddle transitions from a skimming state to a skipping state or vice versa depending on the paddle's weight and angle of attack; it was further observed that a build-up of a water wedge ahead of the paddle increases the contact area as well as the time the paddle stays in contact with the

underlying water, which significantly contributes to the lift on the skimming body.

[57] proposed a model for freely skipping stones on shallow waters; the planing theory of [21] was extended to capture the unsteady interaction between the fluid and solid body from an early impact stage to eventual rebound (separation from water). The model describes the evolution of the body's motion in terms of its skimming angle, centre of mass position and its contact surface with water. For the remainder of the chapter we shall have a review of this skipping stone model and further extend the asymptotic analysis at small impact times; we will also simplify the original model under certain configurations of water entry profiles. The new findings from the asymptotic analysis shall be reconciled with results from other aforementioned research outcomes.

2.2 Model development

Consider a hand-sized stone that is long and thin, whose shape is similar to a flat plate, skipping on a layer of shallow water at high horizontal speed. Suppose this plate has uniform density, with length and width of $2L$ and $2T$ respectively, so that L and T measure the length and width from the plate's centre of mass to its respective edges, and that $L \gg T$. We let h denote the depth of the water layer, it being shallow implies that $L \gg h$. Assuming further that the contact angle θ between the stone and undisturbed water surface is small (i.e. $\theta \sim 10^\circ - 20^\circ$), in two dimensions this can be idealised to a plate with large aspect ratio as shown in Fig. 2.1. Let (u_0, v_0) be such a plate's horizontal and vertical velocity components respectively at the instant of impact; the comparatively large horizontal speed implies $v_0 \ll u_0$ with u_0 and v_0 being negative due to our choice of coordinate system.

When a plate is going through skimming motion on water in three dimensions (3D), a portion of water goes under the body and exits into the downstream behind it; a portion of the water goes around the body via lateral flow and

the rest gets thrown forward ahead of the body in the form of a spray jet. The free surface of the stream and the jet form surfaces of discontinuity, along which the pressure is atmospheric and the velocity is constant and equal to that of the undisturbed upstream flow [7]. The lateral flow component cannot be accounted for in two dimensional modelling, however experimental observations suggest this only accounts for around 30% of the overall downstream flow [21], therefore such neglect in any case should have limited effect on the modelling accuracy in two dimensions (2D).

Introduce a moving Cartesian system (x, y) based on the location of the skimming plate such that the x axis rests at the bottom of the water layer, the y axis points vertically upwards and always passes through the plate's centre of mass, say (x_m, y_m) with $x_m = 0$, see Fig. 2.1. In this frame of reference the plate's centre of mass is capable of moving up or down vertically but remains horizontally still. The plate penetrates the free surface at angle θ, which is subject to change as the plate moves up or down and rotates freely under the influence of hydrodynamic forces. Throughout our analysis this plate is taken to be skipping in the direction of the negative x axis, and the flow is idealised to be incompressible and irrotational.

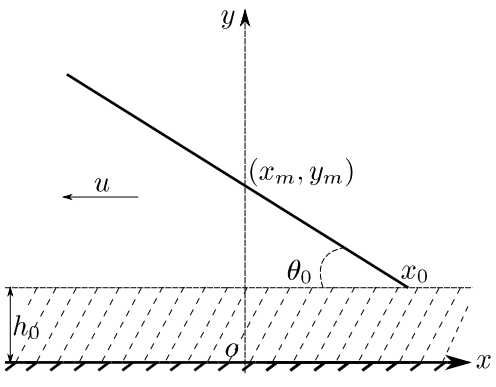

Figure 2.1: Thin flat plate with incident angle θ_0 at the instant of impact with liquid layer at rest, and its body thickness T is ignored for illustration simplicity. θ_0 is small. At this instant the plate's leading edge coincides with its trailing edge at (x_0, h_0), with the plate's centre of mass at $(0, -x_0\theta_0 + h_0)$. The angle θ_0 is small, the shallow liquid layer at rest has depth of h_0 and is small in comparison to the length of the impact plate $2L$.

As the body skims through water, the upstream flow ahead of it can be

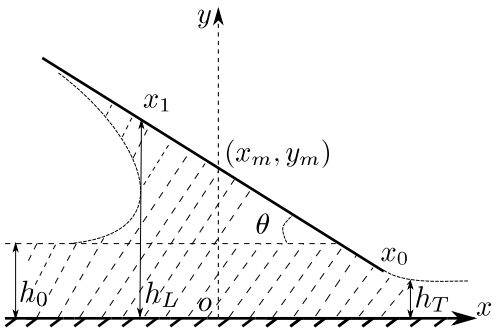

Figure 2.2: Flat body with negligible thickness in skimming motion with water departing smoothly from its trailing edge. As the plate penetrates deeper below the free-surface, water begins to pile-up ahead of its body. The leading edge is denoted as x_1 and the distance between the leading and trailing edges captures the contact surface between fluid and body. This contact surface increases as the body falls deeper into water and decreases as it skips out. Determining the surface area is essential in determining the total lift on the body. h_L and h_T are the depths of the water layer at the leading and trailing edge.

divided into three sub-regional flows: the undisturbed upstream flow, the flow in an elevated "pile-up" region (also known as the "jet-root" or "turn-over" region) ahead of the body, and a spray jet which originates from the jet-root region going tangentially away from the body in the negative x-axis direction. The downstream flow behind the skimming body comprises a wake and undisturbed far downstream flow. Connecting the jet-root region with the downstream wake is the main flow region under the skimming body, this is where we shall focus the majority of our analysis on. As the flow enters the jet-root region from upstream, part of the flow is deflected back to the upstream in the form of a spray jet; part of the flow goes under the body and exits into the downstream. There exists a streamline in this jet-root region that separates such two flows; the intersection between this streamline and the body shall be referred to as the "leading edge", with its horizontal position denoted as x_1. The position of this leading edge is unknown and needs to be determined as part of the flow solution. In a similar fashion the "trailing edge" of the body refers to the point where the flow water separates from the body and enters downstream, and we will refer

to its horizontal position as x_0. In the case of a thin body with sharp trailing edge this position is always known[1], it is given by $x_0 = L\cos\theta$ or approximately $x_0 = L$ for small θ. Once the leading and trailing edge positions are determined together with the known skimming body's surface function, the total contact area between the body and fluid can be determined.

Letting μ denote viscosity of the fluid and assuming incompressibility, we have the Navier-Stokes equations in the following form:

$$\frac{\partial \boldsymbol{u}}{\partial t} + \boldsymbol{u}\cdot\nabla\boldsymbol{u} = -\nabla p + \frac{1}{\mathrm{Fr}}(0,1) + \frac{1}{\mathrm{Re}}\nabla^2\boldsymbol{u}, \qquad (\text{with } \nabla\cdot\boldsymbol{u} = 0). \quad (2.1)$$

Let u_0 be the representative horizontal velocity of the skipping stone, the Reynolds number Re is defined by $\mathrm{Re} = \rho u_0 L/\mu$; the Froude number is given by $\mathrm{Fr} = u_0^2/(gh_0)$. Here ρ is the density of the fluid, g is the acceleration due to gravity.

For a skipping stone similar to the size of an adult's palm of hand (say length $2L \sim 0.1m$) travelling at speed of $u_0 \sim 20km/h$, we readily estimate the Reynolds number to be $\mathrm{Re} \sim 190,000$, Froude number to be $\mathrm{Fr} \sim 50$ and Weber number to be $\mathrm{We} = \rho u_0^2 L/\sigma \sim 17,000$; therefore viscosity, gravity and surface tension on face value have negligible effects and only pressure has a dominant effect on the flow, i.e. we are led to the following approximate form of (2.1):

$$\frac{\partial \boldsymbol{u}}{\partial t} + \boldsymbol{u}\cdot\nabla\boldsymbol{u} = -\nabla p, \qquad (\text{with } \nabla\cdot\boldsymbol{u} = 0). \quad (2.2)$$

We non-dimensionalize the model parameters based on the body length L and horizontal velocity u_0 as follows:

$$\bar{x} = \frac{x}{L},\ \ \bar{y} = \frac{y}{L},\ \ \bar{h} = \frac{h}{L},\ \ \bar{u} = \frac{u}{u_0},\ \ \bar{v} = \frac{v}{u_0},\ \ \bar{t} = \frac{L}{u_0},\ \ \bar{p} = \frac{p}{\rho u_0^2},\ \ \bar{m} = \frac{m}{\rho L^2},\ \ \bar{i} = \rho L^4 i,$$

where m and i are the skipping stone's body mass and moment of inertia respec-

[1]This is opposed to say, a cylindrical shaped object going through skimming motion, where its trailing edge will be unknown and needs to be determined just as does its leading edge position. See Chapter 4 for related discussions on this topic.

tively, and the bar notations are used to denote the non-dimensional variables. However for the sake of simplicity we drop the bars on these non-dimensionalized parameters, all variables from this point on are non-dimensional unless explicitly stated otherwise. The large differences between the horizontal and vertical scales of our problem can be exploited further by introducing the following scalings:

$$y = \epsilon Y, \qquad h = \epsilon H,$$

whereas the horizontal length x and time t are of order unity, and $\epsilon = \frac{h_0}{L} \ll 1$.

The vertical component of fluid momentum equation (2.2) implies that $\frac{\partial p}{\partial Y} = 0$, i.e.:

$$p = p(x, t);$$

further assuming the fluid is irrotational we immediately have $\frac{\partial u}{\partial Y} = 0$. i.e.:

$$u = u(x, t);$$

and (2.2) at leading order can be written as:

$$\frac{\partial u}{\partial t} + u\frac{\partial u}{\partial x} = -\frac{\partial p}{\partial x} \qquad (x_1 \leq x \leq x_0), \tag{2.3a}$$

$$\frac{\partial u}{\partial t} + u\frac{\partial u}{\partial x} = 0 \qquad (x \geq x_0). \tag{2.3b}$$

Determining the leading edge position x_1 is of vital interest for later as from it the total contact area between the liquid and the body and hence the force on the skimming body can be determined.

We now derive the boundary conditions for our model. The kinematic boundary condition for the fluid flow implies that particles at the surface stay

at the surface, hence

$$V = \frac{\partial H}{\partial t} + u\frac{\partial H}{\partial x}; \tag{2.4}$$

we can integrate the incompressibility condition from the base of the fluid flow $Y = 0$ and setting $V = 0$ there to obtain

$$V = -H\frac{\partial u}{\partial x}; \tag{2.5}$$

combining (2.4), (2.5) yields the following relation:

$$\frac{\partial H}{\partial t} + \frac{\partial (uH)}{\partial x} = 0. \tag{2.6}$$

We next concern ourselves with the boundary conditions at the leading edge. Let H_J be the thickness of the spray jet, H_0 and H_T be the far upstream and downstream water depths respectively, the continuity condition then yields:

$$\left(1 - \frac{dx_1}{dt}\right)H_0 = \left(1 - \frac{dx_1}{dt}\right)H_J + \left(1 - \frac{dx_1}{dt}\right)H_T. \tag{2.7}$$

This is the same relation used in [21, 7, 8]. In addition let H_L be the depth of the water layer at the leading edge $x = x_1$ with flow velocity of $u(x_1, t)$, the flux through this leading edge must match with that at the trailing edge:

$$\left(u(x_1, t) - \frac{dx_1}{dt}\right)H_L = \left(1 - \frac{dx_1}{dt}\right)H_T. \tag{2.8}$$

See Fig. 2.2 for a visual illustration.

Underneath the skimming body we expect there to be a high pressure region which provides the body with lift; in the wake and the downstream flow region the pressure is atmospheric p_0, which we shall set to be zero without loss of generality. By Bernoulli's equation we have the following relation for the pressure

differences at the leading edge:

$$p(x_1,t)+\frac{1}{2}\left(u(x_1,t)-\frac{dx_1}{dt}\right)^2=\frac{1}{2}\left(1-\frac{dx_1}{dt}\right)^2. \tag{2.9}$$

In addition the balance of horizontal momentum demands that the force due to pressure differences on the body balances the change of total momentum, that is:

$$p(x_1,t)H_L=H_J\left(1-\frac{dx_1}{dt}\right)^2+H_0\left(1-\frac{dx_1}{dt}\right)^2-H_L\left(u(x_1,t)-\frac{dx_1}{dt}\right)^2;$$

substituting in (2.7), (2.8) and (2.9) and re-arranging gives the following relation:

$$\left(u(x_1,t)-\frac{dx_1}{dt}\right)\Big/\left(1-\frac{dx_1}{dt}\right)=2H(x_1,t)^{-\frac{1}{2}}-1. \tag{2.10}$$

Equations (2.9) and (2.10) comprise the leading edge pressure-jump condition deployed by [21, 57].

As pressure has a dominant effect on the fluid flow underneath the body, by Newton's third law of reciprocity we have the following vertical and angular momentum equations for the body:

$$\int_{x_1}^{x_0}p(x,t)\cos\theta ds=m\frac{d^2y_m}{dt^2}-\frac{m}{\mathrm{Fr}}, \tag{2.11a}$$

$$\int_{x_1}^{x_0}\{(x-x_m)p(x,t)\cos\theta+(y-y_m)p(x,t)\sin\theta\}ds=i\frac{d^2\theta}{dt^2}. \tag{2.11b}$$

Scale the mass and moment of inertia as $M=\epsilon m$, $I=\epsilon i$ respectively; given that θ is small and provided that $\epsilon\mathrm{Fr}$ is large, then the above equations can be written to leading order as:

$$\int_{x_1}^{x_0}p(x,t)ds=M\frac{d^2Y_m}{dt^2}, \tag{2.12a}$$

$$\int_{x_1}^{x_0}(x-x_m)p(x,t)ds=I\frac{d^2\theta}{dt^2}. \tag{2.12b}$$

Notice that the angle θ now has order unity.

Suppose the thickness of the body is $T(x)$, then H, the depth of the liquid layer underneath the body, is given by:

$$H(x,t) = Y_m(t) + (x - x_m)\theta(t) - T(x), \qquad (x_1 \leq x \leq x_0). \tag{2.13}$$

The fluid flow horizontal momentum equation (2.3), mass conservation and kinematic boundary condition (2.6), leading edge pressure jump conditions (2.9) and (2.10), liquid layer depth equation (2.13), skimming plate's momentum equations (2.12) constitute the system of equations that governs the movement of the body and the fluid. In the following section we shall derive a linearised system for this model and seek its analytical as well as numerical solutions.

2.3 Linearised flow

The model which is comprised of (2.3), (2.6), (2.9), (2.10), (2.12) and (2.13), derived in the previous section is difficult to analyse in its current form; more analytical insights and a comparatively simpler numerical solution scheme can be obtained by seeking a linearised form the model. We do so by introducing an asymptotically small variable $\tilde{\epsilon}$ such that $\tilde{\epsilon} \ll 1$, and expand the original system variables as follows:

$$H = 1 + \tilde{\epsilon}\tilde{H} + O(\tilde{\epsilon}^2), \tag{2.14a}$$

$$Y_m = 1 + \tilde{\epsilon}\tilde{Y} + O(\tilde{\epsilon}^2), \tag{2.14b}$$

$$u = 1 + \tilde{\epsilon}\tilde{u} + O(\tilde{\epsilon}^2), \tag{2.14c}$$

$$p = 0 + \tilde{\epsilon}\tilde{p} + O(\tilde{\epsilon}^2), \qquad (x_1 \leq x \leq x_0) \tag{2.14d}$$

$$\theta = \theta_0 + \tilde{\epsilon}\tilde{\theta} + O(\tilde{\epsilon}^2), \tag{2.14e}$$

$$T = \tilde{\epsilon}\tilde{T}. \tag{2.14f}$$

From this point on unless specified otherwise we shall deal exclusively with the linearised $O(\tilde{\epsilon})$ variables, and for the sake of simplicity we drop the tilde signs on these variables. Substituting these linearised variables back into our governing equations, the fluid flow horizontal momentum (2.3) becomes:

$$\frac{\partial u}{\partial t} + \frac{\partial u}{\partial x} = -\frac{\partial p}{\partial x}, \qquad (x_1 \leq x \leq x_0), \tag{2.15a}$$

$$\frac{\partial u}{\partial t} + \frac{\partial u}{\partial x} = 0, \qquad (x \geq x_0); \tag{2.15b}$$

the kinematic boundary condition (2.6) is simplified to:

$$\frac{\partial H}{\partial t} + \frac{\partial H}{\partial x} + \frac{\partial u}{\partial x} = 0; \tag{2.16}$$

the leading edge pressure and momentum jump conditions (2.9), (2.10) become:

$$p(x_1, t) + \left(1 - \frac{dx_1}{dt}\right) u(x_1, t) = 0, \tag{2.17}$$

$$u(x_1, t) = -\left(1 - \frac{dx_1}{dt}\right) H(x_1, t); \tag{2.18}$$

the liquid layer depth equation (2.13) becomes:

$$H(x, t) = Y(t) + (x - x_m)\theta(t) - T(x), \qquad (x_1 \leq x \leq x_0); \tag{2.19}$$

finally the skimming body's momentum equations (2.12) are written as:

$$M\frac{d^2Y}{dt^2} = \int_{x_1}^{x_0} p(x, t)dx, \tag{2.20a}$$

$$I\frac{d^2\theta}{dt^2} = \int_{x_1}^{x_0} (x - x_m)p(x, t)dx. \tag{2.20b}$$

Assuming the skimming body's thickness T is at most quadratic in x, i.e. $T = Ax^2 + Bx + C$ with A, B and C being constants, then by (2.15a), (2.16) the pressure can be at most cubic in x. We therefore express pressure in the

following form:

$$p(x,t) = \gamma_3(t)x^3 + \gamma_2(t)x^2 + \gamma_1(t)x + \gamma_0(t), \tag{2.21}$$

where the γ coefficients are functions of time and need to be solved as part of the system.

In the wake and downstream flow region the pressure is atmospheric and equals to zero, the pressure relation (2.21) yields:

$$p_0 = p(x_0,t) = \gamma_3 x_0^3 + \gamma_2 x_0^2 + \gamma_1 x_0 + \gamma_0 = 0. \tag{2.22}$$

At the body's leading edge a pressure relation can be obtained by combining the linearised leading edge jump conditions (2.17) and (2.18) such that:

$$\gamma_3 x_1^3 + \gamma_2 x_1^2 + \gamma_1 x_1 + \gamma_0 = (Y + x_1\theta)(1 - \frac{dx_1}{dt})^2. \tag{2.23}$$

For the purpose of a thin body analysis we will neglect the thickness of the body for the rest of this chapter and set $T = 0$. The water separation process from a blunt skimming body is analysed in more detail in Chapter 4; the case for which a skimming body with non-negligible thickness is considered in the analysis of Chapter 5.

Setting the body thickness functions' coefficients A, B and C to 0, integrate the equation (2.16) with (2.19) gives the following expression for the fluid horizontal velocity:

$$u(x,t) = D(t) - \frac{x^2}{2}\frac{d\theta}{dt} + x\left(x_m\frac{d\theta}{dt} - \frac{dY}{dt} - \theta\right), \tag{2.24}$$

where $D(t)$ is a function of time and represents the fluid velocity at $x = 0$. Combine this result with the jump condition (2.17) gives us one more relation

for the leading edge pressure in addition to (2.25):

$$\gamma_3 x_1^3 + \gamma_2 x_1^2 + \gamma_1 x_1 + \gamma_0 = [\frac{x_1^2}{2}\frac{d\theta}{dt} + x_1(\frac{dY}{dt} + \theta) - D](1 - \frac{dx_1}{dt}); \quad (2.25)$$

these two coupled non-linear ODEs give the conditions that the pressure at the leading edge must satisfy. The pressure coefficients γ can be obtained by asymptotic analysis of (2.24), (2.22) and (2.15a):

$$\gamma_1 = -\frac{dD}{dt} + \frac{dY}{dt} + \theta, \quad (2.26a)$$

$$\gamma_2 = \frac{1}{2}\frac{d^2Y}{dt^2} + \frac{d\theta}{dt}, \quad (2.26b)$$

$$\gamma_3 = \frac{1}{6}\frac{d^2\theta}{dt^2}. \quad (2.26c)$$

Finally substituting the pressure equation into the body's vertical and angular momentum equations (2.20) we obtain:

$$M\frac{d^2Y}{dt^2} = \frac{\gamma_3}{4}(x_0^4 - x_1^4) + \frac{\gamma_2}{3}(x_0^3 - x_1^3) + \frac{\gamma_1}{2}(x_0^2 - x_1^2) + \gamma_0(x_0 - x_1), \quad (2.27a)$$

$$I\frac{d^2\theta}{dt^2} = \frac{\gamma_3}{5}(x_0^5 - x_1^5) + \frac{\gamma_2}{4}(x_0^4 - x_1^4) + \frac{\gamma_1}{3}(x_0^3 - x_1^3) + \frac{\gamma_0}{2}(x_0^2 - x_1^2). \quad (2.27b)$$

Our task is to solve the system of eight equations comprising (2.22), (2.23) and (2.25) - (2.27) for eight unknowns: γ_0 - γ_3, x_1, Y, θ and D.

2.4 Analysis of water entry at small time

At the instant of impact when time $t = 0$ the body's wetted leading edge coincides with its trailing edge, i.e. $x_1(t) = x_0$ and the height of the body's centre of mass $Y(t)$ at $t = 0$, call it Y_0, is given by $Y_0 = -x_0\theta_0$ in the linearised regime of (2.14). At a time shortly after impact, say for $t \sim O(\delta)$ with $\delta \ll 1$, we expect the system variables to evolve slightly from their original impact states,

therefore we seek their asymptotic expansions of the following form:

$$x_1(t) = x_0 + \delta x_{11}(t) + \delta^2 x_{12}(t) + O(\delta^3), \tag{2.28}$$

$$\theta(t) = \theta_0 + \delta\theta_1(t) + \delta^2\theta_2(t) + \delta^3\theta_3(t) + O(\delta^4), \tag{2.29}$$

$$Y(t) = Y_0 + \delta Y_1(t) + \delta^2 Y_2(t) + \delta^3 Y_3(t) + O(\delta^4), \tag{2.30}$$

$$D(t) = D_0(t) + \delta D_1(t) + \delta^2 D_2(t) + \delta^3 D_3(t) + O(\delta^4), \tag{2.31}$$

with the condition:

$$Y_0 = -\theta_0 x_0 = \text{Const.} \tag{2.32}$$

As the pressure coefficient γ_1 in (2.26a) contains only first order derivatives of t, for $t \sim O(\delta)$ we expect its leading order term to be $O(\delta^{-1})$. By the same line of reasoning we may also expect the leading order terms for rest of the pressure coefficients γ_0, γ_2 and γ_3 to be $O \sim (\delta^{-2})$, however due to the fact that Y and θ are constants at the leading order, all $O(\delta^{-2})$ terms of these coefficients are trivially zero, we are therefore led to the conclusion that all the pressure coefficient terms are at most $O(\delta^{-1})$ and their asymptotic expansions are:

$$\gamma_0 = \frac{1}{\delta}\gamma_{00} + \gamma_{01} + \delta\gamma_{02} + \delta^2\gamma_{03} + O(\delta^3), \tag{2.33a}$$

$$\gamma_1 = \frac{1}{\delta}\gamma_{10} + \gamma_{11} + \delta\gamma_{12} + \delta^2\gamma_{13} + O(\delta^3), \tag{2.33b}$$

$$\gamma_2 = \frac{1}{\delta}\gamma_{20} + \gamma_{21} + \delta\gamma_{22} + \delta^2\gamma_{23} + O(\delta^3), \tag{2.33c}$$

$$\gamma_3 = \frac{1}{\delta}\gamma_{30} + \gamma_{31} + \delta\gamma_{32} + \delta^2\gamma_{33} + O(\delta^3). \tag{2.33d}$$

We now are ready to apply the asymptotic expansions of these variables (2.28) - (2.33d) into our system of equations (2.22), (2.23) and (2.25) - (2.27).

Apply asymptotic expansions to the trailing edge pressure condition (2.22)

and collecting terms of the same order produces, for γ_0:

$$O(\frac{1}{\delta}) : \gamma_{00} = -\gamma_{30}x_0^3 - \gamma_{20}x_0^2 - \gamma_{10}x_0, \tag{2.34a}$$

$$O(1) : \gamma_{01} = -\gamma_{31}x_0^3 - \gamma_{21}x_0^2 - \gamma_{11}x_0, \tag{2.34b}$$

$$O(\delta) : \gamma_{02} = -\gamma_{32}x_0^3 - \gamma_{22}x_0^2 - \gamma_{12}x_0; \tag{2.34c}$$

likewise for γ_1 and with $dt \sim O(\delta)$ in mind we obtain:

$$O(\frac{1}{\delta}) : \gamma_{10} = -\dot{D}_0, \tag{2.35a}$$

$$O(1) : \gamma_{11} = \theta_0 + \dot{Y}_1 - \dot{D}_1, \tag{2.35b}$$

$$O(\delta) : \gamma_{12} = \theta_1 + \dot{Y}_2 - \dot{D}_2; \tag{2.35c}$$

similarly for γ_2:

$$O(\frac{1}{\delta}) : \gamma_{20} = \frac{1}{2}\ddot{Y}_1, \tag{2.36a}$$

$$O(1) : \gamma_{21} = \frac{1}{2}\ddot{Y}_2 + \dot{\theta}_1, \tag{2.36b}$$

$$O(\delta) : \gamma_{22} = \frac{1}{2}\ddot{Y}_3 + \dot{\theta}_2; \tag{2.36c}$$

and for γ_3 we have:

$$O(\frac{1}{\delta}) : \gamma_{30} = \frac{1}{6}\ddot{\theta}_1, \tag{2.37a}$$

$$O(1) : \gamma_{31} = \frac{1}{6}\ddot{\theta}_2, \tag{2.37b}$$

$$O(\delta) : \gamma_{33} = \frac{1}{6}\ddot{\theta}_3. \tag{2.37c}$$

These asymptotic relations of γ will be applied to the model's pressure equations (2.22), (2.23), (2.25) and the skimming body's momentum equations (2.27).

Asymptotic expansions of the first leading edge pressure condition (2.23) gives:

$$O(\frac{1}{\delta}) : \gamma_{30}x_0^3 + \gamma_{20}x_0^2 + \gamma_{10}x_0 + \gamma_{00} = 0, \tag{2.38a}$$

$$O(1) : \gamma_{31}x_0^3 + 3\gamma_{30}x_0^2x_{11} + 2\gamma_{20}x_0x_{11} + \gamma_{21}x_0^2 + \gamma_{11}x_0 + \gamma_{10}x_{11} + \gamma_{01}$$
$$= (1 - \dot{x}_{11})^2(Y_0 + x_0\theta_0) = 0, \tag{2.38b}$$

$$O(\delta) : \gamma_{32}x_0^3 + \gamma_{22}x_0^2 + 3\gamma_{30}x_0x_{11}^2 + 3\gamma_{30}x_0^2x_{12} + 3\gamma_{31}x_0^2x_{11} + \gamma_{20}x_{11}^2$$
$$+ 2\gamma_{20}x_0x_{12} + \gamma_{12}x_0 + \gamma_{10}x_{12} + \gamma_{11}x_{11} + 2\gamma_{21}x_0x_{11} + \gamma_{02} =$$
$$(\dot{x}_{11} - 1)^2(Y_1 + x_0\theta_1 + \theta_0x_{11}) + 2\dot{x}_{12}(\dot{x}_{11} - 1)(Y_0 + x_0\theta_0). \tag{2.38c}$$

The $O(\delta^{-1})$ terms in the above expansion are zero due to (2.34a). At order unity the right-hand side (R.H.S.) of (2.38b) is zero due to (2.32), and substituting values of γ into the left-hand side (L.H.S.) implies:

$$\dot{D}_0 = x_0\ddot{Y}_1 + \frac{1}{2}x_0^2\ddot{\theta}_1, \tag{2.39}$$

hence:

$$D_0 = x_0\dot{Y}_1 + \frac{1}{2}x_0^2\dot{\theta}_1 + D_{const}, \tag{2.40}$$

where D_{const} is a constant and can be determined from the second leading edge pressure condition (2.25). At $O(\delta)$, substituting values of γ into equation (2.38c) and simplifying we obtain the following second order ODE:

$$\frac{1}{2}(\ddot{Y}_1 + x_0\ddot{\theta}_1)x_{11}^2 + (\ddot{Y}_2 + \frac{1}{2}x_0\ddot{\theta}_2 + 2\dot{\theta}_1)x_0x_{11} + (\theta_0 + \dot{Y}_1 - \dot{D}_1)x_{11} =$$
$$(1 - \dot{x}_{11})^2(Y_1 + x_0\theta_1 + \theta_0x_{11}). \tag{2.41}$$

Applying the same asymptotic analysis to the second leading edge pressure

condition (2.25) gives:

$$O(\frac{1}{\delta}) : \gamma_{30}x_0^3 + \gamma_{20}x_0^2 + \gamma_{10}x_0 + \gamma_{00} = 0, \tag{2.42a}$$

$$\begin{aligned} O(1) : {} & \gamma_{31}x_0^3 + 3\gamma_{30}x_0^2x_{11} + 2\gamma_{20}x_0x_{11} + \gamma_{21}x_0^2 + \gamma_{11}x_0 + \gamma_{10}x_{11} + \gamma_{01} \\ & = (1 - \dot{x}_{11})(\frac{1}{2}x_0^2\dot{\theta}_1 - D_0 + x_0\theta_0 + x_0\dot{Y}_1), \end{aligned} \tag{2.42b}$$

$$\begin{aligned} O(\delta) : {} & \gamma_{32}x_0^3 + \gamma_{22}x_0^2 + 3\gamma_{30}x_0x_{11}^2 + 3\gamma_{30}x_0^2x_{12} + 3\gamma_{31}x_0^2x_{11} + \gamma_{20}x_{11}^2 \\ & + 2\gamma_{20}x_0x_{12} + \gamma_{12}x_0 + \gamma_{10}x_{12} + \gamma_{11}x_{11} + 2\gamma_{21}x_0x_{11} + \gamma_{02} = \\ & (1 - \dot{x}_{11})(x_0\theta_1 + x_{11}\theta_0 - D_1 + x_0\dot{Y}_2 + x_{11}\dot{Y}_1 + x_0x_{11}\dot{\theta}_1 + \frac{1}{2}x_0^2\dot{\theta}_2) \\ & + \dot{x}_{12}(D_0 - x_0\theta_0 - x_0\dot{Y}_1 - \frac{1}{2}x_0^2\dot{\theta}_1). \end{aligned} \tag{2.42c}$$

As the two leading edge pressure equations (2.23), (2.25) share the same L.H.S., matching equations (2.38b) and (2.42b) gives:

$$D_0 = x_0\theta_0 + x_0\dot{Y}_1 + \frac{1}{2}x_0^2\dot{\theta}_1, \tag{2.43}$$

hence D_{const} from equation (2.40) is:

$$D_{const} = x_0\theta_0. \tag{2.44}$$

Therefore a short time after impact, the leading order fluid velocity D_0 beneath the impact body's centre of mass is determined by the body's leading order vertical velocity, angular velocity and configurations of system geometry at entry.

Substituting γ expansions into equation (2.42c) gives:

$$\begin{aligned} & \frac{1}{2}(\ddot{Y}_1 + x_0\ddot{\theta}_1)x_{11}^2 + (\ddot{Y}_2 + \frac{1}{2}x_0\ddot{\theta}_2 + 2\dot{\theta}_1)x_0x_{11} + (\theta_0 + \dot{Y}_1 - \dot{D}_1)x_{11} = \\ & (1 - \dot{x}_{11})(x_0\theta_1 + x_{11}\theta_0 - D_1 + x_0\dot{Y}_2 + x_{11}\dot{Y}_1 + x_0x_{11}\dot{\theta}_1 + \frac{1}{2}x_0^2\dot{\theta}_2), \end{aligned} \tag{2.45}$$

which can be combined with (2.41) to obtain an expression for D_1:

$$D_1 = x_0\dot{Y}_2 + \frac{1}{2}x_0^2\dot{\theta}_2 + (Y_1 + x_0\theta_1 + x_{11}\theta_0)\dot{x}_{11} + x_0x_{11}\dot{\theta}_1 + x_{11}\dot{Y}_1 - Y_1. \quad (2.46)$$

Therefore the $\dot{D}_1$ term can be expressed as:

$$\begin{aligned}\dot{D}_1 = {} & x_0\ddot{Y}_2 + x_{11}\ddot{Y}_1 + x_0x_{11}\ddot{\theta}_1 + \frac{1}{2}x_0^2\ddot{\theta}_2 + (Y_1 + x_0\theta_1 + \theta_0x_{11})\ddot{x}_{11} - \dot{Y}_1 \\ & + (2\dot{Y}_1 + 2x_0\dot{\theta}_1 + \theta_0\dot{x}_{11})\dot{x}_{11}. \end{aligned} \quad (2.47)$$

Substituting this result into equation (2.41) gives us a coupled second order ODE which captures the relations between three unknown leading order asymptotic expansion variables of X_1, Y and θ:

$$\begin{aligned}& \theta_0x_{11}(1 - \dot{x}_{11}^2) - (Y_1 + x_0\theta_1 + x_{11}\theta_0)(1 - \dot{x}_{11})^2 + 2x_{11}(\dot{Y}_1 + x_0\dot{\theta}_1)(1 - \dot{x}_{11}) \\ & = (Y_1 + x_0\theta_1 + \theta_0x_{11})x_{11}\ddot{x}_{11} + \frac{1}{2}x_{11}^2\ddot{Y}_1 + \frac{1}{2}x_0x_{11}^2\ddot{\theta}_1. \end{aligned} \quad (2.48)$$

Notice further that D, which represents the fluid's velocity at $x = 0$ is eliminated from this asymptotic system. This relation together with the linearised body momentum equations derived in the subsequent sections comprise the full linearised governing system for the fluid and body motions. In the subsequent analysis we shall focus on asymptotic expansions of the skimming body's vertical and angular momentum equations (2.27a) and (2.27b), and obtain two additional equations involving the three unknowns x_{11}, θ_1 and Y_1.

It is important to note that in the asymptotic analysis of the linear and angular momentum equations, the order of impact body's mass M and moment of inertia I play vital roles in influencing the behaviour of the centre of mass height Y and liquid surface contact angle θ. To understand the significance of these relations, we shall conduct analysis for various orders of M and I in the subsequent sections.

2.4.1 Mass and moment of inertia of order unity

In this section we analyse the effects of a skimming body having body mass and moment of inertia of order unity. For a thin flat body with uniform density, its moment of inertia at most can be $M/4$. However in many physical applications such as a game of skipping stones, the body can be given a spin which stabilises its contact angle with water via gyroscopic effect. This stabilization effect can be modelled in 2D by increasing the body's moment of inertia to be greater than what seemingly possible for a flat body. Hence for an impact body with mass and moment of inertia of both order unity, the vertical momentum equation (2.27a) can be asymptotically expanded as:

$$O(\frac{1}{\delta^2}) : M\ddot{Y}_0 = 0, \tag{2.49a}$$

$$O(\frac{1}{\delta}) : M\ddot{Y}_1 = 0, \tag{2.49b}$$

$$O(1) : M\ddot{Y}_2 = -\gamma_{00}x_{11} - \gamma_{10}x_0x_{11} + \gamma_{20}x_0^2x_{11} - \gamma_{30}x_0^3x_{11} = 0. \tag{2.49c}$$

Given that $\ddot{Y}_1 = 0$, so Y_1 is at most linear with terms of t. Suppose the impact object has an initial vertical velocity of V_0, then at time $t \sim O(\delta)$ we expect:

$$\dot{Y}_1 = Const = V_0, \tag{2.50}$$

i.e. Y_1 can be written as $Y_1 = V_0t + Y_c$ where Y_c is a constant.

Asymptotic expansions of angular momentum equation (2.27b) gives:

$$O(\frac{1}{\delta^2}) : I\ddot{\theta}_0 = 0, \tag{2.51a}$$

$$O(\frac{1}{\delta}) : I\ddot{\theta}_1 = 0, \tag{2.51b}$$

$$O(1) : I\ddot{\theta}_2 = -\gamma_{00}x_0x_{11} - \gamma_{10}x_0^2x_{11} - \gamma_{20}x_0^3x_{11} - \gamma_{30}x_0^4x_{11} = 0; \tag{2.51c}$$

again from (2.51b) we expect θ_1 to be linear in time t for $t \sim O(\delta)$ such that:

$$\dot{\theta}_1 = Const = \omega_0, \tag{2.52}$$

where ω_0 is used to denote the impact body's initial angular velocity upon impact, hence $\theta_1 = \omega_0 t + \theta_c$ where θ_c is a constant.

Given that both Y_1 and θ_1 scales linearly with t a small time after impact, we expect that x_{11} to be at most linear in t, i.e. $\ddot{x}_{11} = \ddot{Y}_1 = \ddot{\theta}_1 = 0$. This implies that (2.48) can be written as:

$$(Y_1 + x_0\theta_1 + 2\theta_0 x_{11})\dot{x}_{11} + 2(V_0 + x_0\omega_0)x_{11} - x_0\theta_1 - Y_1 = 0. \tag{2.53}$$

Differentiating this equation with respect to t and rearranging gives us a quadratic equation for $\dot{x}_{11}$:

$$2\theta_0(\dot{x}_{11})^2 + 3(\dot{Y}_1 + x_0\dot{\theta}_1)\dot{x}_{11} - (\dot{Y}_1 + x_0\dot{\theta}_1) = 0, \tag{2.54}$$

and x_{11} can therefore be found as:

$$x_{11} = \frac{-3(V_0 + x_0\omega_0) + \sqrt{9(V_0 + x_0\omega_0)^2 + 8\theta_0(V_0 + x_0\omega_0)}}{4\theta_0} t. \tag{2.55}$$

We find this result for x_{11} is in agreement with the analysis of Hicks & Smith (2010) [57].

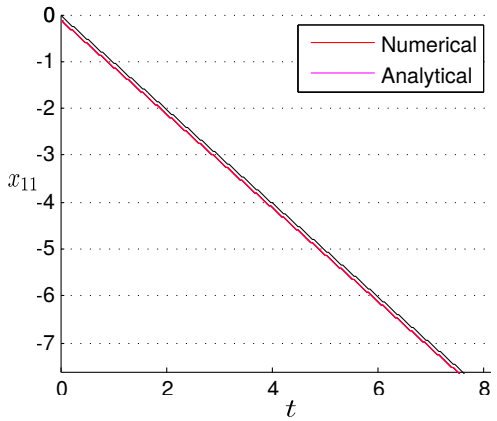

Figure 2.3: Comparing the analytical solution of x_{11} with its numerical solution for the case of M and I order unity. The graph shows that these two results are in excellent agreement.

2.4.2 Impact body with small mass

For the scenarios of a light skimming body, such as $M \sim O(\delta)$, $M \sim O(\delta^2)$ while the moment of inertia I is fixed at order unity, our analysis finds that at early impact times there is no change in the body's vertical velocity, i.e. $\ddot{Y}_1 = 0$. Hence as with the case of M and I both being order unity, the liquid pressure at small time after impact is unable to generate sufficient lift to affect the body's vertical and angular velocities at leading orders.

If the body mass is sufficiently small however, i.e. $M \sim O(\delta^3)$ while I remains order unity, the asymptotic expansions of the governing equations (2.22) - (2.26c) and (2.27b) are the same as those listed in section 2.3 and 2.4.1. The asymptotic expansion for the vertical momentum equation (2.27a) however becomes:

$$\begin{aligned} O(\delta) : M\ddot{Y}_0 = &-\gamma_{31}x_0^3x_{11} - \gamma_{21}x_0^2x_{11} - \gamma_{11}x_0x_{11} - \gamma_{01}x_{11} - \gamma_{30}x_0^3x_{12} \\ &- \gamma_{20}x_0^2x_{12} - \gamma_{10}x_0x_{12} - \gamma_{00}x_{12} - \frac{3}{2}\gamma_{30}x_0^2x_{11}^2 - \gamma_{20}x_0x_{11}^2 \\ &- \frac{1}{2}\gamma_{10}x_{11}^2 = \frac{1}{2}\dot{D}_0x_{11}^2 - \frac{1}{2}\ddot{Y}_1x_0x_{11}^2 - \frac{1}{4}x_0^2x_{11}^2\ddot{\theta}_1; \end{aligned} \tag{2.56a}$$

$$\begin{aligned} O(\delta^2) : M\ddot{Y}_1 = &-\gamma_{31}x_0^3x_{12} - \gamma_{21}x_0^2x_{12} - \gamma_{11}x_0x_{12} - \gamma_{01}x_{12} - \gamma_{32}x_0^3x_{11} \\ &- \gamma_{22}x_0^2x_{12} - \gamma_{12}x_0x_{11} - \gamma_{02}x_{11} - \frac{1}{2}\gamma_{11}x_{11}^2 - \frac{1}{3}\gamma_{20}x_{11}^3 \\ &- \gamma_{21}x_0x_{11}^2 - \gamma_{30}x_0x_{11}^3 - \gamma_{10}x_{11}x_{12} - \frac{3}{2}\gamma_{31}x_0^2x_{11}^2 \\ &- 2\gamma_{20}x_0x_{11}x_{12} - 3\gamma_{30}x_0^2x_{11}x_{12} = -\frac{1}{2}(\theta_0 + \dot{Y}_1 - \dot{D}_1)x_{11}^2 \\ &- \frac{1}{6}x_{11}^3\ddot{Y}_1 - (\frac{1}{2}\ddot{Y}_2 + \dot{\theta}_1)x_0x_{11}^2 - \frac{1}{6}x_0x_{11}^3\ddot{\theta}_1 - \frac{1}{4}x_0^2x_{11}^2\ddot{\theta}_2. \end{aligned} \tag{2.56b}$$

The L.H.S. of the $O(\delta)$ equation is zero since $\ddot{Y}_0 = 0$. Re-arranging this equation (2.56a) gives the same result as (2.39) for $\dot{D}_0$. At $O(\delta^2)$, substituting values of γ into equation (2.56b) and re-arranging we obtain the following

relation for $\ddot{Y}_1$:

$$(M+\frac{1}{6}x_{11}^3)\ddot{Y}_1 = -\frac{1}{6}x_0x_{11}^3\ddot{\theta}_1-\frac{1}{4}x_0^2x_{11}^2\ddot{\theta}_2-\frac{1}{2}(\theta_0+\dot{Y}_1-\dot{D}_1)x_{11}^2-(\frac{1}{2}\ddot{Y}_2+\dot{\theta}_1)x_0x_{11}^2. \tag{2.57}$$

The equation (2.41) obtained from section (2.3) can also be written as a expression of $\ddot{Y}_1$:

$$\begin{aligned}\frac{1}{2}x_{11}^3\ddot{Y}_1 = &-\frac{1}{2}x_0x_{11}^3\ddot{\theta}_1 - \frac{1}{2}x_0^2x_{11}^2\ddot{\theta}_2 - (\theta_0 + \dot{Y}_1 - \dot{D}_1)x_{11}^2 - (\ddot{Y}_2 + 2\dot{\theta}_1)x_0x_{11}^2 \\ &+ x_{11}(1-\dot{x}_{11})^2(Y_1 + x_0\theta_1 + \theta_0x_{11});\end{aligned} \tag{2.58a}$$

combining these two equations yields a second order ODE for Y_1:

$$\ddot{Y}_1 = \frac{x_0x_{11}^3\ddot{\theta}_1 - 6x_{11}(1-\dot{x}_{11})^2(Y_1 + x_0\theta_1 + \theta_0x_{11})}{12M - x_{11}^3}. \tag{2.59}$$

This equation together with (2.48) forms a coupled second order non-linear ODE system for x_{11} and Y_1. Substituting in $\ddot{\theta}_1 = 0$ from (2.51b), re-arranging these two equations and setting $u = \dot{x}_{11}$, $V = \dot{Y}_1$ gives:

$$u = \dot{x}_{11}, \tag{2.60a}$$

$$V = \dot{Y}_1, \tag{2.60b}$$

$$\dot{u} = \frac{\theta_0(1-u^2) + 2(V + x_0\omega_0)(1-u)}{Y_1 + x_0\omega_0 t + \theta_0x_{11}} + \frac{3x_{11}^2(1-u)^2}{12M - x_{11}^3} - \frac{(1-u)^2}{x_{11}}, \tag{2.60c}$$

$$\dot{V} = -\frac{6x_{11}(1-u)^2(Y_1 + x_0\omega_0 t + \theta_0x_{11})}{12M - x_{11}^3}; \tag{2.60d}$$

with the following initial conditions:

$$
\begin{aligned}
&x_{11}(0) = -0, \\
&u(0) = \frac{-3(V_0 + x_0\omega_0) + \sqrt{9(V_0 + x_0\omega_0)^2 + 8\theta_0(V_0 + x_0\omega_0)}}{4\theta_0}, \\
&Y_1(0) = -0, \\
&V(0) = V_0,
\end{aligned}
$$

where ω_0 denotes the body's initial angular velocity at instant of impact and it is known. The initialization value of '-0' for $x_{11}(0)$ and $Y_1(0)$ indicates they should be set to a small value less than zero.

This coupled first order ODE system is solved numerically using a 5th order Adam-Bashforth-Moulton Predictor-Corrector method, see Fig. 2.4. Its result is compared with the full system solution at $t \sim O(\delta)$ and the two results are shown to be in good agreement, see Fig. 2.5.

This particular system configuration where $t \sim O(\delta)$, $M \sim O(\delta^3)$ with the rest of system variables being order unity is significant: under these conditions the hydrodynamic pressure exerted on the impact body from underneath is significant enough to influence x_{11} and Y_1 immediately after the instant of impact. As a result the body is able to complete the transition from initial impact to rebound from the liquid in the $t \sim O(\delta)$ regime. The rebound from the liquid is characterized by the body's leading wetted edge traversing back to the trailing edge (i.e. $x_1 \to 0$). As demonstrated in Fig. 2.5, the solutions obtained via our asymptotic analysis treatment are in good agreement with the numerical solutions of the full system. We therefore reduced the full system of eight equations (2.22) - (2.27) to a system of two coupled ODE equations: (2.48) and (2.59). An interesting observation in Fig. 2.5 is that the body's height and velocity upon exit are greater than its respective entry conditions. This is a phenomenon known as "super-elastic" effect, which is also observed in empirical studies by [37].

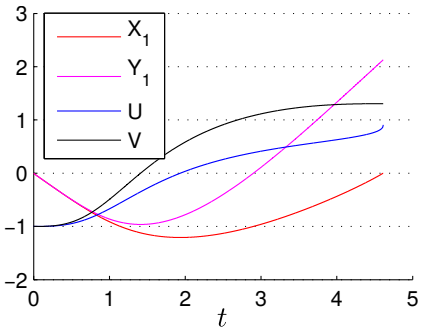

Figure 2.4: Numerical solutions for the system (2.60) with $x_0 = 1$, $x_{11}(0) = -0.1$, $Y_1(0) = -0.1$, $\theta_0 = -2$, $u(0) = -1$, $V(0) = -1$ and $\omega_0 = 0$. The solution demonstrates that for a body with very small body mass, i.e. $M \sim O(\delta^3)$, it is able to complete the transition from initial impact to final exit from the liquid layer inside the $t \sim O(\delta)$ regime.

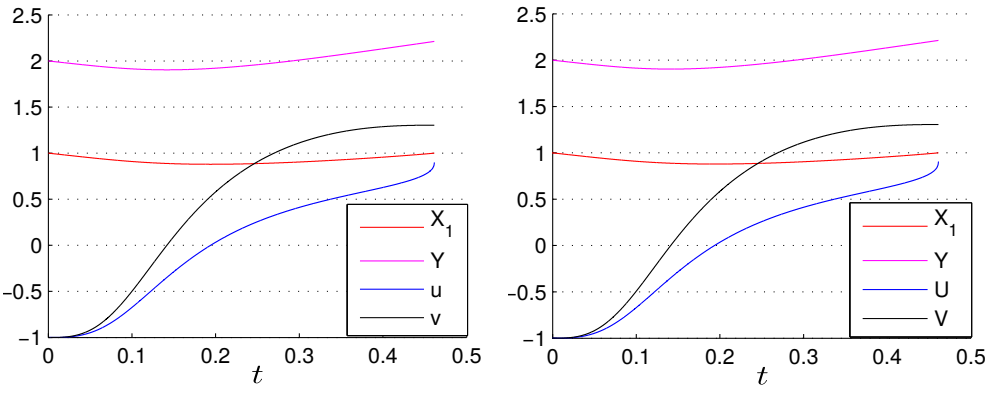

Figure 2.5: Numerical solutions for the configuration of $M \sim O(\delta^3)$ and $I \sim O(1)$. The graph on the left demonstrates the numerical solution of the linearised skimming system in Section 2.3; the graph on the right is obtained by solving the asymptotic system (2.60) combined with the leading order initial conditions of $x_1(0) = 1$, $Y(0) = 2$, $u(0) = 0$ and $V(0) = 0$. The results demonstrate that the two system solutions are in good agreement.

2.4.3 Impact body with small moment of inertia

As shown in the previous section, when mass M is sufficiently small (no greater than $O(\delta^3)$) the liquid pressure has a significant effect on the vertical trajectory of the impact body at a small time after entry. We now analyse the effects of small I on the impact body's incident angle θ.

For the scenarios of $I \sim O(\delta)$ and $I \sim O(\delta^2)$ with M fixed at order unity, our analysis finds the angular velocity is unchanged in such small time, i.e. $\ddot{\theta}_1 = 0$, while $\ddot{Y}_1 = 0$ from the vertical momentum equation (2.49b). Hence just as with the case of M and I being order unity in section 2.4.1, the liquid pressure at small times after impact is unable to generate sufficient lift to affect the body's vertical and angular velocities at leading orders.

For $M \sim O(1), I \sim O(\delta^3)$, the asymptotic expansions of the governing equations (2.22) - (2.26c) and (2.27a) are the same as those listed in section 2.3 and section 2.4.1, however the asymptotic expansions of (2.27b) becomes:

$$\begin{aligned}
O(\delta) : I\ddot{\theta}_0 &= -\gamma_{31}x_0^4x_{11} - \gamma_{21}x_0^3x_{11} - \gamma_{11}x_0^2x_{11} - \gamma_{01}x_0x_{11} - \gamma_{30}x_0^4x_{12} \\
&\quad - \gamma_{20}x_0^3x_{12} - \gamma_{01}x_0x_{11} - \gamma_{30}x_0^4x_{12} - \gamma_{20}x_0^3x_{12} - \gamma_{10}x_0^2x_{12} - \gamma_{00}x_0x_{12} \\
&\quad - 2\gamma_{30}x_0^3x_{11}^2 - \frac{3}{2}\gamma_{20}x_0^2x_{11}^2 - \gamma_{10}x_0x_{11}^2 - \frac{1}{2}\gamma_{00}x_{11}^2 \\
&= -\frac{1}{2}x_0^2x_{11}^2(\frac{1}{2}x_0\ddot{\theta}_1 + \ddot{Y}_1 - \frac{1}{x_0}\dot{D}_0) = 0. \qquad (2.62a) \\
O(\delta^2) : I\ddot{\theta}_1 &= -\gamma_{31}x_0^4x_{12} - \gamma_{21}x_0^3x_{12} - \gamma_{11}x_0^2x_{12} - \gamma_{01}x_0x_{12} - \gamma_{32}x_0^4x_{11} \\
&\quad - \gamma_{22}x_0^3x_{11} - \gamma_{12}x_0^2x_{11} - \gamma_{02}x_0x_{11} - 4\gamma_{30}x_0^3x_{11}x_{12} - 3\gamma_{20}x_0^2x_{11}x_{12} \\
&\quad - 2\gamma_{10}x_0x_{11}x_{12} - \gamma_{00}x_{11}x_{12} - 2\gamma_{31}x_0^3x_{11}^2 - \frac{3}{2}\gamma_{21}x_0^2x_{11}^2 - \gamma_{11}x_0x_{11}^2 \\
&\quad - \frac{1}{2}\gamma_{01}x_{11}^2 - 2\gamma_{30}x_0^2x_{11}^3 - \gamma_{20}x_0x_{11}^3 - \frac{1}{3}\gamma_{10}x_{11}^3 = -\frac{1}{6}x_0x_{11}^3\ddot{Y}_1 \\
&\quad - \frac{1}{6}x_0^2x_{11}^3\ddot{\theta}_1 - \frac{1}{4}x_0^3x_{11}^2\ddot{\theta}_2 - (\frac{1}{2}\ddot{Y}_2 + \dot{\theta}_1)x_0^2x_{11}^2 - \frac{1}{2}(\theta_0 + \dot{Y}_1 - \dot{D}_1)x_0x_{11}^2. \\
&\qquad (2.62b)
\end{aligned}$$

The Y_2 terms in equation (2.62b) can be eliminated by combining it with equa-

tion (2.41), and after simplification we obtain the following equation for θ_1:

$$\ddot{\theta}_1 = \frac{x_0 x_{11}^3 \ddot{Y}_1 - 6x_0 x_{11}(Y_1 + x_0\theta_1 + \theta_0 x_{11})(1-\dot{x}_{11})^2}{12I - x_0^2 x_{11}^3}. \tag{2.63}$$

Given that $Y_1 = Vt + Y_c$ for mass $M \sim O(1)$ as demonstrated in Section 2.4.1, equation (2.63) together with (2.48) form a system of two coupled nonlinear ODEs for two unknowns: x_{11} and θ_1. Rearranging these two equations and setting $u = \dot{x}_{11}$, $w = \dot{\theta}_1$ gives:

$$u = \dot{x}_{11}, \tag{2.64a}$$

$$\omega = \dot{\theta}_1, \tag{2.64b}$$

$$\dot{u} = \frac{\theta_0(1-u^2) + 2(V_0 + x_0\omega)(1-u)}{Y_1 + x_0\theta_1 + \theta_0 x_{11}} + \frac{4x_0^2 x_{11}^3 - 12I}{12Ix_{11} - x_0^2 x_{11}^4}(1-u)^2, \tag{2.64c}$$

$$\dot{\omega} = -\frac{6x_0 x_{11}(Y_1 + x_0\theta_1 + x_{11}\theta_0)(1-u)^2}{12I - x_0^2 x_{11}^3}, \tag{2.64d}$$

with the following initial conditions:

$$x_{11}(0) = -0, \tag{2.65a}$$

$$u(0) = \frac{-3(V_0 + x_0\omega_0) + \sqrt{9(V_0 + x_0\omega_0)^2 + 8\theta_0(V_0 + x_0\omega_0)}}{4\theta_0}, \tag{2.65b}$$

$$\theta_1(0) = +0, \tag{2.65c}$$

$$\omega(0) = \omega_0. \tag{2.65d}$$

The initialization value of '-0' for $x_{11}(0)$ indicates it is set to a small value less than zero, whereas '$+0$' for $\theta_1(0)$ indicates it is set to a small value greater than zero. The numerical solutions of this coupled system suggests that for a body with sufficiently small moment of inertia (I no greater than $O(\delta^3)$), it is able to rebound from the liquid layer within a short time period ($t \sim O(\delta)$) after impact. It is worth noting that this rebound phenomena is not "usual" in the sense that the body separates from the liquid layer with an upward momentum

generated by the pressure from the liquid layer below, rather the body's contact angle with the liquid layer changes rapidly after the instant of impact to one that's more parallel aligned with the undisturbed liquid surface. The "flatting" of the contact angle in effect reduces the body's wetted contact range, this is eventually reduced to a single point at the trailing edge and the body effectively separates from the liquid layer. During this entire process however, the body is still traveling with a downward vertical velocity of V_0. In reality this body would eventually fall onto the liquid layer again at a much smaller contact angle $\theta \sim O(\delta)$, and as we will see in the later section, it will be difficult for the body to achieve a rebound with a small contact angle unless its vertical velocity at impact is also extremely small.

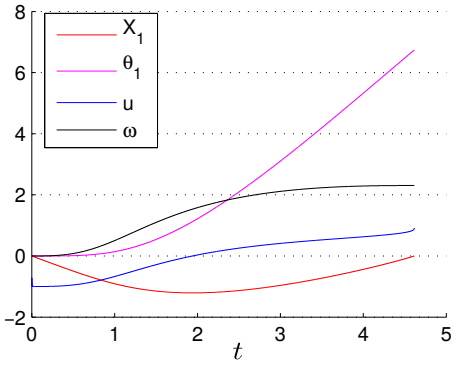

Figure 2.6: Numerical solution of the system (2.64) with initial conditions: $x_{11}(0) = -0.1$, $Y_1 = 0$, $\theta_1(0) = 0$, $u(0) = -1$, $V_0 = -1$ and $\omega(0) = 0$. The solution demonstrates that for a body with very small moment of inertia, i.e. $I \sim O(\delta^3)$, it is able to complete the transition from initial impact to final exit from the liquid layer inside the $t \sim O(\delta)$ regime.

2.4.4 Impact body with small mass and moment of inertia

For the case of an impact body with both small mass and moment of inertia, i.e. $M \sim O(\delta^3), I \sim O(\delta^3)$, the hydrodynamic pressure has noticeable effects on both Y_1 and θ_1 at small time $t \sim O(\delta)$ as indicated from the previous analysis, and the three equations (2.48),(2.59) and (2.63) form a system of non-linear

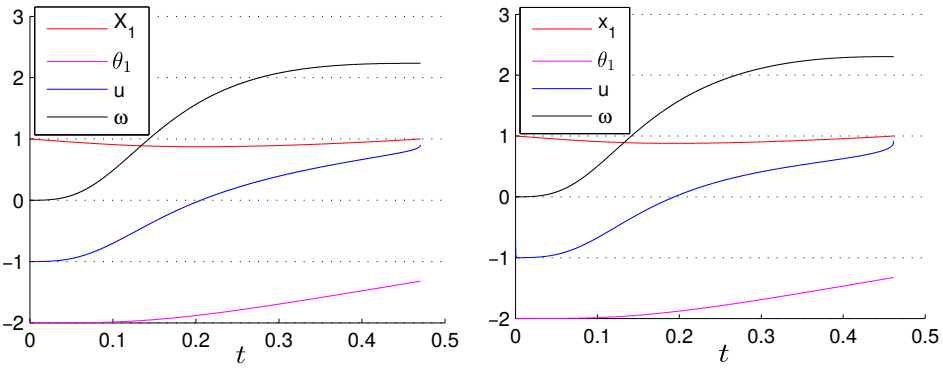

Figure 2.7: Numerical solutions for the configuration of $M \sim O(1)$ and $I \sim O(\delta^3)$. The graph on the left demonstrates the numerical solutions of the full system, while solutions in the right graph are obtained by solving the asymptotic system (2.64) combined with the leading order initial conditions of $x_1(0) = 1$, $\theta_1(0) = -2$, $u(0) = 0$ and $\omega(0) = 0$.

ODEs for the three unknowns x_{11}, Y_1 and θ_1:

$$(Y_1 + x_0\theta_1 + \theta_0 x_{11})x_{11}\ddot{x}_{11} + \frac{1}{2}x_{11}^2\ddot{Y}_1 + \frac{1}{2}x_0 x_{11}^2\ddot{\theta}_1 = \theta_0 x_{11}(1 - \dot{x}_{11}^2)$$
$$- (Y_1 + x_0\theta_1 + x_{11}\theta_0)(1 - \dot{x}_{11})^2 + 2x_{11}(\dot{Y}_1 + x_0\dot{\theta}_1)(1 - \dot{x}_{11}), \tag{2.66a}$$

$$(12M - x_{11}^3)\ddot{Y}_1 - x_0 x_{11}^3\ddot{\theta}_1 = -6x_{11}(Y_1 + x_0\theta_1 + \theta_0 x_{11})(1 - \dot{x}_{11})^2, \tag{2.66b}$$

$$(12I - x_0^2 x_{11}^3)\ddot{\theta}_1 - x_0 x_{11}^3\ddot{Y}_1 = -6x_0 x_{11}(Y_1 + x_0\theta_1 + \theta_0 x_{11})(1 - \dot{x}_{11})^2. \tag{2.66c}$$

These equations can be rearranged to the following:

$$u = \dot{x}_{11}, \tag{2.67a}$$

$$V = \dot{Y}_1, \tag{2.67b}$$

$$\omega = \dot{\theta}, \tag{2.67c}$$

$$\dot{u} = \frac{3\beta x_{11}^2(1 - \dot{x}_{11})^2}{12M - \beta x_{11}^3} + \frac{\theta_0(1 - \dot{x}_{11}^2) + 2(1 - \dot{x}_{11})(\dot{Y}_1 + x_0\dot{\theta}_1)}{Y_1 + x_0\theta_1 + \theta_0 x_{11}} - \frac{(1 - \dot{x}_{11})^2}{x_{11}}, \tag{2.67d}$$

$$\dot{V} = \frac{-6x_{11}(Y_1 + x_0\theta_1 + \theta_0 x_{11})(1 - \dot{x}_{11})^2}{12M - \beta x_{11}^3}, \tag{2.67e}$$

$$\dot{\omega} = \alpha\ddot{Y}_1. \tag{2.67f}$$

where $\alpha = \frac{M}{I} x_0$ and $\beta = 1 + \alpha x_0^2$, with the following initial conditions:

$$x_{11}(0) = -0, u(0) = \frac{-3(V_0 + x_0\omega_0) + \sqrt{9(V_0 + x_0\omega_0)^2 + 8\theta_0(V_0 + x_0\omega_0)}}{4\theta_0},$$
$$Y(0) = -0, V(0) = V_0,$$
$$\theta_1 = +0, \omega(0) = \omega_0,$$

as usual '-0' for $x_{11}(0)$ and $Y(0)$ indicates they are initialized to a small value less than zero; '$+0$' for $\theta_1(0)$ indicates it is set to a small value greater than zero. One immediate observation follows from the above system: the leading order angular acceleration $\ddot{\theta}_1$ evolves on a linear scale with the leading order vertical acceleration $\ddot{Y}_1$ as indicated in equation (2.67f). This is due to the fact that the leading order vertical force and torque from the liquid layer's pressure asserted on the body scales proportionally with one another, i.e. $I\ddot{\theta}_1 = x_0 M\ddot{Y}_1$.

The numerical solutions of the system indicates that the impact body is also able to exit from the liquid layer a short time after impact, but again the rebound does not exhibit the "super-elastic" effect as with the case of $M \sim O(\delta^3)$, $I \sim O(1)$.

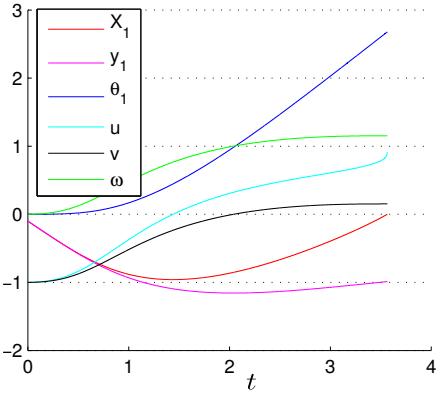

Figure 2.8: Numerical solutions of the system (2.67) with initial conditions of $x_{11}(0) = -0.1$; $Y_1 = -0.1$; $\theta_1(0) = 0$; $u(0) = -1$; $V(0) = -1$ and $\omega(0) = 0$. The solutions demonstrate that for a body with very small mass and moment of inertia, $M \sim O(\delta^3)$, $I \sim O(\delta^3)$, it is able to complete the transition from initial impact to final exit from the liquid layer inside the small time $t \sim O(\delta)$ regime.

2.4.5 Small impact angle analysis

In this section we analyse the effects of a small contact angle has on the motions of a skimming body. Suppose the contact angle between the impact body

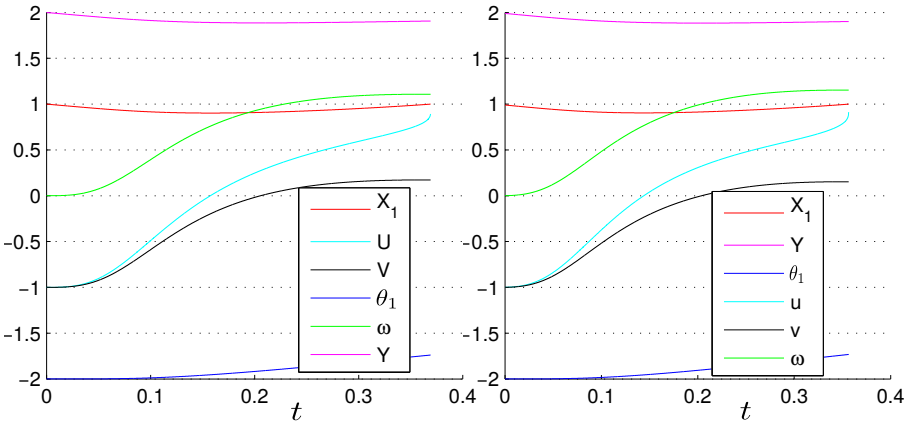

Figure 2.9: Numerical solutions for the configuration of $M \sim O(\delta^3)$ and $I \sim O(\delta^3)$. The graph on the left demonstrates the numerical solutions of the full system, while the graph on the right demonstrates the solutions of the asymptotic system (2.67) combined with the leading order initial conditions of $x_1(0) = 1$; $Y(0) = 2$; $\theta_1(0) = -2$; $u(0) = 0$; $V(0) = 0$ and $\omega(0) = 0$.

and undisturbed liquid surface at impact is very small, say $\theta_0 \sim O(\delta)$, then the body's vertical centre of mass Y_0 and liquid velocity D_0 at impact is also small due to the conditions (2.32) and (2.43), we therefore expand the four independent system variables as follows:

$$\begin{aligned} x_1(t) &= x_0 + \delta x_{11}(t) + \delta^2 x_{12}(t) + \delta^3 x_{13}(t) + O(\delta^3), \\ \theta(t) &= \delta\theta_0 + \delta^2\theta_1(t) + \delta^3\theta_2(t) + \delta^4\theta_3(t) + O(\delta^5), \\ Y(t) &= \delta Y_0 + \delta^2 Y_1(t) + \delta^3 Y_2(t) + \delta^4 Y_3(t) + O(\delta^5), \\ D(t) &= \delta D_0(t) + \delta^2 D_1(t) + \delta^3 D_2(t) + \delta^4 D_3(t) + O(\delta^5). \end{aligned}$$

Similarly we expand the pressure coefficient terms as follows:

$$\begin{aligned} \gamma_0 &= \gamma_{00} + \delta\gamma_{01} + \delta^2\gamma_{02} + \delta^3\gamma_{03} + O(\delta^4), \\ \gamma_1 &= \gamma_{10} + \delta\gamma_{11} + \delta^2\gamma_{12} + \delta^3\gamma_{13} + O(\delta^4), \\ \gamma_2 &= \gamma_{20} + \delta\gamma_{21} + \delta^2\gamma_{22} + \delta^3\gamma_{23} + O(\delta^4), \\ \gamma_3 &= \gamma_{30} + \delta\gamma_{31} + \delta^2\gamma_{32} + \delta^3\gamma_{33} + O(\delta^4). \end{aligned}$$

The trailing edge pressure condition (2.22) now implies the following relations for γ_0:

$$O(1) : \gamma_{00} = -\gamma_{30}x_0^3 - \gamma_{20}x_0^2 - \gamma_{10}x_0, \tag{2.69a}$$

$$O(\delta) : \gamma_{01} = -\gamma_{31}x_0^3 - \gamma_{21}x_0^2 - \gamma_{11}x_0, \tag{2.69b}$$

$$O(\delta^2) : \gamma_{02} = -\gamma_{32}x_0^3 - \gamma_{22}x_0^2 - \gamma_{12}x_0, \tag{2.69c}$$

$$O(\delta^3) : \gamma_{03} = -\gamma_{33}x_0^3 - \gamma_{23}x_0^2 - \gamma_{13}x_0. \tag{2.69d}$$

Substituting the expansions (2.69) - (2.69) into equation (2.26a) and collecting the δ terms gives:

$$O(1) : \gamma_{10} = -\dot{D}_0, \tag{2.70a}$$

$$O(\delta) : \gamma_{11} = \theta_0 + \dot{Y}_1 - \dot{D}_1, \tag{2.70b}$$

$$O(\delta^2) : \gamma_{12} = \theta_1 + \dot{Y}_2 - \dot{D}_2, \tag{2.70c}$$

$$O(\delta^3) : \gamma_{13} = \theta_2 + \dot{Y}_3 - \dot{D}_3. \tag{2.70d}$$

Applying the same treatment to equations (2.26b) and (2.26c) as above gives:

$$O(1) : \gamma_{20} = \frac{1}{2}\ddot{Y}_1, \tag{2.71a}$$

$$O(\delta) : \gamma_{21} = \frac{1}{2}\ddot{Y}_2 + \dot{\theta}_1, \tag{2.71b}$$

$$O(\delta^2) : \gamma_{22} = \frac{1}{2}\ddot{Y}_3 + \dot{\theta}_2, \tag{2.71c}$$

$$O(\delta^3) : \gamma_{23} = \frac{1}{2}\ddot{Y}_4 + \dot{\theta}_3, \tag{2.71d}$$

and:

$$O(1) : \gamma_{30} = \frac{1}{6}\ddot{\theta}_1, \tag{2.72a}$$

$$O(\delta) : \gamma_{31} = \frac{1}{6}\ddot{\theta}_2, \tag{2.72b}$$

$$O(\delta^2) : \gamma_{32} = \frac{1}{6}\ddot{\theta}_3, \tag{2.72c}$$

$$O(\delta^3) : \gamma_{33} = \frac{1}{6}\ddot{\theta}_4. \tag{2.72d}$$

As usual, the second order derivatives of Y and θ terms are to be determined by the asymptotic expansions of vertical and angular momentum equations (2.27a) and (2.27b) later in this section.

Asymptotic expansions of the first leading edge pressure condition (2.23) gives for the following relations:

$$O(1) : \gamma_{30}x_0^3 + \gamma_{20}x_0^2 + \gamma_{10}x_0 + \gamma_{00} = 0, \tag{2.73a}$$

$$O(\delta) : \gamma_{31}x_0^3 + 3\gamma_{30}x_0^2x_{11} + \gamma_{21}x_0^2 + 2\gamma_{20}x_0x_{11} + \gamma_{11}x_0 + \gamma_{10}x_{11} + \gamma_{01} = (Y_0 + x_0\theta_0)(\dot{x}_{11} - 1)^2, \tag{2.73b}$$

$$\begin{aligned} O(\delta^2) : {} & \gamma_{32}x_0^3 + \gamma_{22}x_0^2 + 3\gamma_{30}x_0x_{11}^2 + 3\gamma_{30}x_0^2x_{12} + 3\gamma_{31}x_0^2x_{11} + \gamma_{20}x_{11}^2 \\ & + 2\gamma_{20}x_0x_{12} + 2\gamma_{21}x_0x_{11} + \gamma_{11}x_{11} + \gamma_{10}x_{12} + \gamma_{12}x_0 + \gamma_{02} \\ & = (x_0\theta_1 + x_{11}\theta_0 + Y_1)(\dot{x}_{11} - 1)^2 + 2\dot{x}_{12}(Y_0 + x_0\theta_0)(\dot{x}_{11} - 1). \end{aligned} \tag{2.73c}$$

The order unity terms are trivially zero, and $O(\delta)$ terms of the above equations are zero due to (2.32). The $O(\delta^2)$ terms reveal the condition that the asymptotic expansions of our independent variables (2.69) - (2.69) must obey, substituting the expansions of pressure coefficients γ_0 - γ_3 into the equation (2.73c) and re-arrange gives:

$$\begin{aligned} & \frac{1}{2}(\ddot{Y}_1 + x_0\ddot{\theta}_1)x_{11}^2 + (\ddot{Y}_2 + \frac{1}{2}x_0\ddot{\theta}_2 + 2\dot{\theta}_1)x_0x_{11} + (\theta_0 + \dot{Y}_1 - \dot{D}_1)x_{11} = \\ & (1 - \dot{x}_{11})^2(Y_1 + x_0\theta_1 + \theta_0x_{11}), \end{aligned} \tag{2.74}$$

i.e. the same relation as (2.41).

Asymptotic expansions of the second leading edge pressure condition (2.25) gives:

$$O(1) : \gamma_{30}x_0^3 + \gamma_{20}x_0^2 + \gamma_{10}x_0 + \gamma_{00} = 0, \tag{2.75a}$$

$$O(\delta) : \gamma_{31}x_0^3 + 3\gamma_{30}x_0^2x_{11} + \gamma_{21}x_0^2 + 2\gamma_{20}x_0x_{11} + \gamma_{11}x_0 + \gamma_{10}x_{11} + \gamma_{01} = (\dot{x}_{11} - 1)(D_0 - x_0\theta_0 - x_0\dot{Y}_1 - \frac{1}{2}x_0^2\dot{\theta}_1), \tag{2.75b}$$

$$\begin{aligned} O(\delta^2) : {} & \gamma_{32}x_0^3 + \gamma_{22}x_0^2 + 3\gamma_{30}x_0x_{11}^2 + 3\gamma_{30}x_0^2x_{12} + 3\gamma_{31}x_0^2x_{11} + \gamma_{20}x_{11}^2 \\ & + 2\gamma_{20}x_0x_{12} + 2\gamma_{21}x_0x_{11} + \gamma_{11}x_{11} + \gamma_{10}x_{12} + \gamma_{12}x_0 + \gamma_{02} \\ & = (D_1 - \frac{1}{2}x_0^2\dot{\theta}_2 - x_0\theta_1 - x_0\dot{Y}_2 - x_{11}\dot{Y}_1 - x_{11}\theta_0 - x_0x_{11}\dot{\theta}_1)(\dot{x}_{11} - 1) \\ & + (D_0 - x_0\theta_0 - x_0\dot{Y}_1 - \frac{1}{2}x_0^2\dot{\theta}_1)\dot{x}_{12}. \end{aligned} \tag{2.75c}$$

As with the first leading edge pressure condition implies, the order unity terms are trivially zero; the $O(\delta)$ terms are also zero due to the equation for D_0 (2.43). From the $O(\delta)$ terms we obtain a second relation of our asymptotic expansions:

$$\begin{aligned} & \frac{1}{2}(\ddot{Y}_1 + x_0\ddot{\theta}_1)x_{11}^2 + (\ddot{Y}_2 + +\frac{1}{2}x_0\ddot{\theta}_2 + 2\dot{\theta}_1)x_0x_{11} + (\theta_0 + \dot{Y}_1 - \dot{D}_1)x_{11} = \\ & (1 - \dot{x}_{11})(x_0\theta_1 + x_{11}\theta_0 - D_1 + x_0\dot{Y}_2 + x_{11}\dot{Y}_1 + x_0x_{11}\dot{\theta}_1 + \frac{1}{2}x_0^2\dot{\theta}_2), \end{aligned} \tag{2.76}$$

i.e. the same relation as (2.45).

Asymptotic expansions of the linear momentum equation (2.27a) give:

$$O(1) : M\ddot{Y}_1 = 0, \tag{2.77a}$$

$$O(\delta) : M\ddot{Y}_2 = -\gamma_{00}x_{11} - \gamma_{10}x_0x_{11} - \gamma_{20}x_0^2x_{11} - \gamma_{30}x_0^3x_{11} = 0, \tag{2.77b}$$

$$\begin{aligned} O(\delta^2) : M\ddot{Y}_3 = {} & -\gamma_{30}x_0^3x_{12} - \gamma_{31}x_0^3x_{11} - \gamma_{20}x_0^2x_{12} - \gamma_{20}x_0x_{11}^2 - \frac{3}{2}\gamma_{30}x_0^2x_{11}^2 \\ & - \gamma_{01}x_{11} - \gamma_{00}x_{12} - \gamma_{10}x_0x_{11} - \gamma_{21}x_0^2x_{11} - \gamma_{10}x_0x_{12} - \frac{1}{2}\gamma_{10}x_{11}^2 \\ = {} & -\frac{3}{2}\gamma_{30}x_0^2x_{11}^2 - \gamma_{20}x_0x_{11}^2 - \frac{1}{2}\gamma_{10}x_{11}^2 = 0; \end{aligned} \tag{2.77c}$$

while the asymptotic expansions of the angular momentum equation (2.27b)

yield:

$$O(1) : I\ddot{\theta}_1 = 0, \tag{2.78a}$$

$$O(\delta) : I\ddot{\theta}_2 = -\gamma_{00}x_0x_{11} - \gamma_{10}x_0^2x_{11} - \gamma_{20}x_0^3x_{11} - \gamma_{30}x_0^4x_{11} = 0, \tag{2.78b}$$

$$\begin{aligned} O(\delta^2) : I\ddot{\theta}_3 = &-\gamma_{30}x_0^4x_{12} - \gamma_{31}x_0^4x_{11} - 2\gamma_{30}x_0^3x_{11}^2 - \gamma_{20}x_0^3x_{12} - \gamma_{21}x_0^3x_{11} \\ &- \frac{1}{2}\gamma_{00}x_{11}^2 - \frac{3}{2}\gamma_{20}x_0^2x_{11}^2 - \gamma_{11}x_0^2x_{11} - \gamma_{10}x_0x_{11}^2 - \gamma_{10}x_0^2x_{12} - \gamma_{00}x_0x_{12} \\ &- \gamma_{01}x_0x_{11} = -\frac{3}{2}\gamma_{30}x_0^3x_{11}^2 - \gamma_{20}x_0^2x_{11}^2 - \frac{1}{2}\gamma_{10}x_0x_{11}^2 = 0. \end{aligned} \tag{2.78c}$$

Just as we analysed in section 2.4.1 for the case of M and I being order unity, at a small time after impact the water pressure underneath the impact body is insufficient to affect the body's leading order vertical and angular velocities. In addition we have x_{11} from the relation (2.55) derived in section 2.4.1.

There is one critical difference between the case of $\theta \sim O(\delta)$ and $\theta \sim O(1)$ analysed in section 2.4.1: namely for $\theta_0 \sim O(\delta)$ the body's initial vertical velocity V_0 at impact is also $O(\delta)$, this condition is vital as equation (2.55) implies that if $V_0 \gg O(\delta)$ then x_{11} will have $O(1)$ variation even at small time $t \sim O(\delta)$. This means the wetted contact region reaches the front tip of the impact body at a small time while the body is vertically descending (as indicated in (2.77a)), i.e. the body begins to submerge at small time after impact.

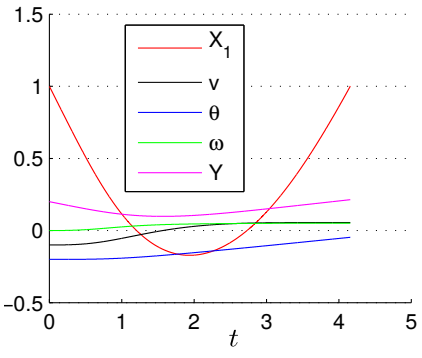

Figure 2.10: Numerical solutions of the asymptotic system of $M, I \sim O(1); \theta \sim O(\delta); V \sim O(\delta)$ with initial conditions $x_1(0) = 1$; $Y(0) = 0.2$; $\theta(0) = -0.2$; $V(0) = -0.1$ and $\omega(0) = 0$. The solutions demonstrate that for a body with small contact angle and small vertical impact velocity, i.e. $\theta \sim O(\delta)$, $V \sim O(\delta)$, it is able to complete the transition from initial impact to final exit from the liquid layer inside the small time $t \sim O(\delta)$ regime.

2.5 Water exit for small mass and moment of inertia

In this section we investigate the behaviour of a skimming body with small body mass and moment of inertia close to the water exit stage. Suppose the body exits from water at a time $t = t_e$, at which point the leading and trailing edges coincide with each other and $x_0(t_e) = x_1(t_e) = 0$. We let $\hat{u}_0$, $\hat{Y}_0$, $\hat{V}_0$, $\hat{\theta}_0$ and $\hat{\omega}_0$ denote the leading edge's horizontal velocity, the body's vertical centre of mass position, its vertical velocity, contact angle with water and angular velocity at the time of exit respectively. These exit values are assumed to be known and can either be obtained from our model equations or alternatively estimated from physical observations. We are interested in a short time period just before the body separates from water such that $0 < t_e - t \ll 1$, therefore we expand the skimming system variables correspondingly as below:

$$x_{11} = 0 - \hat{u}_0(t_e - t) + f(t_e - t), \tag{2.79a}$$

$$Y_1 = \hat{Y}_0 - \hat{V}_0(t_e - t) + g(t_e - t), \tag{2.79b}$$

$$\theta_1 = \hat{\theta}_0 - \hat{\omega}_0(t_e - t) + \alpha g(t_e - t), \tag{2.79c}$$

where α is some constant which arises due to the linear relation between the body's height and contact angle given by (2.19).

Substituting these expressions into the linearised skimming system for small mass and moment of inertia (2.67d) - (2.67f) introduced in Section 2.4.4, after simplification at the leading order we obtain the following two equations for the two unknowns f and g:

$$\ddot{f}(t_e - t) = \frac{(1 - \hat{u}_0 + \dot{f})^2}{\hat{u}_0(t_e - t)}, \tag{2.80a}$$

$$\ddot{g}(t_e - t) = \frac{\hat{u}_0(\hat{Y}_0 + x_0\hat{\theta}_0)(t_e - t)(1 - \hat{u}_0 + \dot{f})^2}{2M}. \tag{2.80b}$$

Equation (2.80a) can be intergrated once to obtain:

$$\dot{f}(t_e - t) = -(1 - \hat{u}_0 + \frac{\hat{u}_0}{\log c_1(t_e - t)}), \tag{2.81}$$

where c_1 is an integration constant, and likewise for equation (2.80b):

$$\dot{g}(t_e - t) = \frac{\hat{u}_0^3(\hat{Y}_0 + x_0\hat{\theta}_0)}{2M} \int_t^{t_e} \frac{t_e - s}{\log^2 c_1(t_e - s)}\, ds + c_2, \tag{2.82}$$

where c_2 is also an integration constant. The evolution of the body's leading edge and vertical positions are highly non-linear, their velocities become singular rapidly as the body get closer to water separation which poses challenges to numerical schemes.

Our numerical solution estimates c_1 to be ~ 0.1127. The comparison of the numerical solution against equation (2.81) is illustrated in Fig. 2.11. The two results show reasonable quantitative and qualitative agreement.

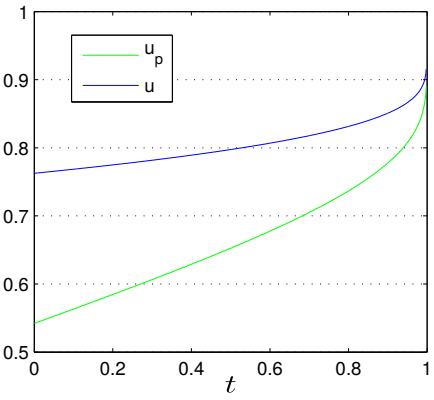

Figure 2.11: Predicted value of u near exit. Blue line is the actual numerical solution of u near exit, and the green line u_p is the predicted value.

2.6 Multiple rebounds

Consider a body skipping over a thin layer of water with velocity $(\bar{U}, \bar{V})$ where $\bar{U} \gg \bar{V}$. The non-dimensionalization analysis from Section 2.2 shows that gravity has a negligible effect during the body skimming on water stage. Once the body rebounds from the water into the air however, gravity becomes a dominant

force until the body re-establishes contact with water[2].

For a body travelling in air with vertical velocity $\bar{V}_0$ where gravity is the only non-negligible force, after time $\bar{t}$ the resulting vertical velocity $\bar{V}_t$ and travelled vertical distance $\bar{S}$ are:

$$\bar{S} = \bar{V}_0\bar{t} + \frac{1}{2}\bar{g}\bar{t}^2,$$
$$\bar{V}_t = \bar{V}_0 + \bar{g}\bar{t}.$$

We non-dimensionalize $\bar{S}$ using water layer depth $\bar{H}$; $\bar{t}$ using the convective timescale $\bar{L}/\bar{U}$; $\bar{V}$ using $\bar{H}\bar{U}/\bar{L}$ and $\bar{g}$ using $\bar{H}\bar{U}^2/\bar{L}^2$. Dropping the bar from these variables to denote their non-dimensionalized counterparts, then the equations become:

$$S = V_0 t + \frac{1}{2}gt^2, \tag{2.84a}$$
$$V_t = V_0 + gt. \tag{2.84b}$$

If we let Y_e^i, V_e^i, θ_e^i, ω_e^i be the body's vertical centre of mass position, vertical exit velocity, exit angle and exit angular velocity respectively upon the i-th rebound from the water layer; let V_0^{i+1}, θ_0^{i+1}, ω_0^{i+1} be their values upon water entry for the $(i+1)$-th time; let t be the time the body travels in mid-air measured from exit from the water to touch down again; S^i be the vertical distance that the body has to travel during this time t upon rebounds from the water for the i-th time, then we can obtain the following governing equations for the motion of the body in air:

$$\frac{1}{2}gt^2 + x_0\omega_e^i t + Y_e^i + x_0\theta_e^i - \frac{V_e^i}{g}(\frac{1}{2}V_e^i + x_0\omega_e^i) = 0, \tag{2.85a}$$
$$V_0^{i+1} = gt, \tag{2.85b}$$
$$\omega_0^{i+1} = \omega_e^i. \tag{2.85c}$$

[2]Note that air-cushioning effect is not taken into account.

Governing equations (2.85a) - (2.85c) enable us to derive the body's $(i+1)$-th water-entry conditions from its i-th water-exit conditions. See Fig. 2.12 for a simulation of a body with small mass and large moment of inertia going through the process of multiple rebounds.

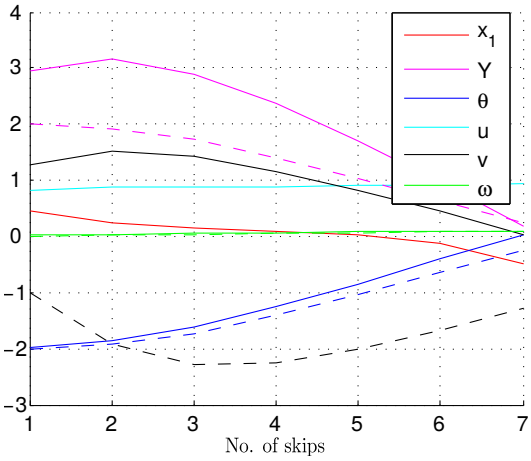

Figure 2.12: A plot shows a body goes through seven rebounds. The dashed lines indicate the entry values of each rebound, the solid lines indicate the exit values of each rebound with mass $M \sim O(\delta)$, moment of inertia $I \sim O(\delta^{-1})$ and $\theta \sim O(1)$.

2.7 Conclusions

We began our analysis of the skimming motions of a thin body by first reviewing the skipping-stone model of [57]. For a shallow water thin body skipping model the position of its leading edge determines the body's surface contact area with water, this has an important role in influencing its skipping motion.

We subsequently analysed the roles of body mass and moment of inertia play on the body's skimming motion via asymptotic analysis. For a body with small mass we demonstrated that it is able to skip out of water at a small time after impact, with its height at exit being greater than its height at initial water entry – a phenomenon known as "super-elastic" as observed by [37]. For a body with small moment of inertia the body's contact angle is subject to rapid change; the "flattening" of the angle reduces the normal lift the body is able to obtain, this is shown by its vertical trajectory at a small time after impact. As a result the body is not able to achieve rapid separation from water. It is worth noting that a

body with large moment of inertia, which measures the body's resistance to the change of its contact angle with water, has a similar effect as the spinning of the body in 3D, i.e. a gyroscopic stabilization effect as proposed by [44]. In essence a large moment of inertia and the gyroscopic effect helps the stone to maintain its optimal contact angle during skipping. Finally we presented a model that captures the characteristics of a stone going through multiple rebounds. It is demonstrated for each skip the stone performs, its contact angle with water surface flattens and its height of rebound decreases, this eventually leads the stone being submersed in water with a flat contact angle.

This skimming model can be extended further by incorporating a parabolic body thickness to the skipping body, giving it a smooth and rounded surface shape profile. This will be discussed further in Chapter 5.

Chapter 3

Collisions, Rebounds and Skimming

Repeated oblique impacts and rebounds of a solid body or bodies on horizontal shallow water are investigated through mathematical modelling. The inclinations from the horizontal are supposed small as the skimming evolves, for a thin typical body shape. The new formulation aimed at improved prediction as well as the background involved are presented together with nonlinear analysis and computation. Comparatively fast or slow collisions and rebounds are found to be of special interest over short time scales.

3.1 Introduction

Collisions, bouncing and skimming (skipping) in fluid-body or fluid-fluid impacts arise in numerous applications, whether of a serious or playful nature. Special mention should be made of phenomena in aircraft icing, storms, engine intakes, ship-slamming and meteor impacts. There is a wide background of recent literature [57, 27, 60, 2, 35, 68, 1, 6, 69, 12, 39, 26, 28, 29], major aspects of which we summarise later in the introduction.

There are also connections to two long-standing distinguished themes of re-

search, namely that of boundary layers and viscous-inviscid interactions stemming from [43, 64, 65, 52, 74, 41, 9] and that of impacts, splashing, rebounds and interfacial interactions stemming especially from [35] (see also [68, 1, 11, 50, 61]). The common features between the themes include their original industrially based motivations and their mechanisms of 'stability, separation and close body interactions' as well as their modern uses (for example in separation, transition, turbulence, stall on the one hand and in icing, storms and the like on the other) and their mechanisms of inner-outer dependence, system reduction, thin-layer dynamics and subtle interactions. Both benefit from analysis, computation, experimental links and improved physical understanding.

Three areas influence the present investigation. Concerning collisions, first, air-water interactions are addressed in [27, 60, 2]. In [2] in particular near-impact behaviour is investigated for a solid body approaching another solid body with two immiscible incompressible viscous fluids occupying the gap in between. The fluids have viscosity and density ratios which are extreme, the most notable combination being water and air, such that either or both of the bodies are covered by a thin film of water. Air-water interaction and the commonly observed phenomenon of air trapping are of concern. The subcritical regime is of most practical significance here in terms of the Reynolds number compared with a critical value, which depends on the two fluid ratios, and it leads physically to the effect of inviscid water dynamics coupling with a viscous-dominated air response locally. This physical mechanism [27] induces touchdown (or an approach to touchdown), which is found to occur in the sense that the scaled air-gap thickness shrinks towards zero within a finite scaled time according to analysis performed hand in hand with computation. A global influence on the local touchdown properties is also identified. Comparisons with computations prove favourable. Air trapping is produced between two touchdown positions, at each of which there is a pressure peak; an oblique approach would not affect the finding unless the approach itself is extremely shallow. The mechanism of air-water interaction leading to air trapping is suggested as a wide-ranging

result.

Secondly, free-surface impacts without air effects are studied in [12, 39]. Here[12] considers the effect of surface roughness. If a surface is sufficiently rough, then models of droplet impact need to include the possibility of many touchdowns between the fluid and the solid. The subsequent simultaneous motion of several contact points is therefore described. In particular, results are presented for the contact point motion during the impact of a sheet of water on to a periodic rough surface. A model for multiple contact point motion is also analysed for cases of deep surface roughnesses. The analysis is complemented by a direct numerical simulation using the volume of fluid method. The effect of surface roughness is to reduce the rate at which the droplet spreads. Comparisons between various roughness shapes are considered numerically and analytically. Possible applications are then discussed, especially in the context of aircraft icing. Follow-up study to allow for ice accretion is in [39].

The third area of direct relevance is fluid-body interactions [26, 28, 29]. Interactions between a finite number of bodies and the surrounding fluid are investigated in [26]. The bodies or modelled grains are thin solid bodies free to move in a nearly parallel formation within a quasi-inviscid fluid. The investigation involves numerical and analytical studies and comparisons. The three main features are a linear instability about a state of uniform motion, a clashing of the bodies (or of a body with a side wall) within a finite scaled time when nonlinear interaction takes effect, and a continuum-limit description of the body-fluid interaction holding for many bodies. Solid-solid and solid-fluid clashing, skimming and bouncing are the concern in [28]. A theoretical study is presented on fluid-body interaction in which the motion of the body and the fluid again influence each other nonlinearly. The clashing refers to solid-solid impacts arising from fluid-body interaction in a channel, while the skimming refers to another area where a thin body impacts obliquely upon a fluid surface. Bouncing usually then follows in both areas. The main new contribution concerns the influences of thickness and camber which lead to a distinct general form of clashing and

hence bouncing. In [29] conditions are investigated under which a body lying at rest or rocking on a solid horizontal surface can be removed by hydrodynamic forces or instead continues rocking. The investigation is motivated by recent observations on Martian dust movement as well as other small- and large-scale applications. The nonlinear theory of fluid-body interaction here has unsteady motion of an inviscid fluid interacting with a moving thin body. Various shapes of body are addressed together with a range of initial conditions. The relevant parameter space is found to be subtle as evolution and shape play substantial roles coupled with scaled mass and gravity effects. Lift-off of the body from the surface generally cannot occur without fluid flow but it can occur either immediately or within a finite time once the fluid flow starts up: parameters for this are found and comparisons are made with Martian observations.

The new work here is directed at the challenge of understanding and predicting repeated oblique impacts and rebounds of a solid body or bodies on shallow liquid, typically water. Such skimming, colliding and bouncing induces splash jets at the leading edge (the unknown moving front of the wetted surface on the body) and can also induce jets at the trailing edge or not, depending on the body shape, on the initial conditions and on the evolution of the complete incompressible fluid-body interaction among other factors. The effects of the major interaction parameters and of different body shapes of concern are to be described by means of nonlinear analysis and computation with a view to connecting with experiments. With many temporal and spatial scales being active the excitement in the modelling here is in seeking justified simplification wherever possible subject to the theoretical model remaining physically realistic.

Section 3.2 below describes the framework for the new work which begins with Figure 3.1 while Section 3.3 presents analysis. Interactive properties for enhanced and reduced downward speeds at impact are addressed in Sections 3.4, 3.5 respectively. Section 3.6 adds further comments including predictions for repeated impacts and rebounds.

3.2 Background model

Experimental results covering collisions, rebounds and skimming in qualitative form are quite plentiful as described in [57, 37] whereas justifiable mathematical models seem few. The present contribution is associated closely with the Hicks-Smith model [57] of skimming in unsteady two-dimensional interactions. Such exciting interactions which offer an example of fluid-body interaction and make several perhaps bold assumptions as delineated later are governed by a scaled nonlinear evolutionary system for the unknown functions $Y, \theta, x_1, D, \gamma_0, \gamma_1, \gamma_2, \gamma_3$. Here in scaled terms Y is the height of the centre of mass of the body, θ is essentially the body's angle of inclination from the horizontal, x_1 is the moving contact point that forms in effect the leading edge for the wetted part of the body at any instant, D is a fluid velocity contribution and $\gamma_0, \gamma_1, \gamma_2, \gamma_3$ are pressure coefficients. Further, x is the horizontal coordinate, y is the vertical coordinate and t denotes time, again in appropriately scaled terms.

The Hicks-Smith model takes a reference frame fixed in the body and a non-dimensional form such that the horizontal velocity, body half-length and typical convective time are unity; the shapes of body and water layer involved are thin and nearly horizontal. The nonlinear shallow-water equations, i.e. unsteady inviscid boundary-layer equations, apply to the fluid flow nominally since the Reynolds number and Froude number are large in practice, as is the Weber number, and therefore to the leading order the viscous, gravitational and surface tension effects are negligible. If in addition the vertical scale of the water layer exceeds that of the body by a factor $1/\Delta$ say then the following modification holds:

$$(h, U, P, Y, \theta, T) = (1, 1, 0, 1, 0, 0) + \Delta(\tilde{h}, \tilde{U}, \tilde{P}, \tilde{Y}, \tilde{\theta}, \tilde{T}) + \ldots, \tag{3.1}$$

where $\Delta \ll 1$ and the terms with tildes are of order unity. The quantities

h, U, P, T denote respectively the height of the body under-surface measured from the bottom of the liquid layer at $y = 0$, the induced flow velocity, the fluid pressure and the body half-thickness in scaled format. Capitals U, V, P signify fluid-flow responses as opposed to u, v used later for essentially the body-motion responses. The trailing edge of the body is taken to be sharp rather than smooth and the liquid free surface detaches from the body there: see Figure 3.1. The unknown leading-edge position x_1 is of order unity generally. The body shape implies

$$\tilde{h}(x,t) = \tilde{Y}(t) + (x - x_m)\tilde{\theta}(t) - \tilde{T}(x), \tag{3.2}$$

where x_m is the horizontal position of the centre of mass; assuming the body has uniform density this position is taken to be zero in our coordinate system. The shallow-water equations give now

$$\tilde{U}_t + \tilde{U}_x = -\tilde{P}_x, \tag{3.3a}$$

$$\tilde{h}_t + \tilde{h}_x + \tilde{U}_x = 0. \tag{3.3b}$$

At the known trailing edge x_0 the equi-pressure Kutta condition to take account of viscous effects due to the sensitive laminar or turbulent boundary layers at the trailing edge implies $\tilde{P}(x_0, t) = 0$, while in the wake region $x > x_0$ we have $\tilde{P}$ being identically zero (atmospheric); the trailing edge position x_0 is normalised to be one. At the unknown leading edge x_1 jump conditions as in [21, 57] yield

$$\tilde{P}(x_1,t) + \left(1 - \frac{dx_1}{dt}\right)\tilde{U}(x_1,t) = 0, \tag{3.4a}$$

$$\tilde{U}(x_1,t) = -\left(1 - \frac{dx_1}{dt}\right)\tilde{h}(x_1,t). \tag{3.4b}$$

Also the vertical momentum balance for the body simplifies to

$$M\frac{d^2\tilde{Y}}{dt^2} = \int_{x_1}^{x_0} \tilde{P}(x,t)dx, \tag{3.5}$$

the horizontal balance confirms that the body moves with constant horizontal velocity unity to leading order, and angular momentum requires

$$I\frac{d^2\tilde{\theta}}{dt^2} = \int_{x_1}^{x_0} x\tilde{P}(x,t)dx. \tag{3.6}$$

Here M, I are the scaled mass and moment of inertia of the body in turn. The liquid in the wetted region $[x_1, x_0]$ is of primary interest.

For a body with parabolic shape $\tilde{T} = A + Bx + Cx^2$ with constants A, B, C, and so from (3.2)

$$\tilde{h}(x,t) = \tilde{Y}(t) + x\tilde{\theta}(t) - A - Bx - Cx^2, \text{ for } x_1 \leq x \leq x_0, \tag{3.7}$$

is also quadratic. In this region (3.3) indicates that $\tilde{P}_{xx}$ is at most linear in x. Therefore we can write

$$\tilde{P} = \gamma_3 x^3 + \gamma_2 x^2 + \gamma_1 x + \gamma_0 \text{ for } x_1 \leq x \leq x_0, \tag{3.8}$$

where γ_n for $n = 0, 1, 2, 3$ are unknown functions of time. The system for zero A, B, C, i.e. a body with negligible thickness is then of the nonlinear form: trailing-edge pressure condition,

$$\gamma_3 x_0^3 + \gamma_2 x_0^2 + \gamma_1 x_0 + \gamma_0 = 0; \tag{3.9}$$

two conditions at the leading edge,

$$\gamma_3 x_1^3 + \gamma_2 x_1^2 + \gamma_1 x_1 + \gamma_0 = (Y + x_1\theta)\left(1 - \frac{\mathrm{d}x_1}{\mathrm{d}t}\right)^2, \tag{3.10}$$

$$\gamma_3 x_1^3 + \gamma_2 x_1^2 + \gamma_1 x_1 + \gamma_0 = \left[\frac{x_1^2}{2}\frac{\mathrm{d}\theta}{\mathrm{d}t} + x_1\left(\frac{\mathrm{d}Y}{\mathrm{d}t} + \theta\right) - D\right]\left(1 - \frac{\mathrm{d}x_1}{\mathrm{d}t}\right), \tag{3.11}$$

where D is an unknown function of time representing the horizontal velocity of

the fluid at the centre of mass, $x = 0$; three momentum-balance effects,

$$\gamma_1 = -\frac{\mathrm{d}D}{\mathrm{d}t} + \frac{\mathrm{d}Y}{\mathrm{d}t} + \theta, \tag{3.12}$$

$$2\gamma_2 = \frac{\mathrm{d}^2Y}{\mathrm{d}t^2} + 2\frac{\mathrm{d}\theta}{\mathrm{d}t}, \tag{3.13}$$

$$6\gamma_3 = \frac{\mathrm{d}^2\theta}{\mathrm{d}t^2}; \tag{3.14}$$

linear and angular momentum of the body,

$$M\frac{\mathrm{d}^2Y}{\mathrm{d}t^2} = \frac{\gamma_3}{4}(x_0^4 - x_1^4) + \frac{\gamma_2}{3}(x_0^3 - x_1^3) + \frac{\gamma_1}{2}(x_0^2 - x_1^2) + \gamma_0(x_0 - x_1), \tag{3.15}$$

$$I\frac{\mathrm{d}^2\theta}{\mathrm{d}t^2} = \frac{\gamma_3}{5}(x_0^5 - x_1^5) + \frac{\gamma_2}{4}(x_0^4 - x_1^4) + \frac{\gamma_1}{3}(x_0^3 - x_1^3) + \frac{\gamma_0}{2}(x_0^2 - x_1^2); \tag{3.16}$$

hence giving eight equations for eight unknowns at each time level in effect. The main assumptions made in the theory include the straight flat geometry of the body, the two-dimensionality of the entire fluid-body interaction, the neglect of air effects, the incompressibility of the quasi-inviscid fluid (water), the shallowness of the water layer and the smallness of the flow angles induced during the motion.

Numerical solutions and certain analytical properties are presented in [57]. The current new work begins with the framework of (3.9)-(3.16) and then moves on to study wider applications for more general body shapes and all-round configurations.

3.3 Fast responses

Figure 3.2 presents our results for the moving contact position, vertical displacement and body-motion velocities from the above framework but in a parameter range rather distinct from previously since the typical time scale is quite short. The results still show the rapid change of leading-edge velocity just prior to lift-off of the body from the water at time t of approximately 0.45, by the way.

With regard to the present investigation and novel formulation computations such as in Figure 3.2 point to a simplification occurring for fast behaviour over a time scale of order E say with the constant E being small and positive, for small mass factors M of order E^3. At first sight the left-hand side of (3.15) might be taken to be negligible when M is small but instead the time scale shrinks to achieve balance there and this then leaves the contribution of the left-hand side in (3.16) as outstanding, a point discussed further near the end of the paper. The solution expands as

$$[Y, \theta, x_1, D, \gamma_n] = [Y_0 + E\hat{Y}(\hat{t}), \theta_0 + E\hat{\theta}(\hat{t}), x_0 + E\hat{x}(\hat{t}), \hat{D}(\hat{t}), E^{-1}\gamma_{0n} + \gamma_{1n}] + \ldots \tag{3.17}$$

with $t = E\hat{t}, n = 0, 1, 2, 3; Y_0, \theta_0, x_0$ are initial values and it is found that $\hat{D} = x_0(\theta_0 + \hat{Y}') + x_0^2\hat{\theta}'/2$. The prime denotes $d/d\hat{t}$. The most significant behaviour in this fast-time response clearly occurs spatially near the incident trailing-edge location. Here $\hat{M} = M/E^3$ and I are of order unity. It is found also that the model can then be reduced to two coupled nonlinear differential equations for $\hat{x}, \hat{Y}$,

$$S\hat{x}\hat{x}'' + \frac{1}{2}\hat{x}^2\hat{Y}'' = \theta_0\hat{x}(1 - \hat{x}'^2) - S(1 - \hat{x}')^2 + 2\hat{x}(\hat{Y}' + x_0\omega_0)(1 - \hat{x}'), \tag{3.18a}$$

$$(12\hat{M} - \hat{x}^3)\hat{Y}'' = -6\hat{x}S(1 - \hat{x}')^2, \text{ with } S \equiv (\hat{Y} + x_0\hat{\theta} + \theta_0\hat{x}), \tag{3.18b}$$

where ω_0 is a prescribed constant and $\hat{\theta} \equiv \omega_0\hat{t}$. Similarly for small moments of inertia I of order E^3 with M of order unity a pair of nonlinear equations holds for $\hat{\theta}, \hat{Y}$, at leading order. If both M, I are of order E^3 then the same approach leaves the three interactive equations

$$S\hat{x}\hat{x}'' + \frac{1}{2}\hat{x}^2\hat{Y}'' + \frac{1}{2}x_0\hat{x}^2\hat{\theta}'' = \theta_0\hat{x}(1 - \hat{x}'^2) - S(1 - \hat{x}')^2 + 2\hat{x}(\hat{Y}' + x_0\hat{\theta}')(1 - \hat{x}'), \tag{3.19a}$$

$$(12\hat{M} - \hat{x}^3)\hat{Y}'' - x_0\hat{x}^3\hat{\theta}'' = -6\hat{x}S(1-\hat{x}')^2, \tag{3.19b}$$

$$(12\hat{I} - x_0^2\hat{x}^3)\hat{\theta}'' - x_0\hat{x}^3\hat{Y}'' = -6x_0\hat{x}S(1-\hat{x}')^2 \tag{3.19c}$$

controlling the nonlinear evolution of $\hat{x}, \hat{Y}, \hat{\theta}$ with scaled time. The following investigation is on the regime of small mass as in (3.18a,3.18b) primarily. It is noted however that computed solutions for all three of the simpler forms just described agree well with the full solutions of (3.9)–(3.16) at small M or I values as exemplified by Figure 3.2 and in more detail in Chapter 2.

The reduced system (3.18a, 3.18b) in which we now set $\hat{u}, \hat{v}$ as $\hat{x}', \hat{Y}'$ for convenience can be normalised by putting

$$[\hat{x}, \hat{Y}, \hat{u}, \hat{v}, \hat{t}] = [\hat{M}^{1/3}\bar{x}, |\alpha|\hat{M}^{1/3}(\bar{Y} - \bar{\beta}\bar{t}), \bar{u}, |\alpha|(\bar{v} - \bar{\beta}), \hat{M}^{1/3}\bar{t}] \tag{3.20}$$

along with $\beta\omega_0 = |\alpha|\bar{\beta}$ where α is the initial angle θ_0. Here β is the initial entry position x_0; the transformation accounts for the influence $\bar{\beta}$, identifies the central dynamics and also expects α to be negative because of the incident downward motion. Thus the system becomes

$$\bar{u} = \bar{x}', \tag{3.21a}$$

$$\bar{v} = \bar{Y}', \tag{3.21b}$$

$$\frac{\bar{u}'}{(1-\bar{u})} = \frac{(2\bar{v} - \bar{u} - 1)}{(\bar{Y} - \bar{x})} + \frac{3\bar{x}^2(1-\bar{u})}{(12 - \bar{x}^3)} - \frac{(1-\bar{u})}{\bar{x}}, \tag{3.21c}$$

$$\bar{v}' = \frac{6\bar{x}(\bar{x} - \bar{Y})(1-\bar{u})^2}{12 - \bar{x}^3}, \tag{3.21d}$$

subject to initial conditions which correspond to knowing the location and downward speed of the impact at first,

$$\bar{x}(0) = \bar{Y}(0) = 0, \tag{3.22a}$$

$$\bar{v}(0) = \bar{v}_0, \bar{u}(0) = \frac{1}{4}(3\bar{v}_0 - [9\bar{v}_0^2 - 8\bar{v}_0]^{1/2}). \tag{3.22b}$$

Primes in the above represent $d/d\bar{t}$. The result for $\bar{u}(0)$ stems from properties

at small times $\bar{t}$. In effect, above all the original system can take (α, M, β) as $(-1, 1, 0)$ in turn without loss of generality and we are left with the task of solving (3.21)-(3.22) in terms of the single parameter $\bar{v}_0$ which represents the scaled downward approach speed.

Numerical results obtained from a straightforward time-marching scheme and checked as regards grid effects are given in Figure 3.3 for a range of values of $\bar{v}_0$. The increasing downward plunge as $\bar{v}_0$ is increased makes physical sense, and we observe the subsequent recovery leading to lift-off in every case calculated. Insight into these fast responses is provided by the analyses in the next two sections and an ensuing study of the physical mechanisms involved.

3.4 Increased downward speed

With more downward entry speed the parameter $\bar{v}_0$ is large and negative. Two or three distinct successive stages are now found to come into operation: see Figure 3.4(a-c).

First, over very small time scales the relevant expressions for $\bar{x}, \bar{Y}, \bar{t}$ are

$$\bar{t} = |\bar{v}_0|^{-1} t^*, \tag{3.23a}$$

$$(\bar{x}, \bar{Y}) = (x^*, Y^*) + \ldots \tag{3.23b}$$

with x^*, Y^* of order unity. Substitution into (3.21) then yields the dominant mechanisms as

$$u^* = x^{*\prime}, \tag{3.24a}$$

$$v^* = Y^{*\prime}, \tag{3.24b}$$

$$u^{*\prime} = \frac{(u^{*2} - 2v^* u^*)}{(Y^* - x^*)} + \frac{3x^{*2} u^{*2}}{(12 - x^{*3})} - \frac{u^{*2}}{x^*}, \tag{3.24c}$$

$$v^{*\prime} = \frac{6x^*(x^* - Y^*)u^{*2}}{12 - x^{*3}}, \tag{3.24d}$$

subject to $(x^*, Y^*, u^*, v^*)(0) = (0, 0, -3/2, -1)$. The large effective velocities

provoked here as the wetting and downward distance both increase quite rapidly are responsible for the reduction in form. Hence the solutions during this first-wetting stage are as depicted in Figure 3.4(a). Of concern next is what happens to the reduced nonlinear system (3.24) as time t^* becomes large and positive. The downward motion tends to dominate as the wetted area "saturates" then. The results coupled with a large-time study indicate that the asymptotic features

$$\begin{aligned} x^* &\sim \alpha_1 + \alpha_2 t^{*-1} + \alpha_3 t^{*-2} + \ldots \\ Y^* &\sim \beta_0 t^* + \beta_1 + \beta_2 t^{*-1} + \ldots \\ u^* &\sim -\alpha_2 t^{*-2} - 2\alpha_3 t^{*-3} + \ldots \\ v^* &\sim \beta_0 - \beta_2 t^{*-2} + \ldots \end{aligned}$$

describe the behaviour then, and indeed substitution into (3.24) shows consistency of these features provided that the relation $(12-\alpha_1^3)\beta_2 = -3\alpha_1\alpha_2^2\beta_0$ holds, which acts to determine the coefficient β_2 in essence. The coefficients $\alpha_1, \alpha_2, \beta_0$ remain arbitrary in the large-t^* features and are believed to depend on overall global properties of the system (3.24) applying for all t^* of order unity. These asymptotic features lead into the structure of the next stage.

The second stage then occurs a little later and has the expansions

$$\bar{t} = |\bar{v}_0|^{-1/2}\tilde{t}, \tag{3.25a}$$

$$(\bar{x}, \bar{Y}) = (\alpha_1 + |\bar{v}_0|^{-1/2}\tilde{x}_1, |\bar{v}_0|^{1/2}\tilde{Y}) + \ldots, \tag{3.25b}$$

where to lowest order α_1 represents the most forward position achieved by the wetting process. So the main governing equations become simply

$$\tilde{u} = \tilde{x}_1', \tag{3.26a}$$

$$\tilde{v} = \tilde{Y}', \tag{3.26b}$$

$$\tilde{u}' = \frac{2\tilde{v}(1-\tilde{u})}{\tilde{Y}}, \tag{3.26c}$$

$$\tilde{v}' = 0 \tag{3.26d}$$

with the relatively deep plunge here associated with $|\bar{Y}| \gg |\bar{x}|$ and $|\bar{v}| \gg |\bar{u}|$

being the major effects accompanying the deceleration in wetting. These lead to the solution $\tilde{x}_1 = \tilde{t} - c_3/\tilde{t}$ + constant, $\tilde{u} = 1 + c_3/\tilde{t}^2, \tilde{Y} = \tilde{\gamma}\tilde{t}, \tilde{v} = \tilde{\gamma}$ where matching requires $c_3 = -\alpha_2$ and fixes $\tilde{\gamma}$ as β_0. The terms $\tilde{t}$ in $\tilde{x}_1$ and 1 in $\tilde{u}$ are the novel leading-order contributions in this stage, pointing to a minimum $\tilde{x}_1$ of $2\alpha_2^{1/2}$ which determines the maximum of the wetted interval and to the depth $|\tilde{Y}|$ reached continuing to increase linearly with time ($0 < \tilde{t} < \infty$ in this stage). See Figure 3.4(b).

In the third and final stage the time scale rises to be of order unity and the trend reversion to lift-off takes place in full. Now

$$\bar{t} = O(1), \tag{3.27a}$$

$$(\bar{x}, \bar{Y}) = (\bar{\bar{x}}, |\bar{v}_0|\bar{\bar{Y}}) + \ldots, \tag{3.27b}$$

and more interactive nonlinear influences come back into play. Substituting into (3.21) shows that the dominant balance now has

$$\bar{\bar{u}} = \bar{\bar{x}}', \tag{3.28a}$$

$$\bar{\bar{v}} = \bar{\bar{Y}}', \tag{3.28b}$$

$$\frac{\bar{\bar{u}}'}{(1-\bar{\bar{u}})} = \frac{2\bar{\bar{v}}}{\bar{\bar{Y}}} + \frac{3\bar{\bar{x}}^2(1-\bar{\bar{u}})}{(12-\bar{\bar{x}}^3)} - \frac{(1-\bar{\bar{u}})}{\bar{\bar{x}}}, \tag{3.28c}$$

$$\bar{\bar{v}}' = -\frac{6\bar{\bar{x}}\bar{\bar{Y}}(1-\bar{\bar{u}})^2}{12-\bar{\bar{x}}^3}. \tag{3.28d}$$

Again the influence of the deepened plunge is evident through comparison with (3.21-3.22). The matching with the earlier stage provides $(\bar{\bar{x}}, \bar{\bar{Y}}, \bar{\bar{u}}, \bar{\bar{v}}) \sim (\alpha_1, \tilde{\gamma}\bar{t}, 1, \tilde{\gamma})$, for $\bar{t} \to 0+$, as the initial conditions in effect. The present stage then takes the body into an underlying upward or outward phase which leads at a finite positive value of time $\bar{t}$ to $\bar{\bar{x}}$ becoming zero which in turn signifies the advent of lift-off. Figure 3.4(c) shows results for a suitable range of values of the constant α_1 and confirms that the appropriate solution is relatively simple at leading order, namely $(\alpha_1 + \bar{t}, \beta_0\bar{t}, 1, \beta_0)$ for all time $\bar{t}$, thus determining the

lift-off time $\bar{t}$ as $-1/\alpha_1$ to the first approximation. The correction term for $\bar{u}$ can be shown to be of order $1/|\bar{v}_0|$ and proportional to $1/\bar{t}^2$, in line with the second stage earlier on.

The tendencies suggested by this increased-speed analysis tie in well with the numerical results described in the previous section. The presence of the short time scale in (3.23) explains the relatively rapid response seen in the previous numerical results, in line with physical expectations that more downward speed should provoke a quicker and perhaps deeper plunge overall. The trend reversal countering the downward plunge is then really seen to begin during the second stage over a slightly longer time scale, prior to the full nonlinear interaction largely reasserting its presence in linearised analytical form during the third stage and forcing the eventual lift-off.

3.5 Decreased downward speed

Lessened downward entry speed corresponds to the parameter $\bar{v}_0$ being small and negative, in which case the whole process occurs within the single order-unity time scale. So now in view of the initial values in (3.22) as well as the dynamics in (3.21) we have the expressions

$$\bar{t} = O(1), \tag{3.29a}$$

$$(\bar{x}, \bar{Y}) = (|\bar{v}_0|^{1/2} x_L, |\bar{v}_0| Y_L) + \ldots (5.1a, b), \tag{3.29b}$$

applying and as a result the governing equations and constraints (3.21-3.22) simplify to the form

$$u_L = x_L', \tag{3.30a}$$

$$v_L = Y_L', \tag{3.30b}$$

$$0 = \frac{Y_L}{x_L^2} + \frac{2u_L}{x_L}, \tag{3.30c}$$

$$v_L' = \frac{x_L^2}{2} \tag{3.30d}$$

with the prime denoting differentiation with respect to $\bar{t}$, at leading order. The influences of horizontal acceleration effects due to the movement of the contact point in the balance (3.21) are secondary in this regime while the corresponding vertical acceleration effects in (3.21) remain primary ones. The values $(x_L, Y_L, u_L, v_L)(0) = (0, 0, -1, -1/2^{1/2})$ are the initial conditions.

The solution of the small nonlinear system (3.30) is expressible in terms of $Z = x_L^2$ which produces the third-order linear system

$$Z''' = -\frac{1}{2}Z \tag{3.31}$$

from (3.30). Hence with powers m_n denoting $\exp[(2n-1)\pi i/3]/2^{1/3}$ for $n = 1, 2, 3$ the solution is simply

$$Z = \sum_{n=1}^{3} a_n \exp(m_n \bar{t}) \tag{3.32}$$

where the complex constants a_n are determined by the initial conditions which require $Z(0) = Z'(0) = 0, Z''(0) = 1$. Thus the values

$$a_n = \frac{1}{3} m_n^{-2} \tag{3.33}$$

are obtained for the constants, whence $Z(\bar{t})$ can be found from (3.32), and the test $Z \geqslant 0$ then determines the complete wetting process up to the occurrence

of lift-off where x_L returns to zero. See Figure 3.5. The trends in (3.29-3.32) again agree qualitatively with those observed in the earlier numerical study as $\bar{v}_0$ is reduced in magnitude, and as a quantitative check the value of just over 4 for the scaled time $\bar{t}$ at lift-off ties in well with the values observed in Figure 3.3 as $|\bar{v}_0|$ decreases.

3.6 Further Comments

The recent works on collisions, rebounds and skimming described in the introduction cover a diversity of applications which are felt to be of much interest and challenge. These produce in particular spin-off suggestions on tackling anew multi-body problems as in [26, 28, 29] and are even linked through the dynamics of fluid-body interactions to predictions and observations on the movement of dust on the planet Mars [29]. They can also include viscous effects as in the theory of air cushioning in [27] which in turn leads on to air-pocket properties in [2] and most recently to [56] who show close and encouraging connections between theory and experimental measurements. (The air-water interaction mentioned earlier comprising interplay of viscous and inviscid effects is potentially relevant throughout the current investigations.) Experimental studies concerning the skimming and skipping of a thin body on a shallow stream of water with fixed velocity are conducted in [37], the results demonstrating interesting phenomena that are qualitatively consistent with our model predictions, in particular the "super-elastic" exit of a skimming body where its vertical velocity is greater on the way out than in. A further connection with experiments in the current broad area is shown by [39] who investigate theoretically the accretion of ice on a solid surface when a super-cooled droplet impacts upon the surface and compare with experimental measurements. The agreement in qualitative terms or in orders of magnitude is quite close and the work also tends to add weight to the view that theory here can provide a means to explore the parameter space over a substantial range of parameter values.

By the same token the use of nonlinear evolution here connects with the present issue's theme of 'stability, separation and close body interactions'. Comparison might suggest indeed that it would be beneficial to address viscous effects near a departure (separation) point of a fluid-fluid interface (for example between air and water) from a fixed solid surface, first of all in steady flow perhaps and later in unsteady flow. Building into the overall theory the important local influence of the viscous effects there would seem to represent another considerable step forward in understanding.

As well as broadly looking back and looking forward as above our prime concern in the study here is to follow through with the research described in Section 3.2 and in Chapter 2. We should add straight away that apart from the technological applications such as in aircraft safety and icing, food-particle sorting and sports applications there are also fun applications (ducks and drakes) and possible relevance to meteor impacts, to cleansing and to forensic examinations from different parts of the research. Again, the scope of the specific analysis in Section 3.3-3.5 may be seen more clearly by means of the original partial differential system in Section 3.2, in order to indicate the main physical features involved. Thus under the small-mass scalings described at the beginning of Section 3.3 but accompanied by

$$x = x_0 + E\check{x} \tag{3.34}$$

with $\check{x} < 0$ during the wetting the effective shape is altered to

$$H(x, \hat{t}) = \hat{Y}(\hat{t}) + (x_0 - x_m)\hat{\theta}(\hat{t}) + \check{x}\theta_0, \tag{3.35}$$

and the angular momentum balance becomes merely

$$I\frac{d^2\hat{\theta}}{d\hat{t}^2} = 0, \tag{3.36}$$

to leading order, which points to $\hat{\theta}$ being $\omega_0\hat{t}$ identically. Apart from that

original system (3.2-3.6) remains intact in scaled quantities provided the integral in (3.5) is taken over the wetted area of course. It then follows however that the pressure response in general is quadratic in the local coordinate instead of cubic as in (3.8) and this can be shown to produce the simplified interaction of Section 3.3 exactly. Further alterations within the above framework lead to the cases of comparatively large and small downward speeds considered in Sections 3.4,3.5. Exploiting this structure for fast collisions and rebounds takes us into future work. The study of fast responses in Sections 3.3-3.5 is concentrated effectively near the trailing edge of the thin impacting body. More generally or more usefully that can be regarded as having the centre of mass of the body positioned relatively far away from the contact area of wetted surface. This view might well be relevant in turn to the classical problem of describing analytically the skimming of a bluff smooth body over a liquid surface as opposed to a thin body skimming as in the present configuration.

Future studies should address the following issues and challenges. First, there is much interesting work to be done to relate the in-water phase (impact and rebound) quantitatively to the in-air phase (usually lasting longer) as far as skimming of a body over water is concerned. Some initial effort on the in-air part is in Chapter 2 with gravity included and incorporating the in-water phase as delineated in Sections 3.2-3.5, over several repeated impacts and rebounds. Clearly the initial and end conditions of the latter largely nonlinear phase associated with touchdown and lift-off respectively interact with those of the largely linear in-air motion. A sample result is shown in Figure 3.6; see also Chapter 2. Second, there is a considerable challenge inherent in rationally modelling many bodies rebounding as in a storm in reality, especially given that the real-world situation is in three dimensions. It may well be the case that a reasonable aim for an in-water description in this context of complexity is one which is more readily calculable; if so the approaches in Sections 3.4, 3.5 indicate a promising possibility there. The question of how much structure or physics must be captured for realistic predictions in any reduced system remains in the back-

ground throughout. Third, there is a need to check in detail on trends similar to those investigated in this paper but for relatively small moments of inertia or for small mass and moment of inertia together, as anticipated in Section 3.3. Fourth, the theory and reduced-system calculation can probably enlarge its scope also: to other shapes of body with a view to including more realism, starting with nonzero thickness coefficients A, B, C introduced in Section 3.2; to consecutive impacts by multiple bodies; to non-shallow water; to smooth bodies, about which similar work is being done in Chapter 5 (some smooth bodies can provoke splash jets at both the leading edge, i.e. the moving front contact point, and the trailing edge, i.e. the rear contact point, during the early stages of impact [73]); to flexible bodies; to three-dimensional interactions. Fifth, and partly to repeat, more useful understanding requires more efforts in handling three spatial dimensions, in handling viscous-inviscid separation of two fluids and in handling more widely air effects in the presence of water, with the objective to link to experiments and observations throughout.

Acknowledgement

We thank numerous colleagues and contacts for their help in this venture, especially Roger Gent, Richard Moser, David Hammond, Peter Hicks, Sasha Korobkin and Tatiana Khabakhpasheva.

3.7 Figures

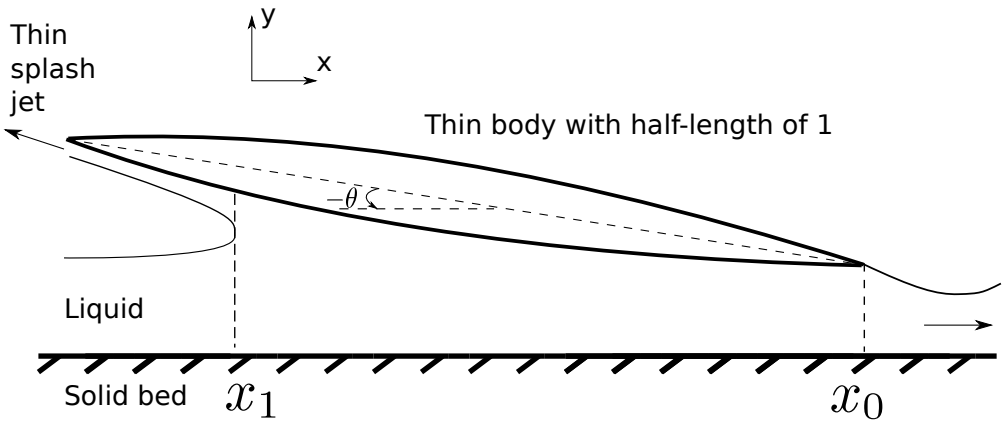

Figure 3.1: The configuration as a thin solid body of normalised half-length unity enters and may go on to bounce and skim over shallow liquid of depth much less than unity. Solid arrows show the direction of liquid motion relative to the solid body. The moving-contact or front position x_1 of the currently wetted under-surface varies with time t and is surrounded by a small Euler zone. Representative angles of inclination from the horizontal are supposed small.

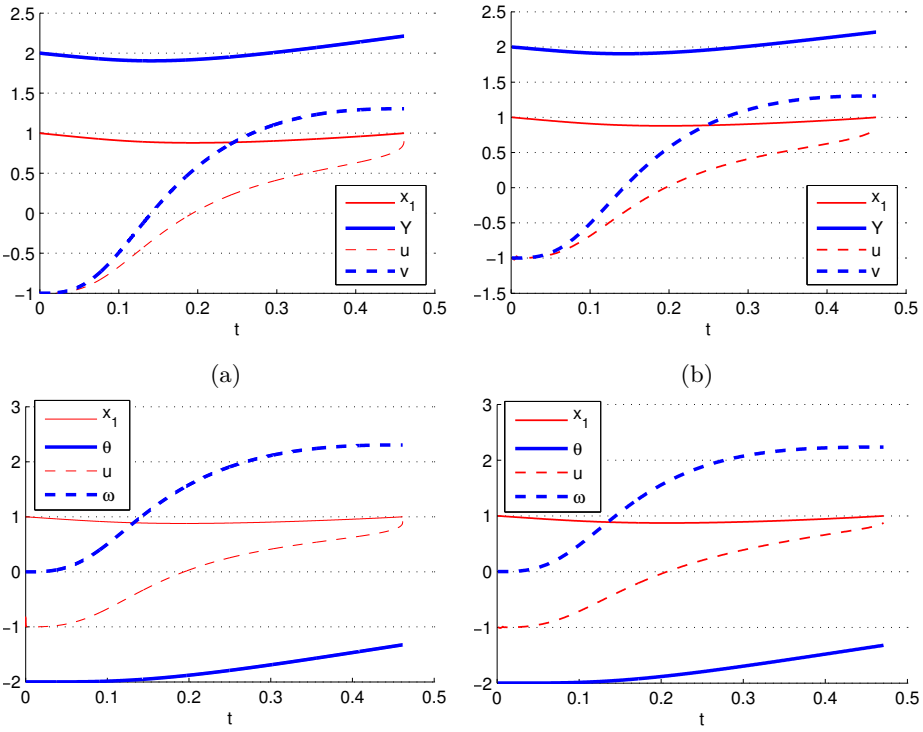

Figure 3.2: Solutions computed for the full fluid-body-interaction system of Section 3.2 and compared with results of the reduced systems of Section 3.3. (a, b) With reduced mass factor for initial conditions $1, 2, 0, 0$ of x_1, Y, u, v in turn: full in (a), reduced version in (b). (c, d) With reduced moment-of-inertia factor for initial conditions $1, -2, 0, 0$ of x_1, Y, u, ω in turn: full in (c), reduced version in (d). Here u, v denote the temporal derivatives of x_1, Y respectively.

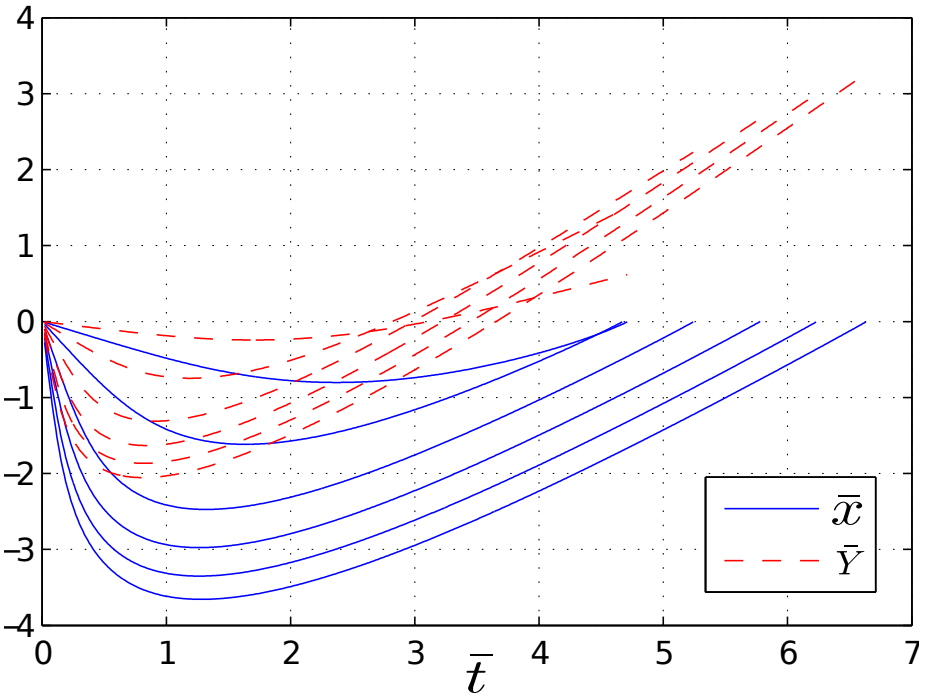

Figure 3.3: Numerical solutions for the scaled front position $\bar{x}$ (solid curves) and centre height $\bar{Y}$ (dashed curves) against scaled time $\bar{t}$ as the effective entry velocity component in the vertical direction is varied from -0.2 to -9.

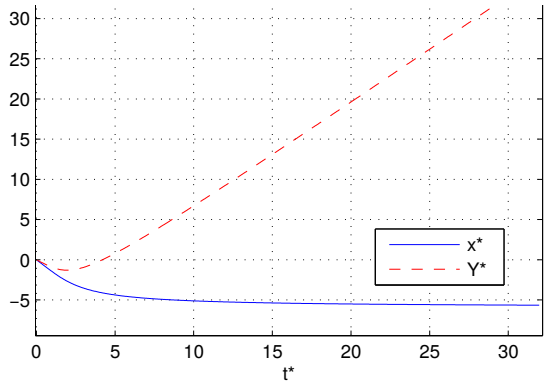

(a) 1st stage solution.

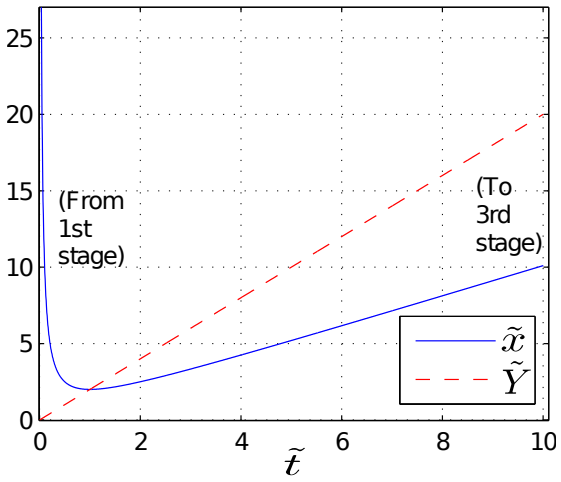

(b) 2nd stage solution.

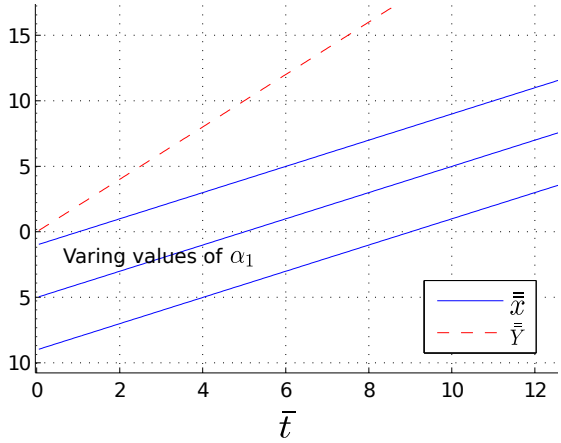

(c) 3rd stage solution.

Figure 3.4: For increased downward entry speed, the successive stages: (a) first stage (rapid dropping), showing in scaled terms the front x^* and height Y^* versus time t^*; (b) second stage (deep turnaround), front perturbation $\tilde{x}_1$ and height $\tilde{Y}$ versus time $\tilde{t}$; (c) third stage (gradual rise to lift-off), front $\bar{\bar{x}}$ and height $\bar{\bar{Y}}$ versus time $\bar{t}$ as depth factor α_1 is varied.

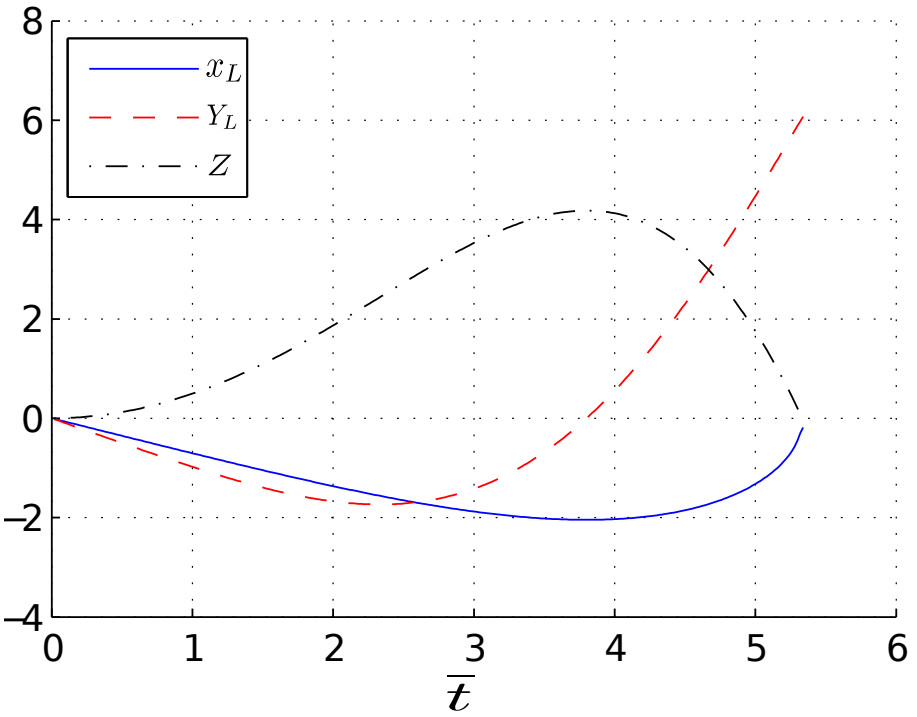

Figure 3.5: For decreased downward entry speed, the scaled front position x_L and centre height Y_L against scaled time $\bar{t}$. Also shown is the function Z which satisfies a linear equation and controls x_L, Y_L.

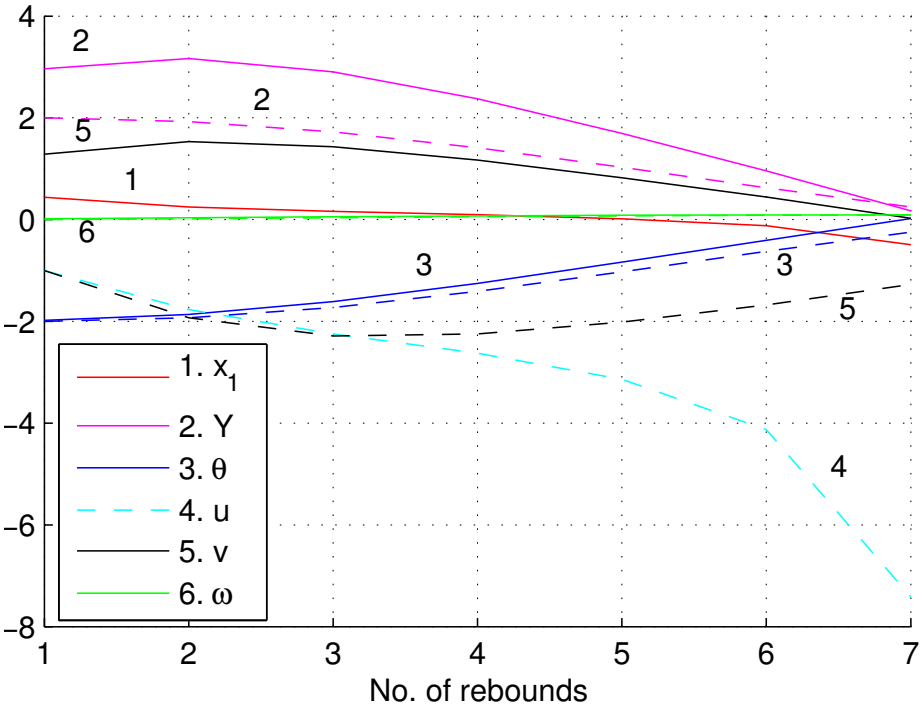

Figure 3.6: A sample case of multiple entry, rebounding and skimming: the total number of rebounds is 7 here. The plots give the consecutive horizontal positions x_1 at each entry, along with (at both entry and rebound) the consecutive vertical heights of the centre of mass, entry angles θ, body-configuration velocities u, v, and angular velocities ω versus the rebound number.

Chapter 4

Free surface separation from a smooth trailing edge

Considering an ellipsoid-like object skimming on a shallow layer of water, in this chapter we concern ourselves with the flow close to this body's trailing end where the flow separation occurs. Assuming the flow separation occurs smoothly, we shall investigate in particular how the flow from underneath the main section of the body may influence the flow behaviour in the separation region and its downstream wake.

One of the difficulties with the skimming problem of a blunt body is that its trailing separation edge position is unknown and needs to be obtained as part of the overall flow solutions; the modelling of such skimming problem shall be presented in Chapter 5. For the purpose of this chapter however we shall assume this trailing separation position is given, and instead focus our analysis on the flow in a small region enclosing this separation edge. We shall begin with a brief review of previous works on solid-fluid impacts, and derive a model for the flow near a blunt skimming body's trailing edge.

Some of the major modelling assumptions here are similar to those made in Chapter 2 for the skimming problem of a flat body. In particular the skimming

body's horizontal velocity is much greater than its vertical velocity; the water is assumed to be shallow, incompressible and irrotational; the effects of viscosity and gravity are negligible; the dead-rise angle, defined as the angle made between the body's contact surface and the undisturbed water free surface, is small. As before, by shallow water we are referring to the horizontal dimensions of the contact region being much larger than the depth of water penetration. Given the small penetration depth, the small dead-rise angle assumption for our skimming body is satisfied if $|\nabla f| \ll 1$, where $f(x, y)$ is the body's surface function.

4.1 Introduction

The phenomenon of smooth blunt bodies impacting on free liquid surfaces has been subject to continuing research since the pioneering work of Von Kármán [70] and Wagner [34]. Such a phenomenon is closely related to a body in skimming motion and deserves a closer discussion. The majority of researches so far are focused on the early stages of impact, during which the velocity can be approximated as being constant; the dead-rise angle between the body and free surface is small, and therefore at the leading order the body can be approximated by a flat plate. Wagner observed during the early stages of a blunt body impact, the free surface elevation is of the same order as the body's penetration depth, and any spray jets are thin and have negligible contribution to the overall flow. The flows under such assumptions, and in particular a set of flow boundary conditions derived under such assumptions, are of such fundamental importance they have been collectively referred to as the Wagner flow, which we shall now briefly discuss.

4.1.1 Introduction to Wagner flow

Consider a blunt body such as an ellipsoid falling vertically onto a layer of water with speed $U(t)$. The water is initially at rest and occupies the lower half-space, denoted by $z < 0$; the body initially touches the water's free surface, $z = 0$,

at a single point. We shall set this initial contact point to be the origin of our Cartesian system $Oxyz$.

As time progresses the body begins to penetrate below the water free surface. Let $h(t)$ denote the depth of the penetration at a given time. Then we have $dh/dt = U(t)$, and the falling body's position is given as $z = f(x, y) - h(t)$, where $f(x, y)$ is the body's surface function. This body's blunt profile implies $|\nabla f| \ll 1$, i.e. the body surface gradient is small everywhere, and thus the dead-rise angle between the body and undisturbed free surface is small as discussed previously. The flow surrounding the body can be divided into three connected regions: a contact region $\Omega(t)$, where the liquid is in direct contact with the body surface; the contact region is surrounded by an elevated jet-root region $\mathcal{J}(t)$, from which the spray jets are emitted; an outer free surface region $\mathcal{F}(t)$, which connects the elevated jet-root region with the far-field stream at rest.

By Wagner's theory when a dead-rise angle is sufficiently small, the spray jets are extremely thin and the size of the jet-root region becomes small, i.e. $\mathcal{J}(t) \to 0$. The flow surrounding the impact body can thus be approximated as being composed of two regions only: $\Omega(t)$ and $\mathcal{F}(t)$, with a contact curve $\Gamma(t)$ which rests somewhere on the body separating the two. Thus if we let $z = \eta(x, y, t)$ be the fluid's free surface, at the leading order the elevation of the free surface matches the penetrating body's vertical position on the contact line $\Gamma(t)$, i.e.

$$\eta(x, y, t) = f(x, y) - h(t), \qquad ((x, y) \in \Gamma(t)). \tag{4.1}$$

This condition is referred to as the Wagner condition. It should be noted that under general circumstances such a condition does not hold, due to the presence of spray jets, and the free surface is not necessarily single-valued everywhere.

Assuming the fluid flow is incompressible and irrotational, we denote the velocity potential of the flow by $\phi(x, y, z, t)$. This potential should be harmonic below the surface and satisfy the mixed boundary conditions such that: a) inside

the contact region $\Omega(t)$ it satisfies $\partial\phi/\partial z = -U(t)$; b) on the free surface $\digamma(t)$ the potential is zero and satisfies the kinematic condition $\partial\eta/\partial t = \partial\phi/\partial z$, i.e.:

$$\nabla^2\phi = 0 \qquad (z < 0), \tag{4.2a}$$

$$\frac{\partial\phi}{\partial z} = -U(t) \qquad (\text{on } \digamma(t)), \tag{4.2b}$$

$$\phi = 0 \qquad (\text{on } \Omega(t)), \tag{4.2c}$$

$$\phi \to 0 \qquad (x^2 + y^2 + z^2 \to \infty). \tag{4.2d}$$

As a consequence of assuming the free surface elevation and body penetration depths are small and of the same order, the free-surface kinematic condition can be linearised onto the undisturbed free surface $z = 0$ at the leading order so that:

$$\eta(x, y, t) = \int_0^t \frac{\partial\phi}{\partial z}(x, y, 0, \tau)d\tau. \tag{4.3}$$

This taken together with (4.1) yields the Wagner equation:

$$f(x, y) = h(t) + \int_0^t \frac{\partial\phi}{\partial z}(x, y, 0, \tau)d\tau. \tag{4.4}$$

Equations (4.2) and (4.4) are known as the Wagner problem and can be solved by either prescribing the body shape function $f(x, y)$ and velocity $U(t)$ to solve for the velocity potential ϕ and contact region $\Omega(t)$, or prescribing the contact region $\Omega(t)$ and $U(t)$ to solve for the velocity potential ϕ and body shape function $f(x, y)$. The first approach where the body shape function $f(x, y)$ is given is known as the direct problem, and the second approach where $f(x, y)$ needs to be inferred from the relation (4.1) is known as the inverse problem.

[77] studied the three-dimensional inverse Wagner problem of ellipsoids, for which the contact line $\Gamma(t)$ takes on an elliptic shape; it is demonstrated that analytical solutions can be obtained when the two semi-axes of this elliptic region grow either with the square root of time or linearly with time. In a follow-up

study, [5] exploited the known leading order analytical solutions of Wagner flows for three-dimensional axisymmetric objects by applying small perturbations to their shapes. Subsequently the flow solution for an impacting object with an approximately axisymmetric shape can be obtained at the leading order. The details of the solutions and findings are outside our scope and shall not be presented: we refer interested readers to the aforementioned papers.

4.1.2 Introduction to free surface separation from a skimming body

Concerning the problem of free surface separation at the trailing edge of a blunt body in skimming motion then, in contrast with the impact problem discussed in the previous section, the time scale here is not necessarily small and the velocity is predominately horizontal. Consider a cross-sectional 2D view of a smooth ellipsoid-like object skimming on a thin layer of water. We assume its horizontal velocity is large in comparison to its vertical velocity, and the contact line between the body and free surface has a large radius of curvature so that the dead-rise angle is small.

We impose a Cartesian coordinate system such that the x-axis coincides with the bottom of the water layer, and the y-axis goes through the object's centre of mass, see Fig. 4.1. The contact line between the body and the fluid free surface at any time is given by $y = f(x,t)$, with $t = 0$ denoting the time of initial touchdown.

For a case of a flat skimming body investigated in Chapter 2, the position of the trailing edge is known while its leading edge position needs to be determined as part of the flow solution. For a blunt skimming body however, both the leading and trailing edge positions are unknown and need to be determined. We write the unknown trailing edge position as $x_T(t)$, where the water departs smoothly from the body, and expect the surface pressure beyond this trailing point to be atmospheric, i.e. $p = p_0 = 0$ for $x \geq x_T(t)$. For the purpose of our analysis in the present chapter we shall assume x_T is given, and focus only on a

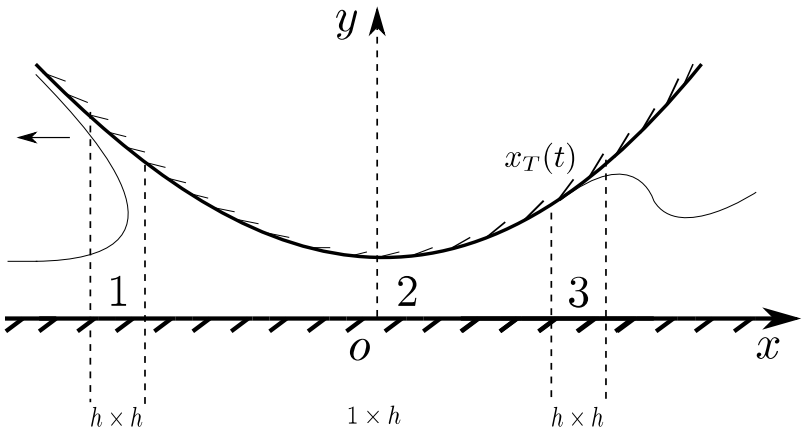

Figure 4.1: The figure depicts a skimming object with smooth blunt shape skipping on a layer of shallow water in the negative direction of the x axis. The flow underneath the body can be divided into three regions: region 1, with dimensions of $O(h) \times O(h)$, is the leading edge jet-root region; region 2 has dimensions of $O(1) \times O(h)$ and is the main flow region underneath the body; finally region 3, with dimensions of $O(h) \times O(h)$, is the trailing edge free surface separation. The separation point is denoted by $x_T(t)$. As with the case of a flat body skimming on water in Chapter 2, we neglect the jet-spray thrown forward by the body.

small region enclosing this separation point. Say the depth of the shallow water is h with $h \ll 1$; we set this region's horizontal scale to be comparable to the water depth so that its size is $\sim O(h) \times O(h)$. This region is depicted as region 3 in Fig. 4.1. In contrast with the case of shallow water skimming where the horizontal flow dominates over its vertical counterpart, in this region both flow components are comparable.

For the remainder of this chapter we shall analyse the influence and interactions of the upstream main body flow with that of the downstream wake in this trailing separation region. We shall pursue both analytical and numerical solutions for our model, and the findings of each are used as a means of cross-validation.

4.2 Model development

In order to perform flow analysis in the region of the flow separation, it is more convenient for us to introduce a Cartesian coordinate system that is based on the trailing separation point as opposed to the object's centre of mass. To do so we zoom in the region of separation of size $O(h) \times O(h)$ and introduce a new coordinate system $O\bar{x}\bar{y}$, where $\bar{x} \equiv (x - x_T(\bar{t}))/h$, $\bar{y} \equiv y/h$ and $\bar{t} \equiv t$; here h is the representitive shallow water depth and as such $h \ll 1$. Under this new coordinate system $\bar{x}$-axis rests at the bottom of the water layer pointing in the direction of downstream, and the trailing separation point resides on the $\bar{y}$-axis.

Neglecting the viscous and gravitation forces by arguments similar to those for a flat body in Chapter 2, we have the following governing equations for the fluid under the skimming body:

$$h\frac{\partial \bar{u}}{\partial \bar{t}} + (\bar{u} - \frac{\partial x_T}{\partial \bar{t}})\frac{\partial \bar{u}}{\partial \bar{x}} + \bar{v}\frac{\partial \bar{u}}{\partial \bar{y}} = -\frac{\partial \bar{p}}{\partial \bar{x}}, \tag{4.5a}$$

$$h\frac{\partial \bar{v}}{\partial \bar{t}} + (\bar{u} - \frac{\partial x_T}{\partial \bar{t}})\frac{\partial \bar{v}}{\partial \bar{x}} + \bar{v}\frac{\partial \bar{v}}{\partial \bar{y}} = -\frac{\partial \bar{p}}{\partial \bar{y}}, \tag{4.5b}$$

with $\bar{x}$, $\bar{y}$ and $\bar{t}$ being order unity; the unknowns are $\bar{u}(\bar{x}, \bar{y}, \bar{t})$, $\bar{v}(\bar{x}, \bar{y}, \bar{t})$, $\bar{p}(\bar{x}, \bar{y}, \bar{t})$.

We let $\bar{y} = \bar{f}(\bar{x}, \bar{t})$ be the skimming object's known surface in contact with water; this contact surface is ahead of the separation point and is therefore defined for $\bar{x} < 0$. Let $\bar{y} = \bar{\eta}(\bar{x}, \bar{t})$ be the unknown water free surface after the separation point, i.e. it is defined for $\bar{x} > 0$. For a small dead-rise angle we can approximate the body-fluid contact surface $\bar{f}$ as a flat plate at the leading order; further assuming the water separates smoothly from the body such that the flow's surface gradient at the departure point is small, we can therefore asymptotically approximate the flow surface as such:

$$\bar{f}(\bar{x}, \bar{t}) = \bar{f}_0(\bar{t}) + h\bar{f}_1(\bar{x}, \bar{t}) + O(h^2), \qquad (\bar{x} < 0); \tag{4.6a}$$

$$\bar{\eta}(\bar{x}, \bar{t}) = \bar{f}_0(\bar{t}) + h\bar{\eta}_1(\bar{x}, \bar{t}) + O(h^2), \qquad (\bar{x} > 0). \tag{4.6b}$$

Note the flow surface functions' share the same leading order approximation $\bar{f}_0$,

which is a function of time only.

The nature of the flow is dominantly horizontal we therefore asymptotically expand the system variables as follows:

$$\bar{u}(\bar{x},\bar{y},\bar{t}) = \bar{u}_0(\bar{t}) + h\bar{u}_1(\bar{x},\bar{y},\bar{t}) + O(h^2), \tag{4.7a}$$

$$\bar{v}(\bar{x},\bar{y},\bar{t}) = h\bar{v}_1(\bar{x},\bar{y},\bar{t}) + O(h^2), \tag{4.7b}$$

$$\bar{p}(\bar{x},\bar{y},\bar{t}) = h\bar{p}_1(\bar{x},\bar{y},\bar{t}) + O(h^2), \tag{4.7c}$$

$$\bar{f}(\bar{x},\bar{t}) = \bar{f}_0(\bar{t}) + h\bar{f}_1(\bar{x},\bar{t}) + O(h^2), \qquad (\bar{x} \leq 0), \tag{4.7d}$$

$$\bar{\eta}(\bar{x},\bar{t}) = \bar{f}_0(\bar{t}) + h\bar{\eta}_1(\bar{x},\bar{t}) + O(h^2), \qquad (\bar{x} \geq 0), \tag{4.7e}$$

where $\bar{u}_0$ is the horizontal incident speed of the fluid under the skimming object. At this point we shall drop the bar signs on the variables for the sake of reading simplicity. Substituting these expansions into the momentum equations (4.5) we obtain the following at the leading order:

$$\frac{\partial u_0}{\partial t} + (u_0 - \frac{\partial x_T}{\partial t})\frac{\partial u_1}{\partial x} = -\frac{\partial p_1}{\partial x}, \tag{4.8a}$$

$$(u_0 - \frac{\partial x_T}{\partial t})\frac{\partial v_1}{\partial x} = -\frac{\partial p_1}{\partial y}. \tag{4.8b}$$

We shall now impose boundary conditions for this flow. At the far upstream region where $x \to -\infty$, the flow ought to match with the main flow from underneath the object. The horizontal flow at the second order can be assumed to take the following form: $u_1 = \lambda_1(t)x$, by incompressibility argument we readily obtain $v_1 = -\lambda_1(t)y$. The momentum equation (4.8) therefore yields:

$$\frac{\partial u_0}{\partial t} + (u_0 - \frac{\partial x_T}{\partial t})\lambda_1 = -\frac{\partial p_1}{\partial x}, \tag{4.9a}$$

$$0 = -\frac{\partial p_1}{\partial y}. \tag{4.9b}$$

Noticing that the L.H.S. of the equation depends only on time, the leading order

pressure term p_1 takes on the following form:

$$p_1(x,t) = q_1(t)x, \qquad (x \to -\infty). \tag{4.10}$$

Therefore if we know the flow velocity from upstream then the pressure gradient q_1 can be inferred, and vice versa. Substituting this pressure relation into the horizontal momentum equation (4.9a) gives:

$$\frac{\partial u_0}{\partial t} + (u_0 - \frac{\partial x_T}{\partial t})\lambda_1 = -q_1(t), \qquad (x \to -\infty). \tag{4.11}$$

Turning our attention to the downstream where $x > 0$, we let $u_1 = k_1(t)x$ to match the wake flow far downstream as $x \to +\infty$. Since the pressure in this downstream region is uniformly atmospheric, the flow momentum equation (4.8) yields the following leading order relation:

$$\frac{\partial u_0}{\partial t} + (u_0 - \frac{\partial x_T}{\partial t})k_1 = 0, \qquad (x \to +\infty).$$

Rearranging gives the following solution to the velocity gradient for far downstream flow:

$$k_1 = -\frac{\dot{u}_0}{u_0 - \dot{x}_T}, \qquad (x \to +\infty), \tag{4.12}$$

where the dot notation denotes differentiation with respect to time. Hence once the horizontal velocities of the separation point and upstream flow are known, the far downstream flow's velocity can be estimated via (4.12).

At the bottom of the water layer the impermeability of the rigid wall implies $v(x,0,t) = 0$ throughout. The surface of the water layer can be divided into two segments: one for $x < 0$ where $y = f(x,t)$, which is the contact surface between the skimming object and water surface; and the other for $x > 0$ where we have the surface of the wake. In each case the leading-order kinematic boundary

condition implies:

$$-\lambda_1 f_0 = \frac{\partial f_0}{\partial t} + (u_0 - \frac{\partial x_T}{\partial t})\frac{\partial f_1}{\partial x}, \qquad (x < 0), \tag{4.13a}$$

$$-k_1 f_0 = \frac{\partial f_0}{\partial t} + (u_0 - \frac{\partial x_T}{\partial t})\frac{\partial \eta_1}{\partial x}, \qquad (x > 0). \tag{4.13b}$$

Since the L.H.S. of equations (4.13) depends on time t only, $\frac{\partial f_1}{\partial x}$ and $\frac{\partial \eta_1}{\partial x}$ are also functions of time only. We can therefore represent the surface functions before and after the departure point as follows:

$$f = f_0(t) + h\mu_1(t)x + O(h^2), \qquad (x < 0), \tag{4.14a}$$

$$\eta = f_0(t) + h\tau_1(t)x + O(h^2), \qquad (x > 0). \tag{4.14b}$$

Substituting this into the leading order kinematic boundary conditions (4.13) and rearranging gives the following relations for μ_1 and τ_1:

$$\mu_1 = -\frac{\lambda_1 f_0 + \dot{f}_0}{u_0 - \dot{x}_T}, \tag{4.15a}$$

$$\tau_1 = \frac{f_0 \dot{u}_0}{(u_0 - \dot{x}_T)^2} - \frac{\dot{f}_0}{u_0 - \dot{x}_T}. \tag{4.15b}$$

As usual if the horizontal velocities of the separation point and upstream flow are known, we can approximate the flow surface profiles in this separation region via (4.15). Hence once the trailing separation position $x_T(t)$ is known, the surface flow profile in the departure region can be obtained.

The difference between the gradients of the flow entering and leaving this departure region is:

$$\tau_1 - \mu_1 = \frac{\dot{u}_0 + \lambda_1(u_0 - \dot{x}_T)}{(u_0 - \dot{x}_T)^2} f_0,$$

which by the fluid's horizontal momentum equation (4.11) is:

$$\tau_1 - \mu_1 = -\frac{f_0 q_1}{(u_0 - \dot{x}_T)^2}.$$

That is to say if the downstream surface gradient is less than the upstream surface gradient $\tau_1 < \mu_1$, then there is an adverse pressure gradient $q_1 > 0$ in the flow under the skimming body up to the separation point, i.e. the pressure rises when the flow is about to separate from the impacting body and it reaches the maximum of zero after separation (see Fig. 4.2). In Chapter 5 we shall investigate more on the phenomenon of adverse pressure gradient close to the trailing separation edge.

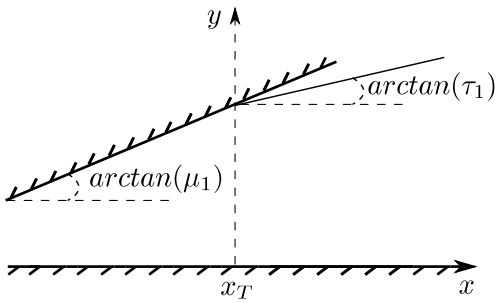

Figure 4.2: A figure illustrates the gradient differences between the incoming flow and the outgoing flow.

We now formulate a local flow model in this small separation region enclosing the departure point x_T. Given that the flow is incompressible we introduce the stream function $\psi(x, y)$ such that:

$$u_1 = \frac{\partial \psi}{\partial y}, \tag{4.16a}$$

$$v_1 = -\frac{\partial \psi}{\partial x}, \tag{4.16b}$$

and without loss of generality ψ is zero at the flow bed where $y = 0$.

Substituting the stream function into the fluid momentum equations (4.8) and simplifying yields:

$$\frac{\partial^2 \psi}{\partial x^2} + \frac{\partial^2 \psi}{\partial y^2} = C(t).$$

As the flow is irrotational throughout and there is no vorticity coming from

upstream, then $C(t) = 0$ and hence we expect the stream function ψ to satisfy the Laplace's equation:

$$\frac{\partial^2 \psi}{\partial x^2} + \frac{\partial^2 \psi}{\partial y^2} = 0, \tag{4.17}$$

subject to the following kinematic and far-field boundary conditions:

$$\psi = 0, \qquad (y = 0), \tag{4.18a}$$

$$\psi = \lambda_1 xy, \qquad (x \sim -\infty), \tag{4.18b}$$

$$\psi = \lambda_1 f_0 x, \qquad (x < 0, y = f_0), \tag{4.18c}$$

$$\frac{\partial \psi}{\partial y} = k_1 x, \qquad (x > 0, y = f_0), \tag{4.18d}$$

$$\psi = \tau_1 xy, \qquad (x \sim +\infty). \tag{4.18e}$$

See Fig. 4.3 for illustration of these boundary conditions. In the following

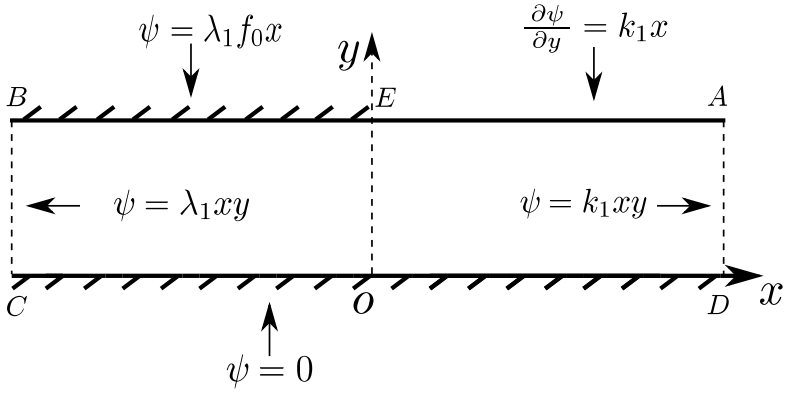

Figure 4.3: The mixed boundary conditions for the stream function ψ in the $O(h) \times O(h)$ departure region, with $\psi = \lambda_1 xy$ to match the incoming stream function profile and $\psi = k_1 xy$ to match the departing stream function profile in the wake.

section we present one method of solution to this flow model.

4.3 Method of solution

We begin by further simplifying the boundary conditions by performing the following substitutions:

$$\tilde{\psi} = \frac{\partial \psi}{\partial x} - k_1 y. \tag{4.19}$$

The benefits of this transform will become clear when we perform conformal mapping at a later stage. The boundary conditions therefore can be rewritten as:

$$\tilde{\psi} = 0, \qquad (y = 0), \tag{4.20a}$$

$$\tilde{\psi} = (\lambda_1 - k_1) y, \qquad (x \sim -\infty), \tag{4.20b}$$

$$\tilde{\psi} = (\lambda_1 - k_1) f_0, \qquad (x < 0, y = f_0), \tag{4.20c}$$

$$\frac{\partial \tilde{\psi}}{\partial y} = 0, \qquad (x > 0, y = f_0), \tag{4.20d}$$

$$\tilde{\psi} = 0, \qquad (x \sim \infty). \tag{4.20e}$$

See Fig. 4.4 for an illustration.

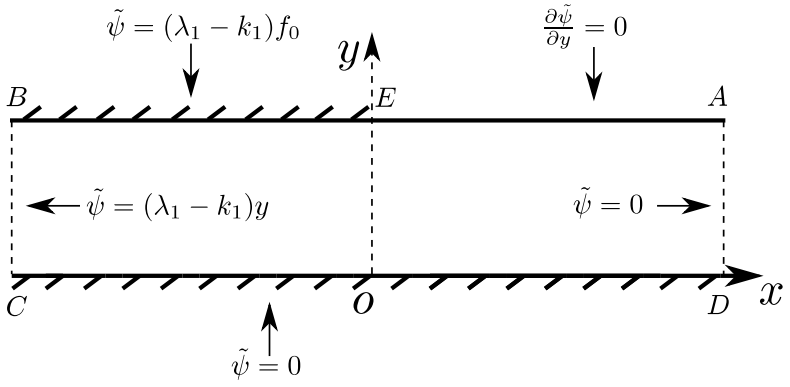

Figure 4.4: Boundary conditions for the stream function $\tilde{\psi}$ in the channel flow in z-plane.

Via the Schwarz-Christoffel transform we can map the effective channel in

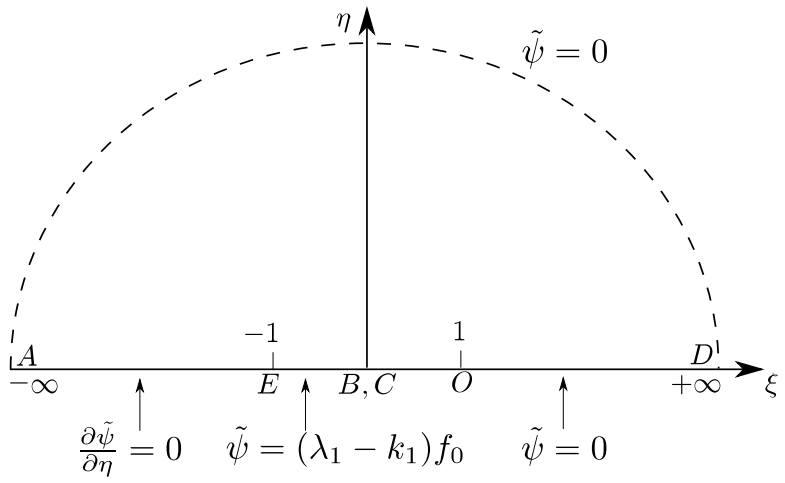

Figure 4.5: Boundary conditions for the stream function $\tilde{\psi}$ in the ζ-plane.

the z-plane to an upper half-plane in the ζ-plane as follows:

$$\zeta = e^{\frac{\pi}{f_0} z}, \tag{4.21}$$

see Fig. 4.5 for illustration.

Introducing a complex potential $\tilde{\phi}$ which is the complex conjugate of $\tilde{\psi}$, and write the following analytic function $F(\zeta) = P(\zeta) + iQ(\zeta) = (\zeta - \zeta_E)^{\frac{1}{2}}(\tilde{\phi}(\zeta) + i\tilde{\psi}(\zeta))$ in the upper half ζ-plane ($\zeta_E = (-1, 0)$) with a branch cut for (ζ_E, ∞) on the real axis, then along the real axis we have:

$$F(\xi) = P(\xi) + iQ(\xi) = (\xi+1)^{\frac{1}{2}}(\tilde{\phi}(\xi) + i\tilde{\psi}(\xi)) = \begin{cases} (\xi+1)^{\frac{1}{2}}(\tilde{\phi}(\xi) + i\tilde{\psi}(\xi)), & (\xi > -1) \\ (-\xi-1)^{\frac{1}{2}}(-\tilde{\psi}(\xi) + i\tilde{\phi}(\xi)), & (\xi < -1) \end{cases} \tag{4.22}$$

that is,

$$(\xi < -1) : \begin{cases} P(\xi) = -(-1-\xi)^{\frac{1}{2}}\tilde{\psi}(\xi), \\ Q(\xi) = (-1-\xi)^{\frac{1}{2}}\tilde{\phi}(\xi), \end{cases} \qquad (\xi > -1) : \begin{cases} P(\xi) = (\xi+1)^{\frac{1}{2}}\tilde{\phi}(\xi), \\ Q(\xi) = (\xi+1)^{\frac{1}{2}}\tilde{\psi}(\xi), \end{cases}$$

(4.23)

as the definitions of the complex conjugate pair P and Q.

As the harmonic conjugate pair $(\tilde{\phi}, \tilde{\psi})$ is analytic in the upper half ζ-plane including the ξ-axis, on the segment $(-\infty, -1)$ of the ξ-axis by virtue of Cauchy-Riemann equations:

$$\tilde{\phi}(\xi) = C, \quad (\xi < -1), \tag{4.24}$$

for some constant C.

Apply the Cauchy-Hilbert relation $P(\xi) = -\frac{1}{\pi}\int \frac{Q(s)}{\xi - s} ds$, on the ξ-axis we have the following relation for $\xi < -1$:

$$-(-1-\xi)^{\frac{1}{2}}\tilde{\psi}(\xi) = -\frac{1}{\pi}\left(\int_{-\infty}^{-1} \frac{(-1-s)^{\frac{1}{2}}\tilde{\phi}(s)}{\xi - s} ds + \int_{-1}^{0} \frac{(1+s)^{\frac{1}{2}}\tilde{\psi}(s)}{\xi - s} ds\right). \tag{4.25}$$

This is tantamount to the results for a Wiener-Hopf approach by the way. Re-arranging and applying the boundary conditions gives:

$$\tilde{\psi}(\xi) = \frac{(-1-\xi)^{-\frac{1}{2}}}{\pi}\left[C\int_{-\infty}^{-1} \frac{(-1-s)^{\frac{1}{2}}}{\xi - s} ds + f_0(\lambda_1 - k_1)\int_{-1}^{0} \frac{(1+s)^{\frac{1}{2}}}{\xi - s} ds\right], \quad (\xi < -1).$$

The first Cauchy integral term on the right does not converge as $\xi \to -\infty$ and therefore the integration constant C must be zero, while the second integral term can be expressed in the following closed form:

$$\tilde{\psi}(\xi) = \frac{2(\lambda_1 - k_1)}{\gamma}\left[\arctan\left(\frac{1}{\sqrt{-\xi - 1}}\right) - \frac{1}{\sqrt{-\xi - 1}}\right], \ (\xi < -1), \tag{4.26}$$

where γ is defined as

$$\gamma = \frac{\pi}{f_0}. \tag{4.27}$$

We now transform this relation back to the real space. From the transform

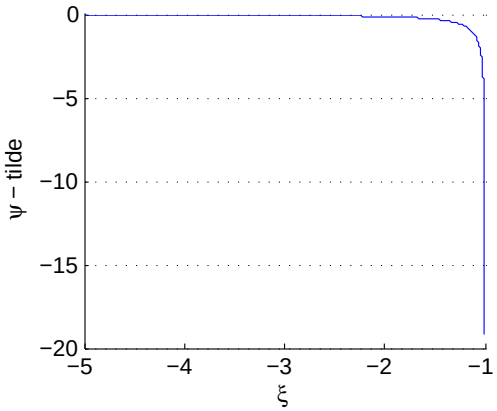

Figure 4.6: A plot shows the evolution of $\tilde{\psi}(\xi)$ as ξ goes away from the singularity point $\xi_E = -1$, here $\frac{\lambda_1 - k_1}{\gamma}$ is set to 1.

mapping (4.21) we have the following relations between (ξ, η) and (x, y):

$$\begin{cases} \xi = e^{\gamma x}\cos(\gamma y), \\ \eta = e^{\gamma x}\sin(\gamma y), \\ x = \frac{1}{\gamma}\log|\xi|, \\ y = \frac{1}{\gamma}\arctan(\frac{\eta}{\xi}). \end{cases} \tag{4.28}$$

Here $\tilde{\psi}(\xi)$ has an inverse square-root singularity at $(-1, 0)$, see Fig. 4.6 for a numerical evaluation of $\tilde{\psi}$ close to $\xi = -1$.

This inverse square-root singularity behaviour makes $\tilde{\psi}$ discontinuous across the point $\xi = -1$ across the flow's surface. This singularity can be removed by adding a real constant term $\frac{2(\lambda_1 - k_1)}{\gamma}$ to $\mathit{\Gamma}(\xi)$ in (4.22), i.e.

$$\mathit{\Gamma}(\xi) = P(\xi) + \frac{2(\lambda_1 - k_1)}{\gamma} + iQ, \tag{4.29}$$

then $\tilde{\psi}(\xi)$ vanishes as $\xi \to -\infty$ and joins onto the boundary condition at $(-1, 0)$ smoothly. Transforming $\tilde{\psi}$ without the inverse square-root term into the real z-plane gives the following:

$$\tilde{\psi}(x) = \frac{2(\lambda_1 - k_1)}{\gamma}\arctan\left(\sqrt{\frac{1}{e^{\gamma x} - 1}}\right), \qquad (x > 0). \tag{4.30}$$

Hence ψ at the surface of the wake can be written as:

$$\psi(x) = k_1 f_0 x + \frac{2(\lambda_1 - k_1)}{\gamma} \int_x^\infty \arctan\left(\sqrt{\frac{1}{e^{\gamma s} - 1}}\right) ds. \tag{4.31}$$

Once k_1 and λ_1 are prescribed, which depends on horizontal velocities of the separation point and upstream flow, then the fluid surface flow in its separation region can be fully determined. Alternatively via viscous boundary layer theory once a separation ratio say, $C_k = \frac{2(\lambda_1 - k_1)}{\gamma} - \gamma^{\frac{1}{2}}$ is prescribed, the surface flow solution can also be fully determined, we shall not pursue this approach at this stage however.

4.4 Numerical solution of the stream function in the thin flow channel

To verify our analytical solution derived from the previous section, a numerical analysis to the flow model (4.17 - 4.18) are also carried out, which we now briefly discuss.

We begin by discretizing the thin channel into the following grid:

$$\begin{aligned} &\Delta x = 2a/N_x, \qquad \Delta y = h/N_y, \\ &x_i = -a + i\Delta x, \quad (i = 0, 1, ...N_x), \\ &y_j = j\Delta y. \qquad\quad (j = 0, 1, ...N_y). \end{aligned} \tag{4.32}$$

For all interior points ($1 \leq i \leq N_x - 1, 1 \leq j \leq N_y - 1$) the Laplace's equation leads to

$$\frac{\psi_{i+1,j} - 2\psi_{i,j} + \psi_{i-1,j}}{\Delta x^2} + \frac{\psi_{i,j+1} - 2\psi_{i,j} + \psi_{i,j-1}}{\Delta y^2} = 0, \tag{4.33}$$

or equivalently:

$$\psi_{i,j} = \frac{\Delta x^2(\psi_{i,j+1} + \psi_{i,j-1}) + \Delta y^2(\psi_{i+1,j} + \psi_{i-1,j})}{2(\Delta x^2 + \Delta y^2)}, \tag{4.34}$$

subject to the boundary conditions as shown in Figure 4.3.

The Neumann boundary condition (4.18d) for the surface flow after the trailing edge $\frac{\partial \psi}{\partial y} = k_1 x$ can be converted numerically to a Dirichlet-type condition in two steps. First we approximate the derivative condition by:

$$\frac{\psi_{i,N+1} - \psi_{i,N-1}}{2\Delta y} = k_1 x_i, \tag{4.35}$$

where $\psi_{i,N+1}$ are additional points just outside the grid, and clearly (4.35) can be written as:

$$\psi_{i,N+1} = \psi_{i,N-1} + 2k_1 \Delta y x_i. \tag{4.36}$$

Therefore the numerical formulation on the boundary where the original Neumann condition applies becomes the following:

$$\frac{\psi_{i+1,N} - 2\psi_{i,N} + \psi_{i-1,N}}{\Delta x^2} + \frac{2\psi_{i,N-1} + 2k_1 \Delta y x_i - 2\psi_{i,N}}{\Delta y^2} = 0 \tag{4.37}$$

or equivalently in the more Dirichlet-like form:

$$\psi_{i,N} = \frac{2\Delta x^2(\psi_{i,N-1} + 2k_1 \Delta y x_i) + \Delta y^2(\psi_{i+1,N} + \psi_{i-1,N})}{2(\Delta x^2 + \Delta y^2)}. \tag{4.38}$$

Equations (4.34) and (4.38) act to determine the solution for ψ on the entire mesh. Successive iterations of the finite difference scheme lead ψ to converge to the solution. Fig. 4.7 demonstrates the numerical solution of this system.

The numerical result is found to be in close agreement with the analytical solution, as indicated by the graph presented in Fig. 4.8.

4.5 Conclusions

The problem of a blunt body impacting on water, initially motivated by modelling of the landing of sea-planes, has been subject to continous research since the early works of [70, 34]. We began by reviewing the classic 2D Wagner flow

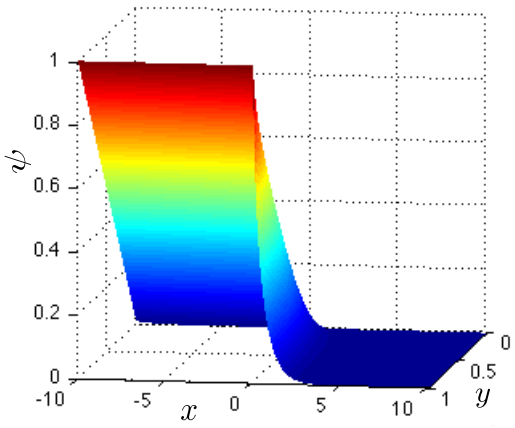

Figure 4.7: Numerical solution of the stream function ψ in the channel $-10 \leq x \leq 10$, $0 \leq y \leq 1$, with $\lambda = -2$ and $\kappa = 1$.

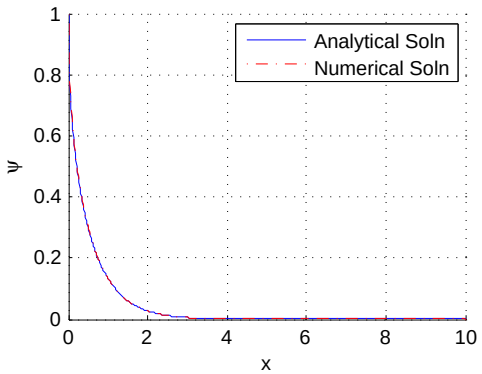

Figure 4.8: Comparison of numerical and analytical solutions in the z plane in the channel $-10 \leq x \leq 10$, $0 \leq y \leq 1$, with $\lambda = -2$ and $\kappa = 1$.

problem for a smooth round body. We subsequently focused our attention on a trailing separation region of a blunt body skimming on shallow water. Under the premise that the trailing separation position is known, perhaps given as part of a solution to the overall skimming flow problem, a localized flow model is derived together with a set of linearised boundary conditions for this separation region. Once the horizontal velocities of the upstream flow and the separation point are prescribed, then both analytical and numerical solutions to the first order have been obtained, which are found to be in close agreement with each other.

Chapter 5

Skimming problems for a smooth blunt body

5.1 Introduction

In this chapter we study the dynamics of a smoothly curved or blunt (bluff) object skimming on a layer of shallow water. The object in question could be a circular cylinder (modelling a sphere in 3D) or a thick but smooth body such as a smooth stone for example. We present a two-stage skimming model, which extends the thin plate skimming model to include a parabolic body thickness configuration. The cross-sectional view of this object has an elongated horizontal profile, and its lower body surface is smooth and strictly convex. In other words the shape of the skimming body is not dissimilar to that of an ellipse, even though such symmetric shape is neither necessary nor assumed.This blunt body could be skimming at an inclined angle as well as having an angular velocity; the angle of inclination is defined as the one made by the plate's major axis and the undisturbed water free surface; this is analogous to the contact angle in the thin plate skimming model, see Fig. 5.1 for illustration.

We assume this blunt body has a large aspect ratio and travels leftwards at

a relatively high horizontal velocity such that the dimensionalization analysis from Chapter 2.2 is applicable here. The implications of these assumptions are that viscosity, gravity and surface tension of the fluid have negligible effects; we expect the hydrodynamic pressure to be the dominant driving force of the flow. In the analysis that follows the water is idealised to be incompressible and irrotational.

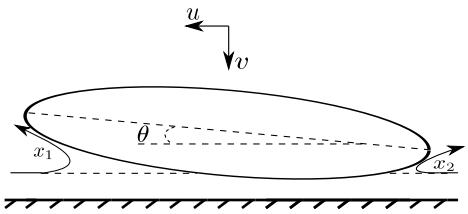

Figure 5.1: A thin body with non-negligible thickness during the impact stage of a skimming process. The body travels leftwards and downwards at a velocity (u, v), and the major axis of the body makes an angle of θ with the undisturbed water surface. The body is smooth and its lower surface which could be in contact with the water is strictly convex. During this stage splash jets are emitted at the leading edge and the trailing edge (denoted by x_1 and x_2 respectively).

Consider the blunt body in skimming motion, with its body geometry resulting in a contact surface with water that is strictly convex; in 2D this surface has moving leading and trailing points whose positions are not known a priori and play a vital role in determining the force exerted on the body. The early mathematical treatments of this problem were pioneered by Von Kármán [70] and Wagner [34] for the landing of seaplanes. Von Kármán's method estimates the contact surface as the intersection between the submersed body and the undisturbed fluid free surface. This approach neglects the water displacement by the submersing body and in effect underestimates the total contact surface. [35] took the free surface elevation into account and proposed that for an impact object with small deadrise angle, at the early stage the penetration depth and the free surface elevation at jet-root regions[1] are small and of the same order. The splash jets emitted from the jet-roots have negligible effect on the body

[1]Please refer to Chapter 2.2 for the formal definitions of deadrise angle and jet-roots.

and the rest of the flow. These observations are used to formulate a linearised contact surface boundary condition that became known as Wagner condition. Since then there has been a considerable amount of research in the field of water entry for solid bodies, particularly for vertical impact problems. Thus [10] studied the vertical entry of a symmetrical wedge and derived a closed form solution for the free surface elevation; [46, 47] conducted numerical studies and experiments on free surface flow for entries of a falling wedge and a circular cylinder; [36, 59] decomposed the flow under the impact body into a jet-root, inner and outer regions, the flow in these regions were analysed by the method of matched asymptotic expansions; [77, 5] extended the Wagner theory to 3D and derived a closed form solution applicable to axisymmetric bodies.

For the field of problems concerning blunt body skimming where a comparatively large horizontal velocity component is present in addition to the vertical one, [67] modified water entry theories for normal vertical impacts to incorporate a tangential horizontal velocity component. Then the skimming process is divided into an initial slamming phase followed by a planing phase at a later stage. It is noted that a body with small deadrise angle can be approximated by an expanding flat plate during the impact stage; at this stage the leading and trailing edges expand away from the initial contact point at a very large speed in relative terms, this speed being unbounded at the instant of impact when time t is 0+. The rapid expansion of the fluid contact area is accompanied by the presence of thin spray jets at both its ends, and asymptotic analysis reveals that the body's horizontal velocity has a negligible effect on the flow at sufficiently small times, i.e. to leading order the Wagner theory for normal impact applies at this stage. During the skimming stage [67] finds that cavitation or separation instability may occur at the smooth trailing edge of a blunt body; to circumvent this scenario a smooth body with sharp trailing edge profile is imposed; and for a shallow water skimming regime it is demonstrated that Tuck & Dixon's travelling wave solution for flat plates [21] can be reached.

As we shall see later in this chapter asymptotic analysis at early impact

times indicates that the fluid pressure in the contact region is initially high, but as time progresses a low and sub-atmospheric pressure region develops under the body and gradually expands towards the trailing edge. This finding is in agreement with that of [73]. This low pressure region eventually reaches the trailing edge. When neglecting any viscous effects it can be argued that air instantly fills this low pressure region under the body, and its pressure at the trailing edge becomes atmospheric abruptly. This phenomenon is in agreement with the trailing edge separation instability for smooth bodies suggested by [67] at the final moments of impacts. At this time the trailing edge position stops moving downstream and the spray jet disappears, which marks the end of the impact stage and the start of the skimming stage. [73] suggests that during skimming the pressure at the trailing edge remains atmospheric as well as having a zero pressure gradient, applying the Brillouin-Villat pressure condition applies at the unknown trailing edge position. These assumptions lead to a discontinuity in the trailing edge position when the body/flow solution transitions from the impact to the skimming stage. [48] experimented with three separation criteria at the trailing edge: the Brillouin-Villat condition, minimisation of change of fluid kinetic energy, and choosing the separation point to be where the body-surface tangent is parallel to its body velocity; in all three cases a discontinuity of the trailing edge position is produced. This suggests that viscous effects at the trailing jet-root region may have an important role in preventing or controlling occurrence of this discontinuity, which is an issue which will be examined further in this study.

Our modelling in effect follows the aforementioned approach of [67, 73] by separating the skimming process into an impact and a planing stage. At the instant of impact there is one initial contact point between the water and the skimming body, i.e. the leading and trailing edges of the body coincide. As the body penetrates below the free surface the two wetted edges travel away from each other along the body's surface and thereby expand the wetted area. Neglecting the effects of gravity and viscosity, the development of the wetted

area is dependent upon the body's geometry, incident angle, vertical and angular velocities, as well as the pressure effects from the flow. Note that the body's horizontal skimming velocity plays no dominant role on the development of the wetted surface. In the sections that follow we present the impact and skimming models. Numerical and analytical treatments will be applied where appropriate to obtain physical insights into this problem, particularly at the early stages of the impact and skimming processes where the dynamics are complex and fast-evolving. It is interesting to note that our analysis finds that the body's inclined contact angle has no leading order effect on the flow during the impact stage, whereas the body's angular velocity plays an important role from the instant of touch-down and influences the development of the leading and trailing edges. The appropriate boundary conditions that should be applied at the trailing edge when it stops traveling downstream remain an open discussion. Analysis for the Brillioun-Villat condition shows this boundary condition change causes the trailing edge to have a sudden "jump" towards the leading edge. In a small-time regime at least, we show that this condition implies that the leading and trailing edges move at a fixed horizontal distance from each other that is proportional to the skimming body's mass, a relation which gives a formal justification to the phenomenon of comparatively slow evolution first observed in [73] via numerical treatments.

5.2 Shallow water impact by a smooth blunt object

In this section we concern ourselves with the impact stage of the skimming process. Consider a smoothly shaped object with large horizontal velocity lands from the air on a shallow layer of water. Suppose the body's major and minor axis lengths are $2L$ and $2T$ respectively, with a large aspect ratio such that $T \sim \epsilon L$ with small parameter $\epsilon \ll 1$. Let h_0 be the depth of the undisturbed shallow water; we shall restrict this to be comparable to the thickness of the

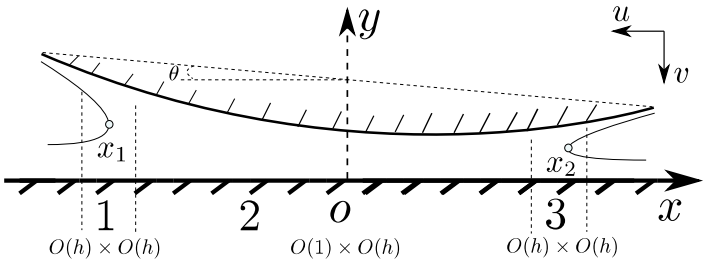

Figure 5.2: A close-up sketch of a blunt body during the impact stage of a skimming process. x_1 and x_2 represent the horizontal positions of the leading and trailing contract edges respectively. Let h denotes the representative depth of the water layer, the jet root regions 1 and 3 have representative scales of $O(h) \times O(h)$, whille the region underneath the impact body has size of $O(1) \times O(h)$. At a sufficiently small time, the contact surface of the body can be approximated by a flat plate at the leading order, and x_1, x_2 move away from each other at an extremely large speed. The contact angle θ has no leading order effect due to the convex body shape.

body, i.e. $h_0 \sim \epsilon L$. Let $\bar{u}$ and $\bar{v}$ be the horizontal and vertical speed of the body skimming on water, where the horizontal speed is much greater than the vertical speed: $\bar{u} \gg \bar{v}$.

Introduce an upper-half Cartesian coordinate system such that the x axis rests at the bottom of the shallow water and point in the direction opposite to the skimming body's horizontal velocity. Its y axis points upwards and goes through the skimming body's centre of mass, whose coordinate is $(0, y_m)$ say. In this configuration the coordinate system travels horizontally with the body, and the undisturbed water flows with velocity $(\bar{u}, 0)$ in the positive direction of the x axis, and the skimming body itself only has vertical and angular motions in this frame of reference. The water free-surface's height is $y = h(x, t)$, while $y = h_0$ is the height of the free surface at rest. The angle between the body's major axis and the water's resting free surface is denoted θ, and its angular velocity is written as ω. See Fig. 5.2 for a depiction of the coordinate system and necessary nomenclatures.

As discussed in the skimming model development of a thin plate in Chapter 2.2, due to the skimming body's large horizontal velocity and length scale,

the flow underneath the body is horizontal at the leading order, the effects of viscosity, gravity and surface tension are negligible to the leading order, and only pressure has a dominant effect on the flow. To this extent the Navier-Stokes equations, water surface kinematic boundary condition as well as the skimming body's vertical and angular momentum equations are the same for the cases of a flat plate and a thick bluff body. We give these equations in (5.1) without further elaboration; we refer to Chapter 2.2 for the non-dimensionalization of the variables and the derivation of governing derivations.

$$\frac{\partial u}{\partial t} + u\frac{\partial u}{\partial x} = -\frac{\partial p}{\partial x}, \qquad (x \in [x_1(t), x_2(t)]), \tag{5.1a}$$

$$\frac{\partial u}{\partial t} + u\frac{\partial u}{\partial x} = 0, \qquad (x \notin [x_1(t), x_2(t)]), \tag{5.1b}$$

$$\frac{\partial h}{\partial t} + \frac{\partial (uh)}{\partial x} = 0, \tag{5.1c}$$

$$h(x,t) = Y_m(t) + x\theta(t) - T(x), \qquad (x \in [x_1(t), x_2(t)]), \tag{5.1d}$$

$$T(x) = Ax^2 + Bx + C, \qquad (A < 0), \tag{5.1e}$$

$$\int_{x_1}^{x_2} p(x,t)dx = M\frac{d^2 Y_m}{dt^2}, \tag{5.1f}$$

$$\int_{x_1}^{x_2} xp(x,t)dx = I\frac{d^2\theta}{dt^2}. \tag{5.1g}$$

The wetted surface of the blunt body has a parabolic shape described by $T(x)$, its coefficients A, B and C are constants and can be calibrated according to the object's body shape. We assume the body's lower surface is smooth and strictly convex; the coefficient A is therefore strictly negative. The water-surface profile underneath the body is given as $h(x,t)$ in (5.1d). This applies to the wetted surface bounded by the leading and trailing contact edges. The initial point of impact (x_0, h_0) is located at the minimum of $h(x,0)$,

$$\left.\frac{\partial h}{\partial x}\right|_{t=0} = \theta_0 - (2Ax_0 + B) = 0,$$

therefore the horizontal position of the initial impact point is

$$x_0 = \frac{\theta_0 - B}{2A}. \tag{5.2}$$

As one would expect the initial contact location is dependent upon the skimming plate's contact angle and contact surface geometry. After touch-down the body and water contact surface goes through a phase of rapid expansion. During this phase the speed at which the leading and trailing edges travel away from the initial impact point is extremely large and, as we shall see later, at the instant of impact it has a singularity of inverse square-root of time. We shall refer to this phase as the impact phase.

During this phase water is pushed away from the impact body's contact surface and spray jets are formed at both leading and trailing edges. As the jets are thrown away from the body into their respective up and down streams, part of the fluid momentum is lost in this process. Under the assumptions of inviscid flow this loss of momentum is balanced by the force caused by the pressure difference between that of the jet root regions and the atmosphere, as in the pressure jump condition used by [21, 57, 73]. The pressure jump condition together with Bernoulli's principle imply the following relations at the leading and trailing edges, which serve as boundary conditions to our impact problem:

$$p(x_1,t) + \frac{1}{2}\left(u(x_1,t) - \frac{dx_1}{dt}\right)^2 = \frac{1}{2}\left(1 - \frac{dx_1}{dt}\right)^2, \tag{5.3a}$$

$$p(x_2,t) + \frac{1}{2}\left(u(x_2,t) - \frac{dx_2}{dt}\right)^2 = \frac{1}{2}\left(1 - \frac{dx_2}{dt}\right)^2, \tag{5.3b}$$

$$\left(u(x_1,t) - \frac{dx_1}{dt}\right) \Big/ \left(1 - \frac{dx_1}{dt}\right) = 2h(x_1,t)^{-\frac{1}{2}} - 1, \tag{5.3c}$$

$$\left(u(x_2,t) - \frac{dx_2}{dt}\right) \Big/ \left(1 - \frac{dx_2}{dt}\right) = 2h(x_2,t)^{-\frac{1}{2}} - 1. \tag{5.3d}$$

Our impact model therefore consists of (5.1) and (5.3). The solution to this integro-differential equations system is challenging as the contact surface is unknown and needs to be determined as part of the solution. The full numerical

treatments to this class of problems have been studied by [20, 73], and their numerical algorithms will not be discussed in depth here. Instead we focus on a linearised formulation of this problem to gain further analytical insights; the findings of our studies will be cross validated with the numerical results [73] qualitatively where possible.

5.3 Linearised impact model development

As discussed in the previous section, during the impact phase the solid-liquid contact surface initially goes through a phase of rapid expansion and spray jets are formed at the boundary of the surface. As time progresses if the skimming body is able to eventually transit from impact to planing phase, the spray jet disappears from the trailing edge. To analyse the impact system behaviour during this phase of rapid contact surface expansion, we focus on a short time after impact such that time t is of order δ where $\delta \ll 1$.

Given that the body's initial vertical velocity is of order unity, we expect the free surface penetration to be small and have the same order as time t. Balancing the terms of the free surface equation (5.1d) suggests that the model's horizontal and angular scales both evolve on a higher order, specifically $x \sim O(\delta^{\frac{1}{2}})$ and $\theta \sim O(\delta^{\frac{1}{2}})$. From the pressure jump conditions (5.3a) and (5.3b) we can deduce that the fluid's horizontal velocity u evolves on the same scale as x, and that the pressure p evolves on the scale of order unity. We therefore asymptotically

expand the system variables as follows:

$$t = \delta\hat{t}, \tag{5.4a}$$

$$x \sim x_0 + \delta^{\frac{1}{2}}\hat{x} + O(\delta), \tag{5.4b}$$

$$Y_m \sim Y_0 + \delta\hat{Y} + O(\delta^2), \tag{5.4c}$$

$$\theta \sim \theta_0 + \delta^{\frac{1}{2}}\hat{\theta} + O(\delta), \tag{5.4d}$$

$$h \sim 1 + \delta\hat{h} + O(\delta^2), \tag{5.4e}$$

$$u \sim \delta^{\frac{1}{2}}\hat{u} + O(\delta), \tag{5.4f}$$

$$p \sim \hat{p} + O(\delta^{\frac{1}{2}}), \tag{5.4g}$$

with δ being small. We shall seek a linearised model by substituting (5.4) into the impact system (5.1) and (5.3). Note that in Wagner theory for vertical impact by body with parabolic shapes (see [68, 59]), the contact edges evolves on the scale of $O(\sqrt{t})$; the free surface penetration evolves on the scale of $O(t)$ and the hydrodynamic pressure is of order $O(t)$. This is the same scaling as our case here for an impact body with large horizontal velocity, suggesting that for a short time after impact the body's horizontal velocity has an negligible effect on the fluid flow.

The contact surface elevation equation (5.1d) after expansion according to (5.4) becomes

$$1 + \delta\hat{h} = Y_0 + \delta\hat{Y} + (x_0 + \sqrt{\delta}\hat{x})(\theta_0 + \sqrt{\delta}\hat{\theta}) - T(x_0 + \sqrt{\delta}\hat{x}). \tag{5.5}$$

At each order we have the following geometrical relations:

$$O(1): \quad 1 = Y_0 + x_0\theta_0 - T(x_0), \tag{5.6a}$$

$$O(\delta^{\frac{1}{2}}): \quad 0 = (\theta_0 - B - 2Ax_0)\hat{x} + x_0\hat{\theta}, \qquad (\hat{x} \in [\hat{x}_1, \hat{x}_2]), \tag{5.6b}$$

$$O(\delta): \quad \hat{h} = \hat{Y} + \hat{x}\hat{\theta} - A\hat{x}^2, \qquad (\hat{x} \in [\hat{x}_1, \hat{x}_2]), \tag{5.6c}$$

and at time $t = 0$ we have the additional condition (5.2), i.e.:

$$\theta_0 = 2Ax_0 + B.$$

We can see that the relation (5.6b) requires either $\hat{\theta} = 0$ or $x_0 = 0$; the former implies the skimming body maintains a constant contact angle and cannot have any initial angular velocity, which is an unphysical requirement and will not be pursued; the latter ($x_0 = 0$) requires the coefficient B of the quadratic function $T(x)$, which controls the declivity of the parabola, to be equal to the initial contact angle:

$$\theta_0 = B. \tag{5.7}$$

We shall impose this condition so that the initial touch-down point is always at position zero as a result of relation (5.2).

Based on asymptotic expansions of (5.4) the Euler equations in (5.1a, 5.1b) at the dominant order become:

$$\frac{\partial \hat{p}}{\partial \hat{x}} + \frac{\partial \hat{u}}{\partial \hat{t}} = 0, \qquad (\hat{x} \in [\hat{x}_1, \hat{x}_2]) \tag{5.8a}$$

$$\frac{\partial \hat{u}}{\partial \hat{t}} = 0; \qquad (\hat{x} \notin [\hat{x}_1, \hat{x}_2]) \tag{5.8b}$$

and the kinematic boundary condition of the free surface (5.1c) becomes:

$$\frac{\partial \hat{h}}{\partial \hat{t}} + \frac{\partial \hat{u}}{\partial \hat{x}} = 0. \tag{5.9}$$

The pressure jump conditions at the leading edge (5.3a, 5.3c) can be simplified to the following forms at the leading order:

$$\hat{p}_1 = \frac{d\hat{x}_1}{d\hat{t}}\hat{u}_1, \qquad \hat{u}_1 = \frac{d\hat{x}_1}{d\hat{t}}\hat{h}_1; \tag{5.10}$$

and likewise at the trailing edge:

$$\hat{p}_2 = \frac{d\hat{x}_2}{d\hat{t}}\hat{u}_2, \qquad\qquad \hat{u}_2 = \frac{d\hat{x}_2}{d\hat{t}}\hat{h}_2. \tag{5.11}$$

Concerning the skimming plate's vertical and angular momentum equations in (5.1f, 5.1g), we find that unless the body's mass M and moment of inertia I are extremely small (i.e. $M \ll 1$ and $I \ll 1$), the force generated by hydraulic pressure underneath the body does not have an effect on the body's momentum shortly after impact, hence at the leading order

$$\frac{d^2\hat{Y}}{d\hat{t}^2} = 0, \tag{5.12a}$$

$$\frac{d^2\hat{\theta}}{d\hat{t}^2} = 0. \tag{5.12b}$$

We therefore expect the body's vertical and angular velocities to be equal to their initial values in a short time period after impact. Supposing the initial values are $\hat{V}_0$ and $\hat{\omega}_0$ respectively, we can immediately write down $\hat{Y}$ and $\hat{\theta}$ as:

$$\hat{Y} = \hat{V}_0\hat{t}, \tag{5.13a}$$

$$\hat{\theta} = \hat{\omega}_0\hat{t}. \tag{5.13b}$$

The governing equations (5.6c), (5.8a), (5.9) and (5.13) together with the initial and boundary conditions (5.10) and (5.11) form our linearised blunt body impact model, which consists of five equations for five unknowns $\hat{Y}(\hat{t})$, $\hat{\theta}(\hat{t})$, $\hat{h}(\hat{x},\hat{t})$, $\hat{u}(\hat{x},\hat{t})$ and $\hat{p}(\hat{x},\hat{t})$.

This model can be simplified further by substituting the contact surface equation (5.6c) into the kinematic boundary condition (5.9) and integrating with respect to x. This enables us to obtain an expression for the fluid velocity $\hat{u}$:

$$\hat{u} = -\big(\frac{1}{2}\hat{\omega}_0\hat{x}^2 + \hat{V}_0\hat{x}\big) - \hat{f}(\hat{t}), \qquad (\hat{x} \in [\hat{x}_1, \hat{x}_2]) \tag{5.14}$$

where $\hat{f}(\hat{t})$ is an unknown function of time to be determined and is a result of spatial integration. Note in particular that we have separated the spatial and time variables in (5.14), which will subsequently enable us to significantly reduce the complexity of our impact system. This fluid velocity expression can be combined with Euler's equation in (5.8a) and integrating with respect to x to give an expression for the pressure $\hat{p}$:

$$\hat{p} = \frac{d\hat{f}}{d\hat{t}}\hat{x} + \hat{g}(\hat{t}), \qquad (\hat{x} \in [\hat{x}_1, \hat{x}_2]) \tag{5.15}$$

where $\hat{g}(\hat{t})$ is also a function of time and comes about as a result of spatial integration.

The pressure jump conditions at the leading and trailing edges (5.10), (5.11) provide the necessary boundary conditions for the fluid velocity and pressure equations (5.14), (5.15). Combining the boundary conditions with these two equations and simplifying allows us to write down the expressions below for functions $\hat{f}(\hat{t})$ and $\hat{g}(\hat{t})$ at the leading edge:

$$\hat{f} = \left[\frac{1}{3}A\hat{x}_1^3 - \frac{1}{2}\hat{\omega}_0\hat{t}\hat{x}_1^2 - \hat{V}_0\hat{t}\hat{x}_1\right]_{\hat{t}}, \tag{5.16}$$

$$\hat{g} = -\frac{1}{2}\left[\frac{1}{3}\hat{\omega}_0\hat{x}_1^3 + \hat{V}_0\hat{x}_1^2 + 2\hat{f}\hat{x}_1\right]_{\hat{t}}. \tag{5.17}$$

Here the subscript $\hat{t}$ denotes differentiation with respect to time $\hat{t}$. Repeating the same procedures at the trailing edge yields the following relations:

$$\hat{f} = \left[\frac{1}{3}A\hat{x}_2^3 - \frac{1}{2}\hat{\omega}_0\hat{t}\hat{x}_2^2 - \hat{V}_0\hat{t}\hat{x}_2\right]_{\hat{t}}, \tag{5.18}$$

$$\hat{g} = -\frac{1}{2}\left[\frac{1}{3}\hat{\omega}_0\hat{x}_2^3 + \hat{V}_0\hat{x}_2^2 + 2\hat{f}\hat{x}_2\right]_{\hat{t}}. \tag{5.19}$$

Eliminating $\hat{f}$ and $\hat{g}$ by combining the equations (5.16) - (5.19) for the leading

and trailing edges then gives:

$$2A(\hat{x}_1^2 + \hat{x}_1\hat{x}_2 + \hat{x}_2^2) - 3\hat{\omega}_0\hat{t}(\hat{x}_1 + \hat{x}_2) - 6\hat{V}_0\hat{t} = 0, \tag{5.20a}$$

$$6\big[A\hat{x}_1^2 - \hat{\omega}_0\hat{t}\hat{x}_1 - \hat{V}_0\hat{t}\big]\frac{d\hat{x}_1}{d\hat{t}} + 6\big[A\hat{x}_2^2 - \hat{\omega}_0\hat{t}\hat{x}_2 - \hat{V}_0\hat{t}\big]\frac{d\hat{x}_2}{d\hat{t}} - \hat{\omega}_0(\hat{x}_1 - \hat{x}_2)^2 = 0. \tag{5.20b}$$

We have therefore arrived at our linearised impact model, which consists of only two equations (5.20) with two unknowns $\hat{x}_1$ and $\hat{x}_2$. In the section that follows we shall apply analytical and numerical analysis to this model.

A note of interest when applying numerical treatments to (5.20): this system has three parameters A, $\hat{V}_0$ and $\hat{\omega}_0$. By applying the following linear transformation to the independent variables $\hat{x}$ and $\hat{t}$,

$$\hat{x} \sim -\frac{\hat{V}_0}{\hat{\omega}_0}\bar{x}, \quad \hat{t} \sim \frac{A\hat{V}_0}{\hat{\omega}_0^2}\bar{t}, \tag{5.21}$$

the impact system (5.20) can be written into a parameter-invariant form which reduces the numerical effort:

$$2(\bar{x}_1^2 + \bar{x}_1\bar{x}_2 + \bar{x}_2^2) + 3\bar{t}(\bar{x}_1 + \bar{x}_2) - 6\bar{t} = 0, \tag{5.22a}$$

$$6\big(\bar{x}_1^2 + \bar{t}\bar{x}_1 - \bar{t}\big)\frac{d\bar{x}_1}{d\bar{t}} + 6\big(\bar{x}_2^2 + \bar{t}\bar{x}_2 - \bar{t}\big)\frac{d\bar{x}_1}{d\bar{t}} + (\bar{x}_1 - \bar{x}_2)^2 = 0. \tag{5.22b}$$

In essence, $\bar{x}_1$ and $\bar{x}_2$ serve as a basis solution from which other solutions for arbitrarily prescribed parameter values of A, $\hat{\omega}_0$ and $\hat{V}_0$ can be derived. Note that when prescribing A we require it to be a negative value so that the body's skimming surface is convex, and $\hat{V}_0$ should also be negative so that the body is initially entering the water rather than exiting from it. The restriction needed for the basic system solution to be valid is $\hat{\omega}_0 \neq 0$, and if this is not the case then the scalings in (5.21) break down and we would need to revert to the fully parameterised system of (5.20).

5.4 Early-time impact behaviour

The linearised model (5.20) provides the basis to analyse the blunt body's interaction with the fluid after initial impact. We consider a short time scale immediately after initial impact such that $\hat{t} \ll 1$. The governing equation of (5.13a) suggests that the system's vertical scale evolves linearly with $\hat{t}$, and the contact surface relation (5.6c) therefore suggests that the system's horizontal scale evolves at the order of $\hat{t}^{\frac{1}{2}}$; we therefore try the following small time asymptotic solutions:

$$\hat{x}_1 = \hat{\mu}_1 \hat{t}^{\frac{1}{2}} + O(\hat{t}), \tag{5.23a}$$

$$\hat{x}_2 = \hat{\mu}_2 \hat{t}^{\frac{1}{2}} + O(\hat{t}). \tag{5.23b}$$

Putting these into system (5.20) yields the following relations:

$$2A(\hat{\mu}_1^2 + \hat{\mu}_1\hat{\mu}_2 + \hat{\mu}_2^2) - 6\hat{V}_0 = 0, \tag{5.24a}$$

$$6\hat{\mu}_1(A\hat{\mu}_1^2 - \hat{V}_0) + 6\hat{\mu}_2(A\hat{\mu}_2^2 - \hat{V}_0) - \hat{\omega}_0(\hat{\mu}_1 - \hat{\mu}_2)^2 = 0. \tag{5.24b}$$

Solving this system of coupled quadratic equations and selecting the roots such that $\hat{\mu}_1 < 0$ and $\hat{\mu}_2 > 0$ based on physical grounds yields the following results:

$$\hat{x}_1 \sim \frac{\hat{\omega}_0 + \left(192AV_0 - 3\hat{\omega}_0^2\right)^{\frac{1}{2}}}{8A}\hat{t}^{\frac{1}{2}}, \tag{5.25a}$$

$$\hat{x}_2 \sim \frac{\hat{\omega}_0 - \left(192AV_0 - 3\hat{\omega}_0^2\right)^{\frac{1}{2}}}{8A}\hat{t}^{\frac{1}{2}}. \tag{5.25b}$$

We can immediately see that for a skimming body with no angular rotation $\hat{\omega}_0 = 0$, its leading and trailing edges evolve away from the initial touch-down point at equal speeds of $(\frac{3\hat{V}_0}{A})^{\frac{1}{2}}$. A positive rotation of the body where $\hat{\omega}_0 > 0$ would result in the leading edge extending away from the touch down point at a faster pace than the trailing edge, and vice-versa for a body with negative rotation, which intuitively makes physical sense. The speed at which the two

edges evolve has an inverse relation with the skimming body's curvature: if the curvature coefficient is small, i.e. $A \ll 1$, the body becomes very similar to that of a flat plate, and then the speed at which the two edges travel away from each other becomes infinitely large.

Fig. 5.3 shows the results for the impact system (5.20) when solved using a 5th order Adam-Bashforth-Moulton Predictor-Corrector numerical scheme as well as its comparison with the small-time asymptotic solutions of (5.25). The parameter values of $\hat{\omega}_0$, A and $\hat{V}_0$ are taken to be 1, -1 and -1 respectively. On a small time scale $\hat{t} \ll 1$, the asymptotes are able to approximate well the behaviours of the two wetted edges, see Fig. 5.3a. The speed at which these two edges travel away from each other is unbounded as $\hat{t} \to 0$ and this rapidly slows down over time as shown in Fig. 5.3b. For a body with positive rotation $\hat{\omega}_0 > 0$, the trailing edge's speed decreases more rapidly when compared with that of the leading edge, and it asymptotically approaches zero over time. Fig. 5.3c shows the fluid flows upstream at the leading edge and downstream at the trailing edge, as indicated by the fluid velocity $\hat{u}_1 < 0$ and $\hat{u}_2 > 0$, signifying the presence of splash jets at both edges with water being pushed away from the body during the impact stage; correspondingly there are positive pressures at both edges as shown in Fig. 5.3d. Notice that the positive angular rotation of the body results in a relative higher pressure at the leading edge compared with the trailing edge, and fluid at the leading edge flows at a higher velocity towards upstream.

Later in the impact stage when time $\hat{t}$ is order unity, the $\hat{t}^{\frac{1}{2}}$ terms cease to be dominant. At large $\hat{t}$ we expect the two wetted edges to evolve on the same order as the body's vertical scale, i.e. $\hat{x}_1$ and $\hat{x}_2$ vary linearly with time and we therefore write $\hat{x}_1$ and $\hat{x}_2$ in the following form:

$$\hat{x}_1 = \hat{\nu}_1 \hat{t}, \qquad \hat{x}_2 = \hat{\nu}_2 \hat{t}, \qquad (\hat{t} \gg 1),$$

where $\hat{\nu}_1$ and $\hat{\nu}_2$ are constants. Substituting into system (5.20) gives the follow-

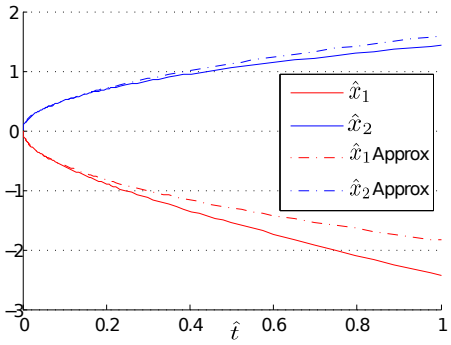

(a) Leading and trailing edges $\hat{x}_1$, $\hat{x}_2$ as time $\hat{t}$ evolves from 0 to 1. The solid lines are the numerical solutions, the dashed lines are the approximation of small time solution (5.25).

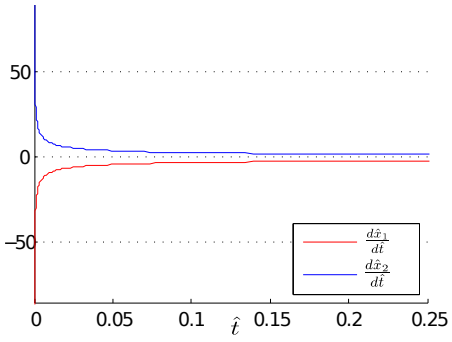

(b) The leading and trailing edge velocities $\frac{d\hat{x}_1}{d\hat{t}}$ and $\frac{d\hat{x}_2}{d\hat{t}}$ as $\hat{t}$ develops.

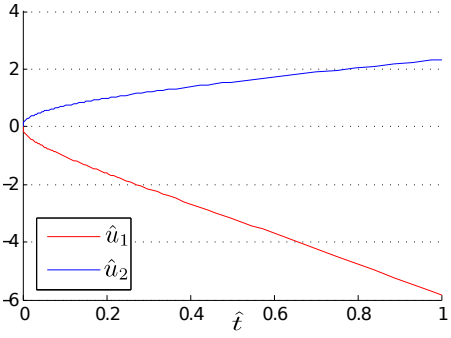

(c) The fluid velocity at the leading and trailing edges $\hat{u}_1$ and $\hat{u}_2$ respectively over time.

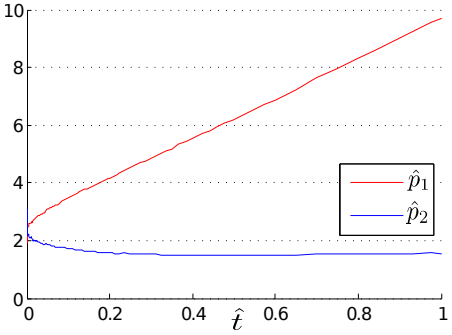

(d) The leading and trailing edge pressure profiles $\hat{p}_1$, $\hat{p}_2$, as well as pressure gradient $\frac{d\hat{p}}{d\hat{x}}$ over time.

Figure 5.3: Solution of the skimming system (5.20) for $\hat{t} \in (0, 1)$. Fig. (5.3a) also shows the asymptotic solution (5.25) valid for small $\hat{t}$. The skimming body is given an positive initial angular velocity $\omega_0 = 1$; its initial vertical velocity V_0 is taken to be -1 and body curvature coefficient A is set to be -1.

ing relations for $\hat{\nu}_1$, $\hat{\nu}_2$ at the leading order of t:

$$2A(\hat{\nu}_1^2 + \hat{\nu}_1\hat{\nu}_2 + \hat{\nu}_2^2) - 3\hat{\omega}_0(\hat{\nu}_1 + \hat{\nu}_2) = 0, \tag{5.26a}$$

$$6\hat{\nu}_1(A\hat{\nu}_1^2 - \hat{\omega}_0\hat{\nu}_1) + 6\hat{\nu}_2(A\hat{\nu}_2^2 - \hat{\omega}_0\hat{\nu}_2) - \hat{\omega}_0(\hat{\nu}_1 - \hat{\nu}_2)^2 = 0. \tag{5.26b}$$

Solving these second order equations yields the following large-time approximations for the horizontal position of the two leading edges based on the direction of the body's angular rotation:

$$(\omega_0 > 0) : \begin{cases} \hat{x}_1 = \frac{\hat{\omega}_0(1+3^{\frac{1}{2}})}{2A}\hat{t}, \\ \hat{x}_2 = \frac{\hat{\omega}_0(1-3^{\frac{1}{2}})}{2A}\hat{t}. \end{cases} \tag{5.27a}$$

$$(\omega_0 < 0) : \begin{cases} \hat{x}_1 = \frac{\hat{\omega}_0(3^{\frac{1}{2}}-1)}{2A}\hat{t}, \\ \hat{x}_2 = \frac{\hat{\omega}_0(3^{\frac{1}{2}}+1)}{2A}\hat{t}. \end{cases} \tag{5.27b}$$

These results suggest that there are no retractions of either edge in the early impact time regime for a skimming body with order unity body mass. In particular for a body with positive rotation its leading edge extends away from the initial touch down point faster than the trailing edge, and vice versa for a body with negative rotation. Fig. 5.4 demonstrates the large-time approximate solution (5.27) compared with the numerical solution of the original impact system (5.20). The results show that the large-time asymptotic solutions describe the evolution of the two edges reasonably well.

5.5 Rapid transition to planing stage

The analysis from Section 5.3 shows that a short time after impact the hydrodynamic pressure underneath the skimming body does not generate sufficient lift to alter its vertical trajectory at the leading order, and the wetted edges extend away from the initial contact point on a square-root of time scale. It is possible however, for the body to go through a rapid transition from impact to the planing phase and stop sinking further into water.

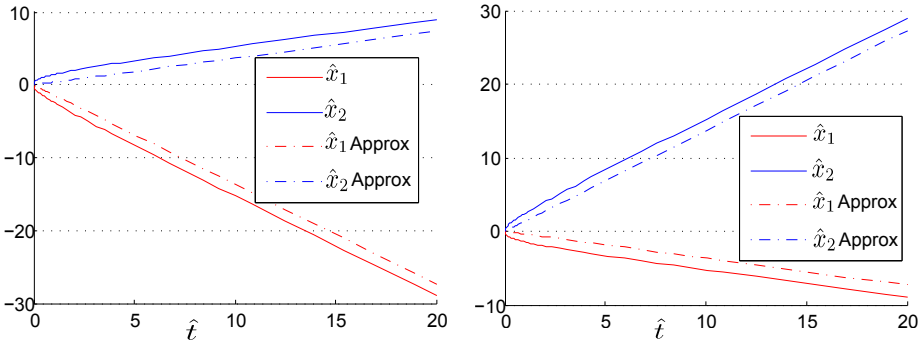

(a) $\hat{\omega}_0 > 0$ (b) $\hat{\omega}_0 < 0$

Figure 5.4: Numerical solution of $\hat{x}_1$, $\hat{x}_2$ via system (5.20) with its large time approximation solution (5.27) in dashed line.

The asymptotic system (5.4) in Section 5.3 suggests that in a short time frame after impact such that $\hat{t} \sim O(\delta)$, if an impact body has sufficiently small body mass such that $M \sim O(\delta^{\frac{3}{2}})$, the body's vertical momentum equation (5.1f) at the leading order $O(\delta^{\frac{1}{2}})$ is no longer trivially zero, instead

$$M\frac{d^2\hat{Y}}{d\hat{t}^2} = \int_{\hat{x}_1}^{\hat{x}_2} \hat{p} d\hat{x}, \tag{5.28}$$

and therefore the body does not penetrate into water at a fixed initial vertical velocity, as it feels the effect of hydrodynamic pressure lift instantaneously. The free surface kinematic boundary condition (5.14) now takes on the following form:

$$\hat{u}(\hat{x},\hat{t}) = -\hat{x}\frac{d\hat{Y}}{d\hat{t}} - \frac{1}{2}\hat{\omega}_0\hat{x}^2 - \hat{f}(\hat{t}), \qquad (\hat{x} \in [\hat{x}_1, \hat{x}_2]) \tag{5.29}$$

and combining with the Euler's equation (5.8a) yields the following expression for pressure $\hat{p}(\hat{x},\hat{t})$:

$$\hat{p}(\hat{x},\hat{t}) = \frac{1}{2}\hat{x}^2\frac{d^2\hat{Y}}{d\hat{t}^2} + \hat{x}\frac{d\hat{f}}{d\hat{t}} + \hat{g}(\hat{t}), \qquad (\hat{x} \in [\hat{x}_1, \hat{x}_2]) \tag{5.30}$$

where the functions $\hat{f}(\hat{t})$ and $\hat{g}(\hat{t})$ result from spatial integrations with respect to x as before. The leading edge boundary conditions (5.10) together with the

free surface boundary condition (5.29) and pressure equation (5.30) give the following expressions for $\hat{f}$ and $\hat{g}$:

$$\hat{f} = \left[\frac{1}{3}A\hat{x}_1^3 - \frac{1}{2}\hat{\omega}_0\hat{t}\hat{x}_1^2 - \hat{x}_1\hat{Y}\right]_{\hat{t}}, \tag{5.31}$$

$$\hat{g} = -\left[\frac{1}{6}\hat{\omega}_0\hat{x}_1^3 + \frac{1}{2}\hat{x}_1^2\frac{d\hat{Y}}{d\hat{t}} + \hat{f}\hat{x}_1\right]_{\hat{t}}. \tag{5.32}$$

Repeating this procedure at the trailing edge we are able to obtain another set of expressions for $\hat{f}(\hat{t})$ and $\hat{g}(\hat{t})$,

$$\hat{f} = \left[\frac{1}{3}A\hat{x}_2^3 - \frac{1}{2}\hat{\omega}_0\hat{t}\hat{x}_2^2 - \hat{x}_1\hat{Y}\right]_{\hat{t}}, \tag{5.33}$$

$$\hat{g} = -\left[\frac{1}{6}\hat{\omega}_0\hat{x}_2^3 + \frac{1}{2}\hat{x}_2^2\frac{d\hat{Y}}{d\hat{t}} + \hat{f}\hat{x}_2\right]_{\hat{t}}. \tag{5.34}$$

Combining and simplifying equations (5.28) - (5.34) produces a set of five differential algebraic equations (DAEs) for five unknowns: $\hat{x}_1$, $\hat{x}_2$, $\hat{Y}$, $\hat{f}$ and $\hat{g}$:

$$\hat{Y} = \frac{1}{3}A(\hat{x}_1^2 + \hat{x}_1\hat{x}_2 + \hat{x}_2^2) - \frac{1}{2}\hat{\omega}_0(\hat{x}_1 + \hat{x}_2)\hat{t}, \tag{5.35a}$$

$$\hat{f} = -\frac{1}{6}\hat{\omega}_0(\hat{x}_1^2 + \hat{x}_1\hat{x}_2 + \hat{x}_2^2) - \frac{1}{2}(\hat{x}_1 + \hat{x}_2)\frac{d\hat{Y}}{d\hat{t}}, \tag{5.35b}$$

$$\hat{f} = \frac{1}{2}\left[\frac{A}{3}(\hat{x}_1^3 + \hat{x}_2^3) - \frac{\hat{\omega}_0}{2}(\hat{x}_1^2 + \hat{x}_2^2)\hat{t} - (\hat{x}_1 + \hat{x}_2)\hat{Y}\right]_{\hat{t}}, \tag{5.35c}$$

$$\hat{g} = -\frac{1}{2}\left[\frac{\hat{\omega}_0}{6}(\hat{x}_1^3 + \hat{x}_2^3) + \frac{1}{2}(\hat{x}_1^2 + \hat{x}_2^2)\frac{d\hat{Y}}{d\hat{t}} + (\hat{x}_1 + \hat{x}_2)\hat{f}\right]_{\hat{t}}, \tag{5.35d}$$

$$(6M + \hat{x}_1^3 - \hat{x}_2^3)\frac{d^2\hat{Y}}{d\hat{t}^2} + 3(\hat{x}_1^2 - \hat{x}_2^2)\frac{d\hat{f}}{d\hat{t}} + 6(\hat{x}_1 - \hat{x}_2)\hat{g} = 0. \tag{5.35e}$$

The nature of this DAEs system makes any analytical treatment a formidable challenge. We shall therefore pursue the route of numerical study first. As with the linearised impact model from the previous section, this DAEs model can still be transformed into a parameter-invariant form by introducing the

following scalings:

$$\hat{t} \sim \frac{A\hat{V}_0}{\hat{\omega}_0^2}\bar{t}, \;\; \hat{x} \sim -\frac{\hat{V}_0}{\hat{\omega}_0}\bar{x}, \;\; \hat{Y} \sim -\frac{A\hat{V}_0^2}{\hat{\omega}_0^2}\bar{Y}, \;\; \hat{f} \sim \frac{\hat{V}_0^2}{\hat{\omega}_0}\bar{f}, \;\; \hat{g} \sim -\frac{\hat{V}_0^2}{A}\bar{g}, \;\; M \sim \frac{\hat{V}_0^3}{A\hat{\omega}_0}\bar{M}. \tag{5.36}$$

Substituting the scaled variables into the model (5.35) leads to:

$$\bar{Y} = -\frac{1}{3}(\bar{x}_1^2 + \bar{x}_1\bar{x}_2 + \bar{x}_2^2) + \frac{1}{2}\bar{t}(\bar{x}_1 + \bar{x}_2), \tag{5.37a}$$

$$\bar{f} = -\frac{1}{6}(\bar{x}_1^2 + \bar{x}_1\bar{x}_2 + \bar{x}_2^2) + \frac{1}{2}\frac{d\bar{Y}}{d\bar{t}}(\bar{x}_1 + \bar{x}_2), \tag{5.37b}$$

$$\bar{f} = \frac{1}{2}\left[\frac{1}{3}(\bar{x}_1^3 + \bar{x}_2^3) - \frac{1}{2}(\bar{x}_1^2 + \bar{x}_2^2)\bar{t} + \bar{Y}(\bar{x}_1 + \bar{x}_2)\right]_{\bar{t}}, \tag{5.37c}$$

$$\bar{g} = \frac{1}{2}\left[\frac{1}{6}(\bar{x}_1^3 + \bar{x}_2^3) - \frac{1}{2}(\bar{x}_1^2 + \bar{x}_2^2)\frac{d\bar{Y}}{d\bar{t}} + (\bar{x}_1 + \bar{x}_2)\bar{f}\right]_{\bar{t}}, \tag{5.37d}$$

$$(6\bar{M} + \bar{x}_1^3 - \bar{x}_2^3)\frac{d^2\bar{Y}}{d\bar{t}^2} - 3(\bar{x}_1^2 - \bar{x}_2^2)\frac{d\bar{f}}{d\bar{t}} + 6(\bar{x}_1 - \bar{x}_2)\bar{g} = 0; \tag{5.37e}$$

we therefore have a model that is invariant of the angular velocity $\hat{\omega}_0$, body curvature coefficient A and initial velocity $\hat{V}_0$.

We solved the system numerically using a 5th order Adam-Bashforth-Moulton Predictor-Corrector method and the results are shown in Fig. 5.5 for a parabolic body with positive angular rotation, whereas for the case of a negative angular rotation the results are presented in Fig. 5.6.

The results indicate that inside the $\hat{t} \sim O(\delta)$ regime, provided the skimming plate's mass is small (i.e. $M \sim O(\delta^{\frac{3}{2}})$) and has an angular rotation (i.e. $\hat{\omega}_0 \neq 0$), we could witness a retraction of either the leading or trailing edge inside this small-time regime. At the instant of touchdown, the speed at which the leading and trailing edges evolve away from the initial contact point is large and unbounded when time $\hat{t}$ is 0+ as stated previously, hence the wetted surface expands very rapidly immediately after impact. This rapid expansion of contact area slows down as time progresses, and for a skimming body with positive angular rotation the trailing edge's velocity eventually drops to zero as demonstrated in Fig. 5.5b. Letting $\hat{t}_c$ denote the critical point in time when

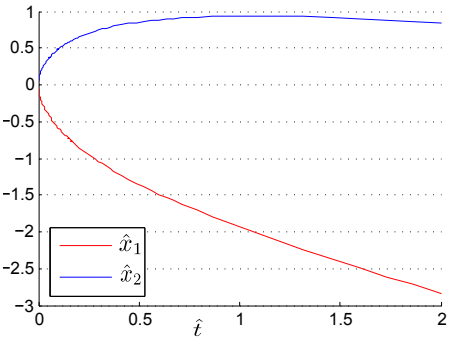

(a) Evolution of leading and trailing edges $\hat{x}_1$, $hatx_2$ w.r.t. time $\hat{t}$.

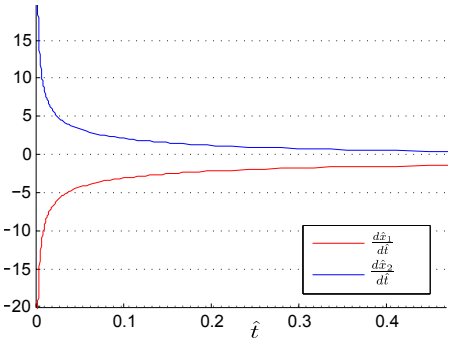

(b) Evolution of leading and trailing edge velocities $\frac{d\hat{x}_1}{d\hat{t}}$, $\frac{d\hat{x}_2}{d\hat{t}}$.

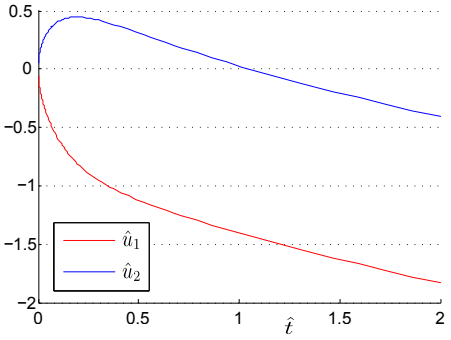

(c) The evolution of fluid velocities $\hat{u}_1$ and $\hat{u}_2$.

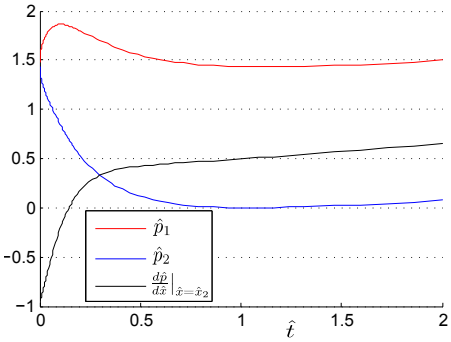

(d) Evolution of leading and trailing edge pressure profiles.

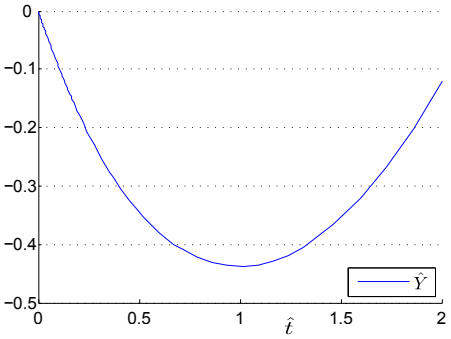

(e) Vertical evolution of the skimming body's centre of mass.

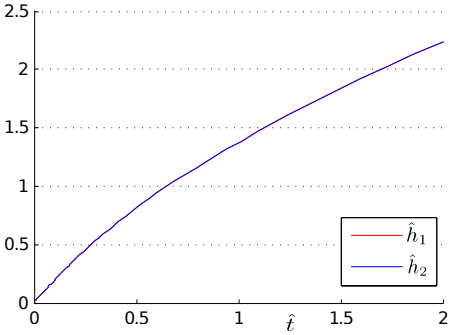

(f) Water surface elevation at the leading and trailing edges.

Figure 5.5: Various profile plots of a skimming body with a positive rotation $\hat{\omega}_0 > 0$. The initial vertical velocity of the body $\hat{V}_0$ is taken to be -1, and the initial angular velocity $\hat{\omega}_0$ is taken to be 1. Under these initial settings the trailing edge $\hat{x}_2$ initially evolves towards the downstream, however at time $\hat{t} \sim 1.0497$ this edge reaches its maximum and begins to retract towards upstream initial contact point.

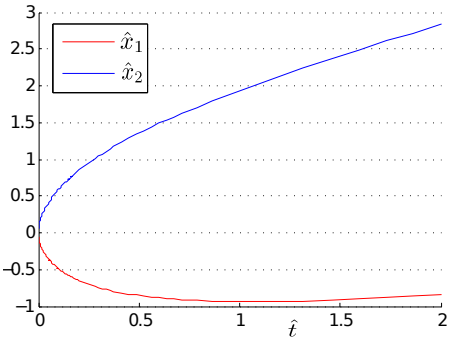

(a) Evolution of leading and trailing edges $\hat{x}_1$, $\hat{x}_2$ w.r.t. time $\hat{t}$.

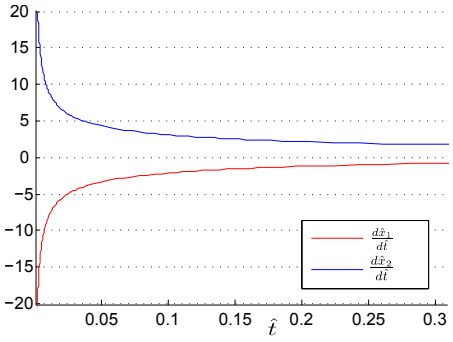

(b) Evolution of leading and trailing edge velocities $\frac{d\hat{x}_1}{d\hat{t}}$, $\frac{d\hat{x}_2}{d\hat{t}}$.

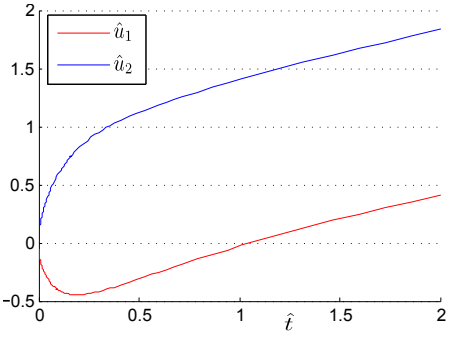

(c) The evolution of fluid velocities $\hat{u}_1$ and $\hat{u}_2$.

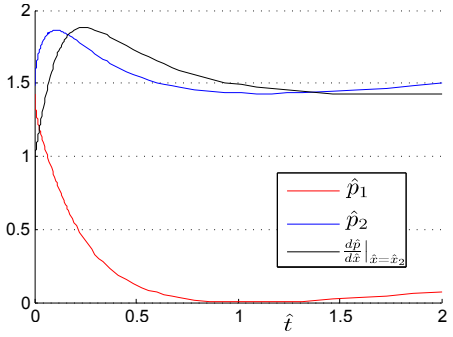

(d) Evolution of leading and trailing edge pressure profiles.

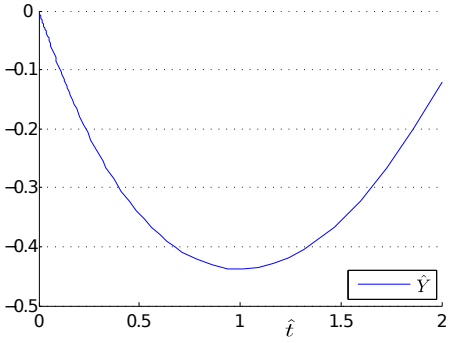

(e) Vertical evolution of the skimming body's centre of mass.

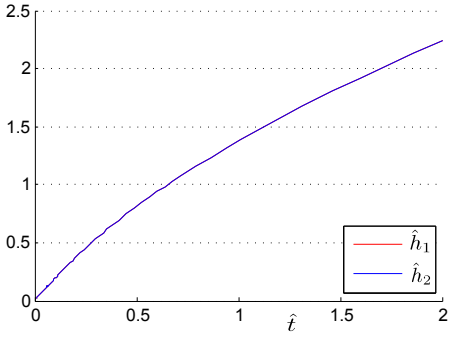

(f) Water surface elevation at the leading and trailing edges.

Figure 5.6: Various profile plots of a skimming body with a negative rotation $\hat{\omega}_0 < 0$. The initial vertical velocity of the body $\hat{V}_0$ is taken to be -1, and the initial angular velocity $\hat{\omega}_0$ is taken to be -1. Under these initial settings the leading edge $\hat{x}_1$ initially evolves towards the upstream, however at time $\hat{t} \sim 1.0497$ this edge reaches its minimum and begins to retract towards downstream initial contact point.

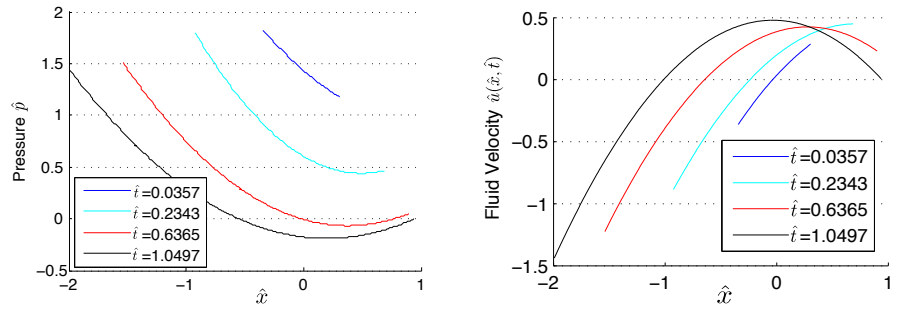

(a) A plot of pressure profiles $\hat{p}$ underneath the skimming body at different times of the impact stage.

(b) A plot of fluid velocity profiles $\hat{u}$ underneath the skimming body at different times of the impact stage.

Figure 5.7: The time evolution of the pressure and fluid velocity underneath the skimming body during the impact stage for a positively rotating body. The time begins from shortly after impact $\hat{t} = 0.0357$ to the end of impact stage at $\hat{t} = 1.0497$ when the trailing edge pressure drops to zero. Notice that the wetted surface area is initially small and increases over time. The initial conditions are $\hat{V}_0 = -1$ and $\hat{\omega}_0 = 1$.

this phenomenon occurs, $\hat{t}_c$ is estimated to be ~ 1.0497 with the initial conditions of $\hat{\omega}_0 = -1$ and $\hat{V}_0 = -1$. Before this critical time is reached we see in Fig. 5.5c that the fluid velocity at the leading edge is negative, i.e. fluid flows away from the skimming body towards upstream. At the trailing edge the fluid velocity is positive, however as the critical time $\hat{t}_c$ is approached it gradually decreases to zero. This also corresponds to the trailing edge pressure $\hat{p}_2$ dropping to zero as dictated by the pressure jump condition (5.11) and illustrated in Fig. 5.5d. The vertical centre of mass position $\hat{Y}$ reaches its minimum at $\hat{t} \sim 0.9887$ shortly before the critical time $\hat{t}_c$, and starts to move upwards and thus is in the early stages of heading towards exiting the water just before the trailing edge pressure drops to zero at $\hat{t} = \hat{t}_c$. In the case of a positive plate rotation, the same behaviour is true except that it occurs at the leading edge. This suggests that the angular velocity of the plate has an important and immediate effect after impact, influencing the evolution of the wetted surface contact area on the plate and thus affecting the pressure lift force on the body. Once the critical time is reached a planing model is needed to describe the remaining stage of the skimming process for times $\hat{t}$ beyond $\hat{t}_c$.

Fig. 5.7a shows a snap-shot of the hydrodynamic pressure under a positively rotating body over time during the impact stage. A short time after impact the pressure is high and positive everywhere, reaching its peak at the leading edge and lowest value at the trailing edge as depicted at $\hat{t} = 0.0357$. As time progresses the wetted surface area grows, the pressure starts to decrease everywhere and eventually a negative pressure region develops near the trailing edge as shown at $\hat{t} = 0.6365$, notice there is an adverse pressure gradient field inside this negative pressure region. This negative pressure region expands over time and eventually reaches the trailing edge: corresponding to this phenomenon the trailing edge fluid velocity drops to zero as shown in Fig. 5.7b.

5.6 Planing stage

The transition from impact to planing stage is marked by the disappearance of the spray jet at the trailing edge. During the planing stage the body stops penetrating deeper into water as demonstrated in Fig. 5.5e and the wetted contact surface ceases to expand. As water from upstream comes in contact with the planing body, part of it is thrown back upstream at the leading edge, and the pressure and momentum jump conditions (5.10) are still applicable at this edge; the rest of the water flows underneath the body and enters the downstream area. Pressure analysis in Fig. 5.7a shows that a region with negative pressure gradient begins to develop near the trailing edge at the end of the impact stage; this phenomenon is consistent with the separation of a high-Reynolds-number incompressible flow passing a bluff body. For the case of a completely submersed body, the presence of a significant adverse pressure gradient field causes the flow to separate from the body, a behaviour which is well analysed using the triple-deck theory (see [41, 24, 14]) for the laminar or turbulent regime. For the planing case where the body is only partially submersed in water, experiments show that in the region of separation near the trailing edge there is a turbulent mixture of air and water. The separation

condition we impose at the trailing edge has significant effect on our model's planing dynamics, and we shall dedicate a significant part of this section to analyse the separation effects.

Under the assumption that the flow separates smoothly from the trailing end of the body with a laminar or turbulent boundary layer, where there is no presence of adverse pressure gradient of the sort we witnessed at the end of the impact stage, then we can impose the Brillouin-Villat (B.V.) pressure condition at this end such that:

$$p(x_2, t) = 0, \qquad \left.\frac{\partial p}{\partial x}\right|_{x=x_2} = 0. \tag{5.38}$$

As we shall see shortly, if the trailing edge pressure gradient imposed at the beginning of the planing stage differs from that observed at the end of impact stage, then a discontinuity of the trailing edge position ensues; under the B.V. condition which imposes a lower pressure gradient, this trailing edge position is more up upstream than that predicted by the Tuck & Dixon conditions. That is to say under the assumptions of smooth separation a discontinuity of the trailing edge position occurs when switching from impact to planing model.

An alternative set of boundary conditions can be imposed by allowing a weak adverse pressure gradient at the end of impact stage. One can speculate that the separation at the trailing edge is perhaps usually turbulent and a weak adverse pressure gradient also exists during the planing stage in the trailing separation region. Such adverse pressure gradient say κ (or $\kappa(t)$ as a function of time) can only be determined via appropriate boundary layer analysis and is beyond the scope of this thesis; a more detailed discussion can be found in [14]. Thus under the assumptions of turbulent separation the trailing boundary conditions can be stated as:

$$p(x_2, t) = 0, \qquad \left.\frac{\partial p}{\partial x}\right|_{x=x_2} = \kappa. \tag{5.39}$$

It can be said that the B.V. conditions of (5.38) are a special case of $\kappa = 0$,

and we shall therefore base our analysis on the separation conditions (5.39) for generality.

The governing equations for the fluid flow and the planing body then are very similar to those of the impact model, the differences being that: 1) in our planing model the time t starts at $t = t^*$, where t^* is the time at the end of impact stage; and 2) at the trailing edge the momentum and pressure jump conditions are replaced by the separation conditions of (5.39). The planing model is then written as follows:

$$\frac{\partial u}{\partial t} + u\frac{\partial u}{\partial x} = -\frac{\partial p}{\partial x}, \qquad (x \in [x_1(t), x_2(t)]), \tag{5.40a}$$

$$\frac{\partial u}{\partial t} + u\frac{\partial u}{\partial x} = 0, \qquad (x \notin [x_1(t), x_2(t)]), \tag{5.40b}$$

$$\frac{\partial h}{\partial t} + \frac{\partial (uh)}{\partial x} = 0, \tag{5.40c}$$

$$h(x,t) = Y_m(t) + x\theta(t) - T(x), \qquad (x \in [x_1(t), x_2(t)]), \tag{5.40d}$$

$$T(x) = Ax^2 + Bx + C, \qquad (A < 0), \tag{5.40e}$$

$$\int_{x_1}^{x_2} p(x,t)dx = M\frac{d^2 Y_m}{dt^2}, \tag{5.40f}$$

$$\int_{x_1}^{x_2} xp(x,t)dx = I\frac{d^2\theta}{dt^2}, \tag{5.40g}$$

with the following boundary conditions at the leading and trailing edges:

$$p(x_1,t) + \frac{1}{2}\left(u(x_1,t) - \frac{dx_1}{dt}\right)^2 = \frac{1}{2}\left(1 - \frac{dx_1}{dt}\right)^2, \tag{5.41a}$$

$$\left(u(x_1,t) - \frac{dx_1}{dt}\right) \Big/ \left(1 - \frac{dx_1}{dt}\right) = 2h(x_1,t)^{-\frac{1}{2}} - 1, \tag{5.41b}$$

$$p(x_2,t) = 0, \tag{5.41c}$$

$$\left.\frac{\partial p}{\partial x}\right|_{x=x_2} = \kappa, \tag{5.41d}$$

where time $t \geq t^*$ so that this model is a continuation in time of the impact model. The unknowns of the equations are Y_m, θ, u, p with κ being a free parameter subject to the condition $\kappa \geq 0$, i.e. maintaining an adverse pressure gradient at the trailing edge. We shall not pursue a direct numerical solution

of this planing model in this thesis but interested readers may refer to the work by [73], where a numerical algorithm is derived to solve this planing problem under the B.V. trailing edge separation condition (5.38). Instead we shall carry on from the impact stage analysis of section 5.5 and investigate the planing behaviour under the assumption of turbulent separation.

5.6.1 Linearised planing model

We continue to work under the asymptotic settings laid out in section 5.5, specifically that the bluff body is able to transition from the impact to the planing stage inside a short time regime such that $t \sim O(\delta)$ with $\delta \ll 1$. The necessary condition for such rapid transition to occur is that the body mass is small ($M \sim O(\delta^{\frac{3}{2}})$) and has a positive angular rotation. Substituting the asymptotic expansions (5.4) into the planing model (5.40) and simplifying gives the following linearised planing model at leading order:

$$\frac{\partial \hat{p}}{\partial \hat{x}} + \frac{\partial \hat{u}}{\partial \hat{t}} = 0, \qquad (\hat{x} \in [\hat{x}_1, \hat{x}_2]) \tag{5.42a}$$

$$\frac{\partial \hat{h}}{\partial \hat{t}} + \frac{\partial \hat{u}}{\partial \hat{x}} = 0, \qquad (\hat{x} \in [\hat{x}_1, \hat{x}_2]) \tag{5.42b}$$

$$\hat{h} = \hat{Y} + \hat{x}\hat{\theta} - A\hat{x}^2, \qquad (\hat{x} \in [\hat{x}_1, \hat{x}_2]) \tag{5.42c}$$

$$M\frac{d^2\hat{Y}}{d\hat{t}^2} = \int_{\hat{x}_1}^{\hat{x}_2} \hat{p} d\hat{x}, \tag{5.42d}$$

$$\frac{d^2\hat{\theta}}{d\hat{t}^2} = 0, \tag{5.42e}$$

with the following boundary conditions at the leading and trailing edges:

$$\hat{p}_1 = \frac{d\hat{x}_1}{d\hat{t}}\hat{u}_1, \tag{5.43a}$$

$$\hat{u}_1 = \frac{d\hat{x}_1}{d\hat{t}}\hat{h}_1, \tag{5.43b}$$

$$\hat{p}_2 = 0, \tag{5.43c}$$

$$\left.\frac{\partial \hat{p}}{\partial \hat{x}}\right|_{\hat{x}=\hat{x}_2} = \hat{\kappa}. \tag{5.43d}$$

Here $\hat{\kappa} = \delta^{\frac{1}{2}}\kappa$ according to the small time scalings of (5.4). Therefore for $\hat{\kappa} \sim O(1)$ the actual pressure gradient at the trailing edge is relatively large.

The linearised planing model can be further simplified by eliminating $\hat{p}_1$, $\hat{h}$, $\hat{u}$ and taking advantage of the fact that $\hat{\theta} = \hat{\omega}_0\hat{t}$ to obtain the following relations:

$$\left[6M + (\hat{x}_1 - \hat{x}_2)^3\right]\frac{d^2\hat{Y}}{d\hat{t}^2} + 3\hat{\kappa}(\hat{x}_1 - \hat{x}_2)^2 = 0, \tag{5.44a}$$

$$\frac{1}{2}(\hat{x}_1 - \hat{x}_2)^2\frac{d^2\hat{Y}}{d\hat{t}^2} + (A\hat{x}_1^2 - \hat{\omega}_0\hat{t}\hat{x}_1 - \hat{Y})\left(\frac{d\hat{x}_1}{d\hat{t}}\right)^2 + \hat{\kappa}(\hat{x}_1 - \hat{x}_2) = 0, \tag{5.44b}$$

$$\begin{aligned}(\hat{x}_1 - \hat{x}_2)\frac{d^2\hat{Y}}{d\hat{t}^2} - (A\hat{x}_1^2 - \hat{\omega}_0\hat{t}\hat{x}_1 - \hat{Y})\frac{d^2\hat{x}_1}{d\hat{t}^2} - (2A\hat{x}_1 - \hat{\omega}_0\hat{t})\left(\frac{d\hat{x}_1}{d\hat{t}}\right)^2 \\ + 2\left(\hat{\omega}_0\hat{x}_1 + \frac{d\hat{Y}}{d\hat{t}}\right)\frac{d\hat{x}_1}{d\hat{t}} + \hat{\kappa} = 0.\end{aligned} \tag{5.44c}$$

Note that analysis from Section 5.5 shows that only a skimming body with positive angular rotation can transition to the planing stage inside the small time regime, and we therefore shall deal exclusively with the case of $\hat{\omega}_0 > 0$ hereafter in this linearised planing regime.

The pressure gradient $\hat{\kappa}$ is a parameter whose value needs to be prescribed subject to physical constraints. Under the B.V. condition such that $\hat{\kappa} = 0$, the planing model (5.44) has two alternative implications: the first is that $\frac{d^2\hat{Y}}{d\hat{t}^2} = 0$ and $\frac{d\hat{x}_1}{d\hat{t}} = 0$; i.e. the body has a constant vertical velocity and its leading edge position is fixed during the entire planing phase; the position of the trailing edge is a function of time and can only be determined based on higher order physics which shall be discussed in Section 5.7. The second alternative implies that the distance between the leading and trailing edges is fixed, and it yields

the following relations:

$$\hat{x}_2 = \hat{x}_1 + (6M)^{\frac{1}{3}}, \tag{5.45a}$$

$$(6M)^{\frac{2}{3}} \frac{d^2\hat{Y}}{d\hat{t}^2} + 2\big(A\hat{x}_1^2 - \hat{\omega}_0\hat{t}\hat{x}_1 - \hat{Y}\big)\big(\frac{d\hat{x}_1}{d\hat{t}}\big)^2 = 0, \tag{5.45b}$$

$$(6M)^{\frac{1}{3}} \frac{d^2\hat{Y}}{d\hat{t}^2} + \big(A\hat{x}_1^2 - \hat{\omega}_0\hat{t}\hat{x}_1 - \hat{Y}\big)\frac{d^2\hat{x}_1}{d\hat{t}^2} + \big(2A\hat{x}_1 - \hat{\omega}_0\hat{t}\big)\big(\frac{d\hat{x}_1}{d\hat{t}}\big)^2 - 2\big(\frac{d\hat{Y}}{d\hat{t}} + \hat{\omega}_0\hat{x}_1\big)\frac{d\hat{x}_1}{d\hat{t}} = 0. \tag{5.45c}$$

The leading edge position $\hat{x}_1$ is continuous when transitioning from impact to the planing stage, the trailing edge position $\hat{x}_2$ however "jumps" to the position of $\hat{x}_1 + (6M)^{\frac{1}{3}}$, and the heavier the object is the further apart the leading and trailing edges are. This discontinuity of the trailing edge is also observed by [73] when the B.V. condition is employed at the trailing edge.

Fig. 5.8 shows the numerical solutions of the planing system (5.44) for varying values of $\hat{\kappa}$ in the range between zero and 0.5076, the latter of which is the adverse trailing edge pressure gradient estimated from the end of the impact stage for $M = 1$ and $\hat{\omega}_0 = 1$. The trailing edge position is only discontinuous for $\hat{\kappa} = 0$. For small values of $\hat{\kappa}$ as illustrated in the case of $\hat{\kappa} = 0.1$, $\hat{x}_2$ converges to $\hat{x}_1 + (6M)^{\frac{1}{3}}$ in equation (5.45a). This convergent behaviour will be discussed in further detail in the analysis of small adverse pressure gradient in Section 5.7.

If on the other hand the imposed adverse pressure gradient is higher than that observed at the end of the impact stage, i.e. $\hat{\kappa} > 0.5076$, the trailing edge position immediately stops its retraction towards the leading edge as witnessed at the end of the impact stage and begins to extend towards the downstream area, as demonstrated in Fig. 5.9 for time $\hat{t} <\sim 1.6$. The question of how large an adverse pressure gradient can be sustained in the trailing separation region in our planing model, and how the planing body behaves accordingly is an intriguing and complex question, which shall be discussed in more detail in the next section.

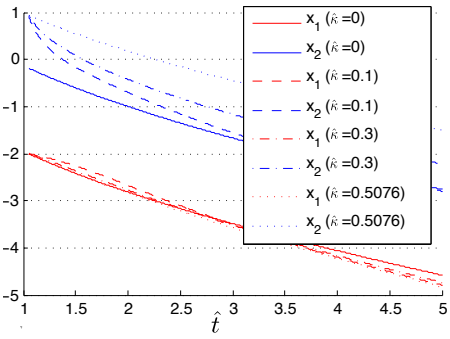

(a) The evolution of the plate's leading and trailing edges during the planing stage.

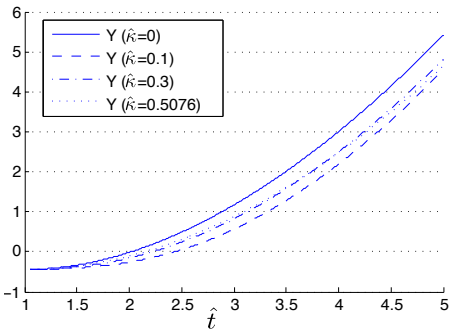

(b) The evolution of the plate's vertical centre of mass position during planing.

Figure 5.8: Plot of the leading and trailing edges, as well as the plate's vertical centre of mass during the planing stage for varying values of trailing edge pressure gradient $\hat{\kappa}$. The body's mass M and rotational velocity $\hat{\omega}_0$ are both taken to be one. For the case of $\hat{\kappa} = 0$ the trailing edge position $\hat{x}_2$ is not continuous when transition from impact to planing stage.

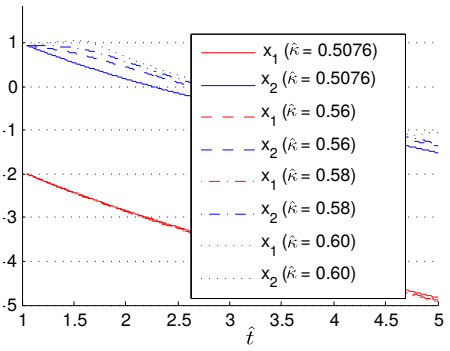

(a) The evolution of the plate's leading and trailing edges during the planing stage for varying values of $\hat{\kappa}$.

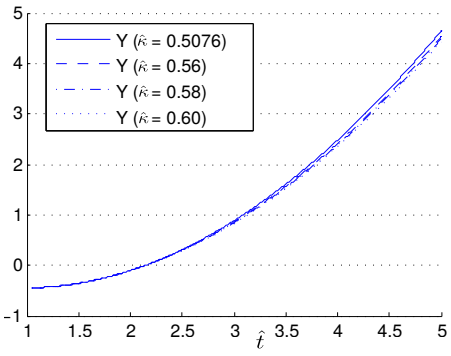

(b) The evolution of the plate's vertical centre of mass position during planing for varying values of $\hat{\kappa}$.

Figure 5.9: Plot of the leading and trailing edges, as well as the plate's vertical centre of mass during the planing stage for varying values of trailing edge pressure gradient greater than observed at the end of impact stage: $\hat{\kappa} > 0.5076$. We can observe that the trailing edge position begins to retract towards the leading edge for $\hat{t} <\sim 1.6$. The body's mass M and rotational velocity $\hat{\omega}_0$ are both taken to be one.

5.6.2 Maximum sustainable adverse pressure gradient at the trailing edge

For a large-Reynolds-number flow past a bluff body, the presence of a region with large adverse pressure gradient on the body is typically associated with turbulent flow separation. The flow separation from a semi-submerged bluff planing body where there is a mixture of air and fluid in its trailing separation region is less studied. Numerical solutions to our planing model (5.44) for varying values of $\hat{\kappa}$ presented in Fig. 5.10 demonstrate an unexpected behaviour of the trailing edge. We shall dedicate this section to investigate the maximum adverse pressure gradient $\hat{\kappa}$ that can be sustained in our model's trailing separation region, and the effects it has on our planing body's behaviour.

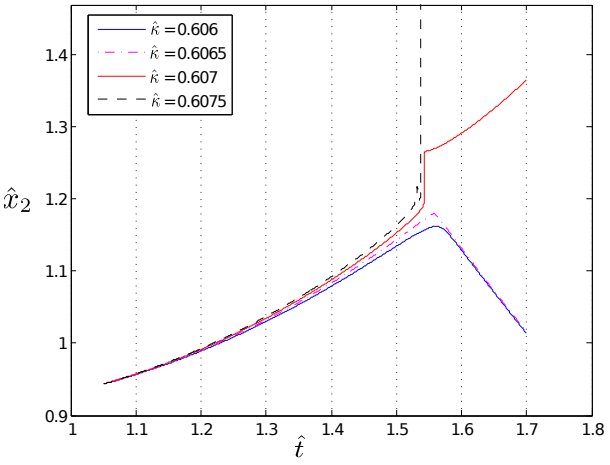

Figure 5.10: The unstable behaviour of trailing edge position $\hat{x}_2$ for values of trailing edge pressure gradient $\hat{\kappa}$ exceeding an unknown upper limit.

We shall work with model equations (5.44a) and (5.44b) and write them in the following form:

$$(6M - \hat{\xi}^3)\frac{d^2\hat{Y}}{d\hat{t}^2} + 3\hat{\kappa}\hat{\xi}^2 = 0, \tag{5.46a}$$

$$\frac{1}{2}\hat{\xi}^2\frac{d^2\hat{Y}}{d\hat{t}^2} - \hat{\kappa}\hat{\xi} + \hat{\eta} = 0, \tag{5.46b}$$

where $\hat{\xi}$ and $\hat{\eta}$ are given as

$$\hat{\xi} = \hat{x}_2 - \hat{x}_1, \tag{5.47a}$$

$$\hat{\eta} = (A\hat{x}_1^2 - \hat{\omega}_0 \hat{t}\hat{x}_1 - \hat{Y})(\frac{d\hat{x}_1}{d\hat{t}})^2, \tag{5.47b}$$

note that $\hat{\xi} > 0$ and $\hat{\eta} < 0$. We can eliminate $\frac{d^2\hat{Y}}{d\hat{t}^2}$ by combining the model equations (5.46) to obtain the following polynomial in $\hat{\xi}$:

$$\frac{1}{2}\hat{\xi}^4 + 6M\hat{\xi} = \hat{\alpha}(6M - \hat{\xi}^3), \tag{5.48}$$

where $\hat{\alpha}$ is given as

$$\hat{\alpha} = \hat{\eta}/\hat{\kappa}, \tag{5.49}$$

and we notice that $\hat{\alpha} < 0$. The left and right hand sides of this equation, denoted as f_L and f_R for convenience, are quartic and cubic functions of $\hat{\xi}$ respectively, i.e.

$$f_L(\hat{\xi}) = \frac{1}{2}\hat{\xi}^4 + 6M\hat{\xi}, \tag{5.50a}$$

$$f_R(\hat{\xi}) = \hat{\alpha}(6M - \hat{\xi}^3). \tag{5.50b}$$

The curve of f_L intersects with that of f_R in the $(\hat{\xi}, f)$ plane for sufficiently small values of $\hat{\alpha}$ ($\hat{\alpha} < 0$). Notice these two curves only intersect in the first quadrant as $\hat{\xi}$, f_R and f_L are strictly non-negative; see Fig. 5.11 for depiction. There is a critical value $\hat{\alpha}_D$ such that these two curves share the same gradient at the point of intersection, and if $\hat{\alpha}$ exceeds the limit $\hat{\alpha}_D$ the two curves do not intersect. This critical value $\hat{\alpha}_D = \hat{\eta}_D/\hat{\kappa}_D$ gives rise to $\hat{\kappa}_D$, which is the maximum adverse pressure gradient that can be sustained at the trailing edge; exceeding this limit the trailing edge position becomes unreachable and our planing model breaks down. To determine $\hat{\xi}_D$ and $\hat{\alpha}_D$ we therefore first differentiate (5.48) with

respect to $\hat{\xi}$ to obtain

$$2\hat{\xi}^3 + 6M = -3\hat{\alpha}\hat{\xi}^2; \tag{5.51}$$

combining the two equations (5.48), (5.51) and simplifying gives the following equation for $\hat{\xi}_D$

$$\hat{\xi}_D^6 - 48M\hat{\xi}_D^3 - 72M^2 = 0, \tag{5.52}$$

for which we can immediately write down its solution:

$$\hat{\xi}_D = [(24 + 18\sqrt{2})M]^{\frac{1}{3}}. \tag{5.53}$$

This corresponds to the maximum distance between $\hat{x}_1$ and $\hat{x}_2$ that can be sustained by our planing model. Notice this limit is dependent on the body mass only and intuitively the heavier the planing body, the wider apart the leading and trailing edges are. From $\hat{\xi}_D$ and (5.51) we obtain the solution for $\hat{\alpha}_D$:

$$\hat{\alpha}_D = -\frac{\sqrt{2}}{2}\left[(24 + 18\sqrt{2})M\right]^{\frac{1}{3}}. \tag{5.54}$$

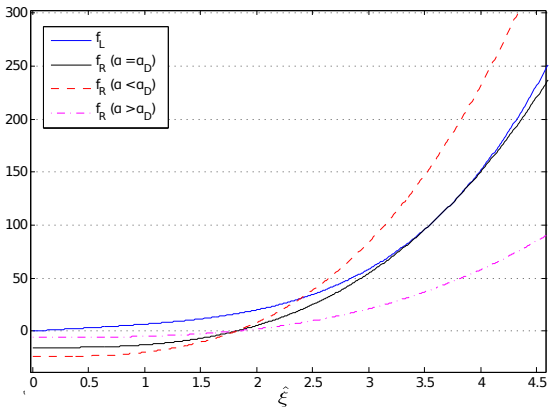

Figure 5.11: A plot of $f_L(\hat{\xi})$ and $f_R(\hat{\xi})$ with respect to $\hat{\xi}$ for various values of $\hat{\alpha}$. Notice that there exists a limit value $\hat{\alpha} = \hat{\alpha}_D$ such that the two curves intersect on the $(\hat{\xi}, f)$ plane with the same gradient. Any values of $\hat{\alpha}$ greater than this limit the curves no longer intersect and our planing model yields no solution.

Having established $\hat{\xi}_D$ and $\hat{\alpha}_D$, the unstable behaviour of the trailing edge solution indicated in Fig. 5.10 can be investigated by seeking the following asymptotic expansions:

$$\hat{t} = \hat{t}_D + \epsilon\bar{t}, \tag{5.55a}$$

$$\hat{\kappa} = \hat{\kappa}_D + \epsilon^2\bar{\kappa}, \tag{5.55b}$$

$$\hat{\xi} = \hat{\xi}_D + \epsilon\bar{\xi}(\bar{t}) + \epsilon^2\bar{\bar{\xi}}(\bar{t}), \tag{5.55c}$$

$$\hat{\eta} = \hat{\eta}_D + \epsilon\bar{\eta}(\bar{t}) + \epsilon^2\bar{\bar{\eta}}(\bar{t}), \tag{5.55d}$$

with $\epsilon \ll 1$. Substituting into the model equations of (5.51) gives the following relations at the leading orders:

$$O(1): \quad \frac{1}{2}\hat{\xi}_D^4 + 6M\hat{\xi}_D - \frac{\hat{\eta}_D}{\hat{\kappa}_D}(6M - \hat{\xi}_D^3) = 0, \tag{5.56a}$$

$$O(\epsilon): \quad 2\hat{\xi}_D^3\bar{\xi} + 6M\bar{\xi} + 3\frac{\hat{\eta}_D}{\hat{\kappa}_D}\hat{\xi}_D^2\bar{\xi} = \frac{\bar{\eta}}{\hat{\kappa}_D}(6M - \hat{\xi}_D^3), \tag{5.56b}$$

$$\begin{aligned} O(\epsilon^2): \quad & 2\hat{\xi}_D^3\bar{\bar{\xi}} + 6M\bar{\bar{\xi}} + 3\frac{\hat{\eta}_D}{\hat{\kappa}_D}\hat{\xi}_D^2\bar{\bar{\xi}} + 3\frac{\bar{\eta}}{\hat{\kappa}_D}\hat{\xi}_D^2\bar{\xi} + 3(\hat{\kappa}_D\hat{\xi}_D^2 + \hat{\eta}_D\hat{\xi}_D)\bar{\xi}^2 \\ & - (6M - \hat{\xi}_D^3)\bar{\bar{\eta}} + (\frac{1}{2}\hat{\xi}_D^4 + 6M\hat{\xi}_D)\bar{\kappa} = 0. \end{aligned} \tag{5.56c}$$

The right-hand-side of (5.56b) is zero by (5.51), we therefore can immediately deduce that $\bar{\eta} = 0$. Subsequently from equation (5.56c) we obtain the following relation for $\bar{\xi}$:

$$\bar{\xi} = -\sqrt{-\frac{\hat{\xi}_D}{\hat{\kappa}_D}\left[\bar{\bar{\eta}} + \bar{\kappa}\frac{2\hat{\xi}_D^3 + 6M}{3\hat{\xi}_D^2}\right]}. \tag{5.57}$$

To see how $\bar{\xi}$ evolves with time we perform Taylor expansion of $\hat{\eta}$ at $\hat{t} = \hat{t}_D$

$$\hat{\eta} = \hat{\eta}_D + \epsilon\bar{t}\hat{\eta}'(\hat{t}_D) + \frac{1}{2}\epsilon^2\bar{t}^2\hat{\eta}''(\hat{t}_D); \tag{5.58}$$

matching this with the expansion in (5.55d) it is evident that

$$\bar{\eta} = \bar{t}\hat{\eta}'(\hat{t}_D) = 0, \tag{5.59a}$$

$$\bar{\bar{\eta}} = \frac{1}{2}\bar{t}^2\hat{\eta}''(\hat{t}_D), \tag{5.59b}$$

and $\bar{\xi}$ can be written as

$$\bar{\xi} = -\sqrt{-\frac{\hat{\xi}_D}{\hat{\kappa}_D}\left[\frac{1}{2}\bar{t}^2\hat{\eta}''(\hat{t}_D) + \bar{\kappa}\frac{2\hat{\xi}_D^3 + 6M}{3\hat{\xi}_D^2}\right]}. \tag{5.60}$$

The solution of $\bar{\xi}$ behaves differently depending on the sign of $\bar{\kappa}$. For the case of negative $\bar{\kappa}$ which corresponds to $\hat{\kappa}$ less than $\hat{\kappa}_D$, $\bar{\xi}$ is well defined and has a maximum at $\bar{t} = 0$, i.e. $\hat{t} = \hat{t}_D$; this can be seen in Fig. 5.12. For the case of positive $\bar{\kappa}$ which corresponds to $\hat{\kappa}$ exceeding the value of $\hat{\kappa}_D$ however, the solution of $\bar{\xi}$ grows to zero quickly and becomes imaginary before $\bar{t}$ reaches zero; this essentially corresponds to $\hat{\xi}$ rapidly reaching the limit of $\hat{\xi}_D$ given in (5.53) and becoming undefined from then on. The solution for $\bar{\kappa} = 0$ i.e. $\hat{\kappa} = \hat{\kappa}_D$, acts as a separatrix of the two aforementioned solution behaviours and $\hat{\xi}$ reaches the limit of $\hat{\xi}_D$ at time $\hat{t}_D$; it subsequently decreases below $\hat{\xi}_D$ as time goes beyond $\hat{t}_D$. The solution for $\bar{\xi}$ thus explains the unstable behaviour of $\hat{x}_2$ shown in Fig. 5.10. Fig. 5.13 demonstrates that $\hat{\eta}'$ is positive and decreases to zero as time grows to $\hat{t}_D$.

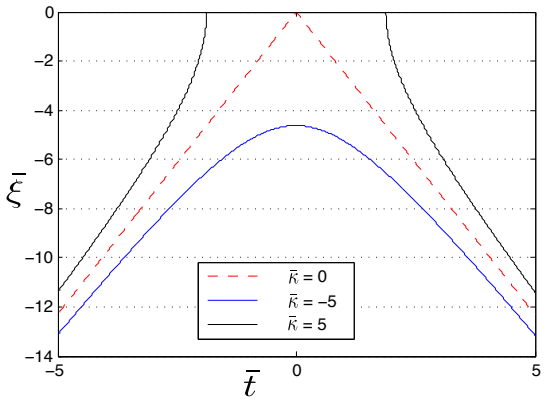

Figure 5.12: Solution to $\bar{\xi}$ in (5.57) with $\bar{\kappa}$ taking values of $-5, 0, 5$. The solution of $\bar{\xi}$ is well defined for $\bar{\kappa} = -5$; for $\bar{\kappa} = 5$, $\bar{\xi}$ grows rapidly and becomes imaginary before $\bar{t}$ reaches zero; solution of $\bar{\xi}$ for $\bar{\kappa} = 0$ acts as a separatrix for the two distinct behaviours.

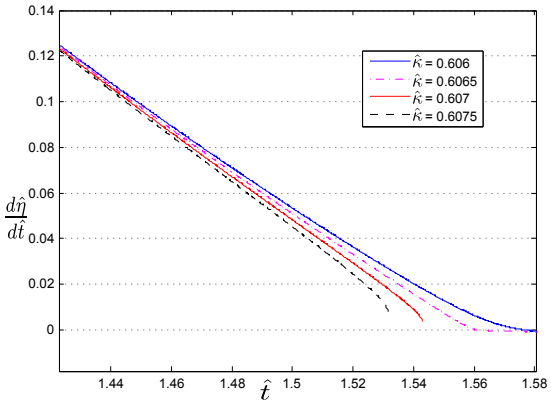

Figure 5.13: Solutions of $\hat{\eta}' = \frac{d\hat{\eta}}{d\hat{t}}$ over time for different values of $\hat{\kappa}$. Notice that $\hat{\eta}'$ is initially positive and decreases over time. It eventually reaches zero at time $\hat{t}_D$. Note that the actual value of $\hat{t}_D$ varies depends on the value of $\hat{\kappa}$ as demonstrated in the figure.

5.7 Small adverse pressure gradient at trailing edge

The previous section The numerical solutions for $\hat{\xi}$ indicate that for $\hat{\kappa}$ sufficiently small, the planing system converges in time to a state such that the leading and trailing edges travel at a fixed distance of $(6M)^{\frac{1}{3}}$ from each other. The trailing edge in particular goes through a phase of rapid adjustment in a short time span. We show that for a planing body subject to small adverse pressure gradient at the trailing separation region, i.e. $\hat{\kappa} \ll 1$, its planing motion can be divided into three consecutive phases.

The first phase of the planing stage begins at the instant when the body completes its impact stage and enters the planing stage. The leading edge during this phase continues to move further upstream, and it does so on a scale of $\hat{\kappa}^{\frac{1}{2}}$. The trailing edge in the meantime evolves on a larger scale of order unity. At the end of the initial planing phase the distance between the two edges becomes $(6M)^{\frac{1}{3}}$, and the time at which this occurs is $\hat{t} = -\frac{\hat{x}_{c1}^2+\hat{Y}_c}{\hat{V}_c+\hat{\omega}_0\hat{x}_{c1}}$. Thus at the end of the initial phase the planing system configured with a small trailing edge adverse pressure gradient converges to that of B.V. configuration. During the second planing stage the system evolves on a time scale of $\hat{\kappa}^{\frac{1}{4}}$, the evolution of the trailing edge slows down from order unity to the same order as the leading edge but with a small adjustment $(O(\hat{\kappa}^{\frac{3}{4}}))$. As time progresses the

planing system eventually exceeds the $O(\hat{\kappa}^{\frac{1}{4}})$ regime and transitions to the final large time scale planing phase. During this phase the leading edge evolves on a scale of order unity and the trailing edge evolves in sync with the leading edge but with a $(O(\hat{\kappa}))$ adjustment.

5.7.1 Initial planing phase

This phase begins when the body transitions from impact to planing stage. Suppose the time when this transition occurs is $\hat{t}_c$, then we are concerned with time $\hat{t} \geq \hat{t}_c$. We let $\hat{\xi}$ denote the horizontal distance between the leading and trailing edges as usual: $\hat{\xi} = \hat{x}_2 - \hat{x}_1$ and $\hat{\xi}$ is strictly non-negative. Let $\hat{x}_{c1}$, $\hat{Y}_c$ and $\hat{V}_c$ denote the horizontal position of the leading edge, vertical position of the centre of mass and vertical velocity respectively at time $\hat{t}_c$. Suppose that the trailing edge pressure gradient $\hat{\kappa}$ is positive but small such that $0 < \hat{\kappa} \ll 1$, then we try the following variable asymptotic expansions:

$$\hat{x}_1 = \hat{x}_{c1} + \hat{\kappa}^{\frac{1}{2}}\check{x}_1(\hat{t}) + O(\hat{\kappa}), \tag{5.61a}$$

$$\hat{\xi} = \check{\xi}_1(\hat{t}) + O(\hat{\kappa}^{\frac{1}{2}}), \tag{5.61b}$$

$$\hat{Y} = \hat{Y}_c + \hat{V}_c\hat{t} + \hat{\kappa}\check{Y}_1(\hat{t}) + O(\hat{\kappa}^2). \tag{5.61c}$$

Substituting these variables into the planing system (5.44) gives the following relations at the leading order:

$$(\hat{x}_{c1}^2 + \hat{Y}_c + \hat{V}_c\hat{t} + \hat{\omega}_0\hat{x}_{c1}\hat{t})\frac{d^2\check{x}_1}{d\hat{t}^2} + 2(\hat{\omega}_0\hat{x}_{c1} + \hat{V}_c)\frac{d\check{x}_1}{d\hat{t}} = 0, \tag{5.62a}$$

$$\frac{1}{2}\check{\xi}_1^2\frac{d^2\check{Y}_1}{d\hat{t}^2} - (\hat{x}_{c1}^2 + \hat{Y}_c + \hat{V}_c\hat{t} + \hat{\omega}_0\hat{x}_{c1}\hat{t})\left(\frac{d\check{x}_1}{d\hat{t}}\right)^2 - \check{\xi}_1 = 0, \tag{5.62b}$$

$$[6M - \check{\xi}_1^3]\frac{d^2\check{Y}_1}{d\hat{t}^2} + 3\check{\xi}_1^2 = 0. \tag{5.62c}$$

This is a system of differential algebraic equations of index 1 and can be re-arranged into the following equivalent form:

$$\frac{d}{d\hat{t}}\left[\zeta^2\frac{d\check{x}_1}{d\hat{t}}\right] = 0, \tag{5.63a}$$

$$\check{\xi}_1^4 + 2\zeta(6M - \check{\xi}_1^3)\left(\frac{d\check{x}_1}{d\hat{t}}\right)^2 + 12M\check{\xi}_1 = 0, \tag{5.63b}$$

$$[6M - \check{\xi}_1^3]\frac{d^2\check{Y}_1}{dt^2} + 3\check{\xi}_1^2 = 0, \tag{5.63c}$$

where $(5.63a)$ is a re-write of $(5.62a)$ in a general Sturm-Liouville form, and the function $\zeta(\hat{t})$ is given as

$$\zeta(\hat{t}) = \hat{x}_{c1}^2 + \hat{Y}_c + (\hat{V}_c + \hat{\omega}_0\hat{x}_{c1})\hat{t}. \tag{5.64}$$

To solve this system of equations we require Cauchy conditions for $\check{x}_1$, $\check{Y}_1$ at the beginning of the planing stage $\hat{t} = \hat{t}_c$. At this time the values of $\hat{x}_{c1}$, $\hat{x}_{c2}$, $\hat{Y}_c$ and $\hat{V}_c$ are known and can be obtained as solutions from the end of the impact stage. Let $\check{Y}_{10}$ and $\check{V}_{10}$ be the initial value and initial first order derivative for $\check{Y}_1$ respectively, from the skimming body's known vertical dynamics at this point we can deduce the following:

$$\check{Y}_{10} \equiv \check{Y}_1\Big|_{\hat{t}=\hat{t}_c} = 0, \qquad \check{V}_{10} \equiv \frac{d\check{Y}_1}{d\hat{t}}\Big|_{\hat{t}=\hat{t}_c} = 0. \tag{5.65}$$

Let $\check{x}_{10}$ and $\check{u}_{10}$ be the initial value and initial first order derivative for $\check{x}_1$ respectively, then $\check{x}_{10}$ is zero by the implications of (5.61a) at time $\hat{t} = \hat{t}_c$. We may be inclined to obtain its initial derivative $\check{u}_{10}$ by taking the leading edge's horizontal velocity from the end of impact stage, whose value is say $\hat{u}_{c1}$ and deduce that $\check{u}_{10} = \hat{\kappa}^{-\frac{1}{2}}\hat{u}_{c1}$ by (5.61a). However setting its initial condition this way is not consistent with the planing model (5.62), to see this we combine the two equations (5.63b, 5.63c) and set $\hat{t} = \hat{t}_c$ to obtain:

$$\frac{3\check{\xi}_{10}^4}{2\check{\xi}_{10}^3 - 12M} - \zeta_0\check{u}_{10}^2 - \check{\xi}_{10} = 0,$$

here $\check{\xi}_{10} = \check{\xi}_1(\hat{t}_c)$, $\zeta_0 = \zeta(\hat{t}_c)$ and $\check{u}_{10} = \check{u}(\hat{t}_c)$. This gives us an initial condition for $\check{u}_{10}$ that is consistent for the planing model:

$$\check{u}_{10} = -\left[\frac{\check{\xi}_{10}^4 + 12M\check{\xi}_{10}}{2\zeta_0(\check{\xi}_{10}^3 - 6M)}\right]^{\frac{1}{2}}. \tag{5.66}$$

Therefore when transitioning from the impact to the planing stage the leading edge's velocity is discontinuous, and the suitable Cauchy conditions for $\check{x}_1$ are:

$$\check{x}_{10} = 0, \qquad \check{u}_{10} = -\left[\frac{\check{\xi}_{10}^4 + 12M\check{\xi}_{10}}{2\zeta_0(\check{\xi}_{10}^3 - 6M)}\right]^{\frac{1}{2}}, \tag{5.67}$$

and we can write down the solution for $\check{x}_1$ from (5.63a):

$$\check{x}_1(\hat{t}) = \Phi_0(1 - \zeta_0\zeta^{-1}), \tag{5.68}$$

where Φ_0 is defined as

$$\Phi_0 = -\frac{\zeta_0}{\hat{V}_c + \hat{\omega}_0\hat{x}_{c1}}\left[\frac{\check{\xi}_{10}^4 + 12M\check{\xi}_{10}}{2\zeta_0(\check{\xi}_{10}^3 - 6M)}\right]^{\frac{1}{2}}, \tag{5.69}$$

this explicit solution for $\check{x}_1$ enables us to write down the following quartic equation of $\check{\xi}_1$ from (5.63b):

$$\zeta^3\check{\xi}_1^4 - 2\Phi_0^2\check{\xi}_1^3 + 12M\zeta^3\check{\xi}_1 + 12M\Phi_0^2 = 0. \tag{5.70}$$

The formula for finding roots of quartic equations are well known and will not be present here explicitly. Out of the four possible solutions for $\check{\xi}_1$ the admissible one should be real, positive and fits the physical context of the system. From (5.63c) we can obtain the solution for $\check{Y}_1$ in a double integral form based on the admissible solution of $\check{\xi}_1$ and initial conditions (5.65):

$$\check{Y}_1 = \iint_{\hat{t}_c}^{\hat{t}} \frac{3\check{\xi}_1^2}{\check{\xi}_1^3 - 6M} d\hat{t}^2. \tag{5.71}$$

The solutions for $\check{x}_1$, $\check{\xi}_1$ and $\check{Y}_1$ are presented in Fig. 5.14. The results

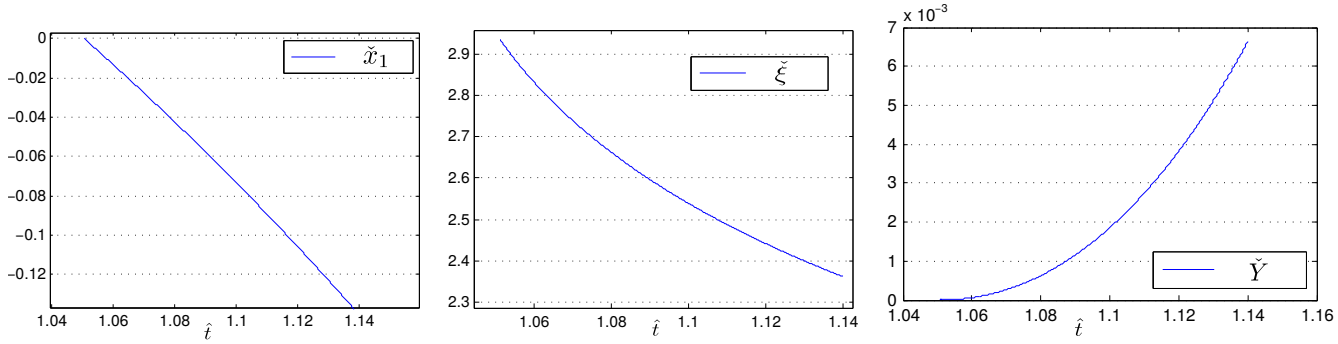

(a) $\check{x}_1$ (b) $\check{\xi}_1$ (c) $\check{Y}_1$.

Figure 5.14: Solutions of the planing system (5.63) with $M = 1$, $\hat{\omega}_0 = 1$, $\hat{\kappa} = 0.1$. The values of $\hat{x}_{c1}$, $\hat{x}_{c2}$, $\hat{Y}_c$ and $\hat{V}_c$ are the results from the final stage of impact model (5.35), their respective values are: -1.9944, 0.9434, -0.4431 and 0.0359.

demonstrate that for a planing body with positive rotation, its leading edge position continues to extend in the direction of upstream as with the impact stage case. The trailing edge position on the other hand also begins to move in the direction of upstream, and it moves at a greater pace compared with that of the leading edge as demonstrated by the decreasing value of $\check{\xi}_1$ in Fig. 5.14b; this signifies that the contact surface between the water and planing starts to decrease. During this phase the planing body continues to emerge from water as shown in Fig. 5.14c.

5.7.2 Planing Phase II

The solution of $\check{x}_1$ given in (5.68) depends inversely on $\zeta(\hat{t})$, and the value of ζ in (5.64) is positive at time $\hat{t}_c$ but decreases as time progresses, see Fig. 5.15. When ζ eventually reaches zero $\check{x}_1$ becomes singular and undefined. We let $\hat{t}_N$ be the time when this singularity occurs, from the definition of ζ in (5.64) $\hat{t}_N$ can be determined as:

$$\hat{t}_N = -\frac{\hat{x}_{c1}^2 + \hat{Y}_c}{\hat{V}_c + \hat{\omega}_0 \hat{x}_{c1}}. \tag{5.72}$$

At this point $\check{\xi}_1$, the horizontal distance between the two wetted edges takes the value of $(6M)^{\frac{1}{3}}$, this can be seen by setting $\zeta(\hat{t}_N) = 0$ in equation (5.70). Thus

at the end of phase I we arrive at the same solution as that given by the B.V. condition, and the time it takes to reach this solution is determined by the state of the system at the end of the impact stage as shown in (5.72). At the end of phase I the planing system no longer evolves on the scales described in (5.61) and we therefore need to seek a new evolution scale for the next planing phase. To determine the appropriate asymptotic scale for the next planing phase, we

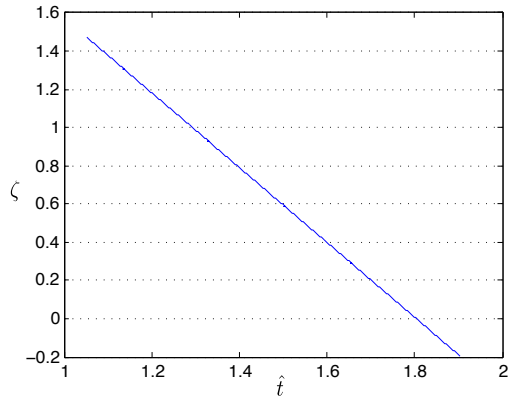

Figure 5.15: Solutions of $\zeta(\hat{t})$ during the planing phase. The values of $\hat{x}_{c1}$, $\hat{Y}_c$ and $\hat{V}_c$ are -1.9944, -0.4431 and 0.0359 respectively. $\zeta(\hat{t}_c)$ is positive; as time increases this eventually decreases to zero, at which point the solution for $\breve{x}_1$ becomes undefined.

examine the time close to $\hat{t}_N$ such that $\hat{t} = \hat{t}_N + \delta_1 \bar{t}$ with $\delta_1 \ll 1$ and $\bar{t}$ being order unity. The solution for $\breve{x}_1$ can be re-written as:

$$\breve{x}_1 = \Phi_0 \left[1 - \frac{\zeta_0}{\delta_1 \bar{t} (\hat{V}_c + \hat{\omega}_0 \hat{x}_{c1})} \right]. \tag{5.73}$$

This suggests that the leading edge position $\breve{x}_1$ at the end of phase I can be scaled as $\breve{x}_1 \sim \delta_1^{-1} \bar{x}_1(\bar{t})$ with $\bar{x}_1(\bar{t})$ being order unity. As $\breve{\xi}_1$ converges to $(6M)^{\frac{1}{3}}$ we can write $\breve{\xi}_1 \sim (6M)^{\frac{1}{3}} - \delta_2 \bar{\xi}_1$ with $\delta_2 \ll 1$ and $\bar{\xi}_1$ being order unity. Substituting this into equations (5.62b, 5.62c) and simplifying yields the following relation:

$$\bar{\xi}_1 = -\frac{\delta_1^3}{\delta_2} \Psi_0 \bar{t}^3, \tag{5.74}$$

which implies $\delta_2 = \delta_1^3$, and Ψ_0 is given as:

$$\Psi_0 = \frac{(6M)^{\frac{2}{3}} (\hat{V}_c + \hat{\omega}_0 \hat{x}_{c1})}{2\zeta_0^2 \Phi_0^2}. \tag{5.75}$$

From $\bar{\xi}_1$ we can obtain the following leading order relation for $\check{Y}_1$ based on the planing body's vertical momentum equation (5.62c):

$$\frac{1}{\delta_1^2}\frac{d^2\check{Y}_1}{d\bar{t}^2} = \frac{1}{\delta_1^3\Psi_0\bar{t}^3},$$

therefore

$$\check{Y}_1 = \frac{1}{2\delta_1\Psi_0\bar{t}} + Y_A\bar{t} + Y_B, \tag{5.76}$$

with Y_A and Y_B being integration constants. Hence towards the end of the phase I we can scale our planing system as follows:

$$\check{x}_1 = \delta_1^{-1}\bar{x}_1, \tag{5.77a}$$

$$\check{\xi}_1 = (6M)^{\frac{1}{3}} - \delta_1^3\bar{\xi}_1, \tag{5.77b}$$

$$\check{Y}_1 = \delta_1^{-1}\bar{Y}_1. \tag{5.77c}$$

To assess how δ_1 relates with the trailing edge pressure gradient $\hat{\kappa}$, we try setting $\delta_1 = \hat{\kappa}^m$ with m being a positive unknown. Combining expansions (5.61) and (5.77) gives the following variable expansions:

$$\hat{x}_1 = \hat{x}_{c1} + \hat{\kappa}^{\frac{1}{2}-m}\bar{x}_1, \tag{5.78a}$$

$$\hat{\xi} = (6M)^{\frac{1}{3}} - \hat{\kappa}^{3m}\bar{\xi}_1, \tag{5.78b}$$

$$\hat{Y}_1 = \hat{Y}_c + \hat{V}_c\hat{t}_N + \hat{\kappa}^m\hat{V}_c\bar{t} + \hat{\kappa}^{1-m}\bar{Y}_1. \tag{5.78c}$$

Substituting these variables into the planing system (5.44) gives the following leading order relations:

$$\bar{\xi}_1 \ddot{\bar{Y}}_1 + 1 = 0, \tag{5.79a}$$

$$\frac{1}{2}(6M)^{\frac{2}{3}} \ddot{\bar{Y}}_1 \hat{\kappa}^{1-3m} - \left[(2\hat{x}_{c1} + \hat{\omega}_0 \hat{t}_N)\bar{x}_1 \hat{\kappa}^{\frac{3}{2}-5m} + (\hat{\omega}_0 \hat{x}_{c1} + \hat{V}_c)\bar{t}\hat{\kappa}^{1-3m}\right]\dot{\bar{x}}_1^2 = 0, \tag{5.79b}$$

$$\left[(2\hat{x}_{c1} + \hat{\omega}_0 \hat{t}_N)\bar{x}_1 \hat{\kappa}^{1-4m} + (\hat{\omega}_0 \hat{x}_{c1} + \hat{V}_c)\bar{t}\hat{\kappa}^{\frac{1}{2}-2m}\right]\ddot{\bar{x}}_1 + \hat{\kappa}^{1-4m}(2\hat{x}_{c1} + \hat{\omega}_0 \hat{t}_N)\dot{\bar{x}}_1^2 + 2\hat{\kappa}^{\frac{1}{2}-2m}(\hat{\omega}_0 \hat{x}_{c1} + \hat{V}_c)\dot{\bar{x}}_1 = 0. \tag{5.79c}$$

Balancing the powers of $\hat{\kappa}$ for each term in all the equations implies $m = \frac{1}{4}$, and (5.78a) becomes:

$$\hat{t} = \hat{t}_N + \hat{\kappa}^{\frac{1}{4}} \bar{t}, \tag{5.80a}$$

$$\hat{x}_1 = \hat{x}_{c1} + \hat{\kappa}^{\frac{1}{4}} \bar{x}_1, \tag{5.80b}$$

$$\hat{\xi} = (6M)^{\frac{1}{3}} - \hat{\kappa}^{\frac{3}{4}} \bar{\xi}_1, \tag{5.80c}$$

$$\hat{Y}_1 = \hat{Y}_c + \hat{V}_c \hat{t}_N + \hat{\kappa}^{\frac{1}{4}} \hat{V}_c \bar{t} + \hat{\kappa}^{\frac{3}{4}} \bar{Y}_1. \tag{5.80d}$$

Therefore in the next phase of the planing stage, the planing body's leading edge and centre of mass moves on a larger scale of $\hat{\kappa}^{\frac{1}{4}}$, while the trailing edge moves on a scale comparable to that of the leading edge but with an $O(\hat{\kappa}^{\frac{3}{4}})$ adjustment. This is in contrast to the initial planing phase during which the trailing edge transitions on a much larger time scale when compared with the leading edge. Substituting these asymptotic expansions of the variables into the governing equations (5.79) and simplifying gives:

$$\bar{\xi}_1 \ddot{\bar{Y}}_1 + 1 = 0, \tag{5.81a}$$

$$\frac{1}{2}(6M)^{\frac{2}{3}} \ddot{\bar{Y}}_1 - \left[(2\hat{x}_{c1} + \hat{\omega}_0 \hat{t}_N)\bar{x}_1 + (\hat{\omega}_0 \hat{x}_{c1} + \hat{V}_c)\bar{t}\right]\dot{\bar{x}}_1^2 = 0, \tag{5.81b}$$

$$\left[(2\hat{x}_{c1} + \hat{\omega}_0 \hat{t}_N)\bar{x}_1 + (\hat{\omega}_0 \hat{x}_{c1} + \hat{V}_c)\bar{t}\right]\ddot{\bar{x}}_1 + (2\hat{x}_{c1} + \hat{\omega}_0 \hat{t}_N)\dot{\bar{x}}_1^2 + 2(\hat{\omega}_0 \hat{x}_{c1} + \hat{V}_c)\dot{\bar{x}}_1 = 0. \tag{5.81c}$$

This system can be solved explicitly via method of matched asymptotic expansions. To do so we first notice that (5.81c) is a second order nonlinear ODE for $\bar{x}_1$ alone and can be re-arranged to the following form:

$$(2\hat{x}_{c1} + \hat{\omega}_0\hat{t}_N)(\bar{x}_1\dot{\bar{x}}_1)' + (\hat{\omega}_0\hat{x}_{c1} + \hat{V}_c)(\bar{t}\bar{x}_1)'' = 0, \tag{5.82}$$

where dot and prime both denote differentiation with respective to time $\bar{t}$. Integrating this twice gives the following expression for $\bar{x}_1$:

$$\frac{1}{2}(2\hat{x}_{c1} + \hat{\omega}_0\hat{t}_N)\bar{x}_1^2 + (\hat{\omega}_0\hat{x}_{c1} + \hat{V}_c)\bar{t}\bar{x}_1 - C_1\bar{t} - C_2 = 0, \tag{5.83}$$

where C_1 and C_2 are constants of integration, which remains to be determined. Since the leading edge's horizontal position is negative under our coordinate system, we can write down the negative root of this equation:

$$\bar{x}_1 = \frac{\sqrt{(\hat{\omega}_0\hat{x}_{c1} + \hat{V}_c)^2\bar{t}^2 + 2(2\hat{x}_{c1} + \hat{\omega}_0\hat{t}_N)(C_1\bar{t} + C_2)} - (\hat{\omega}_0\hat{x}_{c1} + \hat{V}_c)\bar{t}}{2\hat{x}_{c1} + \hat{\omega}_0\hat{t}_N}. \tag{5.84}$$

The unknown constants in this solution can be determined by matching $\bar{x}_1$ with $\check{x}_1$ by Van Dyke's matching principle. For the purpose of matching we shall refer to the solution (5.68) for $\check{x}_1$ as the "outer" solution, and (5.84) for $\bar{x}_1$ as the "inner" solution. The leading two terms expansion of the inner solution (5.84) with $\bar{t} \ll 0$ are:

$$\bar{x}_1 \sim \frac{C_1}{(\hat{\omega}_0\hat{x}_{c1} + \hat{V}_c)} + \frac{C_2}{(\hat{\omega}_0\hat{x}_{c1} + \hat{V}_c)\bar{t}} + O(\frac{1}{\bar{t}^2}).$$

Based on the scaling of (5.77a) we match these terms with the outer solution as:

$$\frac{C_1}{(\hat{\omega}_0\hat{x}_{c1} + \hat{V}_c)} = \delta_1\Phi_0 \approx 0,$$
$$\frac{C_2}{(\hat{\omega}_0\hat{x}_{c1} + \hat{V}_c)\bar{t}} = -\frac{\Phi_0\zeta_0}{(\hat{\omega}_0\hat{x}_{c1} + \hat{V}_c)\bar{t}},$$

we can therefore obtain the following solutions to the integration constants:

$$C_1 = 0, \qquad C_2 = -\Phi_0\zeta_0; \tag{5.86}$$

and the full solution for $\bar{x}_1$ becomes:

$$\bar{x}_1 = \frac{\sqrt{(\hat{\omega}_0\hat{x}_{c1} + \hat{V}_c)^2\bar{t}^2 - 2(2\hat{x}_{c1} + \hat{\omega}_0\hat{t}_N)\Phi_0\zeta_0} - (\hat{\omega}_0\hat{x}_{c1} + \hat{V}_c)\bar{t}}{2\hat{x}_{c1} + \hat{\omega}_0\hat{t}_N}. \tag{5.87}$$

Having solved $\bar{x}_1$ we can subsequently solve $\bar{Y}_1$ by substituting (5.87) into the governing equation (5.81b) and integrating with respect to time twice:

$$\bar{Y}_1 = \frac{2}{3}\frac{[(\hat{\omega}_0\hat{x}_{c1} + \hat{V}_c)^2\bar{t}^2 - 2\Phi_0\zeta_0(2\hat{x}_{c1} + \hat{\omega}_0\hat{t}_N)]^{\frac{3}{2}} - (\hat{\omega}_0\hat{x}_{c1} + \hat{V}_c)^3\bar{t}^3}{(6M)^{\frac{2}{3}}(2\hat{x}_{c1} + \hat{\omega}_0\hat{t}_N)^2} + C_3\bar{t} + C_4, \tag{5.88}$$

where C_3 and C_4 are constants of integration. The leading order expansions for $\bar{Y}_1$ are:

$$\bar{Y}_1 \sim \frac{\Phi_0^2\zeta_0^2}{2(6M)^{\frac{2}{3}}(\hat{\omega}_0\hat{x}_{c1} + \hat{V}_c)\bar{t}} + \left[C_3 - \frac{2\Phi_0\zeta_0(\hat{\omega}_0\hat{x}_{c1} + \hat{V}_c)}{(6M)^{\frac{2}{3}}(2\hat{x}_{c1} + \hat{\omega}_0\hat{t}_N)}\right]\bar{t} + C_4 + O(\bar{t}^{-3}). \tag{5.89}$$

Similarly applying Van Dyke's principle, matching this "inner" solution with "outer" solution of $\check{Y}_1$ expressed in the inner variable $\bar{t}$ yields:

$$\begin{aligned}
&\frac{1}{2\Psi_0} \equiv \frac{\Phi_0^2\zeta_0^2}{(6M)^{\frac{2}{3}}(\hat{\omega}_0\hat{x}_{c1} + \hat{V}_c)\bar{t}}, \\
&\left[C_3 - \frac{2\Phi_0\zeta_0(\hat{\omega}_0\hat{x}_{c1} + \hat{V}_c)}{(6M)^{\frac{2}{3}}(2\hat{x}_{c1} + \hat{\omega}_0\hat{t}_N)}\right]\bar{t} = \delta_1 Y_A\bar{t} \approx 0, \\
&C_4 = \delta_1 Y_B \approx 0;
\end{aligned}$$

therefore the two integration constants are given as

$$C_3 = \frac{2\Phi_0\zeta_0(\hat{\omega}_0\hat{x}_{c1} + \hat{V}_c)}{(6M)^{\frac{2}{3}}(2\hat{x}_{c1} + \hat{\omega}_0\hat{t}_N)}, \qquad C_4 = 0. \tag{5.91}$$

Hence we have obtained the solution for $\bar{Y}_1$ as:

$$\bar{Y}_1 = \frac{2}{3}\frac{[(\hat{\omega}_0\hat{x}_{c1}+\hat{V}_c)^2\bar{t}^2 - 2\Phi_0\zeta_0(2\hat{x}_{c1}+\hat{\omega}_0\hat{t}_N)]^{\frac{3}{2}} - (\hat{\omega}_0\hat{x}_{c1}+\hat{V}_c)^3\bar{t}^3}{(6M)^{\frac{2}{3}}(2\hat{x}_{c1}+\hat{\omega}_0\hat{t}_N)^2} + \frac{2\Phi_0\zeta_0(\hat{\omega}_0\hat{x}_{c1}+\hat{V}_c)\bar{t}}{(6M)^{\frac{2}{3}}(2\hat{x}_{c1}+\hat{\omega}_0\hat{t}_N)}. \tag{5.92}$$

Finally $\bar{\xi}_1$ can be solved by substituting the solution of $\bar{Y}_1$ into the planing equation (5.81a) and obtain:

$$\bar{\xi}_1 = -\frac{(6M)^{\frac{2}{3}}(2\hat{x}_{c1}+\hat{\omega}_0\hat{t}_N)^2\left[(\hat{\omega}_0\hat{x}_{c1}+\hat{V}_c)^2\bar{t}^2 - 2\Phi_0\zeta_0(2\hat{x}_{c1}+\hat{\omega}_0\hat{t}_N)\right]^{\frac{1}{2}}}{2(\hat{\omega}_0\hat{x}_{c1}+\hat{V}_c)^2\left[\left[(\hat{\omega}_0\hat{x}_{c1}+\hat{V}_c)^2\bar{t}^2 - 2\Phi_0\zeta_0(2\hat{x}_{c1}+\hat{\omega}_0\hat{t}_N)\right]^{\frac{1}{2}} - (\hat{\omega}_0\hat{x}_{c1}+\hat{V}_c)\bar{t}\right]^2}. \tag{5.93}$$

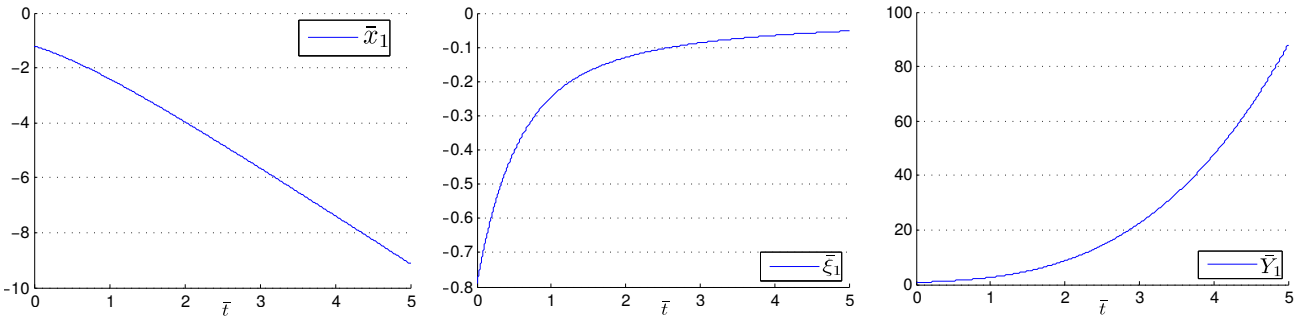

(a) $\bar{x}_1$ (b) $\bar{\xi}_1$ (c) $\bar{Y}_1$.

Figure 5.16: Plots of $\bar{x}_1$, $\bar{\xi}_1$ and $\bar{Y}_1$ over time $\bar{t} \in [0, 5]$. The values of $\hat{x}_{c1}$, $\hat{x}_{c2}$, $\hat{Y}_c$ and $\hat{V}_c$ are the results from the final stage of impact model (5.35), their respective values are: -1.9944, 0.9434, -0.4431 and 0.0359.

The solutions demonstrated in Fig. 5.16 indicates that leading and trailing edge positions in this phase continue to move in the direction of upstream. The pace at which the body moves emerges from the water significantly increases. It becomes evident that as time progresses our planing system will grow out of the $O(\hat{\kappa}^{\frac{1}{4}})$ regime, which will lead to the final large time phase of our planing system.

5.7.3 Planing Phase III

During phase II the solution for $\bar{Y}$ evolves at cubic power of time $\bar{t}$; as time increases it eventually grows out of the $O(\hat{\kappa}^{\frac{3}{4}})$ regime and moves onto the next phase of the planing stage. To identify the appropriate scaling of this next phase we can introduce a new time variable $\breve{t}$ such that $\breve{t} = \hat{\kappa}^n \bar{t}$, with $0 < n < 1$ so that $\hat{\kappa}^n$ is small, i.e. $\hat{\kappa}^n \ll 1$. Based on this new time scaling we can derive the following appropriate variables scalings for this new phase from on phase II solutions:

$$\breve{t} = \hat{\kappa}^n \bar{t},$$
$$\breve{x}_1 = \hat{\kappa}^n \bar{x}_1,$$
$$\breve{\xi}_1 = \hat{\kappa}^{-n} \bar{\xi}_1,$$
$$\breve{Y}_1 = \hat{\kappa}^{3n} \bar{Y}_1.$$

Based on these scalings and the phase II variables expansions in (5.80) we are able to write down the relations of our phase III variables with the linearised planing variables as:

$$\hat{t} = \hat{t}_N + \hat{\kappa}^{\frac{1}{4}-n} \breve{t},$$
$$\hat{x}_1 = \hat{x}_{c1} + \hat{\kappa}^{\frac{1}{4}-n} \breve{x}_1,$$
$$\hat{\xi}_1 = (6M)^{\frac{1}{3}} - \hat{\kappa}^{\frac{3}{4}+n} \breve{\xi}_1,$$
$$\hat{Y}_1 = \hat{Y}_c + \hat{V}_c(\hat{t}_N + \hat{\kappa}^{\frac{1}{4}-n} \breve{t}) + \hat{\kappa}^{\frac{3}{4}-3n} \breve{Y}_1.$$

To determine the unknown we substitute the above expansions into the linearised planing system (5.44), balancing the powers of $\hat{\kappa}$ for each term gives $n = \frac{1}{4}$. This suggests the phase III planing system evolves on the same scale as the linearised planing system, and the small trailing edge pressure gradient has negligible effect during this phase. We can therefore approximate the linearised

planing variables in terms of the phase III variables as:

$$\hat{t} = \breve{t}, \tag{5.96a}$$

$$\hat{x}_1 = \breve{x}_1, \tag{5.96b}$$

$$\hat{\xi}_1 = (6M)^{\frac{1}{3}} - \hat{\kappa}\breve{\xi}_1, \tag{5.96c}$$

$$\hat{Y}_1 = \breve{Y}_1. \tag{5.96d}$$

Substituting the above variable expansions into the the planing system of (5.44) gives the following planing system for phase III:

$$\breve{\xi}_1 \ddot{\breve{Y}}_1 + 1 = 0, \tag{5.97a}$$

$$\frac{1}{2}(6M)^{\frac{2}{3}}\ddot{\breve{Y}}_1 - (\breve{x}_1^2 + \hat{\omega}_0\breve{t}\breve{x}_1 + \breve{Y}_1)(\dot{\breve{x}}_1)^2 = 0, \tag{5.97b}$$

$$(6M)^{\frac{1}{3}}\ddot{\breve{Y}}_1 - (\breve{x}_1^2 + \hat{\omega}_0\breve{t}\breve{x}_1 + \breve{Y}_1)\ddot{\breve{x}}_1 - (2\breve{x}_1 + \hat{\omega}_0\breve{t})(\dot{\breve{x}}_1)^2 - 2(\hat{\omega}_0\breve{x}_1 + \dot{\breve{Y}}_1)\dot{\breve{x}}_1 = 0. \tag{5.97c}$$

It is difficult to obtain explicit solutions to this coupled non-linear ODE system, numerical solutions are therefore pursued and the results are presented in Fig. 5.17. Comparisons with the solutions of the planing system (5.44) show that the phase III planing system is able to capture the planing body's behaviour at large times well.

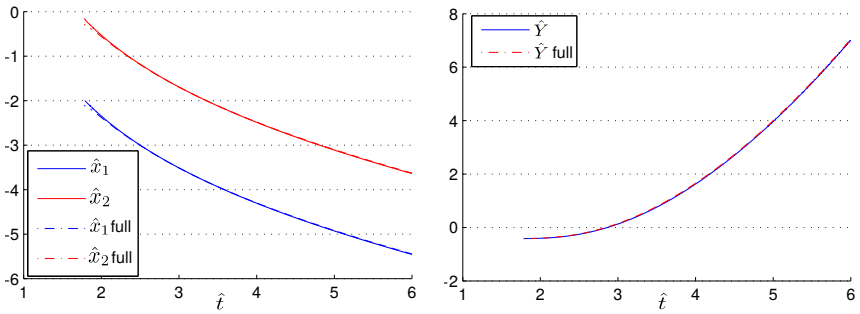

(a) Comparison of numerical solutions for $\hat{x}_1$, $\hat{x}_2$.

(b) Comparison of numerical solutions for $\hat{Y}$.

Figure 5.17: Numerical solutions of the planing system (5.97) compared with the full planing system (5.44) for $\hat{t} > \hat{t}_N$ and $\hat{\kappa} = 10^{-4}$.

The solutions indicate that during this phase the planing body continues to emerge from water; the leading and trailing edges continue to move in the direction of the upstream, with the distance between the two edges fixed at $(6M)^{\frac{1}{3}}$ at the leading order.

In order to see the behaviour of the system at large times, i.e. as $\breve{t} \to \infty$, we introduce the following scaled large time variables:

$$\tilde{t} = \delta \breve{t}, \tag{5.98a}$$

$$\tilde{x}_1 = \delta \breve{x}_1, \tag{5.98b}$$

$$\tilde{\xi} = \breve{\xi}, \tag{5.98c}$$

$$\tilde{Y} = \delta^2 \breve{Y}, \tag{5.98d}$$

where $\delta \ll 1$ and the tilde sign is used to denote large time variables, these variables are all of order unity. Upon substituting the above variables into the phase III planing system we obtain the following system at the leading order:

$$\tilde{\xi}_1 \ddot{\tilde{Y}}_1 + 1 = 0, \tag{5.99a}$$

$$(\tilde{x}_1^2 + \hat{\omega}_0 \tilde{t} \tilde{x}_1 + \tilde{Y}) \dot{\tilde{x}}_1^2 = 0, \tag{5.99b}$$

$$(\tilde{x}_1^2 + \hat{\omega}_0 \tilde{t} \tilde{x}_1 + \tilde{Y}) \ddot{\tilde{x}}_1 + (2\tilde{x}_1 + \hat{\omega}_0 \tilde{t}) \dot{\tilde{x}}_1^2 + 2(\hat{\omega}_0 \tilde{x}_1 + \dot{\tilde{Y}}) \dot{\tilde{x}}_1 = 0. \tag{5.99c}$$

The solution to the system can be written down explicitly with the initial conditions that $\tilde{x}_1(0) = 0$ and $\tilde{Y}(0) = 0$:

$$\tilde{x}_1 = -\frac{1}{2} \hat{\omega}_0 \tilde{t}, \tag{5.100a}$$

$$\tilde{\xi} = -\frac{2}{\hat{\omega}_0^2}, \tag{5.100b}$$

$$\tilde{Y} = \frac{1}{4} \hat{\omega}_0^2 \tilde{t}^2. \tag{5.100c}$$

If we are able to see the planing body lifting off and separating from water, the positions of the leading and trailing edges should eventually coincide as shown by [73] in the numerical solutions of the full planing system (5.40). This is

clearly not the case in our linearised planing model as the large time solutions above demonstrate. Under our linearised planing regime the body will continue to lift upwards as time grows but the distance between the two wetted edges does not decrease. As the body evolves vertically to the squared power of time it will eventually grow out of our linearised regime defined in (5.4), as which point we will need to revert to the full planing system to capture the motion of the planing body.

5.8 Conclusion

In this chapter we investigated the skimming problem of bluff body on shallow water. The skimming process is divided into two consecutive stages: an impact and a planing stage. The impact stage begins from the moment the bluff body touches down on water from air and ends when the trailing edge stops extending towards downstream. If and when this phenomenon occurs the body then transitions to a planing stage.

During the impact stage we demonstrate, in a short time-frame just after touch-down, the body's wetted leading and trailing edges evolve to the square root of time; as time grows their speeds begin to decrease and the two edges eventually evolve linearly with time. On the vertical scale the body penetrates further into water after touching down, this continues until shortly before the end of the impact stage, when the fluid-body contact area grows sufficiently large and the hydrodynamic pressure begins to lift the body upwards. A region of positive (adverse) pressure gradient starts to develop near the trailing edge underneath the body towards the end of the impact stage; this areas grows larger over time and eventually reaches the trailing edge, at which point the trailing edge stops extending towards downstream and impact stage terminates. We find that a body with sufficiently small body mass and a positive rotation, it is able to transition rapidly from the impact to the planing stage.

The value of the adverse pressure gradient at the trailing edge plays a critical

role during the planing stage: there is a maximum adverse pressure gradient that can be sustained at this trailing edge. This upper limit is dependent on, amongst other things - the body's mass, leading edge's position and velocity, as well as the vertical position of the body's centre of mass. Exceeding this adverse pressure gradient limit the flow separation at the trailing edge becomes too turbulent and our linearised planing model breaks down; the body otherwise is able to sustain the planing motion, during which both its leading and trailing edges move in the direction of upstream, and the centre of mass moves upwards during this stage in a process of lifting-off from water.

If on the other hand the adverse pressure gradient is very small and close to being zero, we find that the body's planing motion can be further divided into three phases. In the first phase the trailing edge position goes through a rapid transition towards the upstream direction; in a predetermined time-frame the trailing edge is able to "catch-up" with the leading edge and decrease the horizontal distance between the two edges to a value that is proportional to the body's mass. In the second phase the leading and trailing edges at the leading order move in the direction of upstream linearly with time, the body's vertical position however evolves to the cubic power of time and grows out of this regime in a short period of time. In phase III, the leading and trailing edges continue to evolve linearly with time at the leading order, while the vertical position of the planing body's centre of mass evolves to the squared power of time. We find that under our linearised planing regime we are not able to witness the phenomenon of a planing body achieving complete lifting-off and separation from water, to do so we must wait until the body grows out of our linearised regime to the full planing regime.

The investigation of impact and planing on water brings about another interesting topic - under which circumstances a planing body is not able to obtain sufficient hydrodynamic lift and thus sinks into water. This is the topic we shall investigate in Chapter 6.

Chapter 6

Flooding and sinking of an originally skimming body

6.1 Introduction

The skimming problem of a thin flat plate over shallow water was investigated in Chapter 2. We analysed the physical conditions under which the skimming body is able to obtain sufficient lift and achieve lift-off. One of the assumptions of such a model is that the water's free surface is in contact only with the lower-section (the underneath) of the body, while its upper-section is in contact with air.

The aim of this chapter then, is to investigate the effects of "flooding" over a body in skimming motion. Such a phenomenon occurs frequently in the natural world as well as in the field of engineering. Take surfing, a popular recreational activity for example; observations and surfing experience would tell us that it is very common for a surfboard to be at least partially immersed under water during surfing. Indeed a surfboard at rest while carrying the weight of an adult surfer is typically below water (see Fig. 6.1a), and it is only with speed generated by a wave from its back that the board is able to surf at the ocean's

free surface (Fig. 6.1b). Stone skipping by the seaside is another popular pastime activity. Depending on the surface conditions a stone would penetrate into waves/tides and experience flooding over its entire body. With regard to industrial applications, a ship sailing through rough seas experiences water flooding over the top of its deck, see Fig. 6.1c) - 6.1d) for relevant illustrations. Needless to say then, understanding such interactions between fluid, solid body and air has a wide range of applications.

The modelling of fluid flow past a solid object is well studied and plays an important role in the likes of aeronautical and fluid mechanical engineering [17, 32, 23]. A common set-up for such problems is a body completely immersed in fluid, with the flow often assumed to be steady, see [45] for such a class of problems. Closer to our concerns, [30] investigated a flow past successive multi-blades. A stream-wise pressure jump feature in a localised Euler region at each blade's leading edge is deployed, and the pressure and streamline profiles of the flows are obtained inside the viscous boundary layer around the blade as well as in the flow's wake. [28] analysed flow between two solid walls past a blade with a variable thickness and camber, the blade being free to move in the channel and bounce and clash with the solid boundary walls. [16] studied a flow past a tethered blade. The blade's body is fixed about a pivot point but is free to rotate so that its angle of attack goes through an unsteady evolution with the flow. The entire blade is again assumed to be immersed in water at all times.

We shall concentrate our effort for the rest of the chapter on modelling the flooding phenomenon over a surfboard in skimming (surfing) motion. A surfboard designed for an adult typically has a length of around 2 meters, depth of 0.06 meter and width of 0.5 meter when measured from its widest part. Such a board is usually made of polyurethane and polystyrene forms and weights around 3 kg. When the board is "pushed" by an ocean wave travelling at a sufficiently large speed, it is able to surf at the wave's speed while carrying the weight of a surfer. Ocean waves are often created by winds blowing over the water's surface; the earth's rotation and planetary gravitational effects creates

tidal waves; other natural phenomena such as under-ocean earth-quakes often lead to tsunamis. The typical speed of a wind wave and a tidal wave often exceed 20 km/h, increasing to much higher speeds in the case of hurricanes. Table 6.1 lists some characteristic ocean wind wave speeds under various conditions.

Table 6.1: Ocean wind wave speeds

Wind Speed	**Wave Height**	**Wave Speed**
19 km/h	0.3 m	10.2 km/h
37 km/h	1.5 m	21.4 km/h
56 km/h	4.1 m	32.0 km/h
74 km/h	8.5 m	42.9 km/h
92 km/h	14.8 m	53.4 km/h

Concerning the flow around a surfboard in motion, viscosity and surface tension typically play negligible roles. When a surfboard is pushed into motion by a wave from the rear, the board emerges from water as it gains speed and embarks on a skimming process close to the free surface. Depending on the control by the surfer and flow conditions, the board may again from time to time become completely or partially submerged in water. Since the board travels at a faster speed than the water ahead of it, the board separates the oncoming fluid into two separate streams: one flows above the board and one below, and the depth of the stream above the board compared with that below is usually small. In the study that follows, we shall assume the fluid is incompressible and irrotational. Our analysis will also be restricted to two dimensions, which means our analysis will not be able to account for any lateral flow component around the board. It is worth noting however, a surfboard typically makes relatively small contact angles with the free surface, and under such conditions the lateral flow component is small and accounts for less than 30% of the overall flow past the

body (see [21]).

Our aim is to gain intuitive and analytical insights into the skimming dynamics of a surfboard under flooding conditions. To limit the computational complexity we shall restrict analysis to shallow water, that is to say the depth of the flow is small when compared with the length of the board. In practice this implies that the board is surfing close to shore. We shall analyse the flow both over and below the board, for both partial and complete flooding over the body's upper surface. In particular, we will investigate the conditions under which a skimming board is able to obtain sufficient (or insufficient) lift for it to maintain its skimming motion.

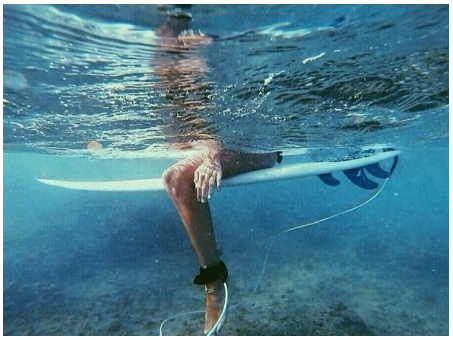

(a) Surfboard at rest.

(b) Surfboard in motion.

(c) Ship in rough sea.

(d) Ship in rough sea.

Figure 6.1: Illustrations of flooding over various types of body in skimming motion. From top left clock-wise: a) a surfboard carrying the weight of an adult surfer at rest, notice that the board's equilibrium position is below the free surface; b) a surfboard gets pushed into motion by an ocean wave from its rear, and the board's rear section is flooded by water; c) a ship sails through rough sea and a wave breaks over its bow, the water floods over the deck from the front; d) a ship sails through rough sea with wave flooding over its deck from the side.

6.2 Sinking model development

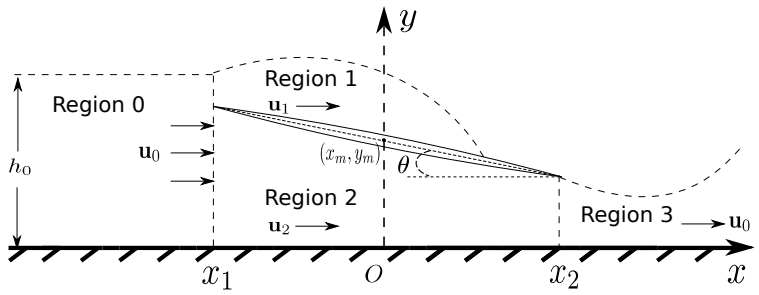

(a) Partial flooding over the body.

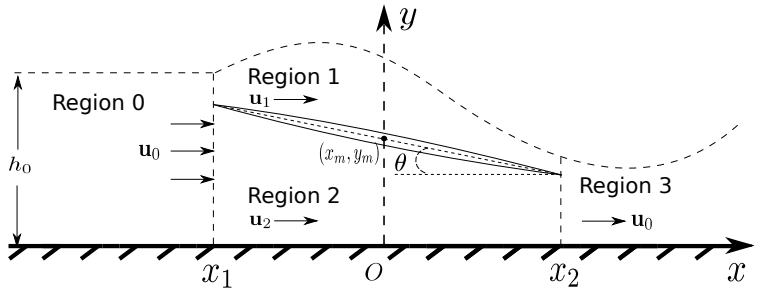

(b) Complete flooding over the body.

Figure 6.2: Sketch of a flat body with negligible thickness immersed in shallow water. The body under consideration travels leftwards while the water is at rest. The Cartesian coordinate system is introduced such that the x axis rests at the flow bed pointing rightwards, and the y axis points upwards and goes through the body's centre of mass. Therefore under this frame of reference the horizontal position of the body's centre of mass is fixed, and the fluid flows from the left to the right of the graph. We let θ denote the angle made between the flat body and the flat flow bed; the body may rotate with an angular velocity of ω.

We begin by simplifying the surfboard problem to a 2D model of a thin body skimming at an angle on a shallow layer of water, with the water flowing both over and below the body. The flow under concern here can be separated into four regions, see Fig. 6.2 for depiction and necessary nomenclature. We conduct our analysis in a frame travelling with the thin body, such that in this frame of reference the horizontal position of the body is fixed and the water flows from left to the right of the frame, with the body free to move vertically as well as rotate about its center of mass $(0, y_m)$.

Let $\bar{\mathbf{u}} = (\bar{u}, \bar{v})$ denote the flow velocity; except in the thin boundary layers we expect $\bar{u} \gg \bar{v}$ everywhere. In the far upstream and downstream regions the undisturbed flow velocity is given by $\bar{\mathbf{u}}_0 = (\bar{u}_0, 0)$. Supposing the body's length is $\bar{L}$, we can non-dimensionalise our model system as:

$$x = \frac{\bar{x}}{\bar{L}}, \;\; y = \frac{\bar{y}}{\bar{L}}, \;\; h = \frac{\bar{h}}{\bar{L}}, \;\; t = \frac{\bar{u}_0 \bar{t}}{\bar{L}}, \;\; u = \frac{\bar{u}}{\bar{u}_0}, \;\; v = \frac{\bar{v}}{\bar{u}_0}, \;\; p = \frac{\bar{p}}{\bar{\rho}\bar{u}_0^2}. \tag{6.1}$$

Here the bar sign is used to denote dimensional variables, and $\bar{p}$, $\bar{\rho}$ are used to denote pressure and water density respectively.

The non-dimensionalised Navier-Stokes equations in 2D can be thus written down in the following form:

$$\frac{\partial \mathbf{u}}{\partial t} + \mathbf{u} \cdot \nabla \mathbf{u} = -\nabla p - \frac{1}{Fr}(0, 1) + \frac{1}{Re}\nabla^2 \mathbf{u}, \qquad (\nabla \cdot \mathbf{u} = 0) \tag{6.2}$$

with Fr and Re being the Froude and Reynolds numbers respectively:

$$Fr = \frac{\bar{u}_0^2}{\bar{g}\bar{h}_0}, \qquad Re = \frac{\bar{\rho}\bar{u}_0\bar{L}}{\bar{\mu}}.$$

For surfboard with length of $\sim 2m$ travelling at speed of $\sim 10km/h$ close to the shore, with depth of say $\sim 0.1m - 0.2m$, we readily obtain the following estimates:

$$Fr \sim O(1), \qquad Re \sim O(10^6).$$

It is therefore evident that the viscous effects are negligible in our flow model, provided there is no substantial separation (see [57, 40, 26, 28, 29]), whereas gravity effects are not.

We can exploit the large aspect ratio of our model by introducing the following scaling:

$$Y = \frac{y}{\epsilon}, \qquad H = \frac{h}{\epsilon}, \qquad V = \frac{v}{\epsilon}, \qquad (\epsilon = \frac{\bar{h}_0}{\bar{L}} \ll 1) \tag{6.3}$$

with $\bar{h}_0$ being the representative undisturbed water depth. Assuming the flow is irrotational, the horizontal flow velocity is essentially uniform across the vertical dimension: $u = u(x,t)$ and is independent of Y. At this point the Navier-Stokes equations (6.2) at the leading order can be written in the following form:

$$\frac{\partial u}{\partial t} + u\frac{\partial u}{\partial x} = -\frac{\partial p}{\partial x}, \tag{6.4a}$$

$$0 = -\frac{\partial p}{\partial Y} - \hat{g}, \tag{6.4b}$$

where $\hat{g}$ is a scaled gravity term:

$$\hat{g} = \frac{\epsilon}{Fr}. \tag{6.5}$$

The vertical pressure distribution in our shallow water model is essentially hydrostatic according to (6.4b).

For the depictions given in Fig. 6.2 then, the flow from upstream in region 0 has a velocity of $\mathbf{u}_0 = (u_0, 0)$ and flow depth of H_0. This flow is split by the thin body into two regions: one above the body in region 1; the other below in region 2. We let $\mathbf{u}_1 = (u_1, \epsilon V_1)$ and H_1 denote the flow velocity and depth respectively in region 1, and the pressure $p_1(x, Y, t)$ is hydrostatic given the shallowness of water. In region 2 the pressure is denoted as $p_2(x, Y, t)$, and flow velocity and depth are given as $\mathbf{u}_2 = (u_2, \epsilon V_2)$ and $H_2(x,t)$ respectively. From the water depths of the region 1 and 2 we can obtain the height of the free surface elevation $\eta(x,t)$:

$$\eta(x,t) = H_1(x,t) + H_2(x,t). \tag{6.6}$$

If the body's upper surface is completely flooded, the flow in region 1 would join the downstream region 3, where the pressure is hydrostatic everywhere and the flow velocity past the body will eventually return to $\mathbf{u}_0$. If on the other hand the board's upper surface is at least partially dry, then there would be a gravity driven wetting process over the dry surface.

Supposing the non-dimensional atmospheric pressure p_0 is zero without losing generality, we can integrate the fluid's vertical momentum equation (6.4b) in region 1 as so:

$$\int_Y^\eta \frac{\partial p_1}{\partial s} ds = -\hat{g}(\eta - Y), \qquad (Y \in [H_{2+}, \eta]),$$

where H_{2+} is the height measured from the flow bed to the upper-surface of the body. Simplifying this equation and rearranging gives:

$$p_1(x, Y, t) = \hat{g}(\eta - Y). \tag{6.7}$$

Hence the pressure in region 1 is hydrostatic as expected. By a similar argument we can obtain the pressure for region 2 by vertically integrating (6.4b):

$$\int_Y^\eta \frac{\partial p}{\partial s} ds = \int_Y^{H_{2-}} \frac{\partial p_2}{\partial s} ds + \int_{H_{2+}}^\eta \frac{\partial p_1}{\partial s} ds = -\hat{g}(\eta - Y), \qquad (Y \in [0, H_{2-}]),$$

here H_{2-} is the height measured from the flow bed to the bottom-surface of the body. Therefore

$$p_2(x, Y, t) = p_2(x, H_{2-}, t) - p_1(x, H_{2+}, t) + \hat{g}(\eta - Y) = \pi_2(x, t) + \hat{g}(\eta - Y), \tag{6.8}$$

with π_2 denoting the hydrodynamic pressure difference on the lower and upper surfaces of the body:

$$\pi_2(x, t) = p_2(x, H_{2-}, t) - p_1(x, H_{2+}, t). \tag{6.9}$$

Note that in the case of a body with negligible thickness such that $H_{2-} \sim H_{2+}$, the hydrostatic pressure above and below the body cancels out and the hydrodynamic pressure π_2 is the only dominant force from the fluid acting on the board. We finally have the following pressure conditions in the two regions

above and below the board:

$$p_1(x, Y, t) = \hat{g}(\eta - Y), \qquad (Y \in [H_{2+}, \eta]); \tag{6.10a}$$

$$p_2(x, Y, t) = \pi_2(x, t) + \hat{g}(\eta - Y), \qquad (Y \in [0, H_{2-}]). \tag{6.10b}$$

Given the pressure conditions in (6.10), the flow's horizontal momentum equation (6.4a) in these two regions can be written as

$$\frac{\partial u_1}{\partial t} + u_1 \frac{\partial u_1}{\partial x} = -\hat{g}\frac{\partial \eta}{\partial x}, \tag{6.11a}$$

$$\frac{\partial u_2}{\partial t} + u_2 \frac{\partial u_2}{\partial x} = -\frac{\partial \pi_2}{\partial x} - \hat{g}\frac{\partial \eta}{\partial x}. \tag{6.11b}$$

As the body moves in water we assume the flow separates smoothly from its sharp trailing edge into the downstream wake, i.e. a Kutta condition applies here. This is equivalent to imposing the following pressure condition at the trailing edge where $x = x_2$:

$$p_1(x_2, H_2, t) = p_2(x_2, H_2, t) = \hat{g}H_1(x_2, t). \tag{6.12}$$

What happens at the leading edge is worth a more detailed discussion. First, in a 2D model the flow from upstream gets spilt into two streams: above and below the body, and therefore the mass conservation law dictates that:

$$u_0 H_0 = 1 = u_1 H_1 + u_2 H_2, \tag{6.13}$$

which is the flux condition imposed at the leading edge of the body. Second, the flow layers above and below the body are different in the sense that, if they start with the same pressure conditions they would usually produce different pressure conditions at the trailing edge [30, 28]. This inconsistency with the Kutta condition is resolved by introducing a localised Euler region at the leading edge, where the interactions between the upstream and downstream flows are concentrated; the length scale of this Euler region is $O(\epsilon\bar{L})$ [30]. Therefore on

the large horizontal scale what we witness is a flow discontinuity, whereby a pressure jump is present when the flow enters the leading edge into region 1 or 2. Across this discontinuity the stream-wise Bernoulli quantity is conserved from the upstream region to the Euler region around the leading edge, so that:

$$p_0 + \frac{1}{2}u_0^2 = p_1 + \frac{1}{2}u_1^2(x_{1+}, t) = p_2 + \frac{1}{2}u_2^2(x_{1+}, t). \tag{6.14}$$

Note that unlike the case of a flat body skimming on water, there is no thrown-forward jet at the leading edge in the flooding case.

Turning our attention to the boundary conditions, at the flow bed $Y = 0$ where the non-penetrable boundary plainly implies

$$V(x, 0, t) = 0. \tag{6.15}$$

On the flow's free surface, given the large aspect ratio we can write the leading order kinematic boundary condition in region 2 as:

$$V(x, H_2, t) = \frac{\partial H_2}{\partial t} + u_2 \frac{\partial H_2}{\partial x}. \tag{6.16}$$

Additionally the fluid's incompressibility condition can be vertically integrated in region 2 to give:

$$V(x, H_2, t) = -H_2 \frac{\partial u_2}{\partial x}, \tag{6.17}$$

and combining these two conditions (6.17), (6.16) we obtain the following conservation equation:

$$\frac{\partial H_2}{\partial t} + \frac{\partial}{\partial x}(u_2 H_2) = 0. \tag{6.18}$$

Similarly in region 1 then, vertically integrating the incompressibility condition

from the upper-surface of the body to the water's free surface leads to

$$V(x,\eta,t) = V(x,H_2,t) - H_1\frac{\partial u_1}{\partial x} = \frac{\partial H_2}{\partial t} + u_2\frac{\partial H_2}{\partial x} - H_1\frac{\partial u_1}{\partial x}, \tag{6.19}$$

while the kinematic boundary condition at the flow free surface is

$$V(x,\eta,t) = \frac{\partial \eta}{\partial t} + u\frac{\partial \eta}{\partial x} = \frac{\partial H_1}{\partial t} + u_1\frac{\partial H_1}{\partial x} + \frac{\partial H_2}{\partial t} + u_2\frac{\partial H_2}{\partial x}. \tag{6.20}$$

Combining (6.19) and (6.20) would yield the following condition for region 1:

$$\frac{\partial H_1}{\partial t} + \frac{\partial}{\partial x}(u_1 H_1) = 0. \tag{6.21}$$

Concerning the momentum equations of the thin body itself, using arguments similar to the flat body skimming case in Chapter 2, we have the following leading order momentum equations:

$$\int_{x_1}^{x_2}(p_2 - p_1)\cos\theta dx = \int_{x_1}^{x_2}\left[\pi_2(x, t+\hat{g}T(x)\right]\cos\theta dx = m(\frac{d^2 y_m}{dt^2} + \hat{g}), \tag{6.22a}$$

$$\int_{x_1}^{x_2}(p_2 - p_1)x\cos\theta dx = \int_{x_1}^{x_2}\left[\pi_2(x,t) + \hat{g}T(x)\right]x\cos\theta dx = i\frac{d^2\theta}{dt^2}. \tag{6.22b}$$

to leading order. Here $T(x)$ denotes the body's thickness; m and i are the scaled mass and moment of inertia such that $m = \bar{m}/\bar{\rho}\bar{L}^2$, $i = \bar{i}/\bar{\rho}\bar{L}^4$; the $\int_{x_1}^{x_2} T(x)dx$ term represents the (scaled) water mass displaced by the solid body.

The typical angle of attack by the surfboard is small from observations, usually in the range of $(-20°, 20°)$ and as such $\cos\theta \sim 1$. We further scale the leading and trailing edge's horizontal positions (x_1, x_2) as $(-1, 1)$ without loss of generality. The momentum equations for the body (6.22) can be written in

the following form:

$$\int_{-1}^{1} \pi_2(x,t)dx = M\big[\frac{d^2Y_m}{dt^2} + \frac{1}{Fr} - \frac{1}{M}\frac{\epsilon}{Fr}\int_{-1}^{1} T(x)dx\big], \tag{6.23a}$$

$$\int_{-1}^{1} \pi_2(x,t)xdx = I\frac{d^2\theta}{dt^2} - \frac{\epsilon}{Fr}\int_{-1}^{1} xT(x)dx, \tag{6.23b}$$

with M and I given as

$$M = \epsilon m, \tag{6.24a}$$

$$I = \epsilon i; \tag{6.24b}$$

and θ now takes on order unity values due to the scaled momentum of inertia I.

The term $-\frac{\epsilon}{Fr}\int_{-1}^{1} T(x)dx$ in (6.23a) represents the buoyancy force exerted on the body. The surfboard example is illustrative here: without taking such force into account, a board carrying the weight of a human would sink when not in surfing motion, which is different from reality (see Figure 6.1a). Buoyancy effect also can play an important role in numerous industrial and other applications. It is convenient for us to introduce a buoyancy parameter $\hat{\mathcal{A}}$ as follows:

$$\hat{\mathcal{A}} = \frac{1}{Fr} - \frac{1}{M}\frac{\epsilon}{Fr}\int_{-1}^{1} T(x)dx. \tag{6.25}$$

Thus $\hat{\mathcal{A}}$ represents the acceleration due to the net effects of buoyancy and gravity. For the case of $\hat{\mathcal{A}} = 0$, the body's buoyancy cancels out its gravitational effect; $\hat{\mathcal{A}} > 0$ represents the case that gravity overcomes buoyancy and vice versa. It is a free model parameter to be prescribed. We shall further neglect the torque force due to buoyancy in the angular momentum equation (6.23b) – and assume the body has a uniform density that any change in angular momentum is purely due to the hydrodynamic effect of the flow. We now can re-write

the body momentum equations as:

$$\int_{-1}^{1} \pi_2(x,t)dx = M(\frac{d^2Y_m}{dt^2} + \hat{\mathcal{A}}), \tag{6.26a}$$

$$\int_{-1}^{1} x\pi_2(x,t)dx = I\frac{d^2\theta}{dt^2}. \tag{6.26b}$$

The horizontal-momentum balance in the body motion is such that the horizontal momentum must remain constant since the horizontal forces are comparatively small [57, 21, 1, 37] and hence the body and the coordinate frame of reference continue to move horizontally with equal uniform speed over the current time scales.

To summarise, we have the following governing equations for the flow above the body in region 1:

$$\frac{\partial H_1}{\partial t} + \frac{\partial}{\partial x}(u_1 H_1) = 0, \tag{6.27a}$$

$$\frac{\partial u_1}{\partial t} + u_1\frac{\partial u_1}{\partial x} = -\hat{g}\frac{\partial}{\partial x}(H_1 + H_2), \tag{6.27b}$$

$$p_1(x,Y,t) = \hat{g}(H_1 + H_2 - Y), \tag{6.27c}$$

$$u_1^2(-1,t) - 2\hat{g}[1 - H_1(-1,t) - H_2(-1,t)] - 1 = 0, \tag{6.27d}$$

$$p_1(1,H_2,t) = \hat{g}H_1(1,t); \tag{6.27e}$$

whereas in region 2 we have:

$$\frac{\partial H_2}{\partial t} + \frac{\partial}{\partial x}(u_2 H_2) = 0, \tag{6.28a}$$

$$\frac{\partial u_2}{\partial t} + u_2\frac{\partial u_2}{\partial x} = -\frac{\partial \pi_2}{\partial x} - \hat{g}\frac{\partial}{\partial x}(H_1 + H_2), \tag{6.28b}$$

$$H_2(x,t) = Y_m + x\theta, \tag{6.28c}$$

$$p_2(x,Y,t) = \pi_2(x,t) + \hat{g}(H_1 + H_2 - Y), \tag{6.28d}$$

$$\pi_2(-1,t) + \frac{1}{2}[u_2^2(-1,t) - 1] + \hat{g}[H_1(-1,t) + H_2(-1,t) - 1] = 0, \tag{6.28e}$$

$$u_1(-1,t)H_1(-1,t) + u_2(-1,t)H_2(-1,t) = 1, \tag{6.28f}$$

$$p_2(1,H_2,t) = \hat{g}H_1(1,t); \tag{6.28g}$$

finally on the solid body we have the following governing equations:

$$\int_{-1}^{1} \pi_2(x,t)dx = M(\frac{d^2Y_m}{dt^2} + \hat{\mathcal{A}}), \tag{6.29a}$$

$$\int_{-1}^{1} x\pi_2(x,t)dx = I\frac{d^2\theta}{dt^2}. \tag{6.29b}$$

We have therefore developed a flooding model for a thin body that is originally in planing motion. This flooding model (6.27) - (6.29) consists of six unknowns u_1, u_2, H_1, Y_m, θ and π_2, with $\hat{g}$, $\hat{A}$ being static parameters prescribed according to our desired physical context. For the reminder of this study we shall analyse this flooding model via both analytical and numerical treatments.

6.3 Linearised flow analysis

The integro-differential system (6.27) - (6.29) is difficult to analyse in its current form. Any solutions will need to be pursued numerically. Before we pursue such solutions, it is possible to gain some insights by first working with a linearised version of this flooding system. To do so we start by introducing a small parameter δ such that $\delta \ll 1$, and asymptotically expand the system variables in

the following manner:

$$\hat{g} = \delta\bar{g}, \tag{6.30a}$$

$$\hat{\mathcal{A}} = \delta\bar{\mathcal{A}}, \tag{6.30b}$$

$$Y_m = 1 + \delta Y_1(t), \tag{6.30c}$$

$$\theta = \theta_0 + \delta\theta_1(t), \tag{6.30d}$$

$$H_1 = 0 + \delta H_{11}(x,t), \tag{6.30e}$$

$$H_2 = 1 + \delta H_{21}(x,t), \tag{6.30f}$$

$$u_1 = 1 + \delta u_{11}(x,t), \tag{6.30g}$$

$$u_2 = 1 + \delta u_{21}(x,t), \tag{6.30h}$$

$$p_1 = 0, \tag{6.30i}$$

$$p_2 = 0 + \delta\pi_{21}(x,t). \tag{6.30j}$$

The basic state here has uniform horizontal velocities of unity in regions 1, 2 for a body which is thin relative to the thickness of the liquid layer, and the flow depth above the body is shallow ($\sim O(\delta)$) compared with the depth below ($\sim O(1)$). Note that to limit the complexity of our linearised system, the gravity and buoyancy effects in our flow model are restricted to be small ($\sim O(\delta)$).

Substituting these expansions into the system (6.27) - (6.29), we obtain the following relations for the flow in region 1:

$$\frac{\partial H_{11}}{\partial t} + \frac{\partial H_{11}}{\partial x} = 0, \tag{6.31a}$$

$$\frac{\partial u_{11}}{\partial t} + \frac{\partial u_{11}}{\partial x} = 0, \tag{6.31b}$$

$$u_{11}(-1,t) = 0. \tag{6.31c}$$

Likewise in region 2 we have the following relations after the asymptotic expan-

sions:

$$\frac{\partial H_{21}}{\partial t} + \frac{\partial H_{21}}{\partial x} + \frac{\partial u_{21}}{\partial x} = 0, \tag{6.32a}$$

$$\frac{\partial u_{21}}{\partial t} + \frac{\partial u_{21}}{\partial x} + \frac{\partial \pi_{21}}{\partial x} = 0, \tag{6.32b}$$

$$\pi_{21}(-1,t) + u_{21}(-1,t) = 0, \tag{6.32c}$$

$$H_{21} = Y_1 + x\theta_1. \tag{6.32d}$$

The flux conditions at the leading edge and Kutta condition at the trailing edge can be written as:

$$H_{11}(-1,t) + H_{21}(-1,t) + u_{21}(-1,t) = 0, \tag{6.33a}$$

$$\pi_{21}(1,t) = 0. \tag{6.33b}$$

The immersed body's momentum equations become:

$$M(\frac{\partial^2 Y_1}{\partial t^2} + \bar{\mathcal{A}}) = \int_{-1}^{1} \pi_{21} dx, \tag{6.34a}$$

$$I\frac{\partial^2 \theta_1}{\partial t^2} = \int_{-1}^{1} x\pi_{21} dx. \tag{6.34b}$$

The flow velocity and depth in (6.31a) and (6.31b) can be solved analytically, their solutions being arbitrary functions of the composite variable $x - t$:

$$H_{11} = \mathfrak{h}(x-t), \tag{6.35a}$$

$$u_{11} = \mathfrak{u}(x-t). \tag{6.35b}$$

Provided that the initial and leading edge boundary conditions for H_{11} and u_{11} are known, their solutions can be fully traced out along the characteristic functions $x-t = c$. For our current analysis we shall suppose there is no flooding

over the top of the body initially, that is to say:

$$H_{11}(x,0) = 0, \tag{6.36a}$$

$$u_{11}(x,0) = 0. \tag{6.36b}$$

The initial condition (6.36b) for the flow velocity u_{11} together with its boundary condition (6.31c) imply that it has the following trivial solution:

$$u_{11}(x,t) = 0, \tag{6.37}$$

therefore the flooding over the top of the body occurs at the same speed as the undisturbed upstream velocity, i.e. $u_1 \equiv u_0$.

In region 2, the flow velocity u_{21} can be solved by substituting (6.32d) into (6.32a) and directly integrating with respect to x:

$$u_{21} = -\frac{x^2}{2}\frac{d\theta_1}{dt} - x\frac{dY_1}{dt} - x\theta_1 - \mathcal{U}(t), \tag{6.38}$$

where $\mathcal{U}(t)$ is function of time as a resultant of the spatial integration. Substituting this solution into (6.32b) and integrating with respect to x we can obtain the following solution for π_{21}:

$$\pi_{21} = \frac{x^3}{6}\frac{d^2\theta_1}{dt^2} + \frac{x^2}{2}\frac{d^2Y_1}{dt^2} + x^2\frac{d\theta_1}{dt} + x\frac{d\mathcal{U}}{dt} + x\frac{dY_1}{dt} + x\theta_1 + \mathcal{P}(t), \tag{6.39}$$

where $\mathcal{P}(t)$ is function of time resulted from the spatial integration. From the solutions of the flow velocity u_{21} and the dynamic pressure π_{21} in region 2, we obtain the following relation based on the linearised Bernoulli's principle at the leading edge (6.32c):

$$\frac{1}{2}\frac{d^2Y_1}{dt^2} - \frac{1}{6}\frac{d^2\theta_1}{dt^2} + \frac{1}{2}\frac{d\theta_1}{dt} - \frac{d\mathcal{U}}{dt} + \mathcal{P} - \mathcal{U} = 0. \tag{6.40}$$

Similarly the flux condition at the leading edge (6.33a) implies:

$$\mathfrak{h}(-1-t)+\frac{dY_1}{dt}-\frac{1}{2}\frac{d\theta_1}{dt}+Y_1-\mathcal{U}=0. \tag{6.41}$$

The Kutta condition at the trailing edge (6.33*b*) together with the pressure equation (6.39) implies:

$$\frac{1}{6}\frac{d^2\theta_1}{dt^2}+\frac{1}{2}\frac{d^2Y_1}{dt^2}+\frac{d\theta}{dt}+\frac{dY_1}{dt}+\frac{d\mathcal{U}}{dt}+\theta_1+\mathcal{P}=0. \tag{6.42}$$

The immersed body's momentum equations can be now written as:

$$(M-\frac{1}{3})\frac{d^2Y_1}{dt^2}-\frac{2}{3}\frac{d\theta_1}{dt}-2\mathcal{P}+M\bar{\mathcal{A}}=0, \tag{6.43a}$$

$$(3I-\frac{1}{5})\frac{d^2\theta_1}{dt^2}-2\frac{dY_1}{dt}-2\frac{d\mathcal{U}}{dt}-2\theta_1=0. \tag{6.43b}$$

We have finally rearranged the linearised flooding model into a system of five equations (6.40) − (6.43) with five unknowns Y_1, θ_1, $\mathfrak{h}(-1-t)$, $\mathcal{U}$ and $\mathcal{P}$. These five equations can be further simplified to the following form:

$$(\mathcal{K}+1)\frac{d^2Y_1}{dt^2}=-\frac{5}{6}\frac{d\theta_1}{dt}-\frac{dY_1}{dt}-\theta_1+\mathcal{U}-M\bar{\mathcal{A}}, \tag{6.44a}$$

$$(\mathcal{L}+\frac{1}{3})\frac{d^2\theta_1}{dt^2}=-\frac{1}{2}\frac{d\theta_1}{dt}+\frac{dY_1}{dt}+\theta_1-\mathcal{U}, \tag{6.44b}$$

$$(6\mathcal{L}+2)\frac{d\mathcal{U}}{dt}=-(3\mathcal{L}+2)\frac{dY_1}{dt}-\frac{3\mathcal{L}}{2}\frac{d\theta_1}{dt}-(3\mathcal{L}+2)\theta_1-3\mathcal{L}\mathcal{U}, \tag{6.44c}$$

$$\mathcal{P}=-\frac{1}{2}\frac{d^2Y_1}{dt^2}-\frac{1}{2}\frac{dY_1}{dt}-\frac{3}{4}\frac{d\theta_1}{dt}-\frac{1}{2}\theta_1+\frac{1}{2}\mathcal{U}, \tag{6.44d}$$

$$\mathfrak{h}(-1-t)=-\frac{dY_1}{dt}+\frac{1}{2}\frac{d\theta_1}{dt}-Y_1+\mathcal{U}. \tag{6.44e}$$

where $\mathcal{K}$ and $\mathcal{L}$ are constants and given as

$$\mathcal{K}=M-\frac{1}{3}, \tag{6.45a}$$

$$\mathcal{L}=3I-\frac{1}{5}. \tag{6.45b}$$

Equations (6.44a) to (6.44c) can be written as a system of linear equations:

$$\begin{bmatrix} \dot{Y}_1 \\ \dot{\theta}_1 \\ \dot{\mathcal{U}} \\ \dot{V}_1 \\ \dot{\omega}_1 \end{bmatrix} = \begin{bmatrix} 0 & 0 & 0 & 1 & 0 \\ 0 & 0 & 0 & 0 & 1 \\ 0 & -\frac{3\mathcal{L}+2}{6\mathcal{L}+2} & -\frac{3\mathcal{L}}{6\mathcal{L}+2} & -\frac{3\mathcal{L}+2}{6\mathcal{L}+2} & -\frac{3\mathcal{L}}{12\mathcal{L}+4} \\ 0 & -\frac{1}{\mathcal{K}+1} & \frac{1}{\mathcal{K}+1} & -\frac{1}{\mathcal{K}+1} & -\frac{5}{6(\mathcal{K}+1)} \\ 0 & \frac{3}{3\mathcal{L}+1} & -\frac{3}{3\mathcal{L}+1} & \frac{3}{3\mathcal{L}+1} & -\frac{3}{6\mathcal{L}+2} \end{bmatrix} \begin{bmatrix} Y_1 \\ \theta_1 \\ \mathcal{U} \\ V_1 \\ \omega_1 \end{bmatrix} - \begin{bmatrix} 0 \\ 0 \\ 0 \\ \frac{M\bar{\mathcal{A}}}{\mathcal{K}+1} \\ 0 \end{bmatrix}, \tag{6.46}$$

where V_1 and ω_1 are defined respectively as:

$$V_1 = \frac{dY_1}{dt}, \tag{6.47a}$$

$$\omega_1 = \frac{d\theta_1}{dt}. \tag{6.47b}$$

We solved the system (6.44) via a finite difference scheme with the following initial conditions: $\bar{\mathcal{A}} = 1$, $Y_1(0) = 0$, $\theta_1(0) = 0$, $V_1(0) = -1$, $\omega_1(0) = 0$, $\mathfrak{h}(-1) = 0$ and $U(0) = Y_1(0) + V_1(0) - 0.5\omega_1(0)$, with $M = 1$ and $I = \frac{1}{4}$. Under such configurations the body is able to obtain sufficient lift to ascend in water, which is signified by the body's vertical velocity V_1 turning positive at $t \sim 0.6$ in Fig. 6.3b. The linear system (6.46) configured with such initial conditions has the following five eigenvalues: $(0, 0, 0.269, -0.873 \pm 0.284i)$. The existence of a positive eigenvalue indicates that our solutions grow exponentially with time: the body's vertical position continues to rise and its contact angle becomes more acute until the solutions grow beyond the linearised regime. We ensure however that h_1 is never negative.

Fig. 6.4 shows the solutions for the water depth above the body. Fig. 6.4a shows the depth of flooding over the leading edge of the body, while Fig. 6.4b demonstrates the water depth over the entire body at various times. We terminate the solution at around $t \sim 2.56$, at which point the body is in vertical ascendency while the water depth above its leading edge is decreased to zero.

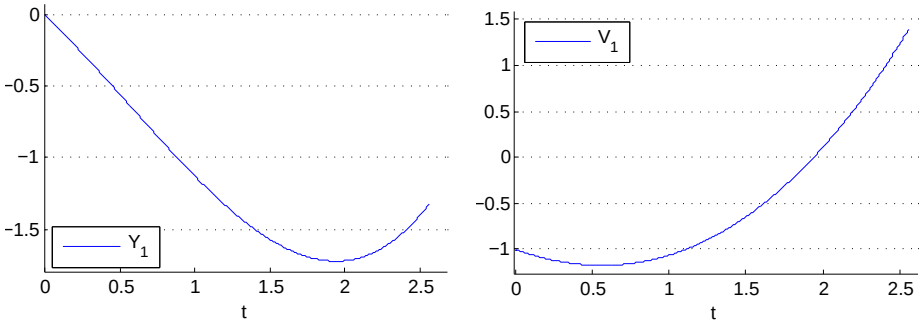

(a) Y_1

(b) V_1

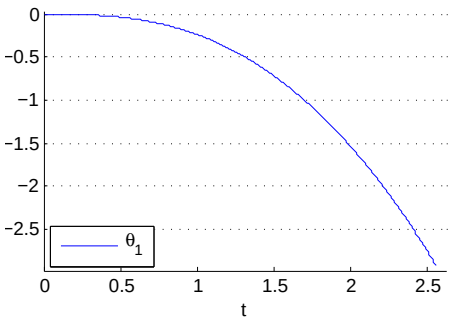

(c) θ_1

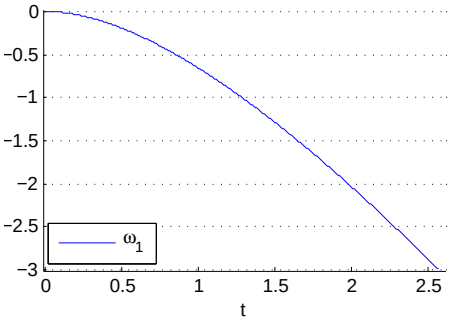

(d) ω_1

Figure 6.3: The linearised vertical and angular motions of a thin body becoming flooded over time. This system is configured with initial conditions of $\theta_1(0) = 0$, $\omega_1(0) = 0$ and scaled vertical velocity of $V_1(0) = -1$. The scaled gravity for the body is set to $\bar{\mathcal{A}} = 1$.

From that time onwards the body changes to a skimming process without flooding as analysed in Chapter 2.

From the modelling of a surfboard's prospective, once the board's initial velocities $(V_1(0), \omega_1(0))$ and vertical position $Y_1(0)$ are known, equation (6.44e) shows that $\mathfrak{h}(-1)$ can be configured to match the incoming flood depth at the leading edge by setting an appropriate value of $\mathcal{U}(0)$, which in turn also has an effect on the velocity of the flow underneath the board and the lift.

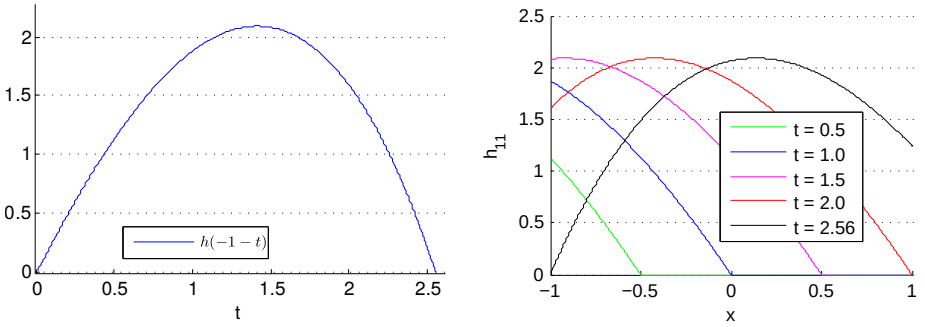

(a) $\mathfrak{h}(-1-t)$ (b) H_{11}

Figure 6.4: (a) shows $\mathfrak{h}(-1-t)$, i.e. the depth of the water above the plate at the leading edge. At $t \sim 2.56$ the depth becomes negative, which signifies the leading edge of the body emerges from water and the flooding process terminates. (b) shows the water depth profile at various times.

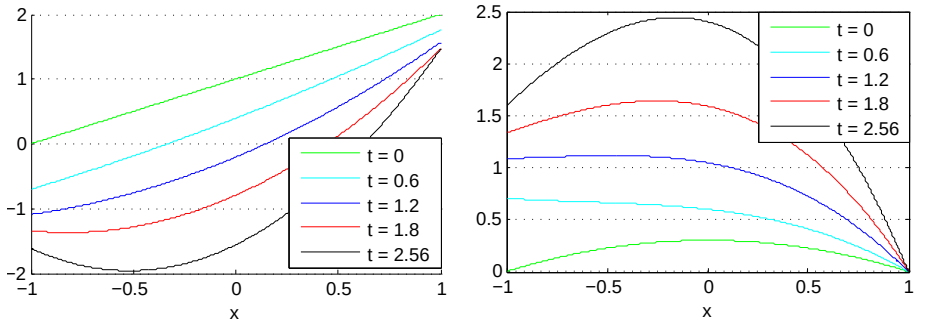

(a) u_{21} (b) π_{21}

Figure 6.5: Solutions of the flow velocity and pressure underneath the body at various times. The flow velocity becomes negative in a region including the leading edge, this corresponds to a positive pressure in such region.

Fig. 6.6 shows the effect of gravity parameter $\bar{A}$ on our linearised flooding model. As it can be seen the greater the gravity effect, the deeper this body

sinks into water before reversing its course. From a modelling prospective, a greater $\bar{A}$ corresponds to a body with less buoyancy in water.

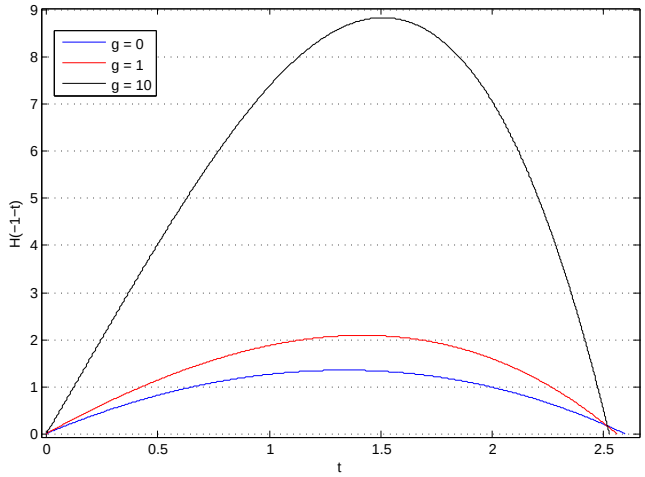

(a) $\mathfrak{h}(-1-t)$

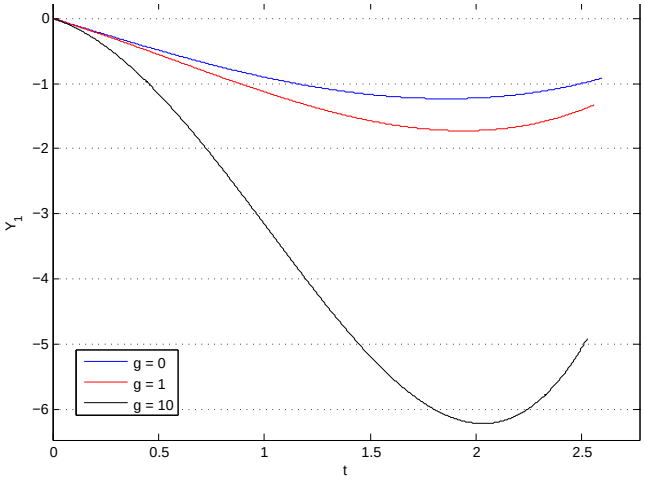

(b) Y_1

Figure 6.6: Solutions of the linearised flooding system for $\mathfrak{h}(-1-t)$ and Y_1 for varying values of gravity parameter $\bar{A}$. The initial conditions for the system are set to $\theta_1(0) = 0$, $\omega_1(0) = 0$ and $V_1(0) = -1$.

6.4 Numerical solutions of the nonlinear flooding system

In this section we introduce a numerical scheme for solving the flooding system of (6.27) - (6.29). The solutions to the flow in region 1 and 2 are coupled with each other via the flux condition at the leading edge and Kutta condition at the trailing edge. A time-marching finite difference scheme will be presented here, which for any given time step first solves the flux condition and the flow in region 1, then solves the flow in region 2 and iterates these two steps until the Kutta condition at the trailing edge is satisfied. We will then present our numerical findings as well as analyse the circumstances under which the model thin body is able to skim or sink under various flooding conditions.

6.4.1 A finite difference scheme

It is useful to rearrange our governing equations into a numerical discretization friendly format. We begin by re-writing the flux condition (6.28f) as a boundary condition for H_1 at the leading edge:

$$H_1(-1,t) = \frac{1}{u_1(-1,t)}\big[1 - u_2(-1,t)H_2(-1,t)\big]. \tag{6.48}$$

The Bernoulli's equation (6.27d) for region 1 has the following leading edge boundary condition for u_1:

$$u_1(-1,t) = \sqrt{1 + 2\hat{g}[1 - H_1(-1,t) - H_2(-1,t)]}. \tag{6.49}$$

In region 2 we spatially integrate the equation (6.28a) from the leading edge to a given point on the body such that

$$\begin{aligned} &\int_{-1}^{x} \frac{\partial H_2}{\partial t} ds + \big[u_2 H_2\big]_{-1}^{x} = 0, \quad \Rightarrow \\ &u_2(x,t) = \frac{1}{H_2(x,t)}\big[\mathcal{C}_u - (x+1)V - \frac{1}{2}(x^2-1)\omega\big], \quad (x \in [-1,1]) \end{aligned} \tag{6.50}$$

with $\mathcal{C}_u$ being a variable that captures the leading edge boundary conditions of region 2:

$$\mathcal{C}_u = u_2(-1,t)H_2(-1,t). \tag{6.51}$$

Likewise we can spatially integrate the fluid momentum equation (6.28b) from the leading edge to a given point on the body so that

$$\int_{-1}^{x} \frac{\partial u_2}{\partial t} ds + \int_{-1}^{x} u_2 \frac{\partial u_2}{\partial s} ds = -\big[\pi_2(s,t)\big]_{-1}^{x} - \hat{g}\big[H_1(s,t) + H_2(s,t)\big]_{-1}^{x} \quad \Rightarrow$$
$$\pi_2(x,t) = -\int_{-1}^{x} \frac{\partial u_2}{dt} ds - \frac{1}{2}u_2^2 - \hat{g}(H_1 + H_2) + \mathcal{C}_p, \quad (x \in [-1,1]) \tag{6.52}$$

with $\mathcal{C}_p$ given as

$$\mathcal{C}_p = \frac{1}{2}u_2^2(-1,t) + \pi_2(-1,t) + \hat{g}[H_1(-1,t) + H_2(-1,t)]. \tag{6.53}$$

Note that Bernoulli's equation (6.28e) in region 2 is

$$\frac{1}{2}u_2^2(-1,t) + \pi_2(-1,t) + \hat{g}[H_1(-1,t) + H_2(-1,t)] = \hat{g} + \frac{1}{2}, \tag{6.54}$$

therefore $\mathcal{C}_p$ can be expressed in the following equivalent form:

$$\mathcal{C}_p = \hat{g} + \frac{1}{2}. \tag{6.55}$$

The dynamic pressure equation (6.52) can be applied at the trailing edge to obtain

$$\pi_2(1,t) = -\int_{-1}^{1} \frac{\partial u_2}{\partial t} dx - \frac{1}{2}u_2^2(1,t) - \hat{g}[H_1(1,t) + H_2(1,t) - 1] + \frac{1}{2}. \tag{6.56}$$

The Kutta condition (6.28g) implies this dynamic pressure should be zero at

this edge, hence

$$\int_{-1}^{1} \frac{\partial u_2}{\partial t} dx + \frac{1}{2} u_2^2(1,t) + \hat{g}[H_1(1,t) + H_2(1,t) - 1] - \frac{1}{2} = 0. \tag{6.57}$$

This condition (6.57) is extremely useful for checking the consistency of our numerical solutions, particularly for u_2 over the grid of $x \in [-1, 1]$. We shall use this condition at each time iteration for solution accuracy checking.

This flooding system can now be discretized using a finite difference scheme. To do so we introduce a time grid $t \in (0, T]$ and spatial grid $x \in [-1, 1]$; these two grids are discretized as:

$$t = i\Delta t, \qquad (\Delta t = T/J, \quad i = 1, 2, ...J); \tag{6.58a}$$

$$x = -1 + j\Delta x, \qquad (\Delta x = 2/K, \quad j = 0, 1, 2, ...K). \tag{6.58b}$$

The boundary conditions (6.48) and (6.49) for u_1 and H_1 can be discretized respectively as

$$u1_0^i = \sqrt{1 + 2\hat{g}[1 - H1_0^{i-1} - H2_0^{i-1}]}, \tag{6.59a}$$

$$H1_0^i = (1 - u2_0^{i-1} H2_0^{i-1})/u1_0^i. \tag{6.59b}$$

The flow equations (6.27a), (6.27b) in region 1 are discretized using an implicit forward Euler method as

$$\frac{u1_j^i - u1_j^{i-1}}{\Delta t} + u1_j^i \frac{u1_j^i - u1_{j-1}^i}{\Delta x} = -\hat{g}[\frac{H1_j^{i-1} - H1_{j-1}^{i-1}}{\Delta x} + \theta^{i-1}], \tag{6.60a}$$

$$\frac{H1_j^i - H1_j^{i-1}}{\Delta t} + \frac{u1_j^i H1_j^i - u1_{j-1}^i H1_{j-1}^i}{\Delta x} = 0. \tag{6.60b}$$

These two equations can be rearranged into the following forms for u_1, H_1 for

$j \in [1, K]$:

$$u1_j^i = \frac{1}{2}\left[\sqrt{(u1_{j-1}^i + \frac{\Delta x}{\Delta t})^2 - 4\hat{g}(H1_j^{i-1} - H1_{j-1}^{i-1} + \Delta x \theta^{i-1})} + u1_{j-1}^i - \frac{\Delta x}{\Delta t}\right], \tag{6.61a}$$

$$H1_j^i = \frac{\Delta x}{\Delta x + \Delta t u1_j^i}\big(H1_j^{i-1} + \frac{\Delta t}{\Delta x} u1_{i-1}^i H1_{j-1}^i\big). \tag{6.61b}$$

For each time step i we solve the boundary conditions in (6.59), and then solve the flow equations (6.60) over the rest of the spatial grid for $j \in [1, K]$.

In region 2 the flow velocity and dynamic pressure equations (6.50), (6.52) can be discretized via forward Euler scheme as

$$u2_j^i = \frac{1}{H2_j^{i-1}}\left[\mathcal{C}_u^i - j\Delta x V^{i-1} - \frac{1}{2}(j^2\Delta x^2 - 2j\Delta x)\omega^{i-1}\right]; \tag{6.62a}$$

$$\pi 2_j^i = -\frac{\Delta x}{\Delta t}\sum_{k=0}^{i}(u2_k^i - u2_k^{i-1}) - \frac{1}{2}(u2_j^i)^2 - \hat{g}(H1_j^i + H2_j^{i-1} - 1) + \frac{1}{2}. \tag{6.62b}$$

The Kutta condition (6.57) at the trailing edge is discretized as

$$\frac{\Delta x}{\Delta t}\sum_{k=0}^{N}(u2_k^i - u2_k^{i-1}) + \frac{1}{2}(u2_N^i)^2 + \hat{g}(H1_N^i + H2_N^{i-1} - 1) - \frac{1}{2} = 0. \tag{6.63}$$

For a given time step i, once the flow equations of (6.62) are solved over the entire spatial grid ($x \in [-1, 1]$), we verify these solutions by checking the Kutta condition (6.63) is satisfied at the trailing edge.

The L.H.S. of (6.63) can be viewed as a function of $\mathcal{C}_u^i$, i.e.:

$$\mathcal{F}(\mathcal{C}_u^i) = \frac{\Delta x}{\Delta t}\sum_{k=0}^{N}(u2_k^i - u2_k^{i-1}) + \frac{1}{2}(u2_N^i)^2 + \hat{g}(H1_N^i + H2_N^{i-1} - 1) - \frac{1}{2}. \tag{6.64}$$

In order to find the root of $\mathcal{F}(\mathcal{C}_u^i)$, we start with an initial estimate of $\mathcal{C}_u^i = u2_0^{i-1}H2_0^{i-1}$, then use the Newton-Raphson method to iteratively find the accurate value of $\mathcal{C}_u^i$ and therefore u_2. The accurate solution of u_2 is in turn used to update the rest of the flow solutions in region 1 and 2 via an iteration cycle.

The thin body's vertical and angular momentum equations in (6.29) are discretized as:

$$Y_m^i = Y_m^{i-1} + \Delta t V^i, \tag{6.65a}$$

$$V_m^i = V_m^{i-1} + \frac{\Delta x \Delta t}{M}(\sum_{j=0}^{K} \pi 2_j^i - \frac{M\hat{A}}{\Delta x}), \tag{6.65b}$$

$$\theta^i = \theta^{i-1} + \Delta t \omega^i, \tag{6.65c}$$

$$\omega^i = \omega^{i-1} + \frac{\Delta x \Delta t}{I} \sum_{j=0}^{K} (j\Delta x - 1)\pi 2_j^i. \tag{6.65d}$$

Finally the depth of the region 2 H_2 can be solved as:

$$H2_j^i = Y_m^i + (j\Delta x - 1)\omega^i, \qquad (i \in (0, J], j \in [0, K]) \tag{6.66}$$

The scaled body mass, moment of inertia and acceleration due to gravity, M, I and $\hat{A}$ respectively, are user-defined input parameters. It should be noted that even though in theory these parameters can be freely prescribed, their values have an impact on the global errors of our numerical scheme.

To see this we first observe that the vertical and angular momentum equations (6.65b), (6.65d) have the terms $\frac{\Delta x \Delta t}{M}$ and $\frac{\Delta x \Delta t}{I}$ in their coefficients. Supposing the values of M and I are extremely small such that $\frac{\Delta x \Delta t}{M} > 1$ and $\frac{\Delta x \Delta t}{I} > 1$, then the rounding and local truncation errors in π_2 are magnified and grow with time, thus increasing our solutions' global errors and rendering the numerical scheme unstable. Therefore for small values of M and I, the grid's mesh sizes need to be sufficiently fine in order to prevent this "error magnification" (or sometimes referred to as "added mass") effect, and consequently increase the computational demand of our numerical scheme. In a similar principle, if the buoyancy parameter $\hat{A}$ is large such that the body's vertical acceleration in (6.65b) is essentially buoyancy driven, the numerical approximation errors in π_2 will have a smaller impact on our flooding system's overall solutions.

In the next section we shall analyse the behaviour of our flooding model via

numerical solutions. In particular we investigate the circumstances under which the solid body is either able to overcome the effects of flooding and achieve eventual lift off from water, or sinking deeper under water and the associated flow behaviour.

6.4.2 Numerical result analysis

For an originally skimming body subject to flooding from its leading edge, depending on the flooding conditions as well as the body's physical characteristics such as buoyancy, our flooding model (6.27) - (6.29) yields two distinct outcomes: the body is either able to withstand the effects of flooding, go through a transition phase fully or partially under water, and eventually emerge from the water again; or it is unable to obtain sufficient lift from the ambient flow and sinks further into water until eventually hitting the solid flow bed. As part of our analysis we shall investigate the conditions under which such two distinct outcomes may be produced, as well as the effects of gravity and body buoyancy in our flooding model.

6.4.2.1 Extreme ground effects

For the purpose of our numerical experiments, the sinking of a body is characterised by the water depth H_2 decreasing close to zero under a section of the body. For a thin flat body with non-zero contact angle this can be either its leading or trailing edge, and as we shall see such a phenomenon is associated with singularities in the solutions of flow velocity and hydrodynamic pressure u_2 and π_2. Hence when the body becomes sufficiently close to the flow bed it produces an extreme ground effect, whereby the flow speed and pressure in a surrounding region become extremely large. At such time our numerical scheme breaks down and a new flooding model taking account of boundary layer and other possible effects will need to be developed.

The re-emergence of the body from underneath the flood on the other hand, is signified by its leading edge rising above the free surface of the incoming

upstream. In our numerical solutions this phenomenon is captured by the water depth variable $H_1(-1,t)$ at the leading edge decreasing to zero. From that point the body ceases to be flooded over by the incoming stream, and any residual water above the body will eventually exit into the downstream flow via the trailing edge. As soon as the upper surface of the body becomes dry the body resumes a skimming motion which is extensively discussed in Chapters 2 and 3. Note that if the scaled acceleration due to gravity $\hat{g} = \frac{\epsilon}{Fr}$ is small, then any hydrostatic effect of the flow above the flooded body can be neglected in our model (6.27) - (6.29), i.e. we can apply the atmospheric pressure condition at the upper surface of the body as soon as the flooding over the leading edge stops. In such a case the body effectively transitions into a skimming motion as soon as the flooding over the leading edge stops before its upper surface is completely dry.

For the purpose of computational simplicity we shall stop our numerical scheme as soon as $H_1(-1,t)$ becomes zero or close to zero, even though we could carry on with the solution by modifying the flux condition at the leading edge to account for $H_1(-1,t) = u_1(-1,t) = 0$ and marching our solutions until the upper surface becomes completely dry.

Fig. 6.7 shows the response for a body that makes an initial angle of $\theta = -0.2$ with the flow bed and has an initial downward velocity of $V_m = -0.1$. This body is initially completely submerged in undisturbed water with free surface height of one, i.e. $H_1(x,0) + H_2(x,0) = 1$, $(x \in [-1,1])$. The solutions of the water depth H_1 at various times are given in Fig. 6.7a; note at the leading edge its depth at $t = 0$ has a positive value of 0.2. As time progresses this body first sinks deeper into water, a short time after ($t \sim 0.99$) it begins a process to emerge from the water again. This can be seen in the solutions of the body's vertical centre of mass position Y_m over time in Fig. 6.7f. The flooding over the body comes to a stop at $t \sim 3.7$, at which point the leading edge of the body rises to the same height as the incoming displaced stream, which is signified by the water depth H_1 decreasing to zero at the leading edge as shown in Fig. 6.7a,

6.7g. Since the flood from the leading edge propagates above the body in the form of shallow water waves, at early times when part of the flow close to the trailing edge has not yet felt the effects of flooding, "sharp-corners" can be seen in the solutions of H_1, u_1, (i.e. Fig. 6.7a, 6.7c at $t \sim 0.92$ and $t \sim 1.85$).

Fig. 6.7g shows the depth of the water over the body at the leading edge over time, $H_1(-1,t)$. At early times ($t <\sim 0.99$) the body descends deeper into water while the flow depth above the body $H_1(-1,t)$ increases; as the body eventually begins to ascend ($t \geq\sim 0.99$) this depth $H_1(-1,t)$ decreases. Fig. 6.7h shows the height of the free surface at the leading edge, i.e. $H_1(-1,t) + H_2(-1,t)$. Note this height is always on the increase from $t = 0$ to $t \sim 3.69$, the time at which the body's leading edge re-emerges from water.

Fig. 6.8 and 6.9 demonstrate the cases where the body's leading and trailing edges are getting close to hitting the flow bed respectively. Under such circumstances we witness an extreme ground effect where the hydrodynamic pressure in a surrounding region under the body becomes large, while the flow speed goes through rapid adjustments in such a region.

In the case of the body's trailing edge moving close to the flow bed, the hydrodynamic pressure under the body increases rapidly in a region close to this edge. However the Kutta condition demands the hydrodynamic pressure to be zero at the edge of flow separation. We therefore witness a rapid decrease of pressure near the body's trailing edge, see Fig. 6.8e; corresponding to such a rapid pressure drop Fig. 6.8d shows the flow speed grows exponentially close to this edge. The pressure and flow velocity gradients $\frac{\partial \pi_2}{\partial x}$, $\frac{\partial u_2}{\partial x}$ become discontinuous at this edge as the body gets sufficiently close to the flow bed and our numerical algorithm breaks down.

On the other hand when the body's leading edge becomes close to hitting the flow bed, a strong adverse pressure gradient develops in region 2 at the leading edge and in a small region after, and the hydrodynamic pressure grows extremely large close to this edge, see Fig. 6.9e. This high pressure phenomenon is also accompanied by a reversed flow in a small region enclosing the leading

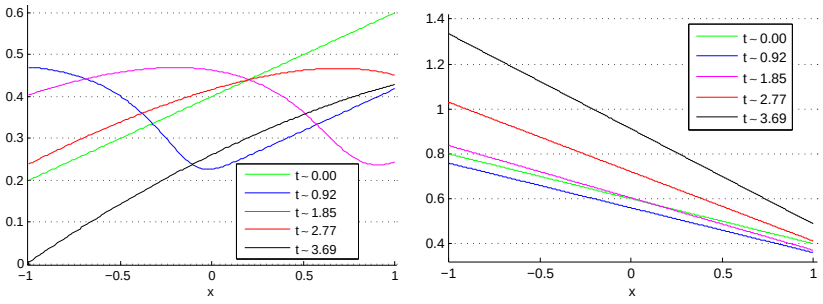

(a) H_1.

(b) H_2.

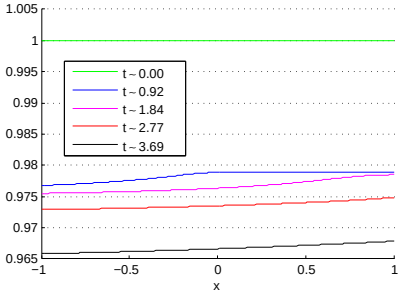

(c) u_1.

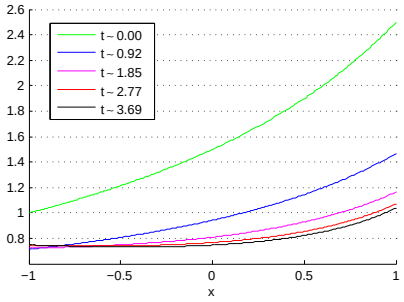

(d) u_2.

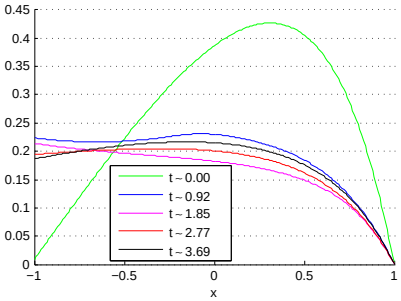

(e) π_2.

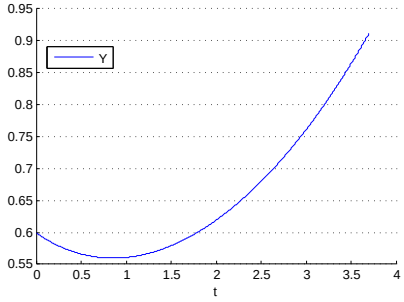

(f) Y_m.

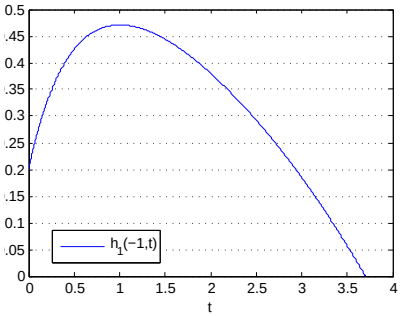

(g) $H_1(-1,t)$.

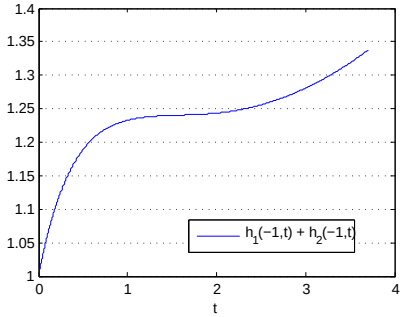

(h) $H_1(-1,t) + H_2(-1,t)$.

Figure 6.7: A body re-emerging from under water over time. The body has scaled mass and moment of inertia of $M = 4$, $I = 1$ respectively, and is configured so that $Y_m(0) = 0.6, \theta(0) = -0.2, V_m(0) = -0.1$ and $\omega(0) = 0$. The scaled gravity and buoyancy terms are $\hat{g} = 0.1$, $\hat{\mathcal{A}} = 0$. The body is initially completely submerged in water and has fresh flood coming over its body from the leading edge. At time $t \sim 3.69$ the leading edge of the body is able to rise above the incoming flood and re-emerge from water.

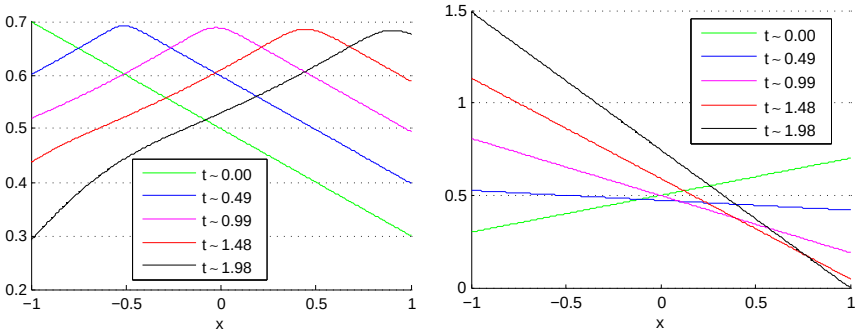

(a) H_1.

(b) H_2.

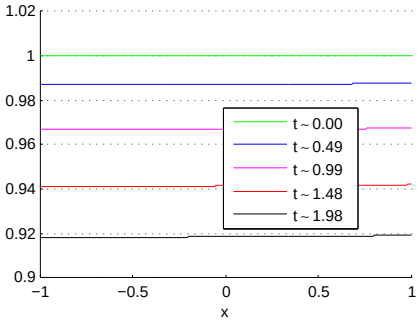

(c) u_1.

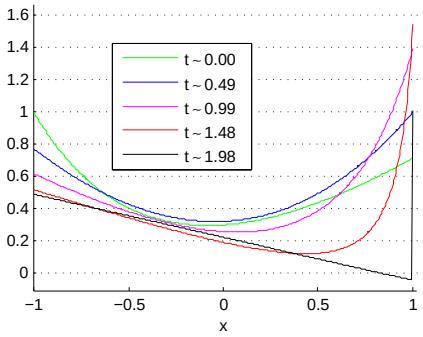

(d) u_2.

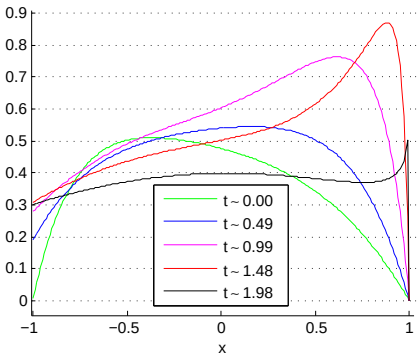

(e) π_2.

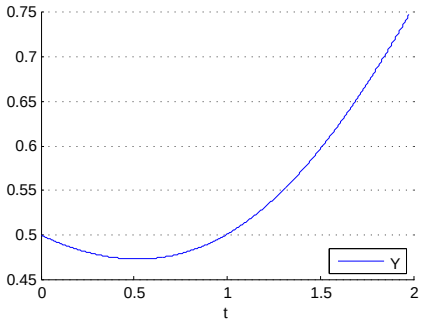

(f) Y_m.

Figure 6.8: A flooded body whose trailing edge becomes close to hitting the flow bed. The body has scaled mass and moment of inertia of $M = 4$, $I = 1$ respectively, and is configured so that $Y_m(0) = 0.5, \theta(0) = -0.2, V_m(0) = -0.1$ and $\omega(0) = -0.5$. The scaled gravity and buoyancy terms are $\hat{g} = 0.1$, $\hat{\mathcal{A}} = 0$. The body is initially completely submerged in water. As the trailing edge of the body gets close to the flow bed, at $t \sim 1.98$ for instance, singularities in the flow speed u_2 and pressure π_2 begin to develop at this edge.

edge, see Fig. 6.9d. As the body gets closer to the flow bed and $H_2(-1,t) \to 0$, the flow speed at this edge becomes negative and unbounded as implied by the conservation relation (6.50). As with the case of the body's trailing edge hitting the flow bed, the pressure and flow velocity gradients $\frac{\partial \pi_2}{\partial x}$, $\frac{\partial u_2}{\partial x}$ grow extremely large, and our numerical algorithm terminates before their solutions become singular.

Given such rapid change of flow velocity and dynamic pressure in a subregion of the under-body flow, we check the stability of our numerical algorithm by solving the flow problem in Fig. 6.9 over three increasingly fine grids. The first grid, denoted as D_1, on which we perform our numerical procedures is set to $(\Delta x, \Delta t) = (10^{-2}, 10^{-3})$. Repeating the procedures on two finer grids D_2 and D_3, which are set to $(10^{-3}, 10^{-4})$ and $(10^{-3}, 5 \times 10^{-5})$ respectively, yields further two sets of solutions. The solutions of u_2 and π_2 derived from these three grids are given in Fig. 6.10. The comparisons demonstrate that the three set of solutions converge as we gradually refine the grid step sizes.

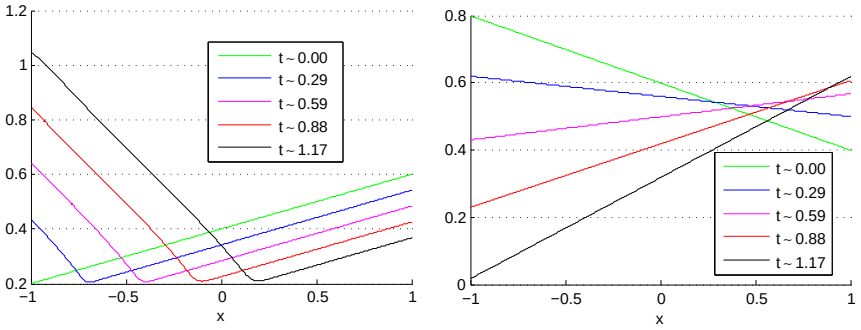

(a) H_1.

(b) H_2.

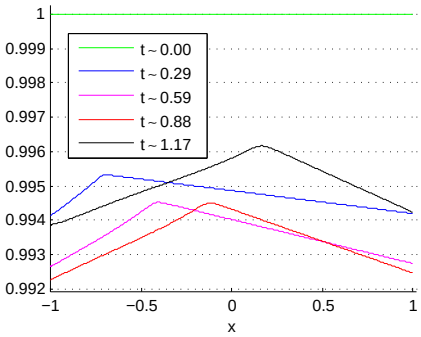

(c) u_1.

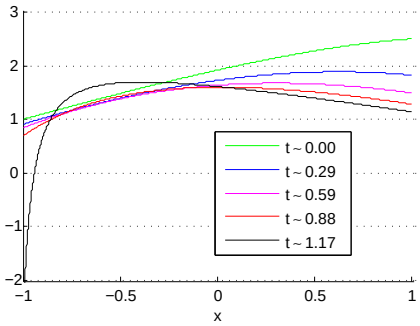

(d) u_2.

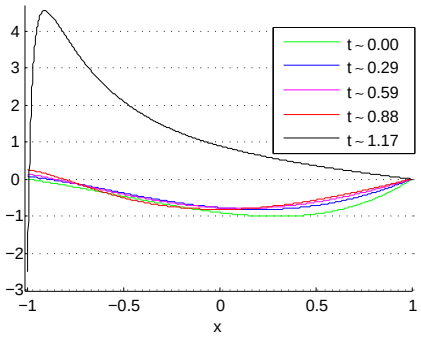

(e) π_2.

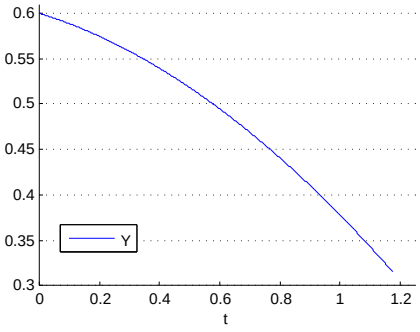

(f) Y_m.

Figure 6.9: A flooded body whose leading edge comes close to hitting the flow bed. The body has scaled mass and moment of inertia of $M = 4$, $I = 1$ respectively, and is configured so that $Y_m(0) = 0.6, \theta(0) = -0.2, V_m(0) = -0.1$ and $\omega(0) = 0.5$. The scaled gravity and buoyancy terms are $\hat{g} = 0.1$, $\hat{\mathcal{A}} = 0$. The body is initially completely submerged in water. As the leading edge of the body comes close to the flow bed, at $t \sim 1.17$ for instance, singularities in the flow speed u_2 and pressure π_2 begin to develop at this edge.

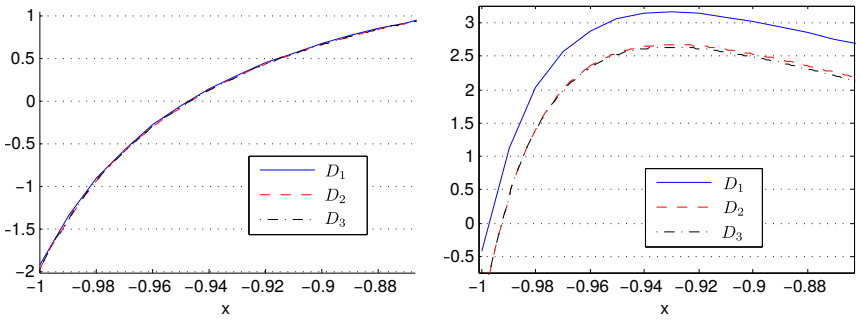

(a) $u_2(x, 1.17)$.

(b) $\pi_2(x, 1.17)$.

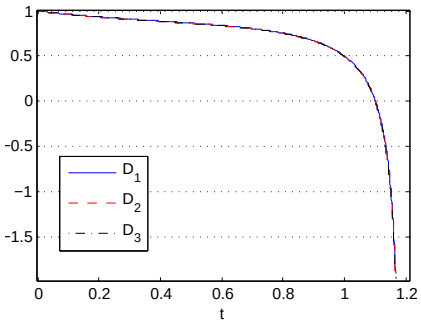

(c) $u_2(-1, t)$.

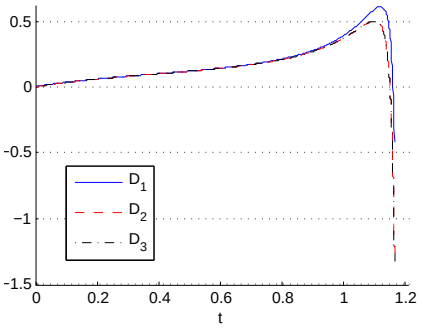

(d) $\pi_2(-1, t)$.

Figure 6.10: Figures demonstrates the convergence of the numerical solutions of u_2, π_2 in the flow region under the body for various grid step sizes. The initial conditions of the system are the same as those given in Fig. 6.9, and the solutions of u_2 and π_2 are sampled at $t = 1.17$, which corresponds to the body's leading edge getting close to hitting the flow bed. The grid step sizes of $D_1 = (\Delta x, \Delta t)$ are set to $(10^{-2}, 10^{-3})$, and D_2, D_3 are set to $(10^{-3}, 10^{-4})$ and $(10^{-3}, 5 \times 10^{-5})$ respectively.

6.4.2.2 Effects of gravity and body buoyancy

In this section we analyse the effects of the body buoyancy as well as gravity in the ambient flow has on the body that is subject to flooding.

The scaled buoyancy parameter $\hat{\mathcal{A}}$ represents the body's acceleration due to the net effects of buoyancy and gravity. $\hat{\mathcal{A}} = 0$ represents the body's buoyancy cancelling out its gravitational effect; $\hat{\mathcal{A}} > 0$ represents gravity overcoming buoyancy and vice versa. Fig. 6.11 shows solutions of the flooding system for the cases of $\hat{\mathcal{A}} = \{-1, 0, 1\}$, and in all cases the body is initially submerged in water. A buoyant body is able to emerge from the water rapidly as can be seen for the case of $\hat{\mathcal{A}} = -1$, whose solutions terminate at $t \sim 0.3$ as its leading edge becomes dry. The solutions for the case of $\hat{\mathcal{A}} = 0$ have been given previously in Fig. 6.7, the body is able to eventually emerge from water at $t \sim 3.69$ after a relatively longer underwater transition period. For the case of $\hat{\mathcal{A}} = 1$ where the body's acceleration due to buoyancy is less than that of gravity, the body sinks rapidly towards the flow bed as can be seen in Fig. 6.11a, and at $t \sim 1.24$ the solutions break down. Note that pressure force on the body, given by $\int_{-1}^{1} \pi_2(s,t)ds$, becomes large as $\hat{\mathcal{A}}$ increases (see Fig. 6.11f), whereas the average flow speed in region 2 decreases more rapidly with increasing values of $\hat{\mathcal{A}}$ (see Fig. 6.11e).

To analyse the effects of gravity we prescribe our flooding system with three configurations of scaled gravity $\hat{g} = \{0, 0.5, 1\}$, where $\hat{g} = \frac{\epsilon}{Fr}$ with $\epsilon \ll 1$ and $Fr \sim O(1)$ for our given surfboard problem. Notice that the flux condition at the leading edge 6.49 in certain ways controls on how large the scaled gravity can be – large values of $\hat{g}$ forces the solution of u_1 becoming imaginary as the free surface height at the leading edge becomes large, specifically our flooding model fails when

$$H_1(-1,t) + H_2(-1,t) > 1 + \frac{1}{2\hat{g}}. \tag{6.67}$$

Fig. 6.11 demonstrates the solutions for the three cases of scaled gravity.

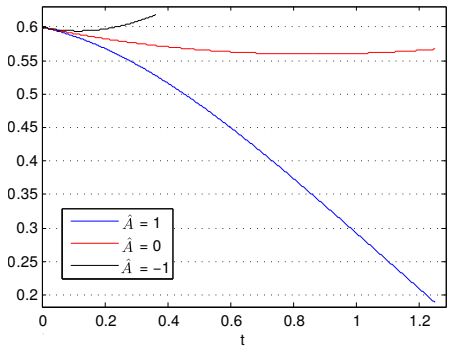

(a) $Y_m(t)$.

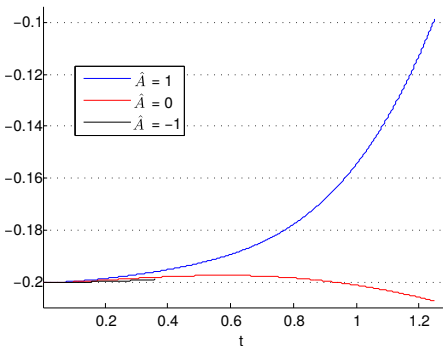

(b) $\theta(t)$.

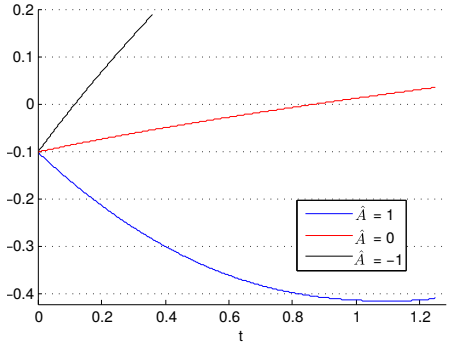

(c) $V(t)$.

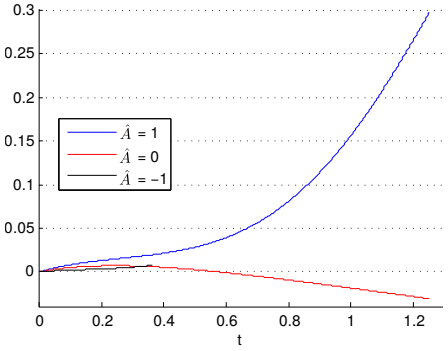

(d) $\omega(t)$.

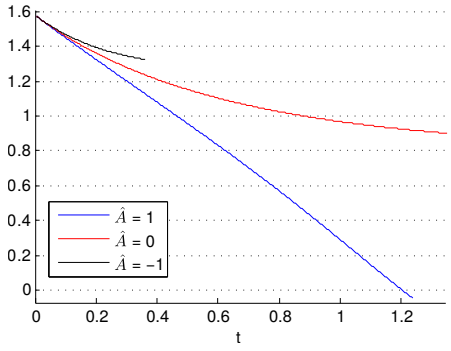

(e) Average u_2 over time.

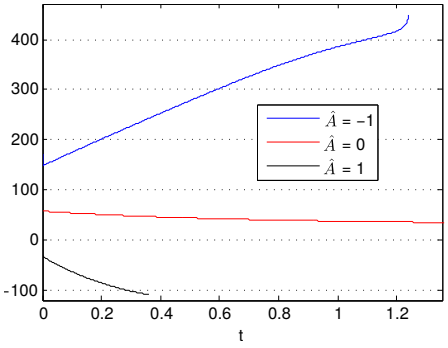

(f) $\int_{-1}^{1} \pi_2(s,t)ds$ over time.

Figure 6.11: Figures show solutions of the flooding system with various configurations of the body buoyancy parameter $\hat{\mathcal{A}}$. The body has scaled mass and moment of inertia of $M = 4$, $I = 1$ respectively, and is configured so that $Y_m(0) = 0.6, \theta(0) = -0.2, V_m(0) = -0.1$ and $\omega(0) = 0$. The scaled gravity term is $\hat{g} = 0.1$. The body is initially completely submerged in water and has fresh flood coming over its body from the leading edge.

As the effects of gravity increases, the time required for the body to emerge from water also increases. This can be seen in Fig. 6.12a as the body's leading edge emerges from water at $t \sim 3.7$ for $\hat{g} = 0$, whereas the required time for the case of $\hat{g} = 0.5$ increases to $t \sim 5.9$. For the case of $\hat{g} = 1$ our flooding system breaks down due to the solution of u_1 becoming imaginary in a very short time ($t \sim 0.2$). The hydrodynamic pressure force exerted on the lower section of the body decreases as the gravity effect increases as can be seen in Fig. 6.12f.

6.5 Conclusions

In this chapter we analysed the effects of flooding has on a body that is originally in a skimming motion, specifically with in mind that of a surfboard carrying the weight of an adult surfer. The water is assumed to be shallow in comparison to the length of the board, and our analysis shows that the flow over the board is mainly gravity driven. Assuming the flow above and the below the board separates smoothly from the body at its sharp trailing edge, a localized pressure jump condition is then imposed at the leading edge to satisfy the Kutta's condition at the trailing edge. Our 2D model is unable to fully account for the buoyancy effect of the body, which in reality has an important role to play in the motions of a surfboard. As such a buoyancy parameter is introduced in the body's momentum equations to compensate for this buoyancy effect.

In a linearised analysis of the flooding model where the flow depth above the board in comparison to that of below is small, we find the original flooding model can be simplified to a system of linear equations. Under our pre-defined conditions such linear system has a positive eigenvalue, and any perturbations to this system grow exponentially with time. The complete flooding model is solved using an implicit finite difference scheme, and various conditions under which a body is either able to emerge from water or sink to the bottom are analysed. In particular we demonstrated that as the board gets close to the flow bed an extreme ground effect occurs, where the pressure becomes extremely large and

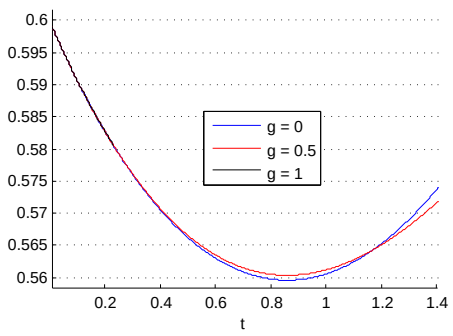

(a) $Y_m(t)$.

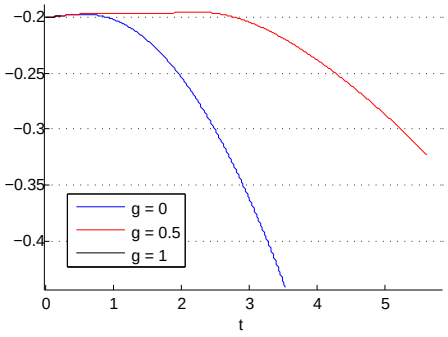

(b) $\theta(t)$.

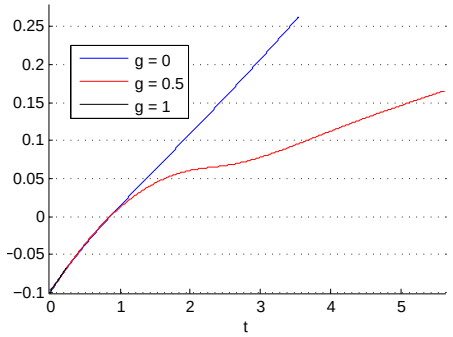

(c) $V(t)$.

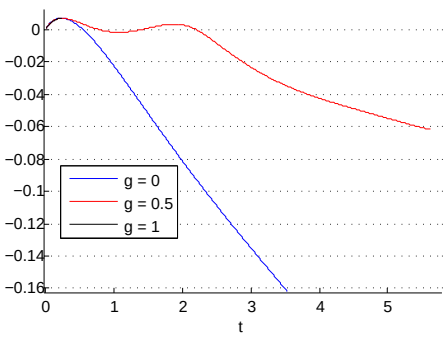

(d) $\omega(t)$.

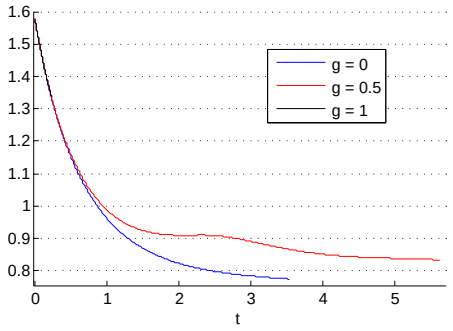

(e) Average u_2 over time.

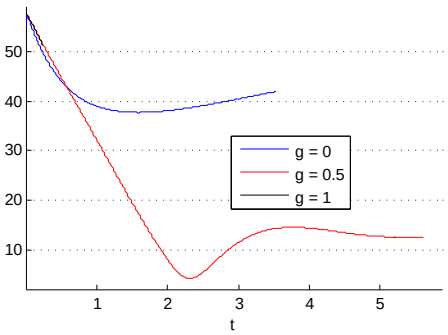

(f) $\int_{-1}^{1} \pi_2(s,t)ds$ over time.

Figure 6.12: Figures show solutions of the flooding system with various configurations of the scaled gravity parameter $\hat{g}$. The body has scaled mass and moment of inertia of $M = 4$, $I = 1$ respectively, and is configured so that $Y_m(0) = 0.6, \theta(0) = -0.2, V_m(0) = -0.1$ and $\omega(0) = 0$. The scaled gravity term is $\hat{g} = 0.1$. The body is initially completely submerged in water and has fresh flood coming over its body from the leading edge.

inverted flow begins to develop. We further analysed how the body's buoyancy and gravity effects in the flow can affect our flooding model. It is shown that the less buoyant the body is, the greater the dynamic pressure force and the slower the flow speed under the bod. Depending on how large the gravity effect is in our model flow, the leading edge flux and pressure jump conditions impose a limit on the free-surface height at this edge. The larger the effect of gravity, the smaller the leading edge free-surface height our flooding model can sustain. Our analysis showed that a larger gravity effect decreases the hydrodynamic lift force on the body and therefore prolongs the time the body spends under water.

Chapter 7

Conclusions and future research

7.1 Conclusions

In this thesis we have provided extensions to some existing shallow water skimming theories, as well as providing new models for skimming, rebound and sinking bodies in shallow water. Our modelling is primarily based on the method of asymptotic analysis which exploits the existence of several small model parameters, such as the contact angle and the ratio of the water depth to the skimming body length.

In Chapter 2 we reviewed and derived the thin body skimming model by Hicks & Smith [57]. Asymptotic analysis was performed to understand the importance of the skimming body's mass and moment of inertia. For a body with small mass we demonstrated that it is able to skip out of water with a "super-elastic" effect. For a body with small moment of inertia the contact angle goes through rapid change when in contact with water. Such "flattening" of the angle reduces the normal lift on the body and reduces its ability to achieve separation from water. In practice a skipping stone is typically given a spin in

order to stabilise its contact angle with water by a gyroscopic effect. Such a stabilisation effect can be captured in our model via an increased moment of inertia. We also presented a model that captures the characteristics of a stone going through multiple rebounds.

Chapter 3 presents a Liu & Smith paper published in *Proc. R. Soc.* 2014. The paper provides further extension of the Hicks & Smith asymptotic model of a lightweight body. The skimming model, after various parameter reductions and transformations, reduced to be solely dependent on the initial condition of the vertical entry velocity. Our analysis demonstrated the skimming process of a body with high entry velocity comprises three distinct pressure-body response stages, with each stage's temporal scale dependent on certain inverse powers of the entry velocity. For a body with comparatively low entry velocity only the pressure-body response regime is present, and direct analytical solutions can be obtained.

Chapter 4 analysed the water separation from a smooth blunt body in skimming motion. The dead-rise angle between the body and the undisturbed free-surface is assumed to be small, and we focused on a small region enclosing the trailing edge where the free-surface separation occurs. Some contrasts of this particular problem with the Wagner related impact problems are, amongst others, that a) we do not expect any splash jet at this edge; b) the position of the trailing edge is not (necessarily) expected to extend further along the body away from the initial impact point; c) the flow's boundary condition can no longer be linearised onto the undisturbed free-surface. We formulated a conventional-looking potential flow problem and obtained solutions to the stream function for this separation region, which are determined by the upstream fluid velocity and pressure.

In Chapter 5 we investigated the shallow water skimming problem of a bluff body. The skimming process is divided into an impact and a planing stage. At the early impact stage the body's leading and trailing edges initially evolve according to the square root of time; as time grows the two edges eventually

begin to evolve linearly with time. The hydrodynamic pressure under the body is initially high everywhere. As the body falls deeper into water a negative pressure region begins to develop near the trailing edge; this negative pressure region grows larger over time and eventually reaches the trailing edge, at which point the trailing edge stops extending further away from the initial impact point and the impact stage terminates. We find that for a body with sufficiently small mass and a positive rotation, it is able to transition rapidly from the impact to the planing stage. The value of the adverse pressure gradient at the trailing edge plays a critical role during the planing stage, and there exists a maximum adverse pressure gradient that can be sustained at this edge. If on the other hand the adverse pressure gradient at the trailing edge is weak, the body's planing motion can be separated into three phases. We note that under our linearised planing regime the planing body is not able to achieve separation from water, to do so we must wait until the body grows out of our linearised regime.

Chapter 6 analysed the effects of flooding on a body that is originally in a skimming motion. The water was assumed to be shallow in comparison to the length of the board, and the flows above and below the board were assumed to separate smoothly from its sharp trailing edge. A localized pressure jump condition is imposed at the leading edge to satisfy the Kutta condition at the trailing edge. We further introduced a buoyancy parameter to compensate for our 2D model's inability to fully capture a body's buoyancy effect. The flooding model was solved using an implicit finite difference scheme, and various conditions under which a body was either able to emerge from water or sink to the bottom were analysed. We demonstrated that as the body gets close to the flow bed an extreme ground effect occurs, where the pressure becomes extremely large and inverse flow begins to develop. We further analysed how the body's buoyancy and gravity effects in the flow can affect our flooding model.

7.2 Future research

There remain many open questions as well as further work on our shallow water skimming theories.

- Concerning the skimming of a flat body in Chapter 2 and 3, under the assumption of smooth separation and in the absence of any gravity and viscous effects, the fluid separates from the sharp trailing edge at a velocity of u_0, i.e. same as that of far upstream. The 2D mass conservation equation, which ignores any lateral flow, implies the thrown-forward splash jet has a speed of u_0 and in turn gives rise to the leading edge momentum condition of (2.10). This skimming theory may appear inconsistent with the early stage of impact in Wagner theory, which predicts a thin but fast jet with speed much greater than u_0. There is in fact no inconsistency however, since the present approach and Wagner's take quite different length scales into consideration. [1] also offers more discussions of the various stages of jet behaviour during impact. By extending the theory to 3D and incorporating the lateral flow we may offer a resolution on such inconsistency. Likewise we also note such inconsistency applies to our skimming model for a blunt body in Section 5.2, where similar momentum condition is applied as a boundary condition at both the leading and trailing edges.

- During skimming part of the body's horizontal momentum is transferred to the fluid. For a small contact angle and in the absence of viscous effects such loss of energy is negligible. However for a body that goes through multiple rebounds and at contact angles that are not always small, such energy loss becomes significant over time and should be incorporated into part of our modelling. On a similar note, a body going through multiple rebounds will experience non-negligible air resistance and this can be incorporated into our model.

- Impacts on fluid by multiple bodies have various industrial and engineering

applications, such as for aircraft flying through cirrus clouds composed of ice crystals. It is estimated that every litre of such cloud on average can contain 30 ice crystals, each with length of around 0.25 millimeters. Multi-body impacts and collisions on an aircraft's damp fuselage would be a practical modeling scenario. Some related multi-body flow interaction problems have been investigated in [26, 30], and extensions to multi-body water entry problems would be interesting.

- Under certain conditions air cushioning effects can have a noticeable effect on the impact problem. This is especially the case when the air to water density ratio is relatively high and the dead-rise angle is sufficiently small. Under such circumstances [53] shows the air cushioning/air trapping effect can have a leading order influence on the flow during impact, particularly for blunt bodies. Similar studies are given in [3, 27, 2, 56, 58]. A further refinement to our models for both flat and blunt bodies would be to account for air cushioning effects during impact.

- As demonstrated in Chapter 6, an originally skimming body that is subjected to flooding is able to rebound from water under certain favourable conditions. As such it would be interesting to extend our skimming model for a thin body in Chapter 2 to incorporate such a phenomenon, in particular in the case of multiple rebounds.

- As investigated in Chapters 5, the fluid separation from a blunt body coincides with a region of low pressure near the trailing edge, where cavitation as well as air-water mixing may occur. Viscosity effects in the separation region have vital implications on the pressure gradient in such a region and on the body's planing motion. Developing a theoretical framework for such a phenomenon would be an important extension to the skimming theory.

The theory of shallow water impact and skimming is far from finished, and there are many important extensions that have not been discussed in our thesis.

In addition to the theoretical modelling aspect, a regrettable omission is an appropriate experiment that may connect our model with physical observations. To this extent there are other related experiments such as [37] that have shown encouraging qualitative agreements with our theory. Additional experiments that involve various smooth body profiles as well as rotations may offer valuable insights to further validate and enhance our existing model.

Appendix A

Numerical scheme

A.1 Asymptotic analysis of skimming object with small mass

The early impact model (5.37) in its current form is difficult to analyse, instead we shall assign it a large mass $M \sim O(\epsilon^{\frac{2}{3}})$ with no initial angular velocity (i.e. $\omega_0 = 0$), then from the analytical results of Section 5.3, we asymptotically expand our system variables as follows:

$$x_1 = -\sqrt{3V_0 t} + \delta x_{11}, \tag{A.1a}$$

$$x_2 = \sqrt{3V_0 t} + \delta x_{21}, \tag{A.1b}$$

$$Y = V_0 t + \delta Y_1, \tag{A.1c}$$

$$f = \delta f_1, \tag{A.1d}$$

$$g = -\frac{3}{2}V_0^2 + \delta g_1, \tag{A.1e}$$

where $\delta \ll 1$. Substituting these variables into model (5.37) gives the following leading order equations:

$$Y_1 = \sqrt{V_0 t}(x_{11} - x_{21}), \tag{A.2a}$$

$$f_1 = -\frac{V_0}{2}(x_{11} + x_{21}), \tag{A.2b}$$

$$f_1 = V_0(x_{11} + x_{21}) + V_0 t(\frac{dx_{11}}{dt} + \frac{dx_{21}}{dt}), \tag{A.2c}$$

$$g_1 = \frac{\sqrt{3}}{2}\big(V_0 t\big)^{\frac{3}{2}}\left[\frac{d^2}{dt^2}\Big(x_{11} - x_{21}\Big) + \frac{3}{t}\frac{d}{dt}\Big(x_{11} - x_{21}\Big) + \frac{3}{4t^2}\Big(x_{11} - x_{21}\Big)\right], \tag{A.2d}$$

$$M\frac{d^2 Y_1}{dt^2} + 3V_0^2\sqrt{3V_0 t} = 0. \tag{A.2e}$$

Equations (A.2b), (A.2c) can be combined to obtain the following relation:

$$x_{11} + x_{21} = Ct^{-\frac{3}{2}}, \tag{A.3}$$

where C is an integration constant. As $t \to 0$ we expect the edges x_1 and x_2 to coincide at one point, i.e. $x_{11}(0) = x_{21}(0) = 0$, therefore the constant C should take on the value of 0, hence

$$x_{11} + x_{21} = 0, \tag{A.4}$$

this relation can be substituted into (A.2) to obtain the following differential equation:

$$\frac{d^2 x_{11}}{dt^2} + \frac{1}{t}\frac{dx_{11}}{dt} - \frac{1}{4t^2}x_{11} = \frac{9V_0^2}{2M}, \tag{A.5}$$

using variation of parameters we obtain the following solutions to (A.2):

$$x_{11} = Kt^{\frac{1}{2}} + \frac{6}{5}\frac{V_0^2}{M}t^2, \tag{A.6a}$$

$$x_{21} = -Kt^{\frac{1}{2}} - \frac{6}{5}\frac{V_0^2}{M}t^2, \tag{A.6b}$$

$$Y_1 = 2\sqrt{\frac{V_0 t}{3}}\left(Kt^{\frac{1}{2}} + \frac{6}{5}\frac{V_0^2}{M}t^2\right), \tag{A.6c}$$

$$f_1 = 0, \tag{A.6d}$$

$$g_1 = \frac{7\sqrt{3}}{2M}V_0^{\frac{7}{2}}t^{\frac{3}{2}} - 2\sqrt{\frac{V_0}{3}} \tag{A.6e}$$

Bibliography

[1] Korobkin A. A. Shallow-water impact problems. *J. Eng Math*, 35, 1999.

[2] Korobkin A. A., Ellis A. S., and Smith F. T. Trapping of air in impact between a body and shallow water. *J Fluid Mech*, 611, 2008.

[3] Korobkin A. A., Ellis A. S., and Smith F. T. Trapping of air in impact between a body and shallow water. *J. Fluid Mech.*, 611, 2008.

[4] Korobkin A. A. and Pukhnachov V. V. Initial stages of water impact. *Ann. Rev. Fluid Mech.*, 20, 1988.

[5] Korobkin A. A. and Scolan Y. M. Three-dimensional theory of water impact. Part 2. Linearized Wagner problem. *J. Fluid Mech.*, 549, 2006.

[6] King A. C., Tuck E. O., and Vanden-Broeck J. M. Air-blown waves on thin viscous sheets. *Phys of Fluids A*, 5, 1993.

[7] Green A. E. The gliding of a plate on a stream of finite depth. *Proc. Camb. Phil. Soc.*, 31, 1935.

[8] Green A. E. The gliding of a plate on a stream of finite depth. Part II. *Proc. Camb. Phil. Soc.*, 32, 1936.

[9] Messiter A. F. Boundary-layer flow near the trailing edge of a flat plate. *SIAM J Appl Math*, 18(1), 1970.

[10] Mackie A. G. The water entry problem. *Q. J. Mech. and Appl. Math.*, 22(1), 1969.

[11] Worthington A. M. On the forms assumed by drops falling vertically on a horizontal plate. *Proc Roy Soc A*, 1876.

[12] Ellis A. S., Smith F. T., and White A. H. Droplet impact on to a rough surface. *Q J Mech Appl Math*, 64(2), 2011.

[13] Noble B. *Methods based on the Wiener-Hopf Technique for the solution of partial differential equations.* Pergamon Press, 1958.

[14] Scheichl B., Kluwick A., and Smith F. T. Break-away separation for high turbulence intensity and large Reynolds number. *J. Fluid Mech.*, 670, 2011.

[15] Clanet C., Hersen F., and Bocquent L. Secrets of successful stone-skipping. *Nature*, 427, 2004.

[16] Kaur D. Motion of a thethered blade beneath a free surface. Master's thesis, University College London, 2013.

[17] Küchemann D. *The aerodynamic design of aircraft.* American Institute of Aeronautics & Astronautics, 2006.

[18] Acheson D. J. *Elementary Fluid Dynamics.* OUP, 2002.

[19] Süli E. *Numerical solution of ordinary differential equations.* Oxford lecture notes, 2006.

[20] Batyaev E. A. and Khabakhpasheva T. I. Initial Stage of the Inclined Impact of a Smooth Body on a Thin Fluid Layer. *Fluid Dynamics*, 48(2), 2013.

[21] Tuck E. O. and Dixon A. Surf-skimmer planing hydrodynamics. *J. Fluid Mech.*, 205, 1989.

[22] Gakhov F. D. *Boundary value problems.* Pergamon Press, 1966.

[23] White F. M. *Fluid Mechanics.* McGraw-Hill Higher Education, 7 edition, 2011.

[24] Smith F. T. The Laminar Separation of an Incompressible Fluid Streaming Past a Smooth Surface. *Proc. R. Soc. Lond.*, 356(1687), 1977.

[25] Smith F. T. Laminar flow of an incompressible fluid past a bluff body: the separation, reattachment, eddy properties and drag. *J. Fluid Mech.*, 92, 1979.

[26] Smith F. T. and Ellis A. S. On interaction between falling bodies and the surrounding fluid. *Mathematika*, 56, 2010.

[27] Smith F. T., Li L., and Wu G. X. Air cushioning with a lubrication/inviscid balance. *J Fluid Mech*, 482, 2003.

[28] Smith F. T. and Wilson P. L. Fluid-body interactions: Clashing, skimming, bouncing. *Philos Transact A Math Phys Eng Sci*, 369(1947), 2011.

[29] Smith F. T. and Wilson P. L. Body-rock or lift-off in flow. *J. Fluid Mech.*, 735, 2013.

[30] Smith F. T. and Bowles R. G. A. Lifting multi-blade flows with interaction. *J. Fluid Mech.*, 415(203-226), 2000.

[31] Carrier G. F., Krook M., and Pearson C. E. *Functions of a complex variable.* SIAM, 2005.

[32] Batchelor G. K. *An introduction to fluid dynamics.* CUP, 1973.

[33] Streckwall H., Lindenau O., and Bensch L. Aircraft ditching: a free surface/free motion problem. *Archives of civil and mechanical engineering*, VII(3), 2007.

[34] Wagner H. Landing of seaplanes. *NACA*, TM(622), 1931.

[35] Wagner H. Über Stoß-und gleitvorgänge an der Oberflaäche von Flüssigkeiten (Phenomena associated with impacts and sliding on liquid surfaces). *Zeitschr. Math. Mech.*, 12, 1932.

[36] Watanabe I. Analytical Expression of Hydrodynamic Impact Pressure by Matched Asymptotic Expansion Technique. *Trans. West-Japan Soc. Naval Arch.*, 71, 1986.

[37] Hewitt I. J., Balmforth N. J., and McElwaine J. N. Continual skipping on water. *J. Fluid Mech.*, 2011.

[38] Oliver J. M. Water entry and related problems. *PhD Thesis*, 2002.

[39] Elliott J. W. and Smith F. T. Ice formation on a smooth or rough cold surface due to the impact of a supercooled water droplet. *J Eng Math*, 3 2015.

[40] Liu K. and Smith F. T. Collisions, rebounds and skimming. *Phil Trans Roy Soc A*, 372, 2014.

[41] Stewartson K. and Williams P. G. Self-induced separation. *Proc. R. Soc. Lond.*, A 312(181), 1969.

[42] Morton K. W. and Mayers D. F. *Numerical solution of partial differential equations.* CUP, 2005.

[43] Prandtl L. Motion of fluids with very little viscosity. *Tech Mem, NACA, Washington*, 452, 1904.

[44] Rosellini L., Hersen F., Clanet C., and Bocquet L. Skipping stones. *J. Fluid Mech.*, 000, 2005.

[45] Milne-Thomson L. M. *Theoretical Hydrodynamics.* Dover Publications, 1971.

[46] Greenhow M. Water entry into initially calm water. *Appl. Ocean Res.*, 9, 1987.

[47] Greenhow M. Water-entry and -exit of a horizontal circular cylinder. *Appl. Ocean Res.*, 10(4), 1988.

[48] Reinhard M., Korobkin A. A., and Cooker M. J. The bounce of a blunt body from a water surface at high horizontal speed. *27th International Workshop on Water Waves and Floating Bodies*, 2012.

[49] Schiffman M. and Spencer D. C. The Force of Impact on a Cone Striking a Water Surface (Vertical Entry). *Comm. Pure Appl. Math.*, 4, 1951.

[50] Lesser M. B. and Field J. E. The impact of compressible liquids. *Ann Rev Fluid Mech*, 15, 1983.

[51] Ablowitz M. J. and Fokas A. S. *Complex Variables*. CUP, 2003.

[52] Lighthill M. J. On Boundary Layers and Upstream Influence. II. Supersonic Flows without Separation. *Proc Roy Soc A*, 217, 1953.

[53] Moore M. R., Ockendon J. R., and Oliver J. M. Air-cushioning in impact problems. *IMA J. Appl Math*, 78, 2013.

[54] Hughes O. F. Solution of the wedge entry problem by numerical conformal mapping. *J. Fluid Mech.*, 56(1), 1972.

[55] Faltinsen O. M., Landrini M., and Greco M. Slamming in marine applications. *J. Engng Maths*, 48, 2004.

[56] Hicks P. D., Ermanyuk E. V., Gavrilov N. V., and Purvis R. Air trapping at impact of a rigid sphere onto a liquid. *J Fluid Mech*, 695, 2012.

[57] Hicks P. D. and Smith F. T. Skimming impacts and rebounds on shallow liquid layers. *Proc. R. Soc.*, 2010.

[58] Hicks P. D. and Purvis R. Air cushioning and bubble entrapment in three-dimensional droplet impacts. *J. Fluid Mech.*, 649, 2010.

[59] Cointe R. and Armand J. L. Hydrodynamic impact analysis of a cylinder. *ASME J. Offshore Mech. Arc. Engng*, 109, 1987.

[60] Purvis R. and Smith F. T. Droplet impact on water layers: post-impact analysis and computations. *Phil Trans Roy Soc A*, 363, 2005.

[61] Scardovelli R. and Zaleski S. Direct numerical simulation of free-surface and interfacial flow. *Mech, Ann Rev Fluid*, 31, 1999.

[62] Edge R. D. The surf skimmer. *Am. J. Phys*, 36, 1968.

[63] Britton R. K. and Bond T. H. An overview of shed ice impact studies in the NASA Lewis Icing Research Tunnel. *NASA Technical Reports Server*, 1993.

[64] Goldstein S. Concerning some solutions of the boundary-layer equations in hydrodynamics. *Proc Camb Phil Soc*, 26(1–30), 1930.

[65] Goldstein S. On laminar boundary-layer flow near a position of separation. *Quart J Mech*, 1(43–69), 1948.

[66] Howison S. D., Ockendon J. R., and Oliver J. M. Deep- and shallow-water slamming at small and zero deadrise angles. *J. Engng Math.*, 42, 2002.

[67] Howison S. D., Ockendon J. R., and Oliver J. M. Oblique slamming, planing and skimming. *J. Engng Math.*, 48, 2004.

[68] Howison S. D., Ockendon J. R., and Wilson S. K. Incompressible water-entry problems at small deadrise angles. *J. Fluid Mech.*, 222, 1991.

[69] Thoroddsen S. T. The ejecta sheet generated by the impact of a drop. *J. Fluid Mech*, 451, 2002.

[70] Von Kármán T. The impact of seaplanes floats during landing. *NACA*, TN(321), 1929.

[71] Khabakhpasheva T. I. Impact of an Elastic Spherical Shell on a Thin Fluid Layer. *Fluid Dynamics*, 50(2), 2015.

[72] Khabakhpasheva T. I. and Korobkin A. A. Inclined impact of smooth body on thin liquid layer. *Proc. 27-th Intern. Workshop on Water Waves and Floating Bodies*, 2012.

[73] Khabakhpasheva T. I. and Korobkin A. A. Oblique impact of a smooth body on a thin layer of liquid. *Proc. R. Soc.*, (469), 2013.

[74] Neiland V. Y. Theory of laminar boundary-layer separation in supersonic flow. *Izv AN SSSR, Mekh Zhidk i Gaza*, 4, 1969.

[75] Gent R. W., Dart N. P., and Candale J. T. Aircraft icing. *Phil. Trans. R. Soc. London.*, A(358), 2000.

[76] Mei X., Liu Y., and Yue D. On the water impact of general two-dimensional sections. *Appl. Ocean Res.*, 21, 1999.

[77] Scolan Y. M. and Korobkin A. A. Three-dimensional theory of water impact. Part 1. Inverse Wagner problem. *J. Fluid Mech.*, 440, 2001.